



UNIVERSITAT_{DE}
BARCELONA

Blood-Brain Barrier Shuttles: From Design to Application

Pol Arranz Gibert



Aquesta tesi doctoral està subjecta a la llicència **Reconeixement- NoComercial – SenseObraDerivada 3.0. Espanya de Creative Commons.**

Esta tesis doctoral está sujeta a la licencia **Reconocimiento - NoComercial – SinObraDerivada 3.0. España de Creative Commons.**

This doctoral thesis is licensed under the **Creative Commons Attribution-NonCommercial-NoDerivs 3.0. Spain License.**

2016

Tesi doctoral

Pol Arranz Gibert



UNIVERSITAT DE
BARCELONA

Blood-Brain Barrier Shuttles: From Design to Application

Pol Arranz Gibert



UNIVERSITAT DE
BARCELONA



Programa de doctorat de química orgànica

Blood-Brain Barrier Shuttles: From Design to Application

Pol Arranz Gibert

Tesi doctoral dirigida per:

Prof. Ernest Giralt Lledó

Universitat de Barcelona
Facultat de Química
Departament de Química Orgànica

Dra. Meritxell Teixidó

IRB Barcelona
Programa de Química i
Farmacologia Molecular

Barcelona, 2016.

CONTENTS

ABBREVIATIONS	i
INTRODUCTION	1
Origins of the Gatekeepers of the Brain—Evolution of Brain Barriers	3
Understanding the Door—Physiology of the Blood-Brain Barrier	8
Reasons to Look Inside—Physiology and Disease of the CNS: Social Impact	14
Devising a Key—Peptides as Therapeutics and for Drug Delivery to the Brain	16
OBJECTIVES	21
RESULTS AND DISCUSSION	25
Chapter 1: Study of Passive Diffusion BBB Shuttles	27
1.1. Peptide-Shuttle Design	32
1.2. Transport Ability of (PhPro) ₄ Shuttle Using the PAMPA Assay	33
1.3. Design and Synthesis of a 16-Stereoisomer Library of (PhPro) ₄	37
1.4. Physicochemical Characterization of Pro ₄ and (PhPro) ₄ Shuttle	38
1.5. Passive Diffusion Transport Studies and Chiral Discrimination at the BBB	41
Chapter 2: Study of Actively-Transported BBB Shuttles through Receptor-Mediated Transcytosis	45
2.1. Previous Studies with HAI Peptide	48
2.2. Amino Acid Replacement Effect on Transport Study Using a Novel Method for Transport Quantification Based on MALDI-TOF MS	55
Chapter 3: Study of Immunogenic Responses to BBB Shuttle Peptides	71
Chapter 4: Attempts to Develop a Therapy for FRDA at the CNS	83
4.1. Protein Replacement Therapy for Friedreich's Ataxia at the CNS—Chemistry with Proteins	92
4.2. Gene Therapy for Friedreich's Ataxia at the CNS—Chemistry with Enveloped Viral Particles	101
CONCLUSIONS	115

EXPERIMENTAL SECTION	119
Materials and Methods	121
Solid-Phase Synthesis of Compounds	123
Peptide and Amino Acid Purification and Characterization	128
Structural Data	130
<i>In Vitro</i> Assays	132
Protein Expression, Purification, Bioconjugation and Characterization	137
HSV-1 Bioconjugation and Characterization	140
<i>In Vivo</i> Experiments	143
 Product Characterization	 145
Amino Acids	147
Peptides	148
Biologics	164
 REFERENCES	 167
 SUMMARY IN CATALAN	 187

ABBREVIATIONS

AAA	amino acid analysis
AAV	adeno-associated virus
ABC	ATP binding cassette
Ac	acetyl
ACH	α -cyano-4-hydroxycinnamic acid
AcOH	acetic acid
AJs	adherens junctions
AM	amino methyl
AME	adsorptive-mediated endocytosis
AMT	adsorptive-mediated transcytosis
amu	atomic mass unit
AO	aminooxy moiety, <i>i.e.</i> aminooxyacetyl
aPhe	4-amino-L-phenylalanine
apoB100	apolipoprotein B100
apoE	apolipoprotein E
apoTf	apotransferrin
ASMS	affinity selection of proteins coupled to MS
AtFH	<i>Arabidopsis thaliana</i> frataxin homolog
ATP	adenosine triphosphate
AU	arbitrary units
AuNPs	gold nanoparticles
BAC	bacterial artificial chromosome
BBB	blood-brain barrier
BBECs	bovine brain endothelial cells
BBMVEC	bovine brain microvascular endothelial cells
BBs	brain barriers
BMECs	brain microvasculature endothelial cells
Boc	<i>tert</i> -butoxycarbonyl
bp	base pair
BPLE	brain polar lipid extract
BSA	bovine serum albumin
<i>C. elegans</i>	<i>Caenorhabditis elegans</i>
Caco-2	human colorectal adenocarcinoma cell line
CBMSO	centro de biología molecular Severo Ochoa
CD	circular dichroism
CDX	candoxin
Cf	5(6)-carboxyfluorescein
CFA	complete Freund's adjuvant
Cl-HOBt	6-chloro-1-hydroxybenzotriazole
CLSM	confocal laser scanning microscopy
CNS	central nervous system
COMU	1-cyano-2-ethoxy-2-oxoethylidenaminooxy)dimethylamino-morpholino carbenium hexafluorophosphate
Conc.	concentration
CoQ10	coenzyme Q10
COSY	correlation spectroscopy
CPP	cell-penetrating peptide
CPs	choroid plexuses
CSD	chemical shift deviation
CSF	cerebrospinal fluid
CyaY	<i>Escherichia coli</i> frataxin
CYPs	cytochrome P450s
DBU	1,8-diazabicyclo[5.4.0]undec-7-ene
Dbz	diaminobenzoic acid

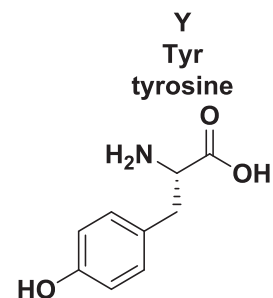
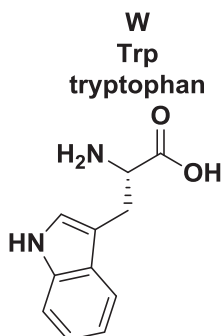
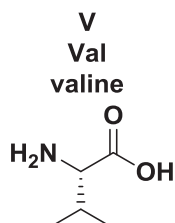
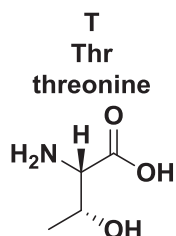
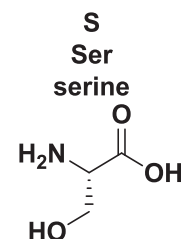
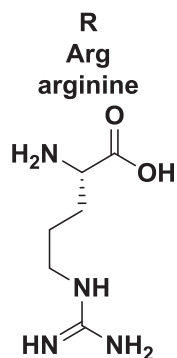
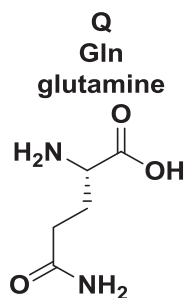
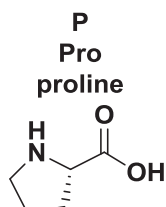
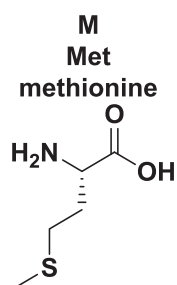
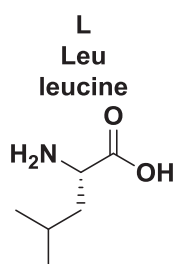
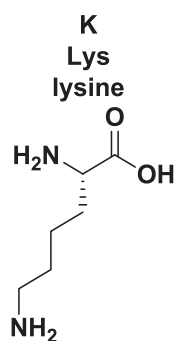
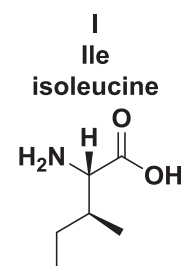
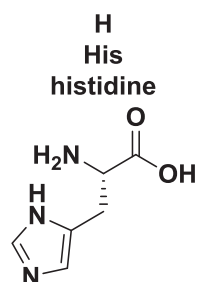
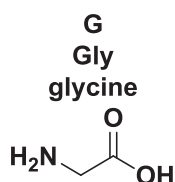
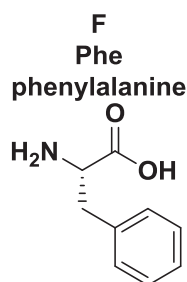
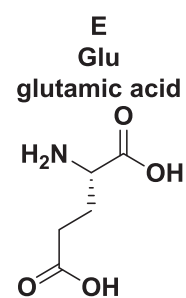
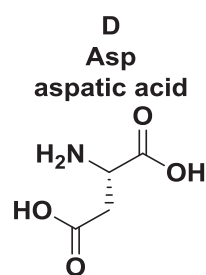
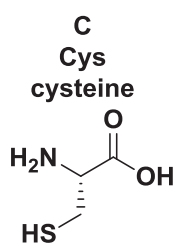
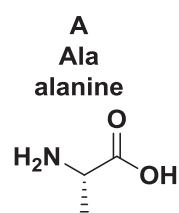
DCC	<i>N,N'</i> -dicyclohexylcarbodiimide
DCM	dichloromethane
D _e	enantiomeric discrimination
DHAP	2,6,-dihydroxyacetophenone
DIPEA	<i>N,N</i> -diisopropylethylamine
DIPCDI	<i>N,N'</i> -diisopropylcarbodiimide
DLS	dynamic light scattering
DM-I	diabetes mellitus type I
DMAP	4-dimethylaminopyridine
DMEM	Dulbecco's modified Eagle medium
DMF	<i>N,N</i> -dimethylformamide
DNA	deoxyribonucleic acid
Dpr	diaminopropionic acid
DSS	sodium-3-(trimethylsilyl)propanesulfonate
DTT	dithiothreitol
<i>E. coli</i>	<i>Escherichia coli</i>
ECL	enhanced chemiluminescence
ECM	endothelial cell medium
ECs	endothelial cells
EDC	1-ethyl-3-(3-dimethylaminopropyl)-carbodiimide
EDT	1,2-ethanedithiol
EDTA	ethylenediamine tetraacetic acid
EFACTS	European Friedreich's Ataxia consortium for translational studies
EGFR	epidermal growth factor receptor
ELISA	enzyme-linked immunosorbent assay
EPO	erythropoietin
eq.	equivalent
Eq.	equation
ESI-MS	electrospray ionization-mass spectrometry
FARA	Friedreich's Ataxia Research Alliance
FDA	food and drug administration
FGE	formylglycine-generating enzyme
fGly	formylglycine
Fmoc	9-fluorenylmethoxycarbonyl
FPh	4-fluoro-L-phenylalanine
FPLC	fast protein liquid chromatography
FRDA	Friedreich's Ataxia
FXN	frataxin
GABA	γ -aminobutyric acid
GFP	green fluorescent protein
GSH	glutathione
HBSS	Hanks' balanced salt solution
HBTU	<i>O</i> -(benzotriazol-1-yl)- <i>N,N,N',N'</i> -tetramethyluronium hexafluorophosphate
hCha	homocyclohexyl-L-alanine
HDAC	histone deacetylase
HeNe	helium-neon
HEPES	4-(2-hydroxyethyl)-1-piperazineethanesulfonic acid
HFIP	hexafluoro-2-propanol
HIV-1	human immunodeficiency virus 1
HOAt	1-hydroxy-7-azabenzotriazole
HOBt	1-hydroxybenzotriazole
holoTf	holotransferrin
HPLC	high-performance liquid chromatography
HPLC-MS	high-performance liquid chromatography coupled to mass spectrometry

HRMS	high-resolution mass spectrometry
HRP	horseradish peroxidase
HsFtx	human frataxin
HSQC	heteronuclear single quantum coherence
HSV-1	herpes simplex virus type 1
hTf	human transferrin
IAA	iodoacetic acid
ICP-MS	inductively coupled plasma mass spectrometry
IDL	intermediate-density lipoprotein
IFA	incomplete Freund's adjuvant
IFN- γ	interferon gamma
IGF-1	insulin/insulin-like growth factor 1
IgG	immunoglobulin G
IgM	immunoglobulin M
IMAC	immobilized metal affinity chromatography
INAA	instrumental neutron activation analysis
<i>i.p.</i>	intraperitoneal
iPSCs	induced pluripotent stem cells
ISCU	iron-sulfur cluster assembly enzyme
JAMs	junctional adhesion molecules
KLH	keyhole limpet hemocyanin
L-DOPA	L-3,4-dihydroxyphenylalanine
LDLR	low-density lipoprotein receptor
LOD	limit of detection
LOQ	limit of quantification
LY	lucifer yellow lithium salt
MAL	maleimide
MALDI	matrix-assisted laser desorption/ionization
MES	2-(<i>N</i> -morpholino)ethanesulfonic acid
MetAPs	methionine aminopeptidases
MHC	major histocompatibility complex
MLS	mitochondrial localization signal
MPP	mitochondrial processing peptidase
MS	mass spectrometry
MTBE	methyl <i>tert</i> -butyl ether
MTT	3-(4,5-dimethylthiazol-2-yl)-2,5-diphenyltetrazolium bromide
MW	molecular weight
nAChR	nicotinic acetylcholine receptor
NADH	nicotinamide adenine dinucleotide
Nbz	<i>N</i> -acyl-benzimidazolinone
NCL	native chemical ligation
neg.	negative
NFS1•ISD11	sulfur donor complex
NHS	<i>N</i> -hydroxysuccinimide
NIP	(<i>R</i>)-piperidine-3-carboxylic acid, or nipecotic acid
<i>N</i> MePhe	<i>N</i> -methyl phenylalanine
NMR	nuclear magnetic resonance
NOESY	nuclear Overhauser spectroscopy
NP	nanoparticle
o/n	overnight
Oxyma	ethyl (hydroxyimino)cyanoacetate
P-gp	P-glycoprotein
pAbs	polyclonal antibodies
PAMPA	parallel artificial membrane permeability assay

pAb	polyclonal antibody
P_{app}	apparent permeability
Pbf	2,2,4,6,7-pentamethyldihydrobenzofuran-5-sulfonyl
PBS	phosphate-buffered saline
PC	phosphatidylcholine
PDA	photodiode array detector
PDB	protein data bank
P_e	effective permeability
PE	phosphatidylethanolamine
PEG	polyethylene glycol
PhPro	<i>cis</i> -3-phenylpyrrolidine-2-carboxylic acid
PI	phosphatidylinositol
Pip	pipecolic acid
PLP	pyridoxal-5'-phosphate
PMP	pyridoxamine-5'-phosphate
PPII	polyproline II
PS	phosphatidylserine
PUFA	polyunsaturated fatty acid
PyBOP	benzotriazol-1-yl-oxytripyrrolidinophosphonium hexafluorophosphate
QD	quantum dot
RC	random coil
ref.	reference
REMD	replica exchange molecular dynamics
<i>rD</i>	<i>retro</i> -D-version/ peptide made of D-amino acids and with the reversed sequence of a parent peptide
RME	receptor-mediated endocytosis
RMSD	root-mean-square deviation
RMT	receptor-mediated transcytosis
RNA	ribonucleic acid
RNAPII	RNA polymerase II
ROS	reactive oxygen species
RP-HPLC	reversed phase-high-performance liquid chromatography
RSV	Rous sarcoma virus
r.t.	room temperature
RVG	rabies virus glycoprotein
SD	standard deviation
SDS	sodium dodecyl sulfate
SDS-PAGE	sodium dodecyl sulfate-polyacrylamide gel electrophoresis
SEC	size-exclusion chromatography
SPPS	solid-phase peptide synthesis
stain.	staining
SUMO	small ubiquitin-like modifier
<i>T</i>	transport
TALE	transcription activator-like effector
TAT	human immunodeficiency virus-1 <i>trans</i> -acting activator of transcription
TBST	tris-buffered saline with Tween 20
<i>t</i> Bu	<i>tert</i> -butyl
TCEP	tris(2-carboxyethyl)phosphine
TEER	transendothelial electrical resistance
TEM	transmission electron microscopy
TFA	trifluoroacetic acid
Tf	transferrin
TfR	transferrin receptor
TGN	<i>trans</i> Golgi network

Tha	4-thiazoyl-alanine
Tic	7-hydroxy-(<i>S</i>)-1.2.3.4-tetrahydroisoquinoline-3-carboxylic acid
TIS	triisopropylsilane
TJs	tight-junctions
TMB	3,3',5,5'-tetramethylbenzidine
TNR	trinucleotide (triplet) repeat
TOCSY	total correlation spectroscopy
TOF	time-of-flight
t_R	retention time
Trt	trityl or triphenylmethyl
UV/Vis	ultraviolet/visible
UWL	unstirred water layer
v/v	volume/volume
VLDL	very low-density lipoprotein
VMD	visual molecular dynamics
vol.	volume
vs.	<i>versus</i>
w/v	weight/volume
w/w	weight/weight
WB	western blot
WT	wild type
X-Gal	5-bromo-4-chloro-3-indolyl- β -D-galactopyranoside
YAC	yeast artificial chromosome
Yfh1	<i>Saccharomyces cerevisiae</i> frataxin

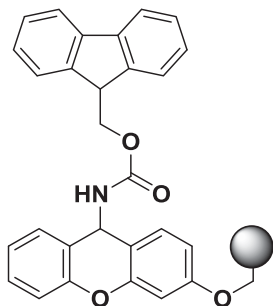
Proteinogenic Amino Acids^a



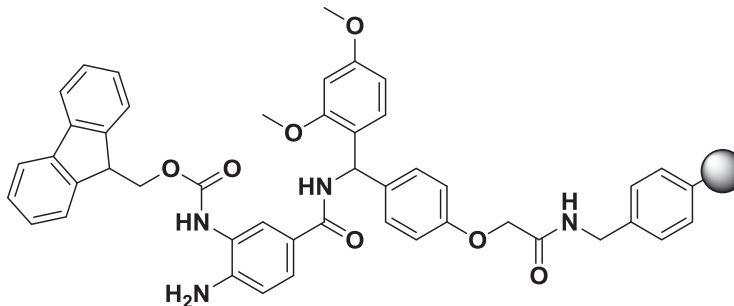
^a L-configurations.

Resins

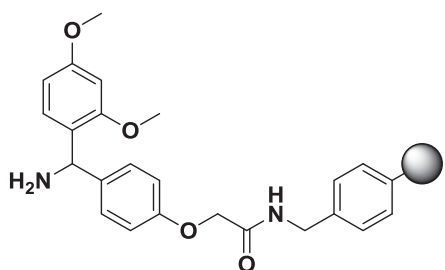
Sieber Amide resin



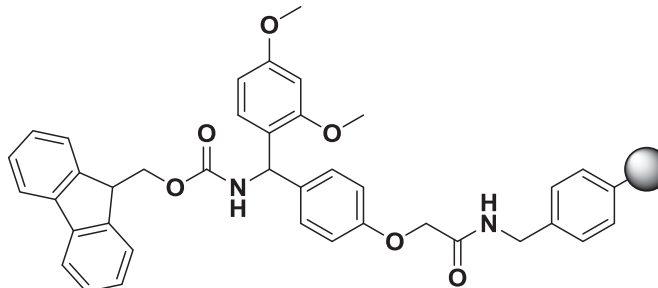
Dawson Dbz AM resin



H-Rink Amide ChemMatrix resin

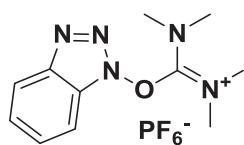


Fmoc-Rink Amide AM resin

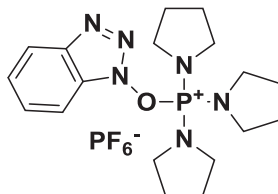


Coupling Reagents and Additives

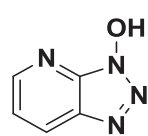
HBTU



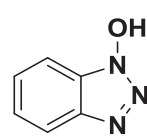
PyBOP



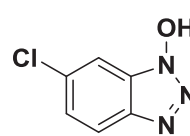
HOAt



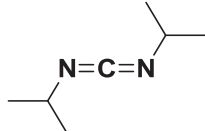
HOBt



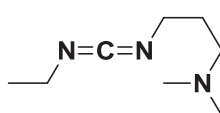
Cl-HOBt



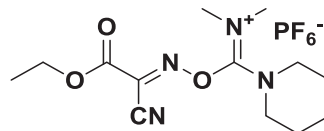
DIPCDI



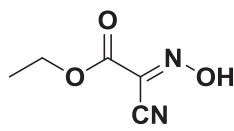
EDC



COMU

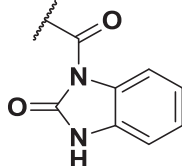


Oxyma

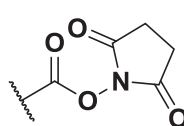


Activating and Protecting Groups

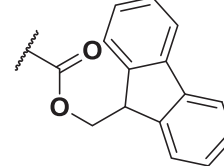
Nbz



NHS-ester



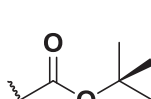
Fmoc



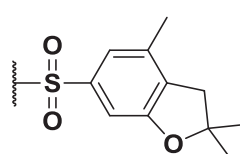
tBu



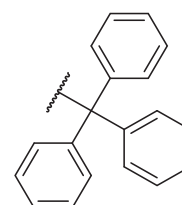
Boc



Pbf



Trt



INTRODUCTION

Origins of the Gatekeepers of the Brain—Evolution of Brain Barriers

Evolution of life led to the emergence of the Metazoa kingdom (animals) more than 600 million years ago,¹ comprising a group of heterotroph pluricellular eukaryote organisms, with differentiated tissues and an embryonic development. Nervous and muscle tissues are present in all organisms with the exception of the subkingdom Parazoa, *i.e.* phyla Porifera (sponges) and Placozoa.^{2,3} Recent studies on comparative genomics have shown that Ctenophora (comb jellies), which have both complex nervous and mesoderm-derived muscular systems, are the most basal animal lineage instead of the subkingdom classically assigned, the Parazoa (**Figure I.1**).⁴⁻⁶

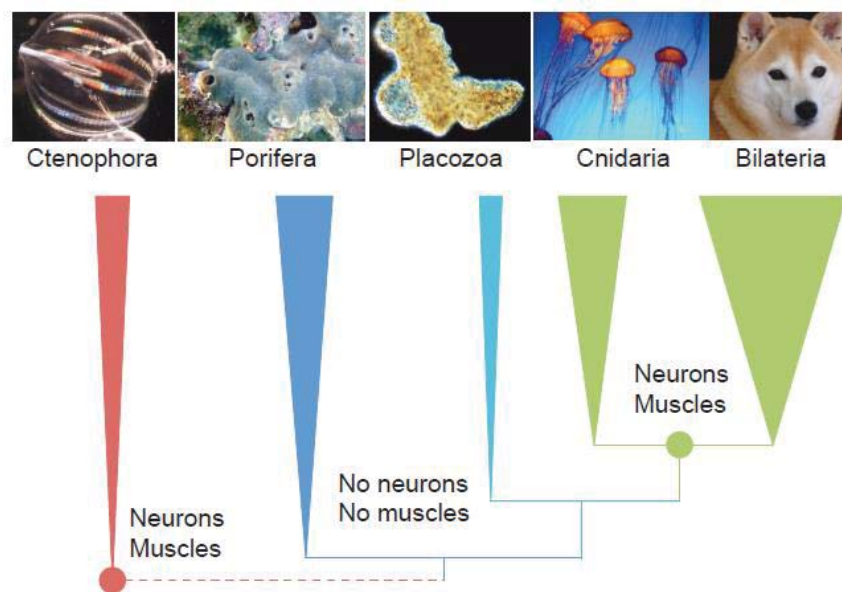


Figure I.1. Relationships between major animal clades. Adapted from Moroz *et al.*⁶

During the embryonic development of most animals (Eumetazoa, including the phyla Ctenophora and Cnidaria, and the clade Bilateria—and therefore the class Mammalia), an early stage known as blastula—a single-layered structure—becomes a three-layered structure, the so-called gastrula (**Figure I.2**), after a process named gastrulation.⁷⁻¹⁰ These three layers—the three germ layers—are known as ectoderm, mesoderm and endoderm. By means of organogenesis each one gives rise respectively to epidermis, neural crest and nervous system;^{11,12} to notochord, cartilage and bone, as well as hematopoietic, endothelial, and vascular smooth and skeletal muscle cells;¹³⁻¹⁵ and to the epithelium of the respiratory and digestive systems, as well as associated organs such as the liver and pancreas.¹⁶

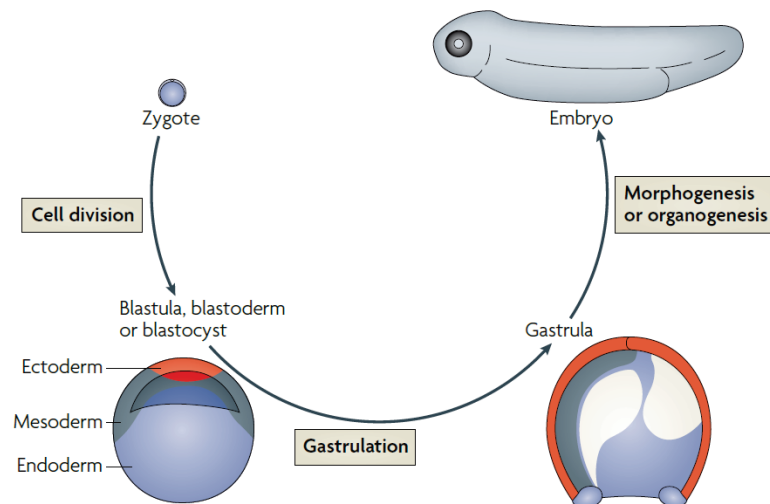


Figure I.2. Developmental steps of embryogenesis. Adapted from Wozniak *et al.*¹⁰

Therefore, the central nervous system (CNS) in humans is the result of millions of years of evolution from a common worm-like ancestor belonging to the clade Bilateria—animals with bilateral symmetry, *i.e.* each side of the organism is the mirror image of the other. Among Bilateria, worms include diverse phyla, such as Platyhelminthes (flatworms), Nematoda (round worms), and Annelida (segmented worms). Flatworms, the simplest bilaterian animals, do not have developed sensory organs or a nervous system but they do have photoreceptors and ganglia—nerve centers—instead.¹⁷⁻¹⁹ The evolutionary stage of the nervous system of flatworms, together with their simplicity, led to use of *Caenorhabditis elegans* (**Figure I.3**), an organism belonging to the phylum Nematoda, to study development in animals but more specifically the nervous system.²⁰⁻²⁴ The evolution of sensory organs and these ganglia led to the formation of a center for integrating and processing the information, namely the CNS.

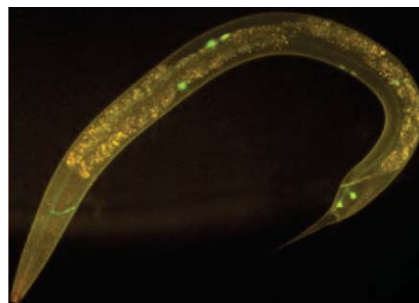


Figure I.3. Neuron-specific transgene (fusion between *mec-4* and GFP) in *C. elegans* in larval stage L2. Adapted from Rankin.²⁰

Although the eyes of vertebrates (phylum Chordata) and cephalopods (phylum Mollusca, *e.g.* squid) are similar (convergent camera-like eyes), they derive from a parallel evolution with a common origin shared with arthropods, although the eye-type does not share structural similarity (**Figure I.4**).²⁵ Similarly, the CNS of these organisms may differ considerably: protostomes (containing the phylum Mollusca) and deuterostomes (containing the phylum Chordata),^{26,27} which differ mainly in embryonic development, where the blastopore becomes the mouth or anus in each case—evolved from a common origin (a diffuse nervous system).¹¹

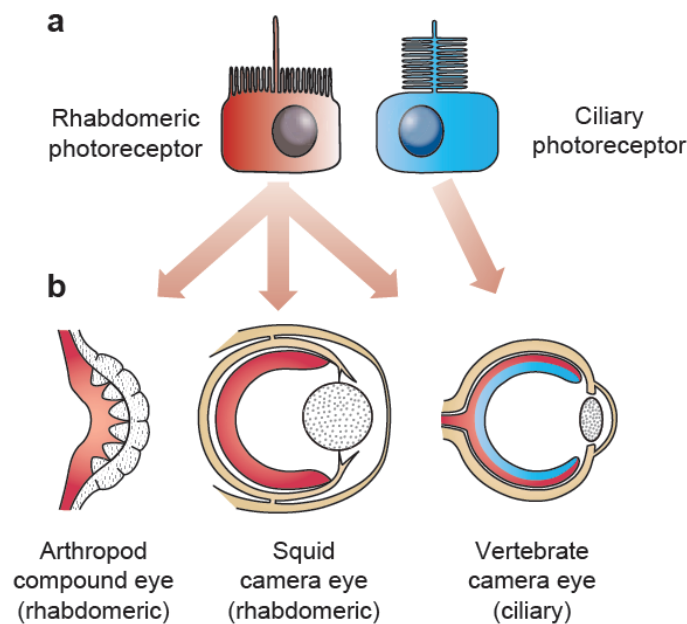


Figure I.4. Eye structures of an arthropod, squid and vertebrate, which arise from a parallel evolution based on a shared history of generative mechanisms and cell types. Adapted from Shubin *et al.*²⁵

The CNS is therefore more than simply a rudimentary system to guide the organism through the environment but also a learning machine with a complex neuronal network that is vital for surveillance. The relevance of the CNS ensured the development of a system to protect it. Mechanical protection of the CNS appeared with the clade Craniata, giving rise to a skull covering the external surface of the encephalon (brain). The subphylum Vertebrata has an additional feature, namely a vertebral column, which replaces the notochord—found throughout the phylum Chordata—and protects the spinal cord.²⁸ However, it is not only mechanical forces that are an issue for the integrity of the CNS, but also metabolites and biohazards. Thus, a cellular structure gave rise to the formation of the blood-brain barrier (BBB) to protect the CNS and regulate influxes and effluxes through it.

Among vertebrates, the subclass Elasmobranchii (sharks and rays) has a BBB formed by perivascular glial end-feet (glial barrier) and not by the endothelium (**Figure I.5**). The glial barrier is a primitive feature shared by some invertebrates that have a BBB (subphylum Crustacea, and classes Insecta), whereas others do not have a BBB (*e.g.* phylum Annelida or lower Mollusca). An intermediate condition is observed in cephalopods, where the barrier is located at the level of the pericyte layer.²⁹⁻³¹

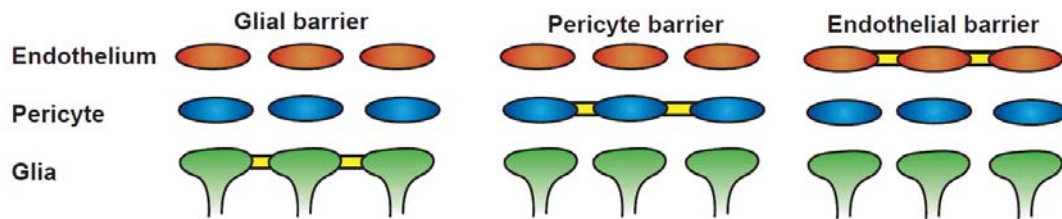


Figure I.5. The blood-brain barrier and the localization of the barrier layer in diverse animals: glial in most invertebrates (*e.g.* *Drosophila*), at the pericytes as observed in *Sepia* (cephalopod), and endothelial in mammals. Designed using Abbott³⁰ and created with Adobe InDesign.

During evolution, the barrier shifted from being glial to endothelial. Thus, mammals have a specialized endothelium that regulates molecular transport through it. This endothelial barrier is also present in other classes of the subphylum Vertebrata, such as Aves, Reptilia and Amphibia.³⁰ In the BBB, diverse levels of regulation are found: (1) specialized structures, so-called tight-junctions (TJs),^{32,33} which tighten the joints between cells, thus greatly reducing gaps between cells and hydrophilic diffusion through them; (2) transporters for specific metabolites, enabling the control of such molecules and buffering the composition of the plasma in diverse situations (*e.g.* meal/digestion, exercise); (3) the ATP binding cassette (ABC) transporter P-glycoprotein (P-gp) and other efflux transporters that pump out lipophilic molecules that are potentially hazardous, such as toxins; (4) the maintenance of low permeability to neurotransmitters and ionic homeostasis, thereby reducing the noise and improving the efficiency of the synapses and thus that of CNS functionality.^{29,34,35}

In addition to the BBB, other cellular barriers appeared (**Figure I.6**): (1) the blood-cerebrospinal fluid (CSF) barrier at the choroid plexuses³⁶ (CPs)—one in each of the four ventricles of the brain—made up of modified ependymal cells that have TJs and adherens junctions (AJs),^{36,37} which produces CSF;³⁸ (2) the ependymal,³⁹ which is an epithelial layer located in the ventricular system of the brain and in the central canal of the spinal cord and,

like CPs, comprises ependymal cells; and (3) the meninges, which are formed by three membranes and two inter-membrane spaces that cover the encephalon and spinal cord—dura mater (external layer), subdural space (thin layer with CSF), arachnoid mater (avascular layer), subarachnoid space (contains CSF), and pia mater (thin vascular layer).^{40,41}

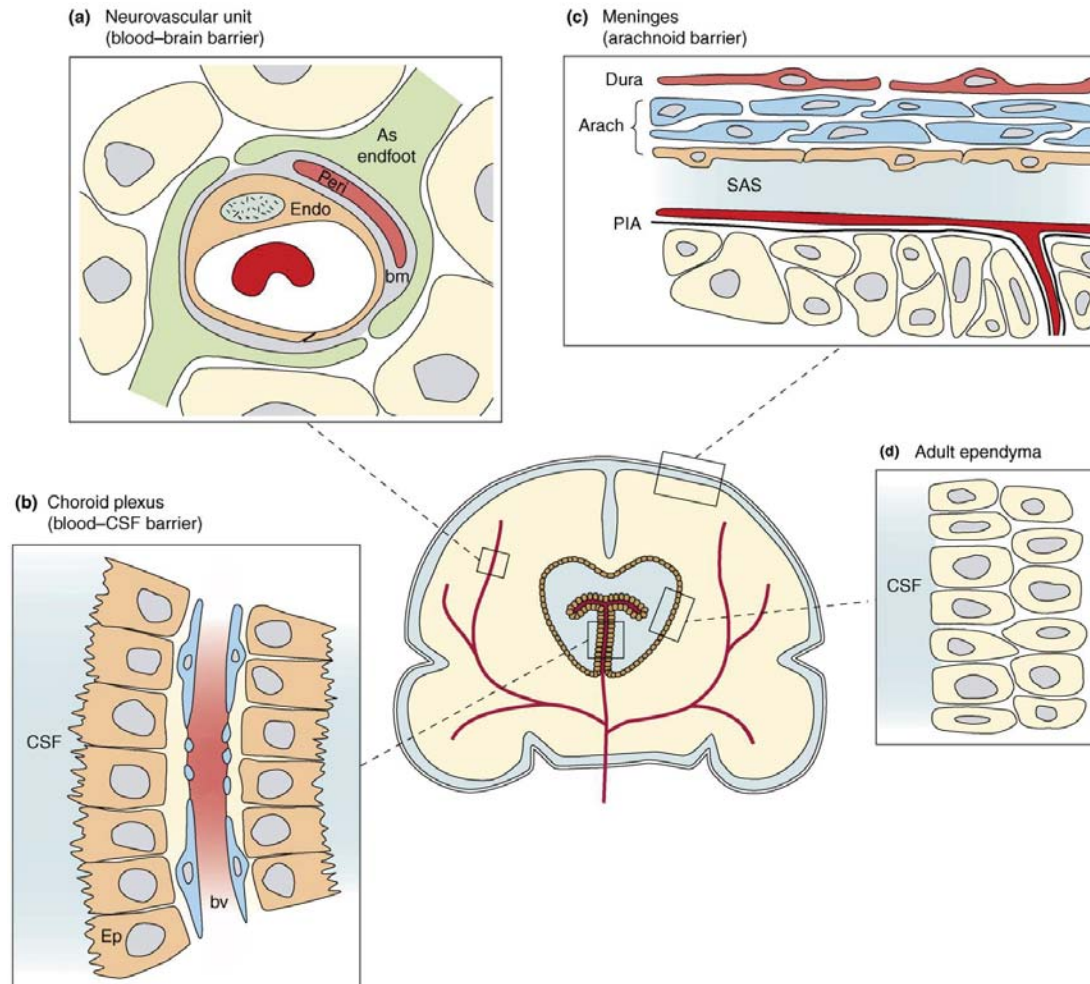


Figure I.6. Brain barriers: (a) blood-brain barrier, (b) arachnoid barrier, (c) choroid plexus and (d) ependyma. Abbreviations: Endo, endothelial cell; Peri, pericyte; bm, basement membrane; As, astrocyte; Ep, epithelial cells; bv, blood vessels; Dura, dura mater; Arach, arachnoid membrane; SAS, subarachnoid space; PIA, pial surface. Adapted from Saunders *et al.*⁴¹

Understanding the Door—Physiology of the Blood-Brain Barrier

Although the BBB exerts greater and more strict regulation of access to the brain than the other three brain barriers (BBs), it accounts for a large surface of exchange (20 m^2)⁴² with blood and thus has been envisioned as an important route by which to deliver drugs into the CNS. In recent decades, diverse approaches have been addressed to replace the aggressive invasive or pseudo-invasive treatments used to date to overcome the BBs. These treatments include surgical and non-surgical strategies like intracerebral injections or temporal disruption of the BBB (solvent-⁴³ or ultrasound-mediated),⁴⁴ respectively, both involving a physical disruption of a BB—meninges and BBB, respectively—and thus the risks of permanent tissue damage and infection.

On the other hand, achieving drug delivery by means of the cell transport machinery requires a complete understanding of cell metabolism, mechanics, and transport mechanisms. Since the BBB is mainly an endothelial (non-fenestrated)⁴⁵ barrier, the molecular basis of such a structure is described in detail after a short summary of the principal structural components, the so-called neurovascular unit (**Figure I.7**).⁴⁶ These components include several cell types—endothelial cells (ECs, addressed later on), pericytes, astrocytes, and neurons, as well as the extracellular matrix. Pericytes are in close-contact with ECs and have recently been demonstrated to play a key role in BBB differentiation by regulating BBB-specific gene expression in ECs and inducing the polarization of astrocyte end-feet.^{47,48} Astrocytes regulates at the same time the BBB features of ECs, such as by modulating the tightness of TJs and the expression of transporters and enzymes.⁴⁹ It is known that there is a relationship between regional neuronal activity and blood flow, whereas it has been purposed the regulation BBB permeability by neurons—*i.e.* neurons can regulate the BBB function.^{50,51} Finally, the extracellular matrix helps to preserve the integrity of the BBB by providing an anchor point for ECs, mainly through the interaction of integrins with laminin and the regulation of intercellular communication. ECs, pericytes and astrocytes secrete extracellular matrix molecules thereby contributing to the formation of this matrix, the major components of which are collagen type IV, laminin and fibronectin.^{45,51}

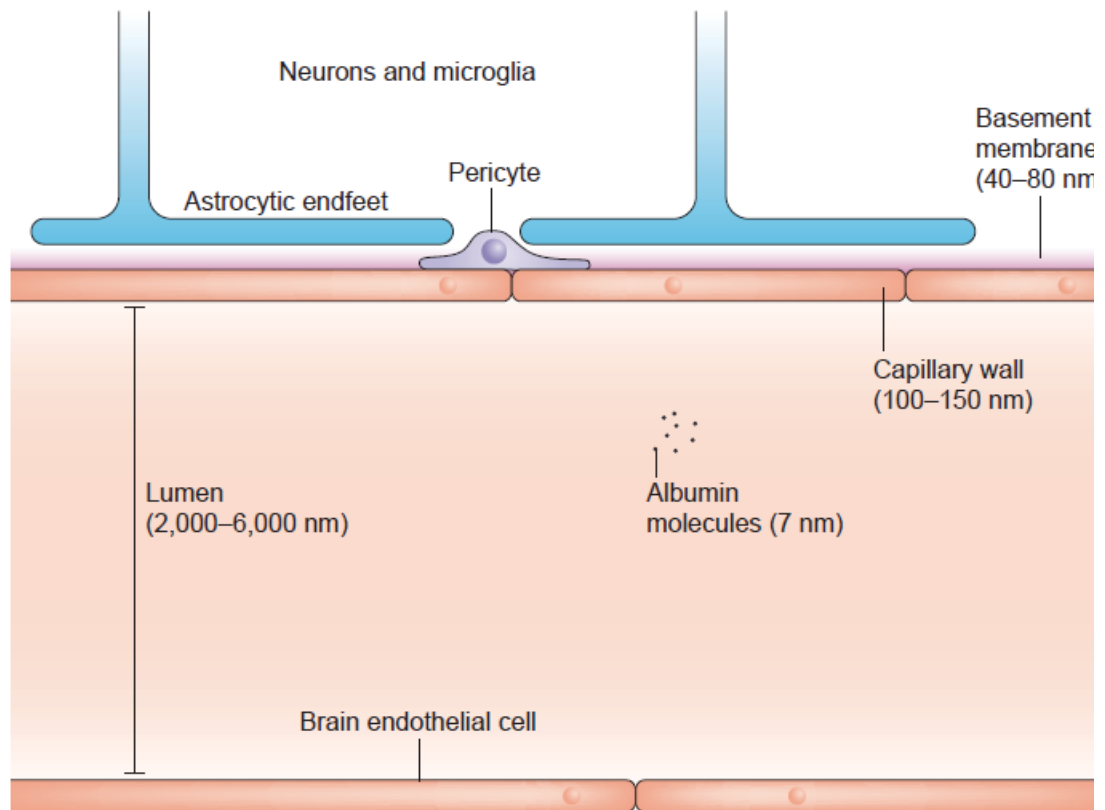


Figure I.7. Blood-brain barrier structure—components of the neurovascular unit: endothelial cells, pericytes, astrocytes, neurons, and basement membrane (extracellular matrix). Adapted from Banks.⁴⁶

As previously described, TJs play a central role in the organization of brain microvasculature ECs (BMECs)—two differentiated faces are separated by TJs, the basal and the apical side, facing the brain parenchyma (abluminal side) and the lumen of the capillaries (luminal side), respectively (**Figure I.7**). These structures are composed by diverse integral transmembrane proteins (occludin, claudins, and junctional adhesion molecules (JAMs)) and accessory/anchoring proteins (ZO-1, ZO-2, cingulin, etc.).^{51,52} Although TJs are primarily responsible for the low permeability through the intercellular cleft of BMECs, AJs also restrict the cell-cell distance, and thus permeability, ubiquitously in the vasculature. AJs are mediated through homophilic interactions between vascular endothelial-cadherin expressed in adjacent cells.^{51,53}

In addition, to further preventing the entry of undesirable entities into the CNS, the BBB is also an enzymatic barrier,⁵⁴ combining efflux pumps (*e.g.* P-gp) with exo- and endoenzymes, such as cytochrome P450s (CYPs).⁵⁵

Hydrophilic (diffusion) transport is highly impeded by TJs, which can be crossed by only small hydrophilic entities like ions and water molecules, and by cell membranes, which account for most of the surface of the BBB (20 m²),⁴² blocking most compounds. Therefore, entry of molecules into the brain across the BBB would be minimal unless specific mechanisms were available for this purpose.

In this regard, more than 100 years ago, Goldmann reported that intrathecal (1913) and parenteral (1909) injections of water-soluble dyes—trypan blue—in adult rats did and did not stain the brain, respectively.⁵⁶ He also realized that the CP exerted a protective function. Previously, in 1885, Ehrlich did similar experiments but did not coin the term “blood-brain barrier” or describe it appropriately—even saying “*I am unable to accept that the vascular endothelium, as such, exercises different functions in different organs, so that, for example a liver capillary is permeable for certain substances that will not pass through other capillaries*”.⁵⁶ Nonetheless, gases and compounds with certain characteristics, namely those showing relatively high lipophilicity, a small size and low number of H-bond donors or acceptors—better defined by the Lipinski “rule of five”—,⁵⁷ are able to diffuse through the lipid bilayer of cell membranes in a process known as lipophilic passive diffusion. This is one of the classical routes to overcome the BBB and deliver drugs into the CNS, although it is limited by the aforementioned rules.

In addition to the previously mentioned transport (diffusion) pathways, cells also have mechanisms that require energy, such as that used in the hydrolysis of ATP or exchanged from a positive electrochemical gradient. ECs at the BBB display much lower rates of endocytosis and transcytosis compared to those at the peripheral endothelium.⁴⁹ These mechanisms can be divided in those that use the following: (1) transport proteins, and endocytic mechanisms including (2) adsorptive-mediated (AME) and (3) receptor-mediated endocytosis (RME). Transport proteins can be classified on the basis of stoichiometry and type of energy used: transporters which favor the movement of specific small molecules or ions down its concentration gradient—uniport, included as facilitated diffusion, which does not imply the use of energy—, or against it but favored by the simultaneous transport—cotransport—of other species (at the same (symport) or opposite (antiport) side of the cell membrane) down their gradient. Additionally, pumps utilize ATP hydrolysis as source of energy to move small molecules or ions against electrochemical gradient.⁵⁸

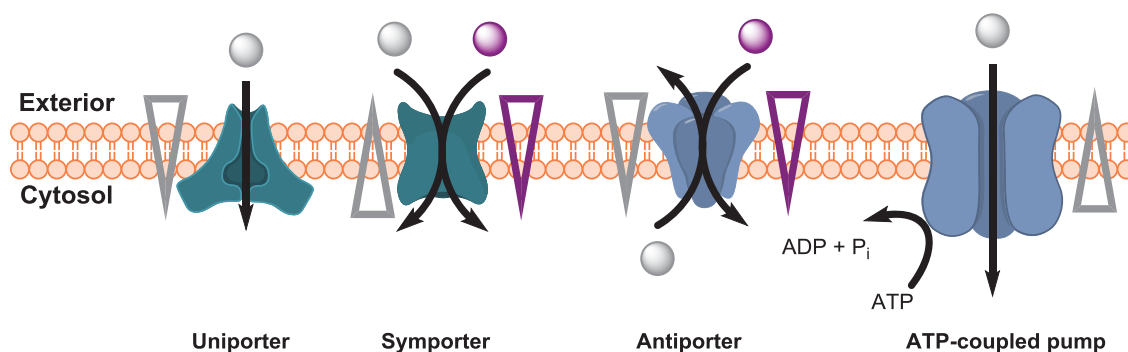


Figure I.8. Transport protein mechanisms: uniport, symport, antiport, and ATP-coupled pumps.

Created using ChemBioDraw.

AME and RME are endocytic mechanisms classified on the basis of the nature of their interaction with the membrane entity that recognizes the molecule that uses each mechanism. The former entails positively charged molecules that are attracted electrostatically by cell membranes—glycocalyx—, which are negatively charged.⁵⁹ Thus, its nature conditions the lack of selectivity to differentiate between tissues or cell types. Conversely, RME is based on the internalization of an extracellular receptor, which recognizes a ligand that is likely to be co-transported with the receptor, such as transferrin receptor (TfR) and its ligand transferrin (Tf).⁶⁰

Classifying endocytic mechanisms into these two groups (AME and RME) is interesting for drug delivery purposes since it highlights the type of delivery system; however, it does not account for the cellular mechanism of internalization involved. For further understanding, the cellular basis of endocytosis and the diverse mechanisms involved are described—phagocytosis, macropinocytosis, clathrin-dependent, caveolin-dependent or independent (of these two mechanisms) endocytosis.^{61,62}

Phagocytosis is an actin-dependent and receptor-mediated process that entails the engulfment of large particles (usually over 0.5 μm in diameter)—a process that includes Fc- and complement-receptors, but also integrins, lectins and lipopolysaccharide-receptor.⁶³ Frequent in phagocytic cells such as monocytes, macrophages and tissue dendritic cells, phagocytosis has also been observed in pericytes^{64,65} and astrocytes.⁶⁶ Pinocytic activity—actin-dependent uptake of solutes in the fluid phase or adsorbed to the cell membrane—^{67,68} has been reported to be very low in BMECs.⁶⁹

Consistent with its name, clathrin-dependent internalization is dependent on the recruitment and formation of a clathrin-coated pit, which contributes to the formation of a

vesicle. Finally, vesicle scission is produced by the mechanochemical enzyme dynamin. Although the induction of the mechanism is fostered in some cases by interaction with the ligand receptor, for example epidermal growth factor receptor (EGFR), in others the internalization is constitutive, such as in the case of TfR.⁷⁰

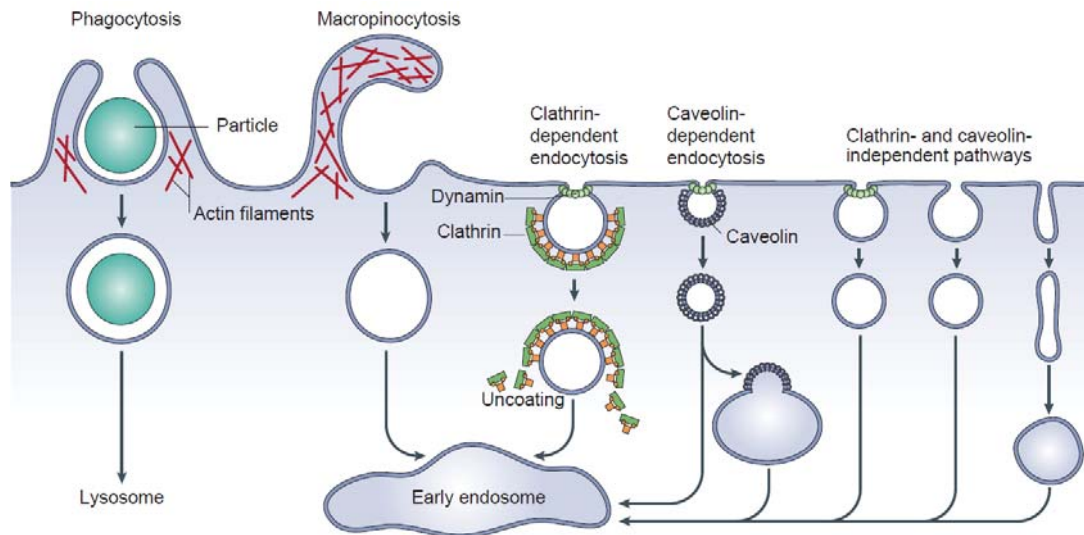


Figure I.9. Endocytic mechanisms: phagocytosis, macropinnocytosis, and clathrin- and caveolin-dependent and -independent endocytosis. Adapted from Mayor *et al.*⁶¹

In contrast, the other endocytic mechanisms are not clathrin-dependent and are classified on the basis of the proteins involved in the internalization process. Caveolin-dependent endocytosis recruits caveolin-1 protein to trigger vesicle formation; and again dynamin is responsible for scission. This mechanism might be involved in the internalization of some receptors that do internalize by clathrin-dependent endocytosis—EGFR is internalized via the caveolin-dependent route after ubiquitination. The remaining mechanisms, some dynamin-dependent and others not, are still not well understood.⁶¹

Although the BBB is an immunological barrier, leukocytes can cross it through a process called diapedesis, a process defined as the transmigration of these cells from one side of ECs to the other. Diapedesis is known to occur through either paracellular or transcellular transmigration. Both have the same initiation process comprising the following steps: rolling of leukocytes through the EC surface, while interacting with selectins; G protein-mediated signaling, leading to arrest leukocytes with the help of integrins; and finally, leukocytes on the surface of ECs can proceed with diapedesis (**Figure I.10**).⁷¹⁻⁷³ In the case of paracellular transmigration, JAMs have been reported to play a role in the regulation of the paracellular migration of leukocytes.⁷⁴ On the other hand, the

transendothelial process requires the membrane-associated signaling protein caveolin-1.⁷⁵ In this regard, viruses and bacteria can infect leukocytes and be transported to the basolateral side of the BBB via the so-called “Trojan horse” mechanism; other pathogens cross by themselves using the paracellular or transcellular pathways.^{76,77}

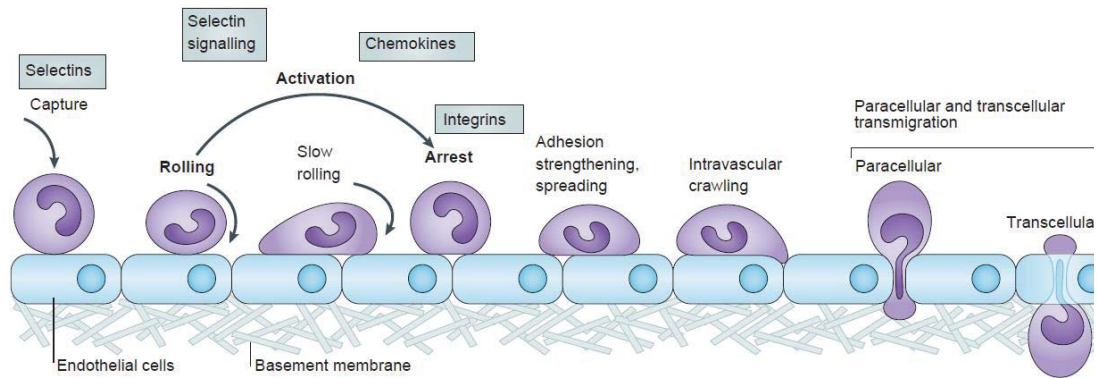


Figure I.10. Leukocyte “Trojan horse” mechanism. Adapted from Ley *et al.*⁷⁸

Reasons to Look Inside—Physiology and Disease of the CNS: Social Impact

The transport logistics at the BBB entails high restriction. In this regard, it has been reported that >98% of small molecule drugs and ~100% of large therapeutics do not cross this barrier.⁴³ The increase in research efforts devoted to drug delivery, especially to the brain, reflects scientific and social interest in this field. In this regard, there has been an exponential trend in the number of publications addressing drug delivery or drug delivery to the brain (**Figure I.11**), with 332,776 and 18,817 articles published and 34,756 and 603 patent applications to date, respectively.^b

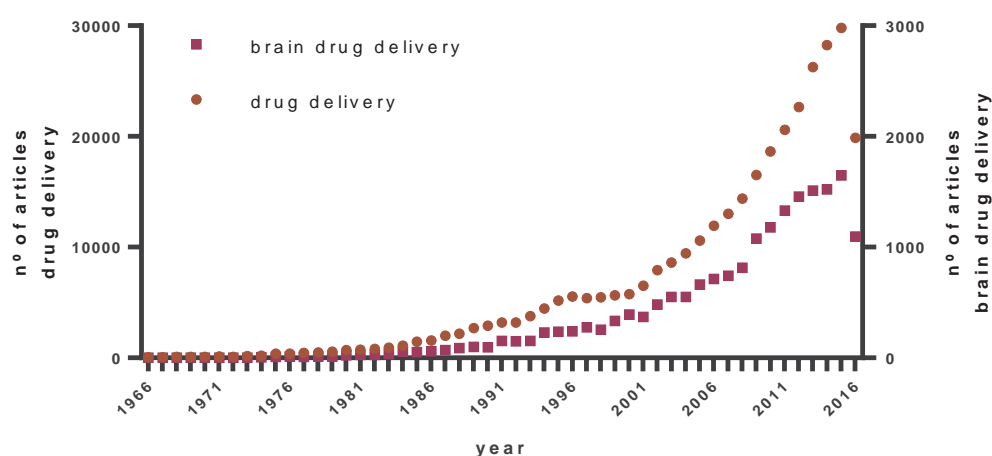


Figure I.11. Articles published on drug delivery and brain drug delivery from 1966 to October 2016—Web of Science™ (Thomson Reuters). Created using GraphPad.

These efforts are the direct consequence of three interrelated factors, namely (1) the aforementioned obstacle posed by the BBB with respect to drug delivery to the brain, (2) the social impact of CNS diseases, and (3) the derived economic cost of ineffective treatments and thus long care periods for patients. In this regard, in 2010, the cost of brain disorders in Europe amounted to €798 billion, doubling the figure in 2004—€386 billion. Statistically, these disorders entailed an average cost per capita of €1,550 in 2010.^{79,80} In **Figure I.12**, the European statistics for brain disorders in 2010 are shown as three categories: number of subjects, cost per subject, and total costs.⁸¹

^b Data obtained from Web of Science™ (Thomson Reuters) and PatentScope™ (World Intellectual Property Organization, WIPO), at October 19th 2016.

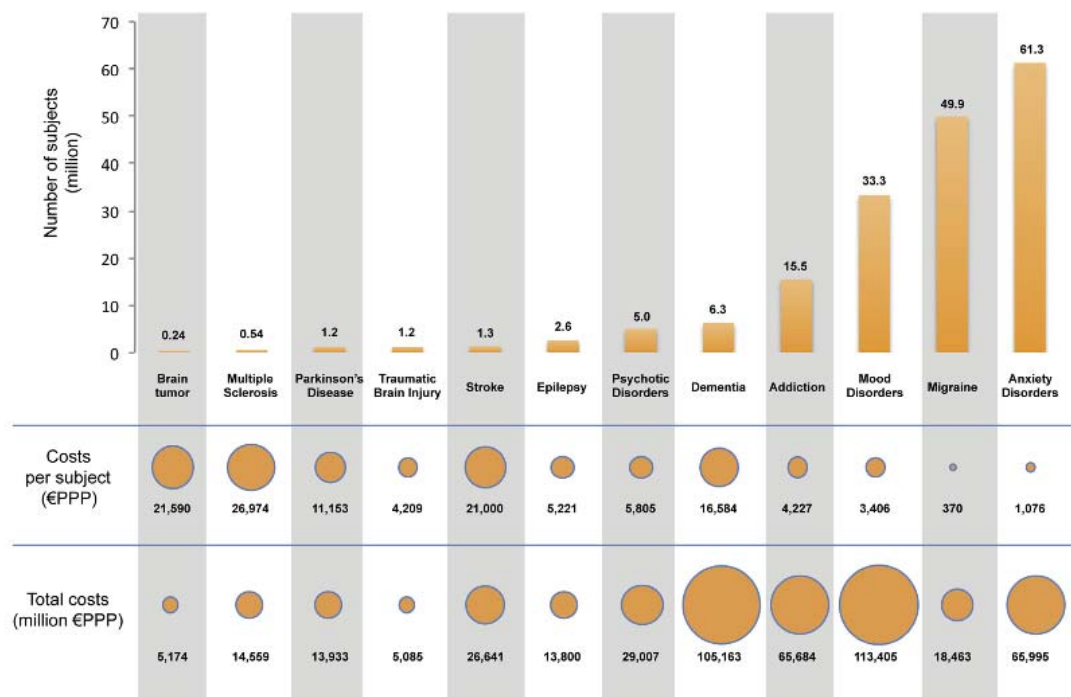


Figure I.12. Costs of brain disorders in Europe in 2010. Adapted from DiLuca *et al.*⁸¹

Devising a Key—Peptides as Therapeutics and for Drug Delivery to the Brain

Peptides are sequences of concatenated amino acids through an amide bond. They are distinguished from proteins classically by their size—considering peptides to be sequences shorter than 50 residues. Nevertheless, sometimes the same molecule is considered both peptide and protein. Rather than size, a more appropriate way to classify these polymers may be on the basis of structure—*i.e.* primary, secondary, tertiary and quaternary structures. Primary and secondary structures equate to the amino acid sequence and the first homogeneous three-dimensional arrangement, respectively. Peptides could be considered sequences that adopt a secondary structure while proteins could be defined as having a tertiary structure, namely the second three-dimensional arrangement (homo- or heterogeneous). Nevertheless, the quaternary structure, defining the assembly of diverse molecules, can be adopted by both peptides and proteins (**Figure I.13**). Therefore, proteins are more complex than peptides when analyzed as single molecules, but this may not be the case when quaternary structure is taken into account.

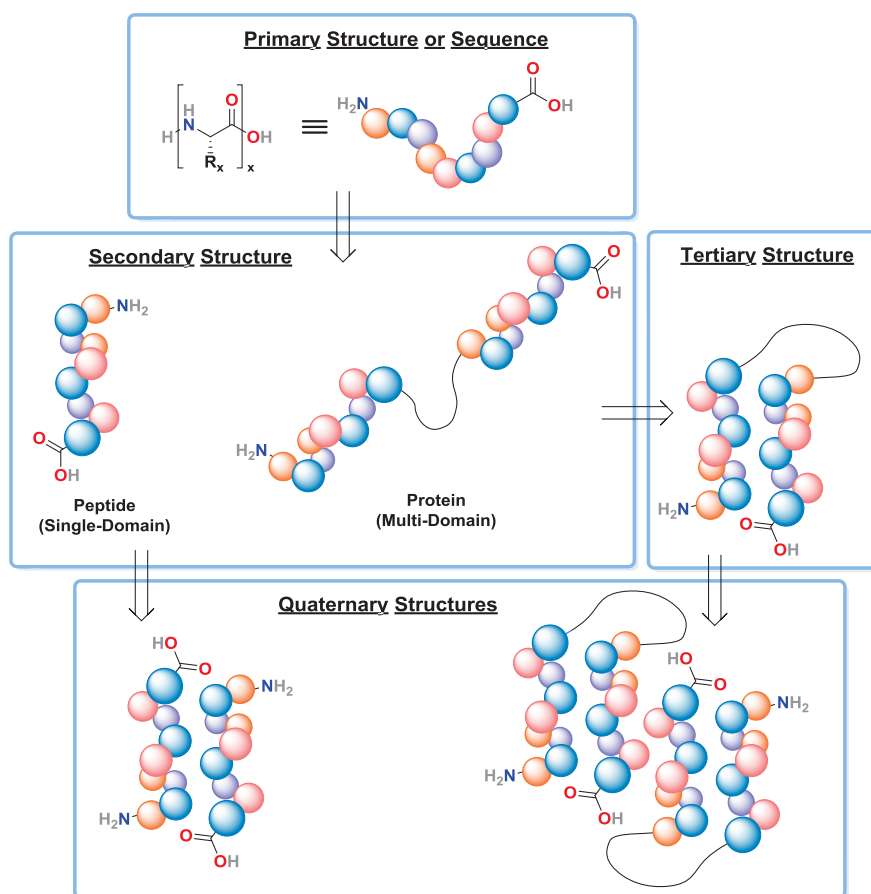


Figure I.13. Peptide and protein structures: primary, secondary, tertiary (proteins) and quaternary. Created using ChemBioDraw.

The properties of peptides make them unique therapeutic molecules. They are well-characterized thanks to the synthetic strategy called solid-phase peptide synthesis (SPPS).⁸² This methodology significantly reduces the production costs. With respect to the biological properties of peptides, these molecules generally show better specificity and affinity for therapeutic targets than small molecules and broader administration routes compared with biologics. However, the (proteolytic) stability of peptides is their weak point. Nevertheless, some peptides have a highly resistant profile conferred by their three-dimensional rearrangement,⁸³ and diverse strategies can be applied to improve the stability of labile peptides.⁸⁴ Thus, in most cases, peptides combine the best properties of two worlds, small molecules and biologics (**Table I.1**), except for a controversial property, namely immune response, where the performance of peptides is likely to fall between the two other drug categories.

Table I.1. Comparison of small molecules, peptides and biologics.

Compound	Small Molecule	Peptide	Biologics
Synthesis	chemical	chemical/SPPS	biological production
Cost	low	low	high
Characterization	well-defined	well-defined	hard
Specificity/Affinity	limited	medium/high	high
Administration	oral/cutaneous/injected	cutaneous/injected	injected
Stability/Metabolism	cytochrome metabolism	enzyme proteolysis (highly labile)	enzyme proteolysis (medium)
Immunogenicity	low	low-medium	high

Like proteins, peptides abound in nature as effector molecules. A number of peptides can cross the BBB using the transport mechanisms previously mentioned. However not all BBB crossing peptides use the same mechanism of uptake. In this regard, several relatively long neuropeptides (*e.g.* neuropeptide Y⁸⁵ and orexin A,⁸⁶ with a 36 and 33 amino acid sequence, respectively) have been shown to cross the BBB by simple diffusion. On the

other hand, glutathione (GSH), composed by three amino acids, namely γ -L-glutamyl-L-Cys-L-Gly, is transported into the CNS by a carrier-mediated saturable transport mechanism.^{87,88} Similarly, opiate peptides such as enkephalins and antiopiates such as Tyr-MIF-1 are also transported by carrier-mediated systems, in this case the so-called peptide transport system 1 (PTS-1).⁸⁹⁻⁹¹ Nevertheless, enkephalins also cross the BBB through non-saturable mechanisms.⁹¹

Endocytic mechanisms are also used by a range of peptides and proteins. Protegrin 1 (PG-1), an 18-amino acid antimicrobial peptide isolated from leukocytes, is able to form pores in bacterial membranes, and several authors have reported the use of diverse analogs as agents for brain delivery via AME.⁹² Discovered in 1988, HIV TAT 48–57 peptide derives from the transcriptional *trans*-activator protein of the human immunodeficiency virus 1 (HIV-1).^{93,94} The peptide crosses cell membranes, probably through an adsorptive-mediated mechanism, and has been used for drug delivery to the CNS.^{92,95} A recent study using TAT-conjugated quantum dots (QDs) revealed new insights of the mechanism underlying the capacity of this peptide to transport nanoparticles.⁹⁶ Deriving from the third helix of the Antennapedia homeodomain of *Drosophila*,^{97,98} penetratin has been used for similar purposes. These peptides, rich in positive residues, are known as cell-penetrating peptides (CPPs),⁹⁹⁻¹⁰¹ a name that reflects their capacity to cross biological membranes.

Peptides and proteins internalized by RME have a key advantage over those internalized by AME, in that they interact with a particular membrane receptor which might be over- or singularly-expressed in a specific cell-type or tissue. Endogenous ligands of each receptor, which are endocytosed, are susceptible to applications in drug delivery. Among these, the low-density lipoprotein receptor (LDLR) family recognizes various ligands like apolipoprotein B100 (apoB100) and E (apoE), which are embedded in the outer lipid-membrane of various^c lipoprotein particles.¹⁰² The latter, apoE (as a full-length protein or analogs), has been extensively used for drug delivery to the brain.¹⁰³⁻¹⁰⁵ Hepatitis C virus uses this mechanism (LDLR-mediated) to enter cells.¹⁰⁶ Nicotinic acetylcholine receptor (nAChR) is an ionotropic receptor that is highly expressed in the brain, including in BMECs.¹⁰⁷ A 16-amino acid peptide derived from a toxin from *Bungarus candidus*, Candoxin (CDX), was used as ligand of nAChR for drug delivery to the CNS.¹⁰⁸ In

^c Low-, very low-, intermediate-density lipoproteins (LDL, VLDL, IDL, respectively) and chylomicrons.

addition, peptides derived from a rabies virus¹⁰⁹ glycoprotein (RVG) have been extensively used for the same purpose.^{110,111}

Tf and its receptor (TfR) are involved in one of the mechanisms of endocytosis most widely used for drug delivery. These molecules are involved in iron metabolism and transport. At pH 7.4 (cell surface), diferric Tf (holoTf) binds to TfR, whereas apoTf does not. At pH 5.5 (endocytic vesicle) iron is dissociated but apoTf remains bound to TfR. Finally, apoTf is recycled to the cell wall and dissociated at pH 7.4.^{112,113} TfR is highly expressed in brain capillaries,^{114,115} but also present in CP epithelial cells and neurons.¹¹⁶ Gold nanoparticles containing Tf have been reported to cross the BBB.¹¹⁷

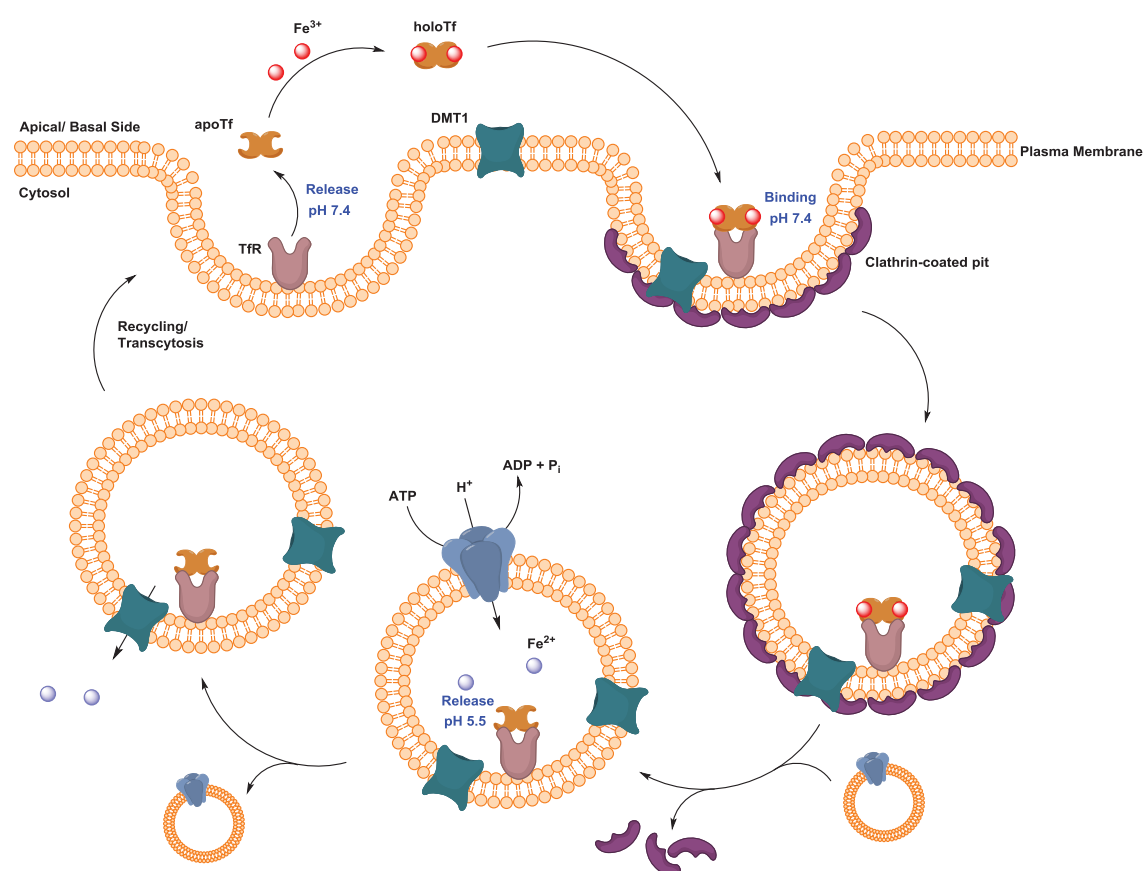


Figure I.14. Entry of iron into the cells via Tf-TfR. At pH 7.4—cell surface—, diferric Tf (holoTf) binds to TfR, whereas apoTf does not; and at pH 5.5—endocytic vesicle—iron is dissociated upon reduction by NADH:ferricyanide oxidoreductase¹¹⁸ and then transported to the cytosol by the divalent metal transporter 1 (DMT1); however, apoTf remains bound to TfR. Finally, apoTf is recycled to the cell membrane and dissociated at pH 7.4. Created using ChemBioDraw.

The term “Molecular Trojan horse” has been coined for a range of brain vectors including endogenous peptides, modified proteins, and peptidomimetic monoclonal antibodies.^{119,120} In this regard, monoclonal antibodies targeting TfR have been used for the delivery of drugs to the brain.¹²¹ Nevertheless, “Molecular Trojan horse” would be a more suitable description for the aforementioned “Trojan horse” mechanism used by viruses and bacteria, which, after infecting leukocytes, are transported to the basolateral side of the BBB.^{76,77} In this regard, the brain delivery of serotonin by monocytes following phagocytosis of liposomes has been reported.¹²²

In this thesis, the peptides used as molecular shuttles for brain delivery are referred to as “BBB shuttles”. These shuttles are peptides with the ability to carry cargos across the BBB either through active¹²³⁻¹²⁵ or passive transport mechanisms.^{126,127} The great advantage of BBB shuttles is that they can confer the ability to cross the BBB to a wide range of molecules through simple chemical conjugation strategies. Thus they are able to significantly expand the therapeutic space of potential CNS drugs. BBB shuttles can therefore serve as powerful facilitators of drug delivery to the brain.

OBJECTIVES

This thesis addresses four main objectives, one per chapter. The first three objectives are focused on basic research on BBB shuttles, whereas the last one has a more applied character.

Objective 1: To design, synthesize and evaluate a new family of passive diffusion BBB shuttles.

- 1.1. To improve the low solubility of the “gold standard” (NMePhe)-based BBB shuttle peptides.
- 1.2. To enhance their shuttle capacity (maintaining the transport after cargo attachment).
- 1.3. To study the role of the stereochemistry in passive diffusion.

Objective 2: To study a new family of BBB shuttle peptides working through receptor-mediated transcytosis (RMT), and to develop a methodology based on the combined use of MALDI-TOF MS with *in vitro* cell-based models of the BBB to assess the transport through the BBB.

Objective 3: To study and compare the immunological responses elicited by BBB shuttles made by L-amino acids and their *retro*-D-versions, made by D-amino acids.

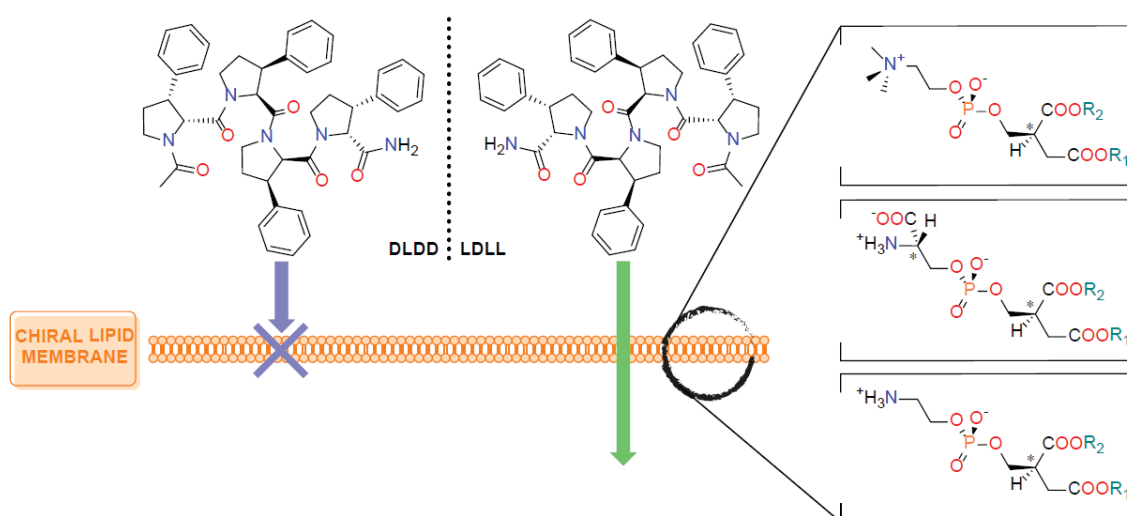
Objective 4: To perform a series of preliminary studies with the final goal of developing a therapy for Friedreich’s Ataxia (FRDA) at the central nervous system (CNS).

- 4.1. To study the viability of a protein replacement therapy for FRDA based on direct conjugation of BBB shuttles to frataxin (FXN).
- 4.2. To improve bioconjugation methods to modify HSV-1 particles with BBB shuttles to develop a gene therapy for FRDA at the CNS.
- 4.3. To characterize the physicochemical and biological properties of these viral particles before and after bioconjugation.

RESULTS AND DISCUSSION

Chapter 1

Study of Passive Diffusion BBB Shuttles



This chapter is partially based on the following article:

Arranz-Gibert, P.; Guixer, B.; Malakoutikhah, M.; Muttenthaler, M.; Guzmán, F.; Teixidó, M.; Giralt, E. Lipid Bilayer Crossing—The Gate of Symmetry. Water-Soluble Phenylproline-Based Blood-Brain Barrier Shuttles. *J. Am. Chem. Soc.* **2015**, *137*, 7357.

Passive transport encompasses two main pathways, namely paracellular (hydrophilic) and transcellular (lipophilic) diffusion. The former allows small hydrophilic entities to cross the BBB. However, this pathway is extremely hindered at this barrier due to the presence of tight junctions,¹²⁸ and therefore it is not ideal for drug delivery. In contrast, transcellular lipophilic diffusion involves transport through the much larger lipid bilayer, which provides a direct correlation between concentration and transport. The lipid bilayer of the plasma membrane can be considered a *macroreceptor* that can simultaneously interact with many ligands, thus accounting for the greatest proportion of the cell surface. This layer is therefore the preferred target for the delivery of small-molecule therapeutic drugs.¹²⁹ Theoretically, transport through this mechanism is facilitated by the movement of the fatty acid side chains in the membrane, which form holes (“kinks”) through which molecules can diffuse across the membrane.^{130,131} The concentration of the kinks is estimated to be between 10 and 50 mM. This concentration is a function of the conformational changes that can be adopted by fatty acid hydrocarbon, which are related to the ratio of saturated/ unsaturated fatty acids in the membrane and cholesterol.¹³²

There are currently two main approaches to design therapeutics able to cross the BBB through transcellular lipophilic diffusion. The first, and most commonly implemented

approach in the pharmaceutical industry, is based on a set of rules covering molecular size, presence of H-bond acceptors/donors, and lipophilicity, thereby attempting to increase the likelihood of the molecule crossing the BBB.^{57,133} The second approach is the design of BBB shuttles, which forms a major research line in our laboratory.

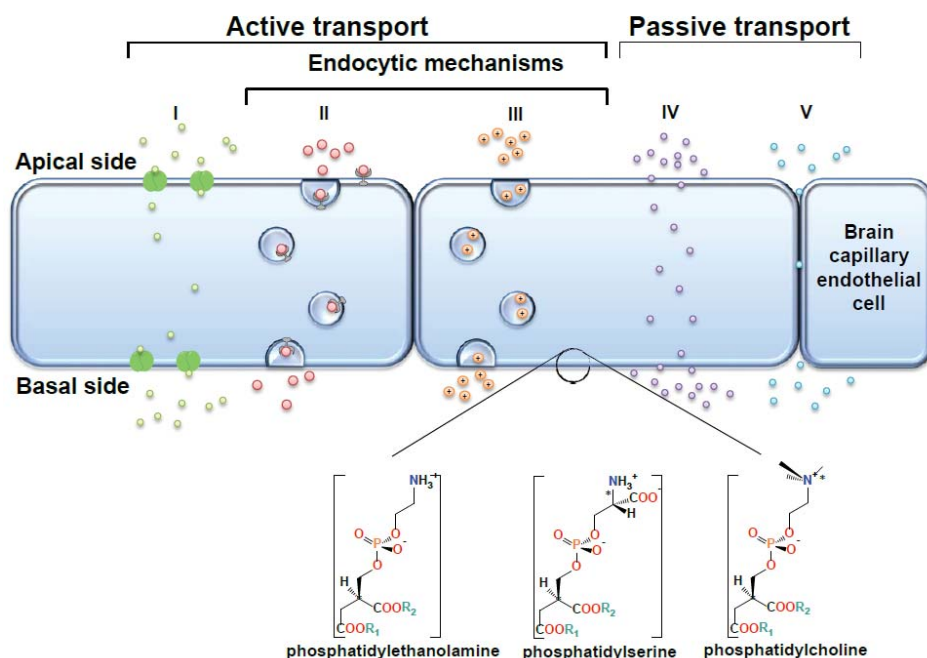


Figure 1.1. Transport mechanisms at the BBB. Active transport comprises (I) carrier-mediated transport and endocytic mechanisms—(II) receptor- and (III) adsorptive-mediated transcytosis. Passive transport is described by (IV) transcellular lipophilic diffusion and (V) paracellular hydrophilic diffusion. Transcellular lipophilic diffusion is dependent on the lipid composition of the cell, which comprises mainly phospholipids. Created with Microsoft PowerPoint and Adobe Illustrator.

While chiral complexity in drug-receptor activation, receptor-mediated transcytosis and protein-protein interactions has been extensively studied, the chiral interaction of entities with the membrane of the BBB endothelial cells is still poorly understood. Some studies have addressed a range of lipid structures,¹³⁴⁻¹³⁶ and enantiomeric discrimination of dipeptides by bio-membranes has also been reported.¹³⁷⁻¹³⁹ However, the chiral interactions between the BBB and BBB shuttles have not been studied before. Considering the chiral nature of phospholipids, one of the main components of plasma membranes, and our continuous efforts in improving BBB shuttle design, we set out to study the transport properties of different BBB shuttle stereoisomers.

Additionally, we wanted to improve the water-solubility of our BBB shuttles. Earlier work identified aromatic *N*-methylated peptides, both cyclic¹²⁶ and linear,¹⁴⁰⁻¹⁴³ as highly permeable compounds for lipid membranes. Efforts in our laboratory led to the development of (*N*MePhe)-based peptides, the gold-standard of passive diffusion BBB shuttles (**Figure 1.2**).^{141,142} The wider use of this class of BBB shuttle for clinical applications was however limited by the intrinsic low water-solubility of these molecules ($< 1 \mu\text{M}$).

Hence, we set out to advance the mechanistic knowledge and design opportunities of BBB shuttles by (1) studying the impact of chirality on their transport capabilities, and (2) by improving their water-solubility properties towards clinical applications. In order to achieve both goals, we sought to design and synthesize a library of novel chiral BBB shuttles that would provide further insight into the impact of chirality at the BBB, while at the same time tackling the long-standing problem of water-solubility.

1.1. Peptide-Shuttle Design

(NMePhe)-based BBB shuttles¹⁴⁰⁻¹⁴³ were taken as the base for the design of a new class of water-soluble BBB shuttles. Our aim was for these shuttles to retain high BBB effective permeability (P_e)¹⁴⁴ while improving their low water-solubility. At the same time, we wanted to have control of chirality to study the transport capacity of different stereoisomers. For these purposes, we chose the proteogenic amino acid proline, which has a conformationally restricted side-chain (advantageous for a chiral library design) and excellent water-solubility (around 300 mM, the tetraproline), in spite of the hydrophobic character of its side-chain. Additionally, polyprolines are also highly conformationally constrained compounds^{145,146} that have been used extensively for the design of water-soluble dendrimers and cell-penetrating peptides (CPPs).¹⁴⁷

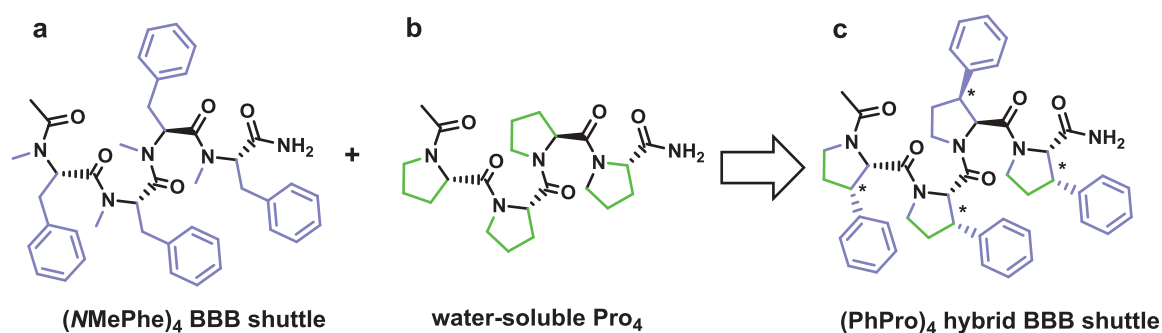


Figure 1.2. Structure of (a) the gold-standard passive diffusion BBB shuttle (NMePhe)₄, (b) hydrophilic polyproline unit Pro₄, and (c) designed (PhPro)₄ hybrid; all *homo-L*, C-terminal amide, and N-terminal acetylated. Created using ChemBioDraw.

We anticipated that a hybrid design of proline analogs containing a phenyl ring could merge the ability to cross the BBB with a simultaneous improvement of water-solubility (**Figure 1.2**). Furthermore, phenyl and pyrrolidine rings have been described as two of the most common substructures in the chemical makeup of CNS drugs.¹⁴⁸ Thus, we turned our attention to peptides derived from *cis*-3-phenylpyrrolidine-2-carboxylic acid (PhPro) (**Figure 1.2c**).

1.2. Transport Ability of (PhPro)₄ Shuttle Using the PAMPA Assay

To establish whether this new hybrid class of BBB shuttles retained its anticipated transport properties, we used the PAMPA assay to perform BBB transport studies of (PhPro)₄, which was initially synthesized with the commercially available racemic building block, Fmoc-*cis*-3-phenylpyrrolidine-2-carboxylic acid (**Figure 1.3**). The PAMPA assay, introduced by Kansy *et al.*,¹⁴⁹ allows the parallel evaluation of passive diffusion transport of various compounds through a mixture of lipids, thus emulating the biological barrier of interest. A selected lipid mixture is deposited onto a filter, which is divided into two compartments. Lipids are chosen in function of the composition of the barrier, *i.e.* in our study a mixture of porcine brain polar lipid extract was used. The compartments above and below the filter contained only buffer and the molecule to test in buffer, respectively. Magnetic stirring was applied for 4 h in donor wells, thus mimicking the stirring that red blood cells produce in brain capillaries. This approach almost totally reduced the unstirred water layer (UWL). Afterwards, each well was quantified by UV-absorption after injection into a RP-HPLC system. Time and concentration used were optimized to achieve a satisfactory relation signal-to-noise during quantification and to prevent back-diffusion, *i.e.* the experiment was performed while the transport rate was constant. Finally, propranolol (a β -adrenergic receptor blocker with high brain penetration) was used as a positive control.

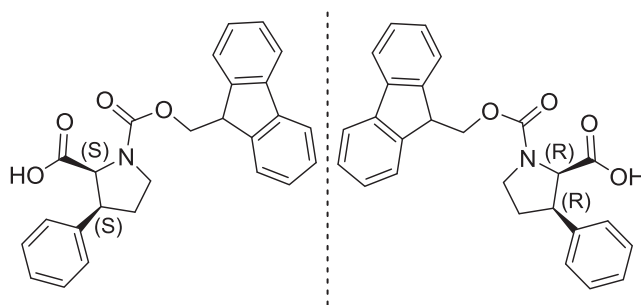


Figure 1.3. Fmoc-*cis*-3-phenylpyrrolidine-2-carboxylic acid structure: (left) L- and (right) D-configurations. Created using ChemBioDraw.

The formula for P_e calculation is shown in **Eq. 1.1**:

$$P_e = \frac{-218.3}{t} \log \left(1 - \frac{2C_A(t)}{C_D(t_0)} \right) \cdot 10^{-6} \text{ cm/s} \quad (1.1)$$

where t is the running time (4 h), $C_A(t)$ is the concentration of the compound in the acceptor well at time t , and $C_D(t_0)$ is the compound concentration in the donor well before running the PAMPA assay ($t_0 = 0$ h). Permeability is considered excellent with values >

$4.0 (\cdot 10^{-6})$ cm/s, uncertain between 2.0 and $4.0 (\cdot 10^{-6})$ cm/s and poor with values below $2.0 (\cdot 10^{-6})$ cm/s.¹⁴⁴

The suitability of the PhPro amino acid as a BBB shuttle building block was confirmed by comparing the transport of (NMePhe)₄, Pro₄ and (PhPro)₄ peptides, C-terminal amide to confer higher stability and N-terminal acetylated to mimic the same charge state as when a cargo is attached (**Table 1.1** and **Figure 1.4**). The (PhPro)₄ tetrapeptide displayed similar transport properties as (NMePhe)₄. Pro₄, as expected,¹⁴² displayed a marked reduction in transport, reaching almost zero (**Table 1.1**), highlighting the relevance of the phenyl ring—the most common molecular substructure in the chemical makeup of CNS drugs—¹⁴⁸ in the design of BBB shuttles.

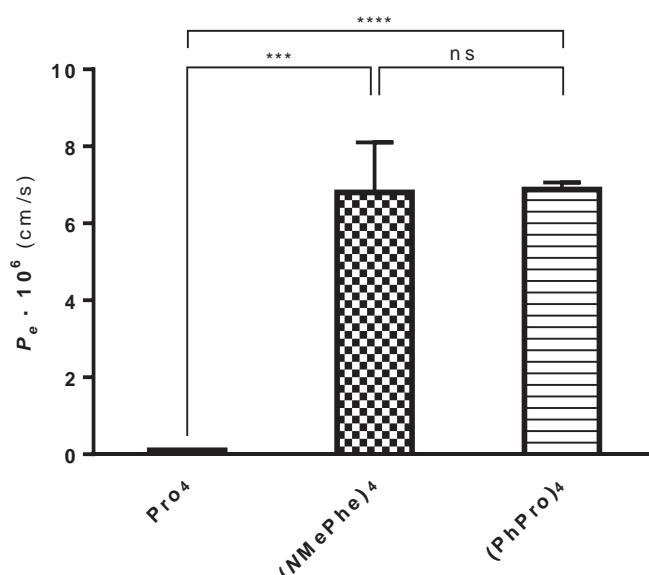


Figure 1.4. PAMPA transport values for the initial peptides involved in the design of the water-soluble BBB shuttle: *homo*-L Pro₄ and (NMePhe)₄ peptides and the 16-stereoisomer mixture of (PhPro)₄ peptide (n = 3; mean ± SD; significance: ns ≡ not significant ($p \geq 0.05$), ** ≡ very significant ($0.001 \leq p < 0.01$), *** ≡ extremely significant ($0.0001 \leq p < 0.001$), **** ≡ extremely significant ($p < 0.0001$)). Created using GraphPad.

Additionally, and in order to demonstrate the transport capacity of (PhPro)-based peptides as BBB shuttles, two therapeutically important cargos, nipecotic acid (NIP) and L-3,4-dihydroxyphenylalanine (L-DOPA), were coupled to the peptides (**Figure 1.5**) instead of an acetyl moiety. Although L-DOPA and NIP have enormous potential as CNS drugs,¹⁵⁰⁻¹⁵² neither one can cross the BBB by itself via passive diffusion (**Table 1.1**).^{141,153}

Table 1.1. Transport (%) and effective permeability (P_e) values for *homo*-L Pro₄ and (NMePhe)₄ peptides and the 16-stereoisomer mixture of (PhPro)₄ peptide, as well for (NMePhe)₄ and (PhPro)₄ attached to a therapeutically relevant cargo (L-DOPA and NIP) ($n = 3$; mean \pm SD). The transport values for (NMePhe)-based peptides were published previously).^{141,142}

Compound	Transport (%)	$P_e \cdot 10^6$ (cm/s)
Pro ₄	0.02 \pm 0.00	0.01 \pm 0.00
(NMePhe) ₄	12.7 \pm 2.1	6.8 \pm 1.3
(PhPro) ₄	12.6 \pm 0.3	6.88 \pm 0.18
L-DOPA	0.0 \pm 0.0	0.0 \pm 0.0
L-DOPA(NMePhe) ₄	2.4 \pm 0.2	1.10 \pm 0.10
L-DOPA-(PhPro) ₄	16.7 \pm 1.7	9.9 \pm 1.5
NIP	0.0 \pm 0.0	0.0 \pm 0.0
NIP-(NMePhe) ₄	2.8 \pm 0.2	1.40 \pm 0.10
NIP-(PhPro) ₄	19 \pm 3	11 \pm 2

L-DOPA is a prodrug that has been used for the last forty years to treat Parkinson's disease,¹⁵⁴ however, its uptake mechanism is limited since it has to compete with other amino acids for amino acid transporters. To improve uptake efficacy and to avoid interference with amino acid transporters, the challenge of ensuring L-DOPA delivery through other mechanisms must be tackled. Furthermore, L-DOPA derivatization through an amide bond can prevent side effects in the periphery by inhibiting the decarboxylation reaction and enhancing the transport of this molecule to the brain.^{153,155-159} Once in the brain, L-DOPA is enzymatically converted to dopamine by aromatic L-amino acid decarboxylase.

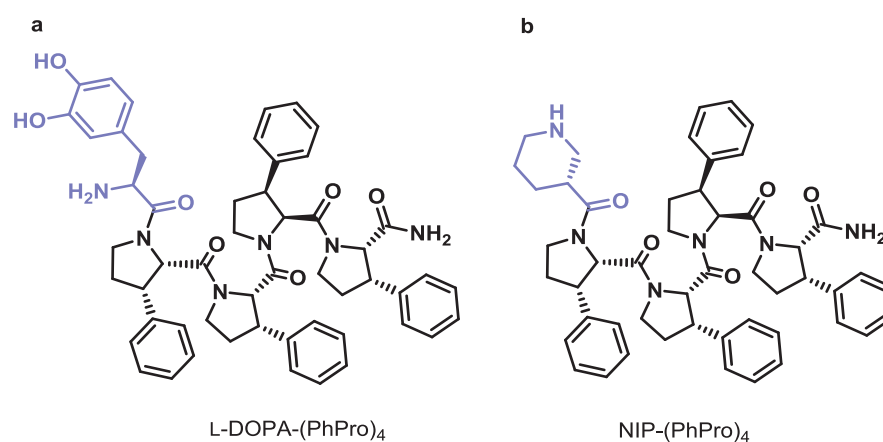


Figure 1.5. Structures for (a) L-DOPA-(PhPro)₄ and (b) NIP-(PhPro)₄ as *homo*-L configurations.

Created using ChemBioDraw.

Nipecotic acid (NIP) is a GABA reuptake inhibitor with great therapeutic potential if it would be able to cross the BBB.¹⁶⁰⁻¹⁶² GABA is the primary inhibitory neurotransmitter in the CNS, and decreased levels of this molecule are associated with several brain disorders. The levels of this amino acid in the CNS can be increased either by supplying GABA or its agonists, or via GABA reuptake inhibitors, such as NIP.

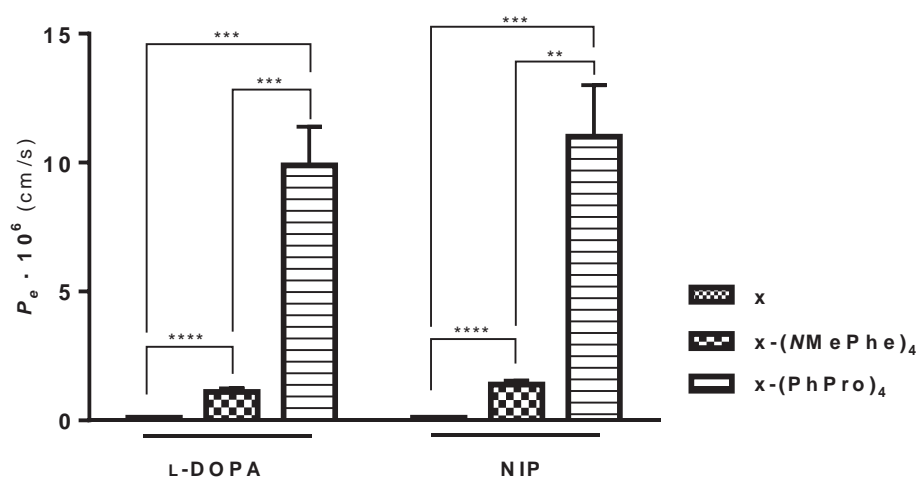


Figure 1.6. PAMPA transport values for peptides attached to a cargo (L-DOPA and NIP) was evaluated, as well as that of the cargos alone ($n = 3$; mean \pm SD; significance: ns \equiv not significant ($p \geq 0.05$), ** \equiv very significant ($0.001 \leq p < 0.01$), *** \equiv extremely significant ($0.0001 \leq p < 0.001$), **** \equiv extremely significant ($p < 0.0001$)). Created using GraphPad.

Hence, the BBB transport capacity of (PhPro)₄ peptide carrying L-DOPA or NIP was evaluated and compared to the gold-standard (NMePhe)₄ equivalent (**Figure 1.6**). x-(PhPro)₄ was synthesized using Fmoc-SPPS ($x \equiv$ acetyl, L-DOPA (L-3,4 dihydroxyphenylalanine) or NIP ((*R*)-piperidine-3-carboxylic acid)). (PhPro)-based peptides displayed superior permeability to their (NMePhe)-based analogs. Unlike acetylated (PhPro)₄ peptide and its (NMePhe)₄ analog, which did not display significant differences in permeability, (PhPro)₄ carrying either of the two cargos showed higher permeability (7-fold; with extremely significant differences) compared to its (NMePhe)₄ analog. Furthermore, the ability to cross the BBB appeared to be independent of the type of cargo attached (*i.e.* its BBB shuttle capacity was not altered). This observation contrasted with the findings for the (NMePhe)-based analogs, which showed a significant reduction in the capacity to cross the BBB (**Table 1.1** and **Figure 1.6**). In contrast, the transport capacity of Pro₄ tetrapeptide was close to zero ($P_e = 0.01 \cdot 10^{-6}$ cm/s), as was that of the two cargos (NIP and L-DOPA).

1.3. Design and Synthesis of a 16-Stereoisomer Library of (PhPro)₄

In order to study the impact of chirality at the BBB, we devised a library of 16 stereoisomers of the (PhPro)₄ peptide (**Figure 1.7**). For the 16-stereoisomer library, we first had to separate the two PhPro enantiomers of the commercially available racemic mixture. After chiral separation of the two compounds, each PhPro enantiomer, L- and D-PhPro ((*S,S*)- and (*R,R*)-3-phenylpyrrolidine-2-carboxylic acid, respectively), was assigned by the specific rotation published previously.^{163,164} All peptides were synthesized by manual Fmoc-SPPS.^{82,165,166} The 16 stereoisomers of this library arose from the permutation of the two amino acid enantiomers in each position and were synthesized via Houghten's "tea bag" method.¹⁶⁷⁻¹⁶⁹ All peptides were synthesized with a C-terminal amide to confer higher stability and were N-terminal acetylated to mimic the same charge state as when a cargo is attached. Additionally, the use of a non-natural amino acid (and in some cases also the use of the D-amino acid version) confers improved protease resistance, overcoming one of the main drawbacks of using peptides as therapeutic agents.

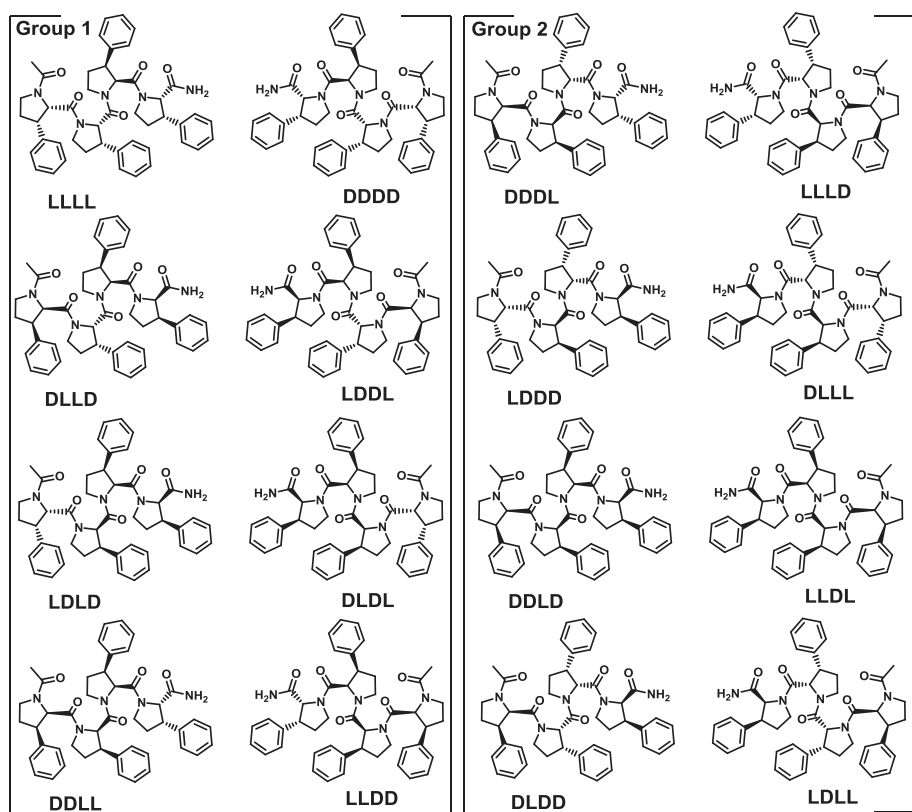


Figure 1.7. The library of the 16 (PhPro)₄ stereoisomers; the peptides are split into two transport-symmetry groups, where Group 1 contains the peptides with higher symmetry and lower enantiomeric discrimination, and Group 2 comprises the less symmetric peptides related to a higher enantiomeric discrimination. Created using ChemBioDraw.

1.4. Physicochemical Characterization of Pro₄ and (PhPro)₄ Shuttle

Circular dichroism (CD) studies were carried out to confirm the correct (PhPro)₄ enantiomeric assignment. The spectra of both *homo*-L and *homo*-D (PhPro)₄ were compared to the *homo*-L and *homo*-D Pro₄ analog control peptides (synthesized with enantiomerically pure building blocks). As expected, the *homo*-L tetrapeptides (LLLL) displayed a negative CD spectrum, contrary to the *homo*-D (DDDD) ones, which displayed a positive one (**Figure 1.8**), thus confirming our initial assignment. The CD spectra of Pro₄ peptides recorded a higher signal, thereby suggesting a more defined secondary structure (*i.e.* PPII conformation generally observed with polyproline compounds¹⁷⁰ compared to the (PhPro)₄ tetrapeptides). The PhPro-peptides studied by CD did not present a known structure-assigned spectrum.

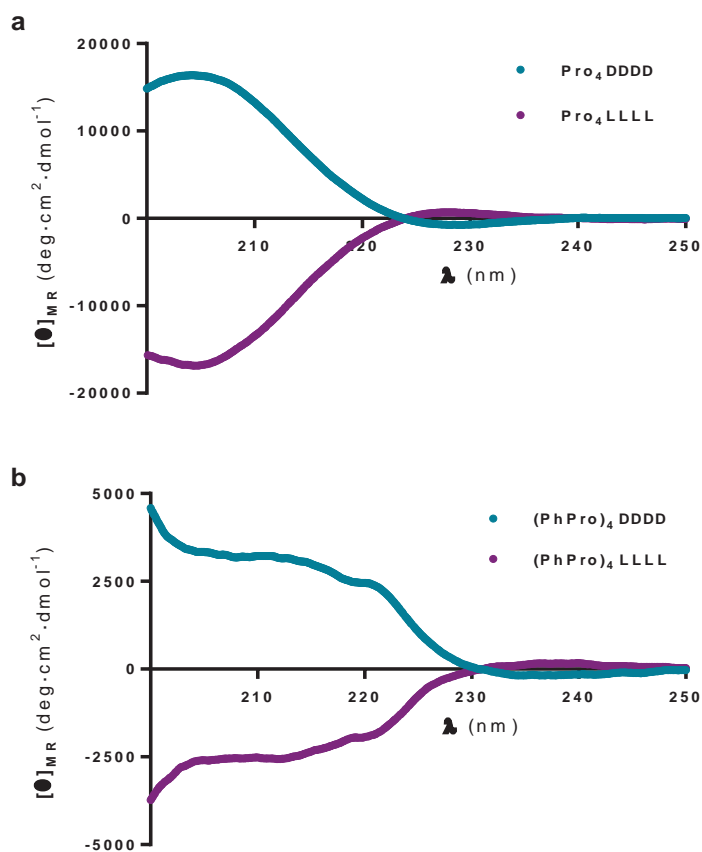


Figure 1.8. Circular dichroism spectra of pairs of enantiomers; *homo*-D (blue) and *homo*-L (purple) of (a) Pro₄, displaying a PPII conformation (*homo*-L/ *homo*-D with a weak maximum or minimum at 228 nm and a strong minimum or maximum at 203 nm, respectively); and (b) (PhPro)₄. Created using GraphPad.

Analytical RP-HPLC characterization of the 16 stereoisomers further added to the characterization, showing complex chromatographic profiles (**Figure 1.9a**) that were identical between pairs of enantiomers. Each peak of the profile corresponded to a conformer with an interconversion rate faster than $\frac{1}{15} \text{ min}^{-1}$ (length of the injection cycle), since reinjection of any of the collected peaks resulted in the same RP-HPLC chromatogram observed earlier (**Figure 1.9b**). In some cases, RP-HPLC characterization at higher temperature (60°C) resulted in a single peak (**Figure 1.9c**). Only the stereoisomers DDLD and LLDL yielded a single RP-HPLC peak, indicating a preferential conformational arrangement compared to the other stereoisomers.

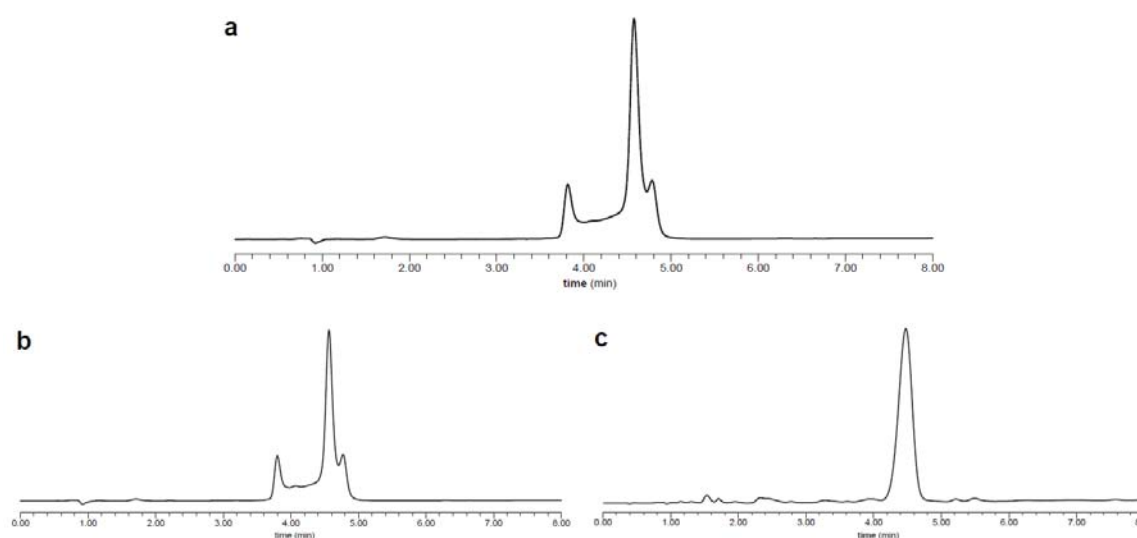


Figure 1.9. RP-HPLC chromatograms of the DLDD (PhPro)₄ stereoisomer (gradient from 50 to 80% CH₃CN in 8 min, symmetry C₁₈ column) (a) at room temperature (r.t.), (b) after chromatographic peak (any of the three peaks observed) reinjection at r.t, and (c) at 60°C. Created with Adobe InDesign.

This observation was confirmed by CD, which showed a significantly different spectrum (maximum/ minimum at 222 nm, respectively) compared to the other stereoisomers (**Figure 1.10**). Additionally, both of these enantiomers gelled after solvent (DIPEA/DCM, 1:1, v/v) evaporation, thereby indicating the adoption of a specific conformational arrangement that favors this process (not observed with the other stereoisomers). Each peptide was identified by RP-HPLC-MS and MALDI-TOF MS, and the observed masses of the individual stereoisomers were in good agreement with the theoretically calculated molecular weights.

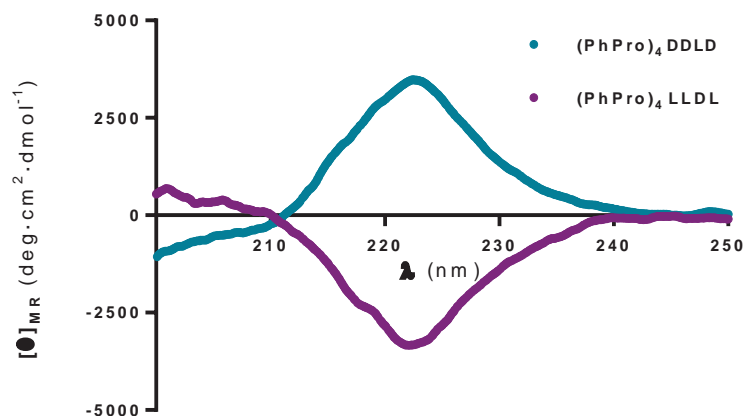


Figure 1.10. Circular dichroism spectra of DDL (blue) and LLDL (purple) pairs of enantiomers of (PhPro)₄. Created using GraphPad.

Since PhPro was chosen to improve the water-solubility of these BBB shuttles, we determined this parameter by weighing the lyophilized peptide from a known volume of a saturated solution. Low water-solubility represents a long standing problem of current BBB shuttles with for example (NMePhe)₄, the “gold-standard” passive transport BBB shuttle, having a water-solubility that is lower than 1 μM . The (PhPro)₄ tetrapeptides registered water-solubility in the range of 1–5 mM, which can be considered a significant improvement (1,000–fold) to that shown by (NMePhe)₄ tetrapeptides.¹⁴² The solubility of Pro₄ peptide was 300 mM.

1.5. Passive Diffusion Transport Studies and Chiral Discrimination at the BBB

Chirality plays a key role in many cellular processes and we were interested if this is also the case during passive diffusion of BBB shuttles through the BBB. To study this phenomenon, we built a 16-stereoisomer tetrapeptide library via sequentially permuting each of the four positions with L- and D-PhPro enantiomers. The passive diffusion of these peptides through the BBB was evaluated using the PAMPA assay. The majority of the (PhPro)₄ stereoisomers displayed high diffusion through the BBB lipids, except two peptides (DDL D and its *retro*-peptide DLDD), with significantly lower transport rates (**Table 1.2** and **Figure 1.11**).

Table 1.2. Transport (%) and effective permeability (P_e) values for the 16-stereoisomer library of (PhPro)₄ peptide (n = 3; mean \pm SD).

Compound	Transport (%)	$P_e \cdot 10^6$ (cm/s)
DDDD	15.2 \pm 0.5	8.6 \pm 0.3
LLLL	14.3 \pm 0.3	7.95 \pm 0.15
DDDL	12.34 \pm 0.13	6.72 \pm 0.07
LLLD	17 \pm 5	10 \pm 3
DDL D	7.1 \pm 0.2	3.64 \pm 0.13
LLDL	14 \pm 2	7.8 \pm 1.2
DLDD	1.76 \pm 0.09	0.85 \pm 0.04
LDLL	12.8 \pm 0.6	7.0 \pm 0.3
LDDD	9.27 \pm 0.10	4.86 \pm 0.05
DLLL	12.8 \pm 0.6	7.0 \pm 0.4
DDL L	11.2 \pm 1.2	6.0 \pm 0.6
LLDD	13.5 \pm 0.9	7.4 \pm 0.5
DLDL	12.7 \pm 0.7	7.0 \pm 0.4
LDLD	12.7 \pm 1.0	7.0 \pm 0.6
LDDL	10.61 \pm 0.08	5.65 \pm 0.04
DLLD	10.5 \pm 0.8	5.6 \pm 0.4
Propranolol	22.6 \pm 0.5	14.3 \pm 0.3

Almost all the 16 stereoisomers displayed excellent transport properties (with P_e range of 4.86-10 ($\cdot 10^{-6}$) cm/s) similar to the gold-standard (NMePhe)₄, which displays a transport capacity of 6.8 ($\cdot 10^{-6}$) cm/s (**Table 1.2** and **Figure 1.11**). Only DDL D and DLDD displayed significantly lower P_e values (3.64 and 0.85 ($\cdot 10^{-6}$) cm/s, respectively). Interestingly, the

DDLDD/LLDDL pair was identified earlier via analytical RP-HPLC and CD analysis displaying a pronounced but distinct secondary structure compared to the other stereoisomers (**Figure 1.10**).

Chirality discrimination of the 16 stereoisomers at the BBB was determined by pairing the individual enantiomers and determining the enantiomeric discrimination value (D_e) (**Table 1.3**). D_e is defined as the excess ratio of the transport of each pair of enantiomers, the higher (T_H) minus the lower (T_L), then divided by the lower (T_L):

$$D_e = \frac{T_H - T_L}{T_L} = \frac{T_H}{T_L} - 1 \quad (1.2)$$

By definition, this parameter ranges between 0 (no discrimination) and infinite (absolute discrimination). We observed values from 0.0 to 6.1 (**Table 1.3**). Differentially, the DLDD/LDLL pair of enantiomers showed the highest discrimination, followed by its *retro*-pair, DDLDD/LLDDL, which displayed a value of 1.0.

Table 1.3. Passive diffusion transport enantiomeric discrimination (D_e) values for each pair of enantiomers (n = 3; mean \pm SD). Two groups are differentiated on the basis of the symmetry and enantiomeric discrimination (Group 1, higher symmetry, lower enantiomeric discrimination; Group 2, lower symmetry, higher enantiomeric discrimination).

Group	Enantiomer Pair	Enantiomeric Discrimination
1	DLDD/ LLDDL	0.00 \pm 0.00
	LDDL/ DLLD	0.01 \pm 0.08
	DDDD/ LLLL	0.06 \pm 0.04
	LLDD/ DDLL	0.21 \pm 0.13
2	DLDD/ LLDDL	0.38 \pm 0.07
	LLDD/ DDLL	0.4 \pm 0.4
	LLDD/ DDLL	1.0 \pm 0.3
	DLDD/ LLDDL	6.1 \pm 0.4

To further study the impact of chirality on the transport of this family of BBB shuttles, we classified pairs of enantiomers into two categories on the basis of the similarities between their transport (**Figure 1.11**). The peptide enantiomer pairs containing two units of each PhPro amino acid enantiomer in their sequence (DDLL/LLDD, DLDD/LLDD and LDDL/DLLD) and the *homo*-peptides (LLLL/DDDD) showed similar transport between enantiomers (Group 1). Among this group, *homo*-peptides showed the highest transport and the LDDL/DLLD pair the lowest.

The transport values of the other enantiomer pairs with only one PhPro amino acid permutation (Group 2) varied significantly within the pairs (**Figure 1.11**). DDL D and its *retro*-peptide (DLDD) showed the poorest transport capacity, mainly due to membrane retention (60 and 87%, respectively; data not shown). Their enantiomers (LLDL and LDLL, respectively), however showed excellent and to Group 1 similar transport properties (7.8 and 7.0 ($\cdot 10^{-6}$) cm/s, respectively). This clearly shows that within two enantiomers the transport properties can be significantly different (*e.g.* 7-fold for DLDD and LDLL), strongly suggesting that chirality plays an important role in passive diffusion.

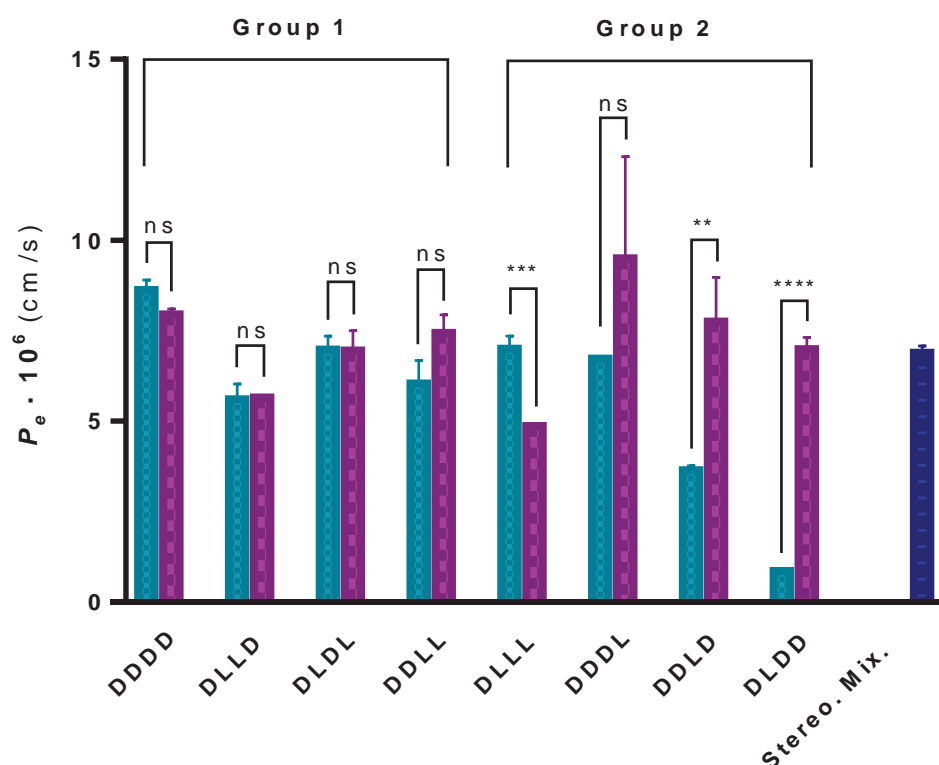


Figure 1.11. PAMPA transport values for the 16 individual stereoisomers, paired by enantiomers, and the 16-stereoisomer mixture (dark blue column). Light blue column corresponds to the peptide configuration displayed on the graph (*e.g.* first column = DDDD); purple column corresponds to the enantiomer of the peptide configuration displayed on the graph (*e.g.* first column = LLLL) ($n = 3$; mean \pm SD; significance: ns \equiv not significant ($p \geq 0.05$), ** \equiv very significant ($0.001 \leq p < 0.01$), *** \equiv extremely significant ($0.0001 \leq p < 0.001$), **** \equiv extremely significant ($p < 0.0001$)). Created using GraphPad.

In order to delve deeper into the chirality-transport relationship, a symmetry model was devised. Assuming two approximations, considering that the peptide termini (*N*-

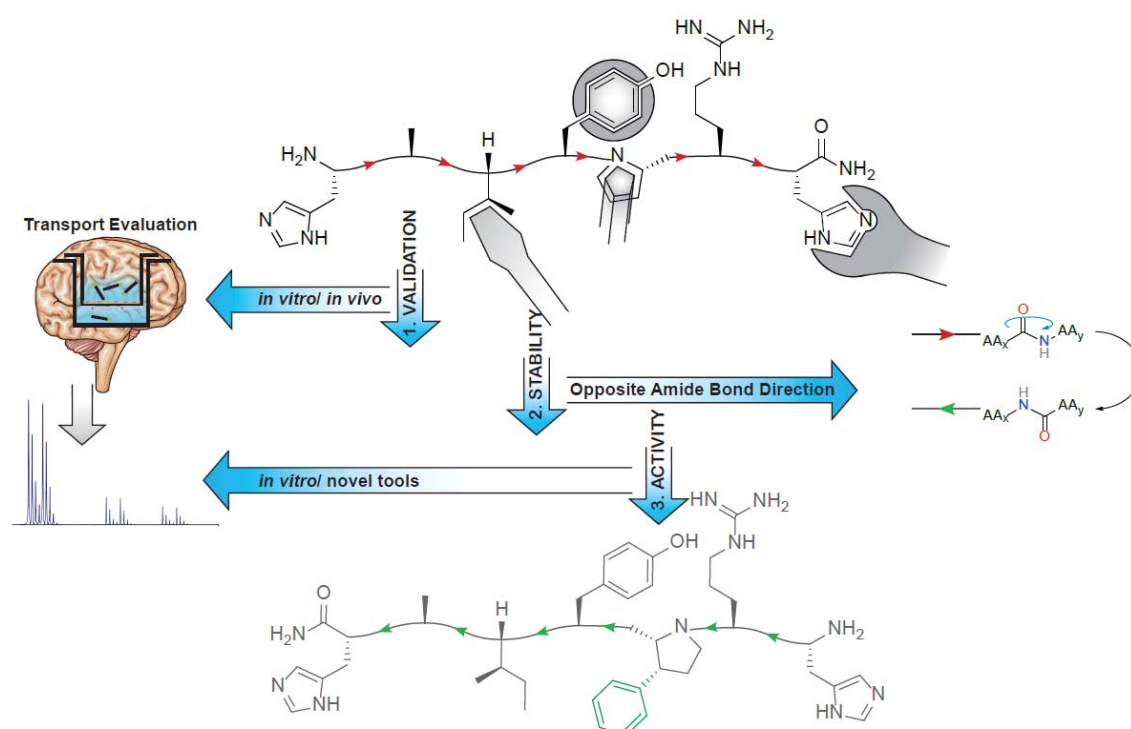
terminal acetylated and C-terminal amide) do not interfere in the symmetry and the peptide bond has no direction, *i.e.* *retroenantiomeric*-peptides would be identical;¹⁷¹⁻¹⁷³ two enantiomer pair groups were differentiated. Group 1, with the lowest enantiomeric discrimination (D_e) values, contains all *quasi-meso* isomers.^d Group 2, with higher D_e values, lacks this *quasi-meso* character (and can be considered as less symmetric than Group 1). Furthermore, the pairs of enantiomers from Group 1 are *retroenantio*-peptides between them but not those belonging to Group 2. Interestingly, the LDLL/ DLDD pair presented a very high D_e (6.1) (**Figure 1.11** and **Table 1.3**).

These results show that passive diffusion through biological membranes can be highly enantiomerically selective. Enantiomeric discrimination is a clear event in passive transport and can lead to high enantioselectivity. We could show that symmetry plays a crucial role in this process such that the greater the symmetry (Group 1), the lower the enantioselectivity. A desymmetrization step could therefore be employed to obtain compounds with high selectivity to distinct lipid compositions, *i.e.* different biological barriers, cell types or disease regions, and even cellular regions, as the lipid composition differ among them.¹⁷⁴⁻¹⁸² We envisage in future work the intriguing possibility to design chiral shuttles with the unique potential to target membrane-specific cell types. This has potential applications in oncology where it can be used to target tumors since their membrane composition often significantly differs from healthy cells.¹⁸³⁻¹⁸⁶

^d By *quasi-meso* we mean compounds that, assuming that the peptide termini are not relevant and peptide-bond has not directionality, have an accessible aquiral conformation and therefore would be *meso* forms.

Chapter 2

Study of Actively-Transported BBB Shuttles through Receptor-Mediated Transcytosis



This chapter will give rise to the following article:

Arranz-Gibert, P.; Prades, R.; Guixer, B.; Guerrero, S.; Araya, E.; Ciudad, S.; Kogan, M. J.; Giralt, E.; Teixidó, M. HAI Peptide and its Derivatives: Chemical Tools to Study and Enhance the Biostability and Bioactivity of BBB Shuttles. Submitted to *J. Am. Chem. Soc.*

Although BBB shuttle peptides transported through active mechanisms show promise, there are few examples in the literature.¹⁸⁷ These derive from the use of phage display of peptides against a receptor that crosses the BBB through receptor-mediated transcytosis (RMT)¹⁸⁸ to the refinement (*e.g.* computational or medicinal chemistry approaches, like following bioisosterism rules) of those already known.⁸⁴ In all these cases, several experimental tools are required to assess and confirm their performance as effective BBB shuttles, which could be limited by the concentration-sensitivity relationship (assayed). We then selected a novel peptide candidate actively transported through RMT to further push the chemical tools currently used in the field.

Dr. Roger Prades during his thesis pursued the study and improvement of a BBB shuttle candidate (namely HAI) by chemically modifying its structure to obtain a more biostable molecule. We then designed novel methods to study this class of peptide and refined the bioactivity of the peptide by using non-natural amino acids.

2.1. Previous Studies with HAI Peptide

2.1.1. Studying the Selected Candidate—Mechanistic *in vitro* Studies, *in vivo* Transport Efficiency and Biostability

HAI peptide, with the amino acid sequence HAIYPRH, was found by Lee *et al.* by phage display against the human transferrin receptor (TfR).¹⁸⁸ Highly expressed in brain capillaries, TfR mediates the delivery of iron to the brain.¹¹⁵ It is also expressed in choroid plexus epithelial cells and neurons.¹¹⁶ One of the main advantages of this peptide is that it interacts in a region of the TfR that does not overlap with the native binding site of transferrin, thereby avoiding physiological effects on the protein function *in vivo* and consequently making this peptide very attractive from the therapeutic point of view. HAI has been studied for diverse applications such as tumor-targeting¹⁸⁹ and oral drug delivery.¹⁹⁰ Its potential as a BBB shuttle has recently been addressed by Kuang *et al.*¹⁹¹ Given that other peptides interacting with the TfR have the capacity to cross the BBB⁸⁴ and that the BBB endothelium is characterized by high presence of TfR¹¹⁴—a feature that can selectively enhance brain targeting—here study the potential applications of HAI as a BBB shuttle. Dr. Roger Prades initiated the study of this peptide during his PhD thesis. A series of experiments were performed to ensure that HAI delivery is TfR-dependent, and at the same time to establish whether it competes with Tf—an observation previously reported.^{188,192} HAI transport (cellular internalization) was promoted by the addition of Tf, the natural ligand of TfR, which might induce the internalization and transcytosis of the aforementioned receptor by the cells (**Figure 2.1a,b**). Thus, the peptide did not compete with Tf for the same binding pocket at TfR. Moreover, competition assays revealed that HAI competes with itself for internalization (**Figure 2.1c**), and incubation of cells with increasing concentrations of the peptide led to the saturation of internalization (**Figure 2.1d**). Both observations indicate that HAI is actively transported. In addition, this peptide co-localizes with Tf when cells are incubated with carboxyfluorescein (Cf)-labeled HAI (Cf-HAI) and Alexa555-Tf (**Figure 2.1e**). This observation thus demonstrates that the internalization of HAI occurs through clathrin-mediated endocytosis, as already described for the TfR-Tf pair.

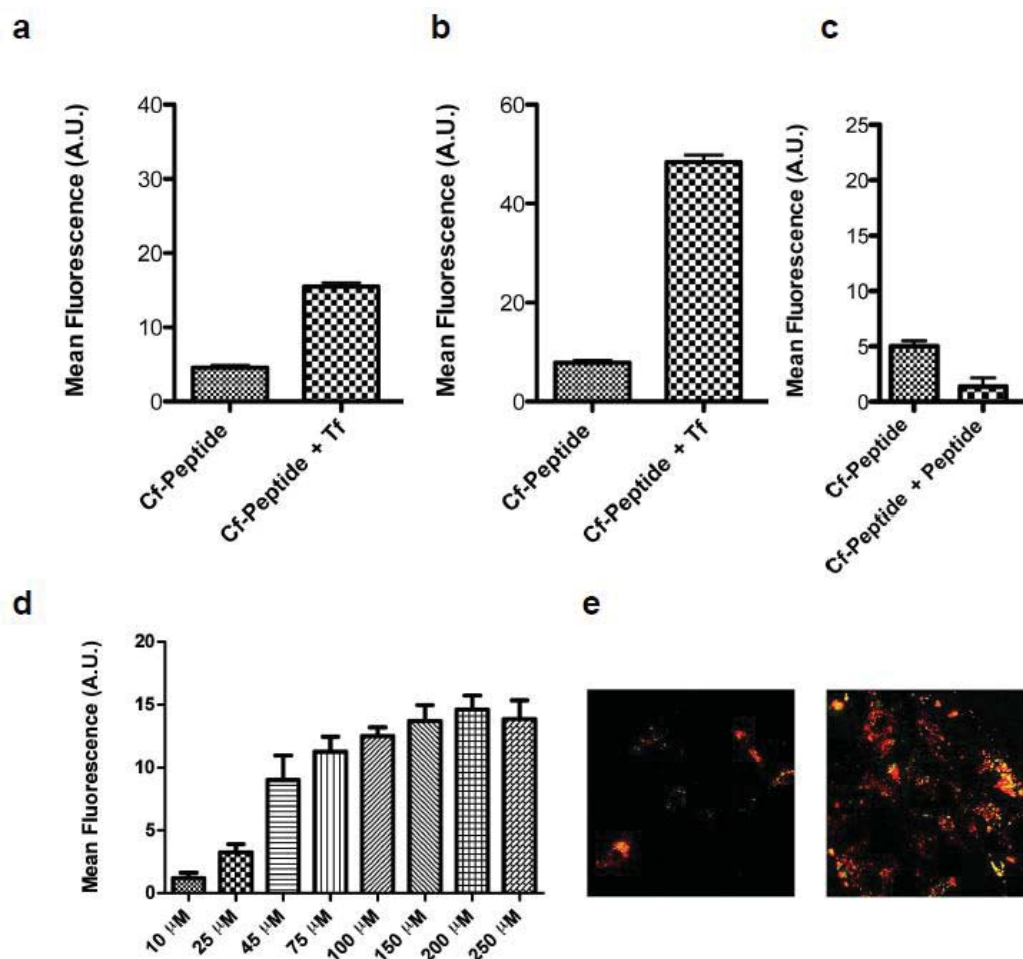


Figure 2.1. Studies of the internalization mechanism of HAI (mean \pm SD): flow cytometry results after incubating (a) bovine brain endothelial cells (BBECs) or (b) rat astrocytes with Cf-HAI at 50 μ M in the absence or presence of transferrin, (c) co-incubation of Cf-HAI with HAI (competition assay), (d) incubation of BBECs with a range of concentrations of Cf-HAI, and (e) co-incubation of (left) BBECs or (right) rat astrocytes (co-localization experiments) with Cf-HAI at 50 μ M with fluorescently labeled transferrin (AlexaFluor555). Adapted from Dr. Prades' thesis.¹⁹³

Furthermore, HAI was characterized by circular dichroism (CD). This approach revealed a profile like that of a random coil conformation, with a negative band at 197 nm and a weak band at 220 nm. Toxicity assays demonstrated that the peptide is not toxic for BBECs or rat astrocytes, when these cells are incubated with this peptide at a concentration of 50 μ M for 24 h.

To study the *in vitro* and *in vivo* potential of HAI to deliver a larger cargo to the CNS, gold nanoparticles (AuNPs) were decorated with this peptide. and their transport was evaluated using the bovine BBB *in vitro* model (Figure 2.2a).^{194,195} In these models, two

compartments are separated by a membrane containing a monolayer of endothelial cells which mimics either the intestinal barrier or BBB. One compartment contains the peptide, which is incubated for 2 h. The amount of peptide in each compartment is then analyzed to determine apparent permeability (P_{app} , in cm/s) and transport (T , in %). We ensured that the size of our AuNPs and conjugates were adequate (*i.e.* small enough) for *in vivo* purposes but at the same time larger than 20 nm and thus avoiding alteration of the peptide structure.¹⁹⁶ Incubation of the cells with AuNP-HAI at a concentration of 5 nM caused an increase in transport by more than two orders of magnitude, up to $1.7 (0.1) \times 10^{-7}$ cm/s, compared to AuNPs $(0.970 (0.003) \times 10^{-9}$ cm/s). In addition, HAI conjugates showed slightly higher permeability than AuNP-THR, $1.40 (0.07) \times 10^{-7}$ cm/s, results obtained with a previously studied BBB shuttle (THR) carrying the same NPs.¹²³

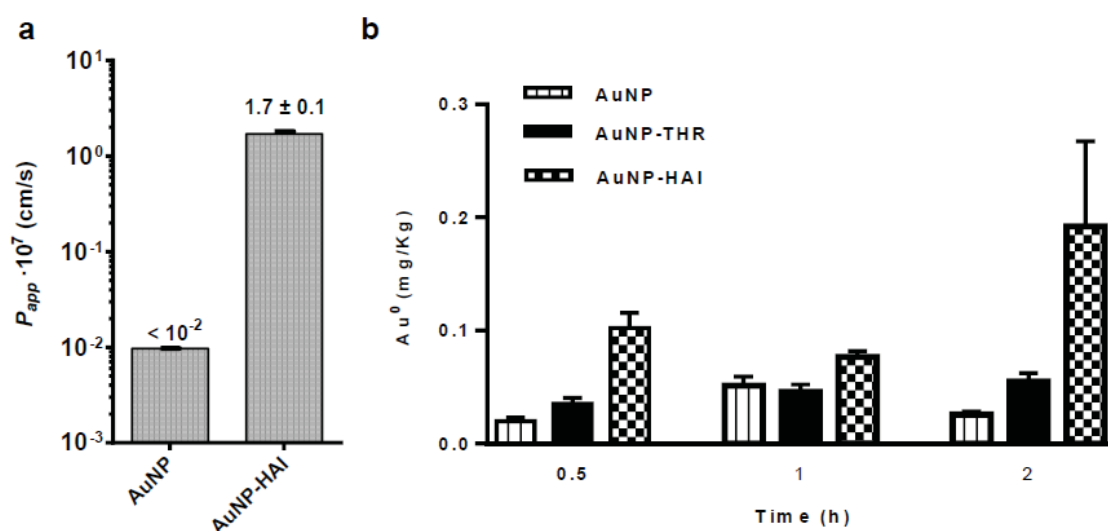


Figure 2.2. *In vitro* and *in vivo* transport of AuNPs (mean \pm SD). Using the same *in vitro* bovine BBB transport model used for the peptides analyzed previously; (a) apparent permeability (P_{app}) was obtained for AuNPs and AuNP-HAI. Then, (b) *in vivo* studies were performed in rats to confirm the capacity of HAI to deliver AuNPs into the CNS. In these experiments, the corresponding AuNPs were injected *i.p.* using 1.86 mg gold content per kg of body weight, and the gold content in the brain was determined by INAA at several time points (0.5, 1, 2 h). Created using GraphPad and Microsoft PowerPoint.

Thanks to a collaboration with the group of Prof. Marcelo J. Kogan, *in vivo* studies were performed to compare the delivery of AuNP, AuNP-HAI and AuNP-THR to the brain in rats (the latter results, compared from Prades *et al.*).¹²³ Animals were euthanized at 0.5, 1 and 2 h after the *i.p.* injection. After PBS perfusion, brains were excised, lyophilized, and dried. Instrumental neutron activation analysis (INAA) and inductively coupled plasma

mass spectrometry (ICP-MS) are currently the ‘gold standards’ for quantifying gold in tissues.¹⁹⁷ To measure gold content in the brain (expected to be low or very low), we used INAA. The samples were then irradiated with neutrons, thereby converting ¹⁹⁷Au to ¹⁹⁸Au. The quantification of the γ -ray emitted from the samples allowed us to determine the gold content in each sample. A progressive accumulation of gold in brain tissue was observed, reaching much higher amounts than the reported trace levels found in the CNS (2×10^5 mg/kg fresh tissue).¹⁹⁷ The conjugation of AuNPs to HAI and THR increased the concentration of this metal in the brain with respect to naked AuNPs (**Figure 2.2b**). Remarkably, AuNP-HAI showed greater penetration than AuNP-THR.

Hence, HAI showed excellent transport through the BBB, thus emerging as a promising BBB shuttle. Nevertheless, peptides formed by L-amino acids have a short *in vivo* half-life, which can reduce their potential bioactivity. The protease sensitivity of this peptide was tested at a concentration of 150 μ M in HBSS/human serum 90:10 (v/v) for 24 h. At several time points, an aliquot was extracted, precipitated serum proteins with methanol and then analyzed by RP-HPLC. The peptide showed a half-life in serum of around 5 min, a much shorter time than that expected for a drug-like compound. The potential proteolytic sites were analyzed by MALDI-TOF, which revealed three main proteolytic sensitive sites: H-HA↓I↓YPR↓H-NH₂ (where ↓ shows the cleavage between two consecutive residues).

2.1.2. Tuning Protease-Resistance: N-Methylation of Labile Positions vs. the Retro-D-Version Approach

Several strategies can be used to increase the *in vivo* stability of a peptide composed of L-amino acids. It was selected the N-methylation of sites sensitive to proteolysis and the *retro*-enantio approach, which is a topological mimic with a reversed sequence order and inversed stereochemistry in each α -carbon (*i.e.* made by D-amino acids).¹⁹⁸ The N-methylated peptide designed was H-HA(NMe)I(NMe)YPR(NMe)H-NH₂, which contained the sensitive sites (see previous section) protected by an N-methyl group,^{199,200} namely (NMe)HAI. The *retro*-enantio peptide (or *retro*-D) was H-hrpyiah-NH₂ (where the lowercase letter denotes D-amino acid), namely *r*D-HAI. Thus, the stability of these two peptides in serum was studied (**Figure 2.3**). Both displayed excellent protease resistance (half-life above 24 h).

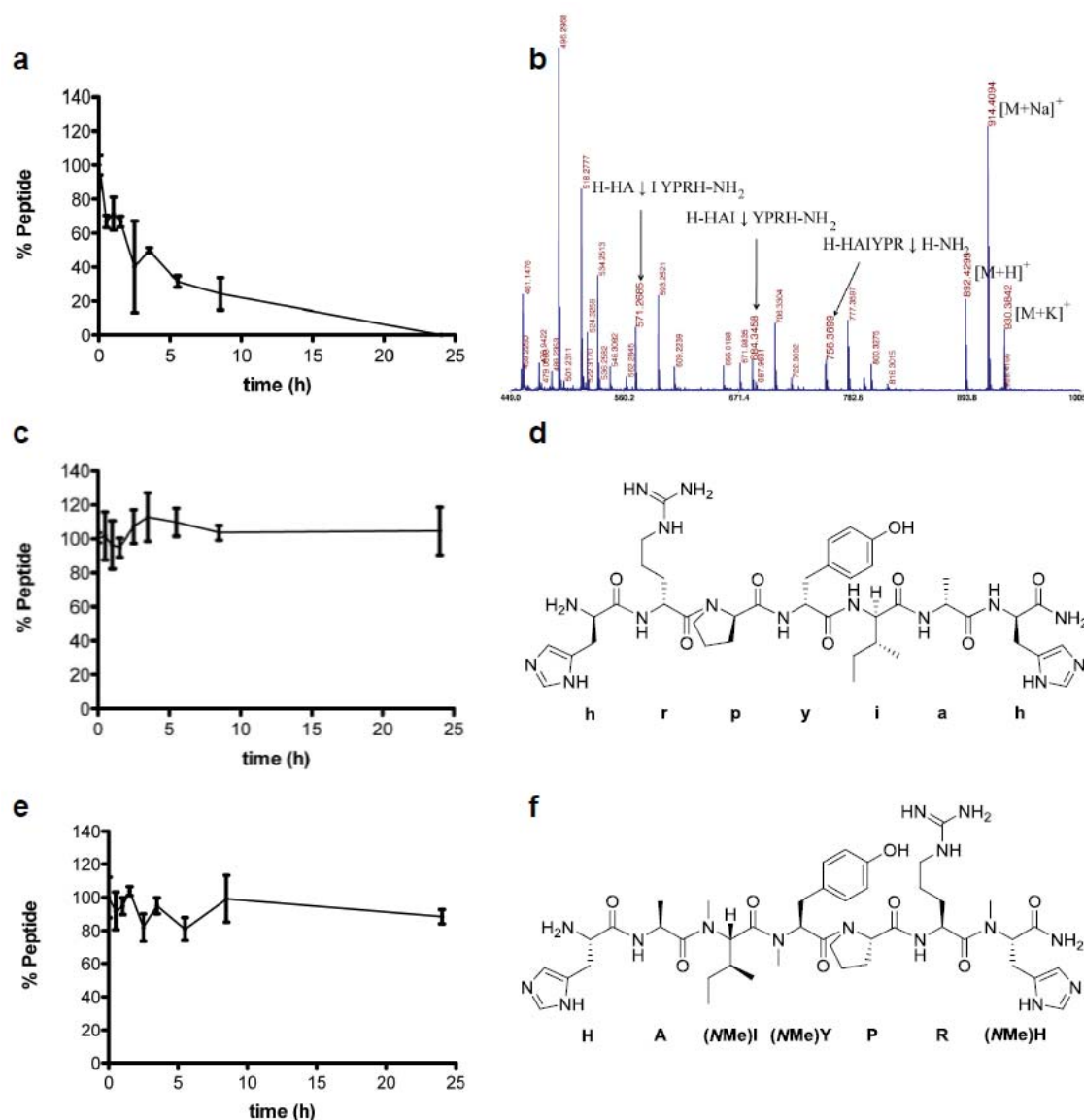


Figure 2.3. Stability of HAI, *rD*-HAI and (NMe)HAI in human serum: (**a**, **c** and **e**) graphic representation of the remaining peptide vs. time for each peptide (mean \pm SD), respectively; (**b**) MALDI-TOF traces at 30 min; (**d** and **f**) structures of the peptides *rD*-HAI and (NMe)HAI, respectively. Adapted from Dr. Prades' thesis.¹⁹³

Characterization of the peptides by CD revealed a random coil conformation like that of the parent version, meaning that in solution they do not adopt a preferential conformation. Similarly, like the parent peptide, the two derived protease-resistant analogs did not show toxicity up to 50 μ M, as indicated by the MTT assay at 24 h.

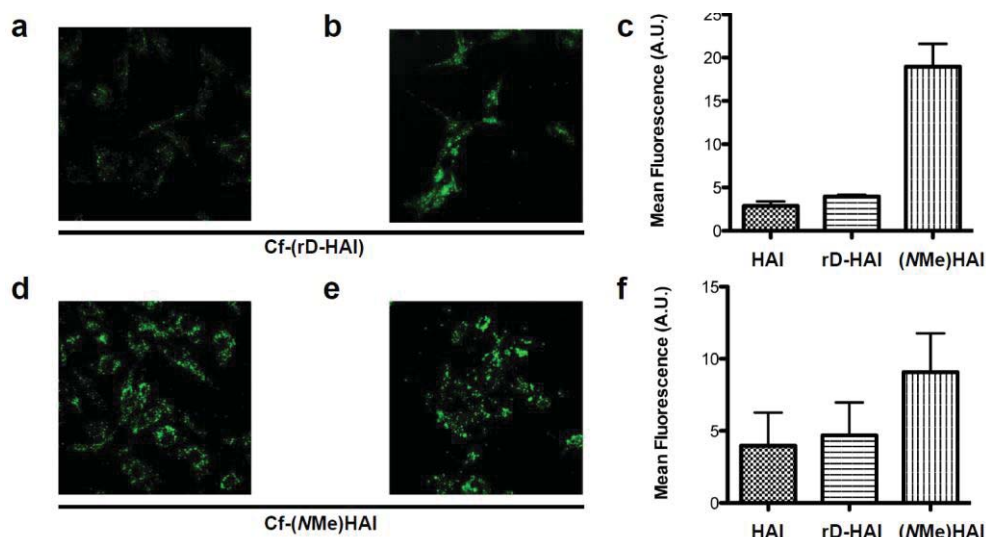


Figure 2.4. Peptide internalization by cells. Confocal laser scanning microscopy (CLSM) images of (a, d) BBECs and (b, e) rat astrocytes incubated with the candidates at a concentration of 50 μM at 37°C for 3 h. Flow cytometry results (mean \pm SD) after incubating (c) BBECs and (f) rat astrocytes with the candidates at a concentration of 50 μM (peptide 3 was incubated at 15 μM) for 3 h at 37°C. Adapted from Dr. Prades' thesis.¹⁹³

The capacity of these peptides to be internalized by and transported through the endothelium of the BBB or intestine was then studied. Thus, their transport capacity was evaluated using two *in vitro* barrier models, namely in an intestine (Caco-2 assay)²⁰¹ and in the previously used BBB model. All the peptides were detected by MALDI-TOF MS in the acceptor wells. The (NMe)HAI analog displayed a 2-fold increase in internalization with respect to the parent version (**Figure 2.4**), while rD-HAI maintained the internalization rate in BBECs and rat astrocytes. However, the *in vitro* barrier model of the BBB revealed a drastic change in transport rate (**Table 2.1**), rD-HAI showing the highest value (around 1.5 times the rate of the parent version), while (NMe)HAI recorded an intermediate value. Thus, we selected rD-HAI as the best analog derived from HAI.

Table 2.1. Caco-2 and *in vitro* bovine BBB model permeability results (mean \pm SD). Candidates were incubated for 2 h at 37°C using HBSS as buffer, and then analyzed by RP-HPLC to determine transport and P_{app} .

Peptide	Caco-2		BBB	
	$P_{app} \cdot 10^{10}$ (cm/s)	Transport (%)	$P_{app} \cdot 10^6$ (cm/s)	Transport (%)
HAI	2.0 ± 0.8	0.7 ± 0.3	9 ± 5	10 ± 3
rD-HAI	1.2 ± 1.0	0.4 ± 0.3	14 ± 2	17 ± 3
(NMe)HAI	0.60 ± 0.01	0.200 ± 0.003	11.7 ± 1.3	13.9 ± 1.6

To ensure that *rD*-HAI crosses the BBB through active transport, we proceeded to test its mechanism of transport. The peptide was assayed at increasing concentrations in an *in vitro* BBB model and saturation was reached (**Figure 2.5**); additionally, average transport increased when *rD*-HAI was assayed together with Tf (**Figure 2.5**).

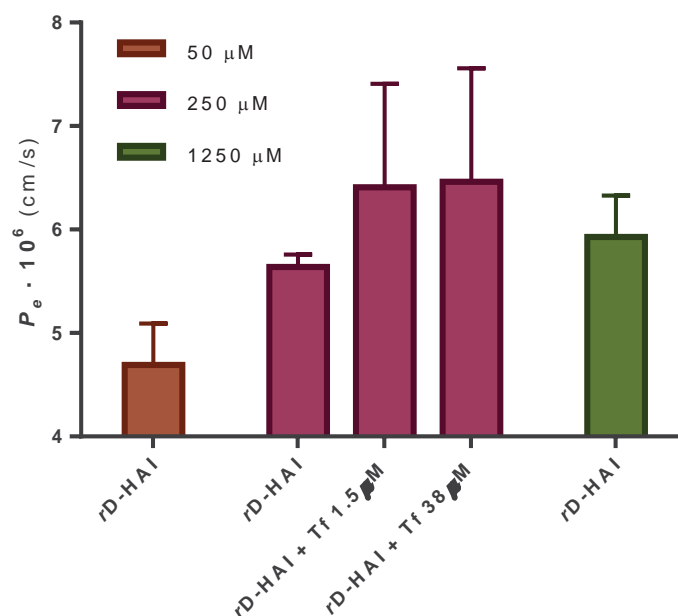


Figure 2.5. Peptide transport results (mean ± SD; n = 3) from the *in vitro* human BBB cell-based model assay. *rD*-HAI was assayed at three concentrations (50, 250 and 1250 μM) and with Tf (1.5 or 38 μM). Saturation is reached when increasing concentration and also if Tf is added. Created using GraphPad.

2.2. Amino Acid Replacement Effect on Transport Study Using a Novel Method for Transport Quantification Based on MALDI-TOF MS

2.2.1. Design of a Peptide Shuttle Library

In this thesis, we studied the effect of amino acid replacement on the capacity of HAI to cross the BBB. For this purpose, we chemically designed a library of HAI-based BBB shuttles: a set of HAI analogs containing single modifications in four of the seven available positions. Amino acid substitutions were chosen by side-chain analogy with the original residue in the parent peptide (**Figure 2.6c**).

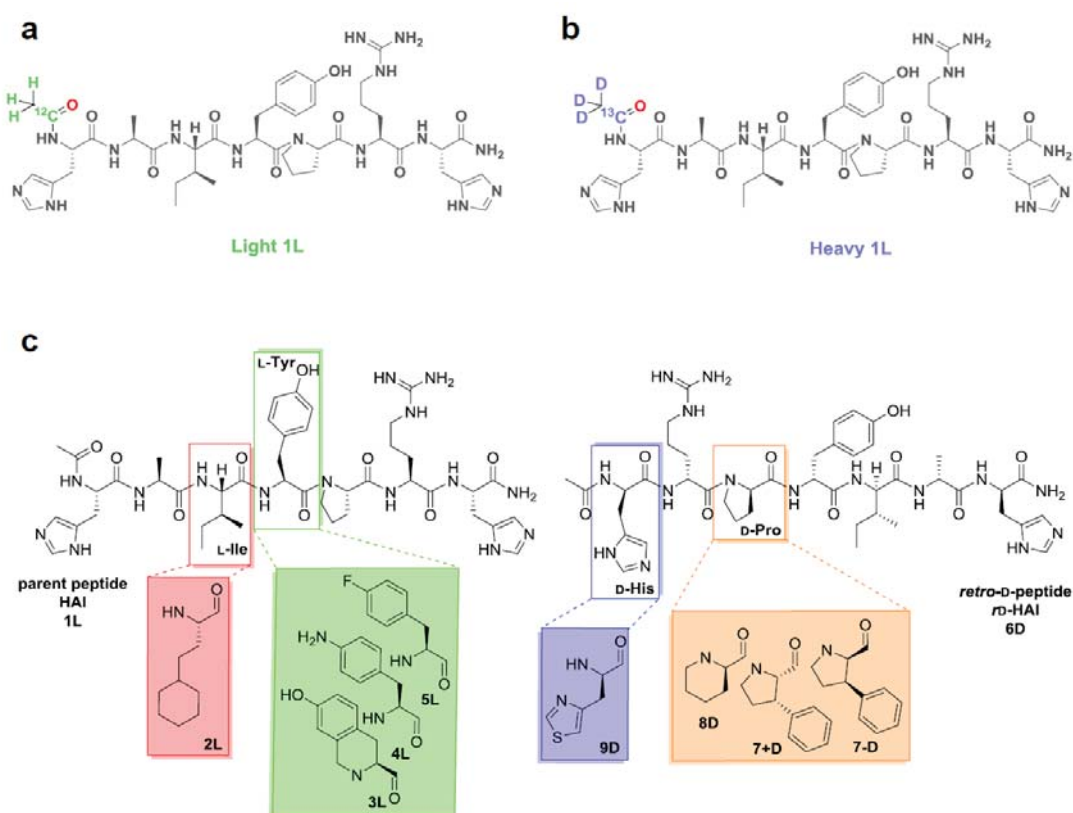


Figure 2.6. The H-HAIYPRH-NH₂ peptide BBB shuttle (1L): (a) light and (b) heavy versions containing an isotopically labeled acetyl moiety; and (c) the library of analogs of the parent (HAI or 1L) on the left, and the *retro*-D-version (*rD*-HAI or 6D) and its analogous modifications on the right. Created using ChemBioDraw and Microsoft PowerPoint.

Two analogy descriptors, bulkiness and bioisosterism,^{202,203} were used to fine-tune the shuttle-receptor interaction. Hydrocarbon side-chains were substituted by either longer chains or analogs containing rings (saturated or aromatic). Heteroatoms were replaced by bioisosteres^{202,203} (OH in tyrosine by NH₂ or F; imidazolyl in histidine by thiazolyl moiety),

chemical substitutions with similar physicochemical properties which can exert similar but modulated biological effect. In addition, half the peptides were derivatives of *rD*-HAI. Therefore, in order to identify key residues involved in the ligand-receptor (peptide shuttle-TfR) interaction,^{204,205} we studied the molecular features necessary for molecular recognition (*i.e.* the pharmacophore) of the peptide.

2.2.2. Design of a MALDI-TOF MS Method for *in vitro* Transport Quantification

In vitro transport models, either cell-based or non-cellular, are key tools for research into active and passive transport, respectively.^{195,206-208} The use of such models usually involves peptide transport quantification by RP-HPLC with photodiode array (PDA) detection and identification by MS.⁸⁴ Both cell-based and PAMPA²⁰⁹ models use a transwell system with donor (blood side) and acceptor (brain side) compartments. At the end of the assay, concentrations of the assayed compound in the acceptor well are usually very low (one or two orders of magnitude lower compared to the donor well). Thus, RP-HPLC coupled to PDA often requires large amounts of peptide (upper micromolar range) in the donor compartment, thus implying the evaluation of these compounds at high concentrations and/or over long periods. Other methods may enhance detection sensitivity but require unsuitable modifications of the structure of the peptide. Attaching a fluorophore to the peptide—usually at the *N*-terminus—can increase detection up to the nanomolar range.²¹⁰ Nevertheless, the fluorophore can enhance peptide permeation through other mechanisms, as some of these compounds have been described to be internalized by cells.²¹¹ Similar issues are encountered with a stable isotope dilution method for cell-penetrating peptide (CPP) quantification in *in vitro* assays by MS:^{212,213} the tag contains a biotin moiety that can be internalized by other mechanisms.²¹⁴ Although quantum dots (QDs) could be used as fluorescent probes, several related issues such as size, coating, and high cost make them unsuitable for this purpose.²¹⁵ The use of radiolabeled peptides/proteins has also been described²¹⁶ and although they allow an improvement in quantification, specific facilities and trained operators are required. Such a method involves a cumbersome manipulation process and often the labeling of tyrosine residues,²¹⁶ thus requiring the presence of this amino acid in the peptide sequence. Moreover, side-chain labeling of peptides may interfere with the peptide-receptor interaction. In addition, compounds must be assayed in buffer²¹⁷ (or pretreated before analyzed) when RP-HPLC-

PDA is used for quantification, since cell culture media cannot be injected into the HPLC (or HPLC-MS) system. Furthermore, the components of the media lead to peak-overlapping, and thus quantification cannot be performed accurately. Therefore, these experimental constraints impede the obtention of more reliable transport data and hinder mechanistic studies. Such studies call for peptide concentrations around the limit between the micro- and nanomolar ranges or even below, in order to ensure non-saturated or non-crowded transport in carrier-mediated or endocytic mechanisms (e.g. receptor- and adsorptive-mediated transport), respectively.^{218,219}

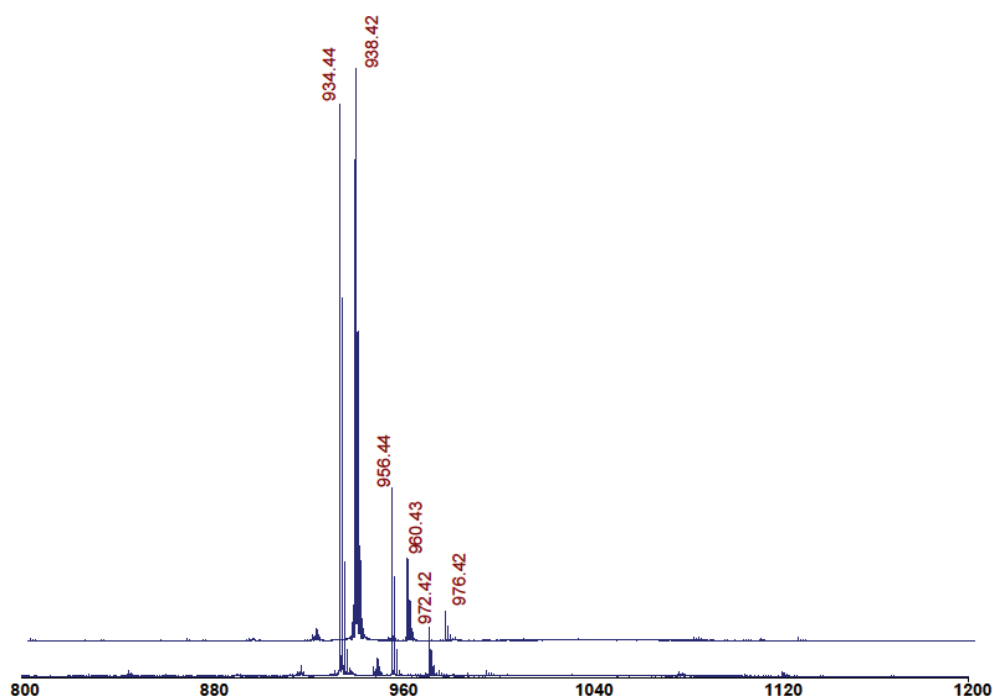


Figure 2.7. MALDI-TOF spectra of the pure HAI (1L) peptide (x axis units as $[m/z]$). Light and heavy peptides are displayed on the lower and upper the part of the spectrum, respectively. Created using Adobe Illustrator.

Thus, we envisaged a method that allowed the following: (1) evaluation of a peptide shuttle as a single molecule with minimal modification; (2) simultaneous identification (integrity assurance) and transport quantification; (3) improvement in data quality compared to that provided by RP-HPLC-PDA; (4) use of low peptide concentrations—a crucial feature for mechanistic studies; and (5) increase in the versatility of these *in vitro* models. We then designed a method based on MALDI-TOF MS, since MS is characterized by a high sensitivity, and MALDI instruments are characterized by their robustness without the need for an LC system coupled in line, as usually happens ESI MS.

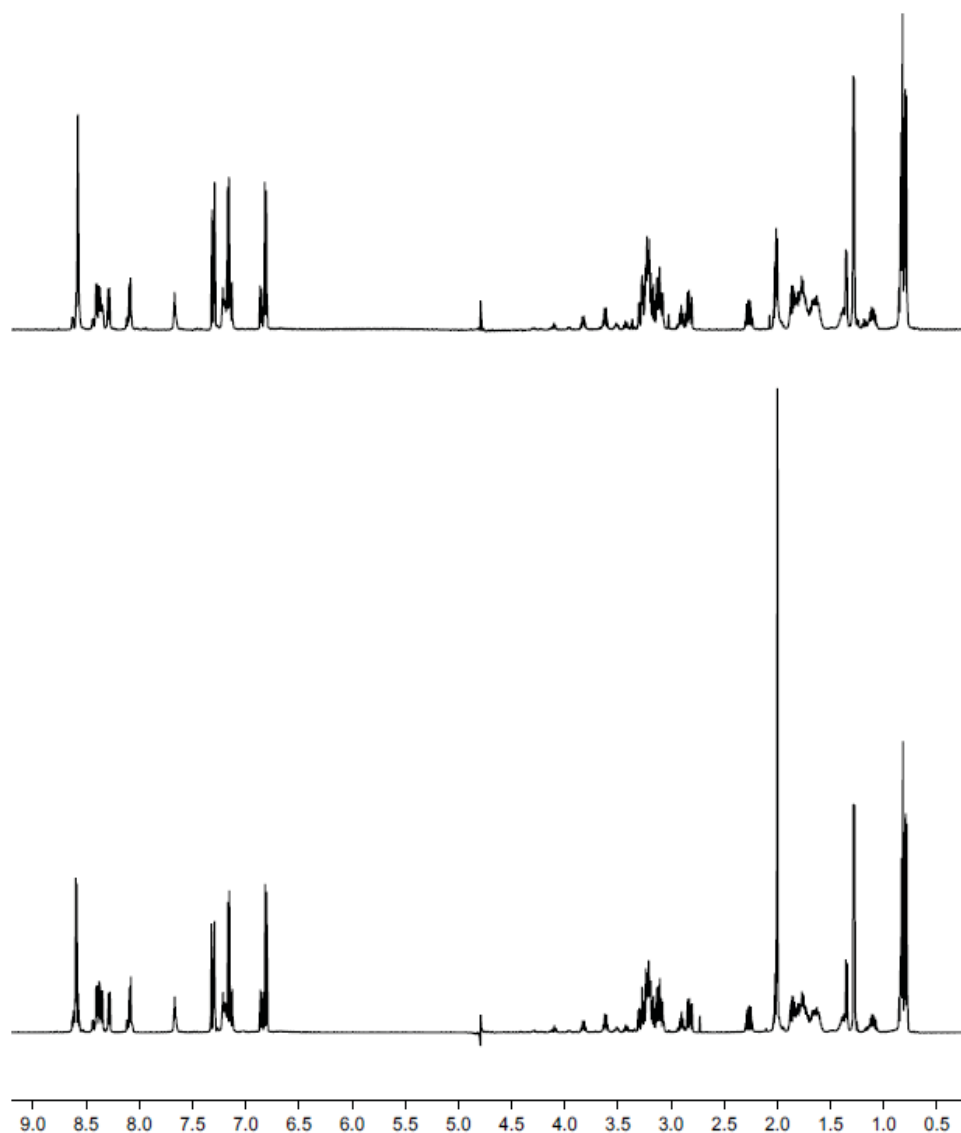


Figure 2.8. ^1H -NMR spectra of the pure HAI (1L) peptide (x axis units as ppm). Heavy and light peptides are displayed on the upper and the lower part of the spectrum, respectively. Created using Adobe Illustrator.

Precise peptide quantification by MS can be achieved only when using an internal standard with a similar mass and the same probability of desorption/ionization and detection. Thus, the ideal candidate for this purpose is the same peptide but isotopically labeled.²²⁰ Here, in order to develop a new method suited for transport quantification by MS, instead of using isotopically labeled amino acids we selected a small acetyl moiety with two isotopic versions—one light and one heavy. This molecule can be easily coupled at the *N*-terminus of peptides through a straightforward *N*-terminal acetylation. The two acetyl isotopic versions are designed to avoid peak-overlap with the relevant isotopic peaks of the peptide shuttle (the second, third and fourth isotopic peaks for low molecular weight

molecules such as peptide shuttles) arising from the relative natural abundance of each atom isotope. To fulfill these requirements, we chose a heavy isotopically labeled acetyl moiety containing three deuterium atoms and one carbon-13 (**Figure 2.6b**) and displaying +4 amu compared to the standard light version (**Figure 2.6a**). Thus, the *N*-terminus of each peptide was differentially acetylated through the reaction with the respective symmetric anhydride (characterization by MALDI-TOF MS (**Figure 2.7**) and ¹H-NMR (**Figure 2.8**) of the pure peptides showed a +4 amu increase and the disappearance of the methyl signal from the acetyl moiety in heavy peptides, respectively with each technique). The presence of this acetyl moiety, which masks the NH₂ terminus (positive) charge, resembles that of a cargo at the *N*-terminal of the shuttle.

2.2.3. Transport Analysis of the Peptide Shuttle Library

Peptides were evaluated through the *in vitro* bovine BBB cell-based model previously used with HAI and the two protease resistance versions (**Figure 2.9a**). Transport (*T*) and permeability (*P_{app}*) for all peptides were quantified by RP-HPLC-PDA and by MALDI-TOF MS (**Figure 2.9b**). The former method determined transport by applying the ratio between the peak areas integrated in the chromatograms from the acceptor and donor wells, further corrected by the volumes injected and the volumes contained in each well (see **Eq. 2.1**). The latter entails the spiking of the heavy version of the peptide as internal standard into an aliquot of the light peptide (**Figure 2.9b**). The MS intensity for light/heavy ratios for acceptor and donor wells is representative of the relative amount of peptide in each well when corrected by their volume (detailed in **Eq. 2.2**).

$$T = \frac{Q_A^I(t)}{Q_D^I(t_0)} \times \frac{V_D^I}{V_A^I} \times \frac{V_A^W}{V_D^W} \times 100 (\%) \quad (2.1)$$

where $Q_A^I(t)$ and $Q_D^I(t_0)$ account for the integrated area in the HPLC chromatograms of acceptor (at time $t = 2h$) and donor (at time $t_0 = 0$) wells, respectively; V_D^I and V_A^I are the injected volumes from donor and acceptor wells, respectively; and V_A^W and V_D^W are the volumes in each acceptor and donor well, respectively.

$$T = \frac{Q_A^{Light}(t)/Q^{Heavy}}{Q_D^{Light}(t_0)/R \times Q^{Heavy}} \times \frac{V_A^W}{V_D^W} \times 100 (\%) \quad (2.2)$$

$Q_A^{Light}(t)/Q^{Heavy}$ accounts for the relative amount of the light peptide in the acceptor well (at time t) compared with a prepared dilution of the heavy isomer (at $2\ \mu\text{M}$). $Q_D^{Light}(t_0)/R \times Q^{Heavy}$ determines the relative amount of light peptide in the donor well (at time $t = 0$) compared with a prepared dilution of the heavy isomer (at $200\ \mu\text{M}$; *i.e.* in our case $R = 100$).

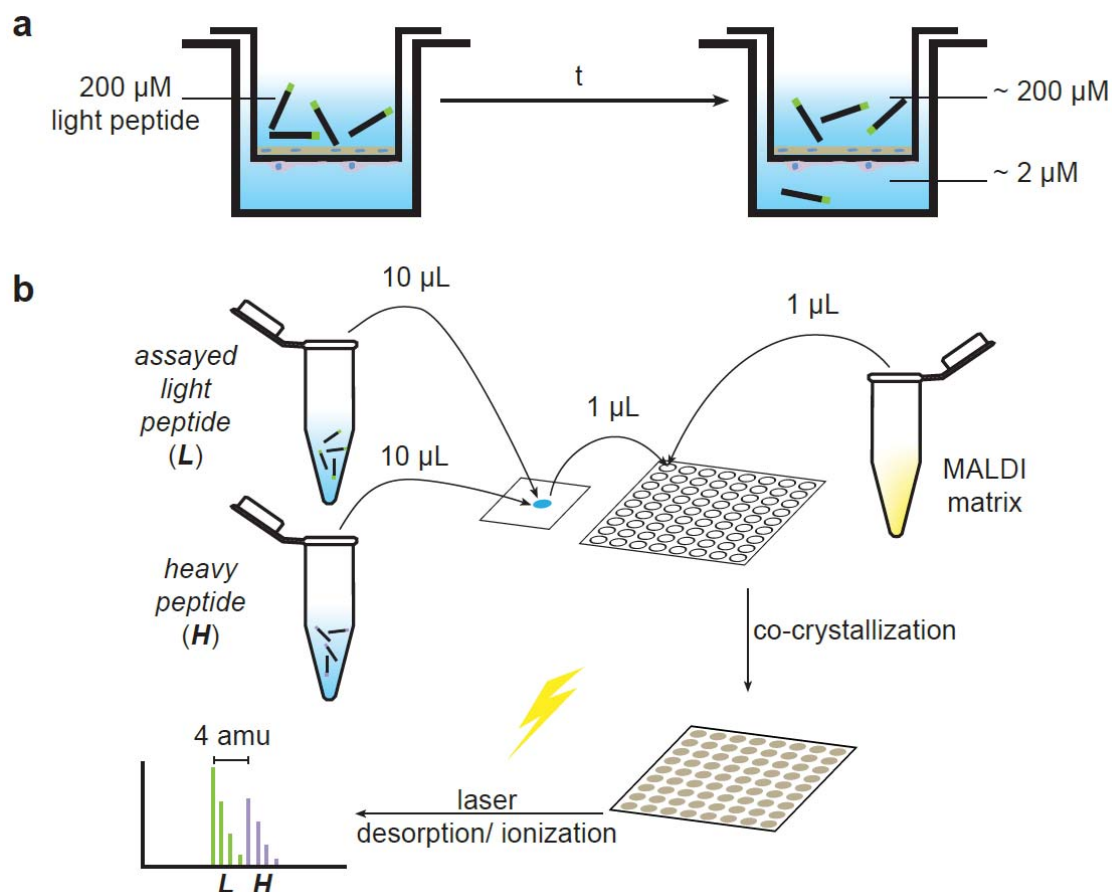


Figure 2.9. Scheme of the transport quantification method by MALDI-TOF MS. The *in vitro* BBB cell-based model (a) is performed in a transwell system where a membrane cultured with endothelial cells delimits two compartments (donor and acceptor). The donor compartment contains the light peptide before starting the experiment; at the end of the assay, a certain amount of peptide has been transported to the acceptor compartment (if $200\ \mu\text{M}$ is assayed in the donor compartment, around $2\ \mu\text{M}$ needs to be quantified in the acceptor compartment). Thus, (b) two aliquots of the heavy peptide are prepared, one at $200\ \mu\text{M}$ and another at $2\ \mu\text{M}$; $10\ \mu\text{L}$ of the assayed light peptide (from acceptor or donor compartments) and $10\ \mu\text{L}$ of the heavy version, at similar concentrations, are mixed. Subsequently, $1\ \mu\text{L}$ of this mixture and $1\ \mu\text{L}$ of an appropriate MALDI matrix (*e.g.* ACH matrix solution) are placed on a MALDI plate. Finally, the spectra are acquired. Created using Adobe InDesign.

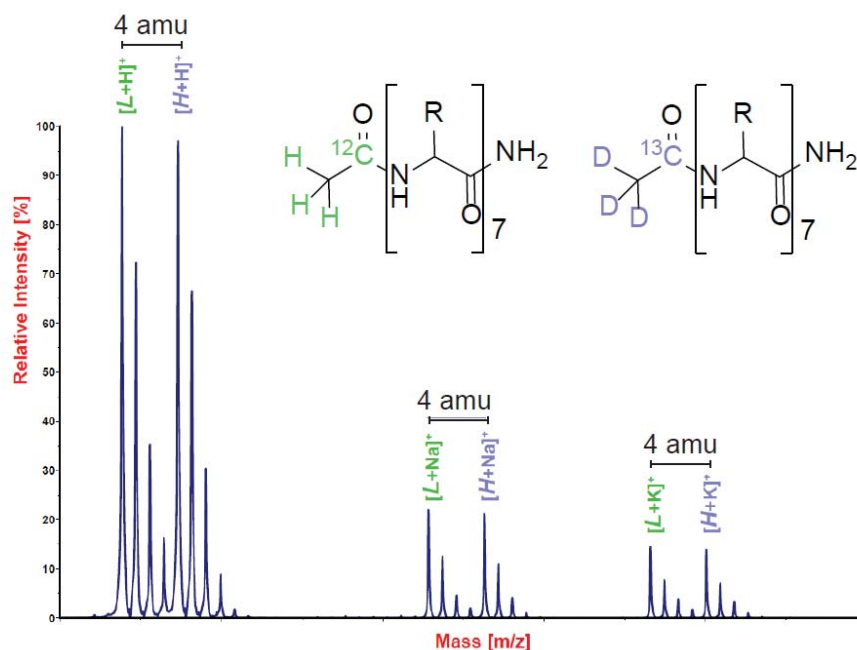


Figure 2.10. A spectrum obtained from a solution containing light and heavy versions of 9D peptide at 2 μM is shown. Light and heavy peptides are observed as the m/z of the peptides plus H^+ , Na^+ or K^+ . In all cases, isotopic homolog peaks between light and heavy peptides display a 4-amu mass difference. Created using Adobe InDesign and ChemBioDraw.

In general, transport (see **Eq. 2.3**) can be described by the total amount of peptide in the acceptor well at time t , $Q_A(t)$, divided by the initial amount in the donor well, $Q_D(t_0)$, while apparent permeability (P_{app}) is widely used in the literature and normalizes transport by the transwell area, volume in donor well and time (see **Eq. 2.4**). To simplify discussion, here results are discussed in terms of transport (as percentage in **Table 2.2**, or normalized by the parent peptide (1L) in **Figure 2.11**).

$$T = \frac{Q_A(t)}{Q_D(t_0)} \times 100 (\%) \quad (2.3)$$

$$P_{app} = \frac{dQ_A(t)}{dt} \frac{1}{A} \frac{1}{Q_D(t_0)} V_D \approx \frac{Q_A(t)}{t} \frac{1}{A} \frac{1}{Q_D(t_0)} V_D = \frac{V_D}{t} \frac{1}{A} \frac{Q_A(t)}{Q_D(t_0)} = \frac{V_D}{t} \frac{1}{A} \frac{T}{100} (\text{cm/s}) \quad (2.4)$$

All the peptides were assayed at 200 μM to ensure maintenance above the RP-HPLC-PDA limit of quantification (LOQ) (assuming a value of 2% transport, around 1 μM of peptide needs to be quantified when concentrations are corrected by donor/acceptor well ratio, *i.e.* by dividing additionally per 4). In spite of the high amount of peptide assayed, quantification by RP-HPLC-PDA was below the LOQ in some cases. In these cases, an approximate value was determined.

Initially, the data obtained by these two methods was compared by analyzing differences in transport within the same sample as mean \pm standard deviation (SD). Small discrepancies were observed but no significant differences were detected.

Nevertheless, significance within the same method differed considerably (**Figure 2.11**). RP-HPLC quantification displayed the main significant differences in transport between D-peptides (6D, 7+D, 7-D, 8D and 9D) and L-peptides (1L, 2L, 3L, 4L and 5L). On the basis of this observation, one could infer that the D-peptides showed higher transport, probably owing to the labile structure of L-peptides in a biological environment (*i.e.* in an *in vitro* BBB cell-based model—the BBB is known to also be an enzymatic barrier)^{208,221,222} and the greater stability of D-peptides conferred by the inverse configuration. Only peptide 9D showed significant differences with other D-peptides (7+D and 8D) (**Figure 2.11a**).

Table 2.2. Transport values (mean \pm SD; n = 3) from the *in vitro* bovine BBB cell-based model assay, either quantified through RP-HPLC-PDA or by MALDI-TOF MS. Results are presented as transport (%) or apparent permeability (cm/s).

Peptide	RP-HPLC-PDA		MALDI-TOF MS	
	Transport (%)	$P_{app} \cdot 10^6$ (cm/s)	Transport (%)	$P_{app} \cdot 10^6$ (cm/s)
1L (HAI)	2.9 \pm 1.4	2.5 \pm 1.1	3.8 \pm 1.4	3.2 \pm 1.2
2L	3.9 \pm 0.9	3.3 \pm 0.7	3.4 \pm 0.7	2.8 \pm 0.6
3L	2.0 \pm 0.8	1.7 \pm 0.6	2.5 \pm 1.2	2.1 \pm 1.0
4L	2.0 \pm 0.9	1.6 \pm 0.8	2.1 \pm 0.5	1.8 \pm 0.4
5L	3.4 \pm 1.6	2.9 \pm 1.3	3.1 \pm 1.6	2.6 \pm 1.3
6D (rD-HAI)	5.3 \pm 1.8	4.5 \pm 1.5	3.1 \pm 0.9	2.6 \pm 0.7
7+D	6.8 \pm 1.2	5.7 \pm 1.0	7 \pm 2	5.7 \pm 1.9
7-D	5.7 \pm 1.8	4.8 \pm 1.5	7 \pm 3	6 \pm 2
8D	7.2 \pm 0.9	6.1 \pm 0.8	7.5 \pm 1.0	6.3 \pm 0.8
9D	4.4 \pm 0.5	3.7 \pm 0.4	2.9 \pm 1.2	2.4 \pm 1.0

On the other hand, MALDI-TOF MS quantification evidenced the relevance of proline substitution by any of the three cyclic amino acid analogs (in peptides 7+D, 7-D and 8D) as transport enhancers (**Figure 2.11b**). Significant differences in transport were observed only for peptides 7+D, 7-D and 8D when compared with the rest. These peptides showed a 2-fold increase in transport compared to the parent peptide (peptide transport normalized by the parent peptide (1L) is shown in **Figure 2.11b**). Thus, the proline residue in rD-HAI

(6D) seems to be a key pharmacophoric site^{204,223} that leads to an improvement in transport when substituted by a bulkier residue.

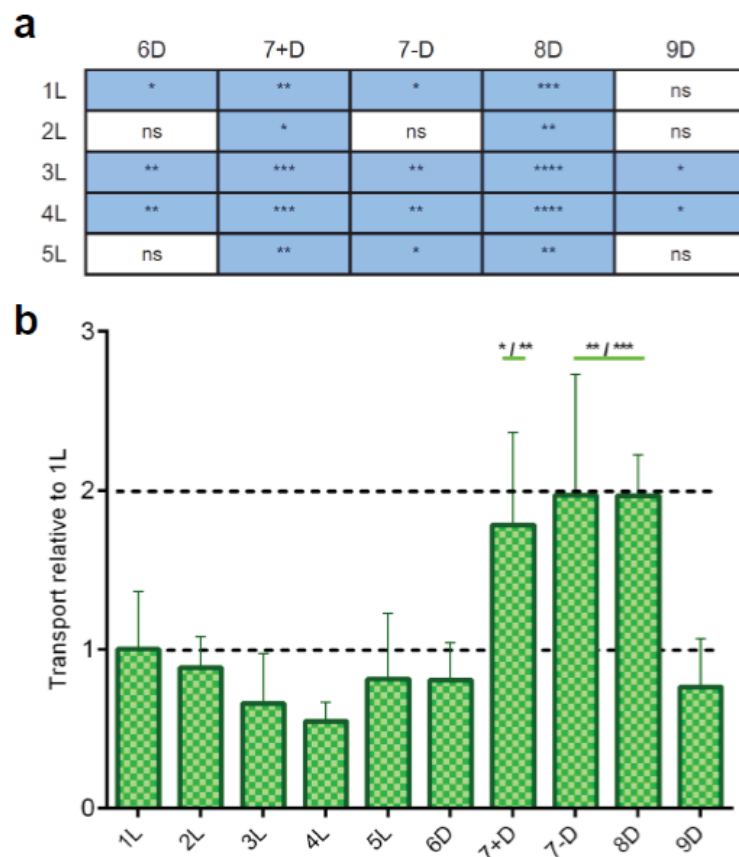


Figure 2.11. Peptide transport results from the *in vitro* bovine BBB cell-based model assay obtained through RP-HPLC-PDA (in **blue**) or MALDI-TOF MS (in **green**) quantifications; **(a)** RP-HPLC-PDA transport quantification significance between L- and D-peptides (additionally, peptide 9D showed significant differences (*) with 7+D and 8D); **(b)** MALDI-TOF MS transport quantification significance. Significance: ns \equiv not significant ($p \geq 0.05$), * \equiv significant ($0.01 \leq p < 0.05$), ** \equiv very significant ($0.001 \leq p < 0.01$), *** \equiv extremely significant ($0.0001 \leq p < 0.001$), **** \equiv extremely significant ($p < 0.0001$). Created using GraphPad and Adobe InDesign.

Finally, to further study their transport ability and test the versatility of our method for quantification, we selected the peptides that showed the greatest transport capacity, namely 7-D and 8D (7+D was discarded as it recorded the same transport as 7-D, but the residue replaced is an L- instead of D-amino acid). However, we have previously reported the use of the amino acid substitution in the non-natural residue in 7-D for passive diffusion transport purposes. In that case, the amino acid in question (PhPro, *i.e.* phenylproline) was used as a building block for the tetrapeptide PhPro₄, which showed excellent passive diffusion transport.¹²⁷ Passive diffusion was ruled out as the mechanism responsible for

transport when the peptides (1L, 6D, 7-D and 8D) were assayed by PAMPA, an *in vitro* physico-chemical model where the transport by passive diffusion of compounds is evaluated through a membrane containing the lipid composition of interest (in our case, a porcine brain polar lipid extract (BPPE) to mimic the BBB lipid barrier). The standard parameter that quantifies transport independently of time and concentrations is effective permeability (P_e), shown in the **Eq. 2.5**:

$$P_e = \frac{-218.3}{t} \text{Log} \left(1 - \frac{2C_A(t)}{C_D(t_0)} \right) \times 10^{-6} \text{cm/s} \quad (2.5)$$

where t is the running time (4 h), $C_A(t)$ is the concentration of the compound in the acceptor well at time t , and $C_D(t_0)$ is the compound concentration in the donor well before running the PAMPA assay ($t_0 = 0$ h). Transport (%) values were obtained by dividing the amount of peptide in the acceptor well at time t , $C_A(t)$, by the amount in the donor well at time zero, $C_D(t_0)$, multiplied by 100.

Table 2.3. Passive diffusion (effective permeability) of the peptides 1, 6D, 7-D and 8D studied by PAMPA (n = 3; mean \pm SD).

Peptide	$P_e \cdot 10^6$ (cm/s)
1L (HAI)	0.18 \pm 0.11
6D (rD-HAI)	0.34 \pm 0.06
7-D	0.33 \pm 0.16
8D	0.34 \pm 0.08

All of the peptides showed permeability values below 0.4×10^{-6} cm/s (**Table 2.3**). Note that when these values fall below 2.0×10^{-6} cm/s compounds are considered to be poorly transported by passive diffusion.¹⁴⁴

Table 2.4. Transport values (mean \pm SD; n = 3) from the *in vitro* human BBB cell-based model assay, quantified by MALDI-TOF MS. Peptides were assayed using Ringer-HEPES buffer or supplemented ECM medium.

Peptide	Ringer-HEPES Buffer		Supplemented ECM Medium	
	$P_{app} \cdot 10^6$ (cm/s)	Transport (%)	$P_{app} \cdot 10^6$ (cm/s)	Transport (%)
1L (HAI)	7.7 \pm 1.5	4.8 \pm 0.9	0.4 \pm 0.2	0.26 \pm 0.11
7-D	11.6 \pm 2.6	7.2 \pm 1.6	3.4 \pm 0.8	2.1 \pm 0.5
8D	10.6 \pm 0.6	6.6 \pm 0.3	1.7 \pm 0.9	1.1 \pm 0.5

Here we tested the protease resistance (in human serum) of these two *all*-D-peptides containing a non-natural moiety (7-D and 8D). Both showed high resistance to protease degradation, as previously observed for the *retro*-D-version of HAI, *r*D-HAI. With these optimal candidates, we moved on to a more sophisticated *in vitro* human model of the BBB, made using brain-like endothelial cells, generated from human cord blood-derived hematopoietic stem cells co-cultured with bovine pericytes. The aforementioned peptides were assayed as in the other BBB model in either Ringer-HEPES buffer (the one commonly used in these assays) or supplemented ECM medium. The use of medium in this assay allows (1) extension of the incubation time and (2) use of more reliable conditions to those found physiologically. In this assay, the transport of the analogs 7-D and 8D was around 1.5 times higher than that observed for the parent peptide 1L (HAI). However, when 7-D and 8D were assayed in medium, they showed 8- and 4-fold the transport values of the parent peptide (**Figure 2.12**). Thus, although 7-D and 8D appeared to show similar transport performance, a more realistic analysis of their shuttle capacity revealed that 7-D was twice as good as 8D, in spite of the latter exceeding the transport capacity of the parent peptide (**Figure 2.12**).

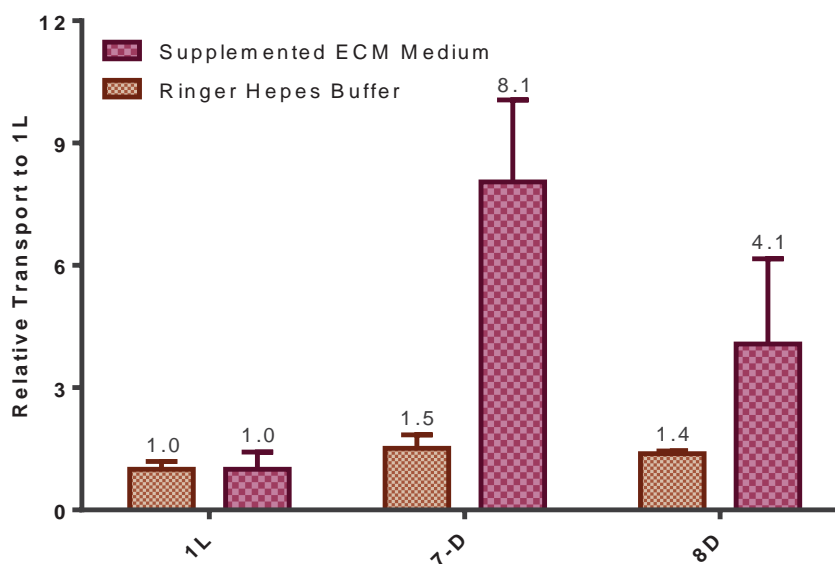


Figure 2.12. Peptide transport results from the *in vitro* human BBB cell-based model assay: relative transport of 1L, 7-D and 8D peptides with respect to 1L when assayed with Ringer-HEPES buffer or supplemented ECM medium. Created using GraphPad.

2.2.4. Performance and Broader Applicability of the MALDI-TOF MS Method for Transport Quantification

To further analyze the results and compare the two methods (MALDI-TOF MS and RP-HPLC-PDA), the transport of each replica was compared individually (**Figure 2.13**). Consistent with the previous results, although small differences were revealed, the relative discrepancy between the two methods (RP-HPLC-PDA and MALDI-TOF MS) remained around 20%.

These discrepancies are most likely due to RP-HPLC-PDA quantification errors since some of the acceptor wells were below the LOQ of this technique. Indeed, these data suggest that MALDI-TOF MS is a more suitable tool for transport quantification than RP-HPLC-PDA, since we were evaluating an already described hit (HAI) and its analogs at relatively high concentration (200 μ M), all of them containing 3 aromatic rings (two histidine and one tyrosine residues, or analogs) and thus displaying a relatively high UV absorption.

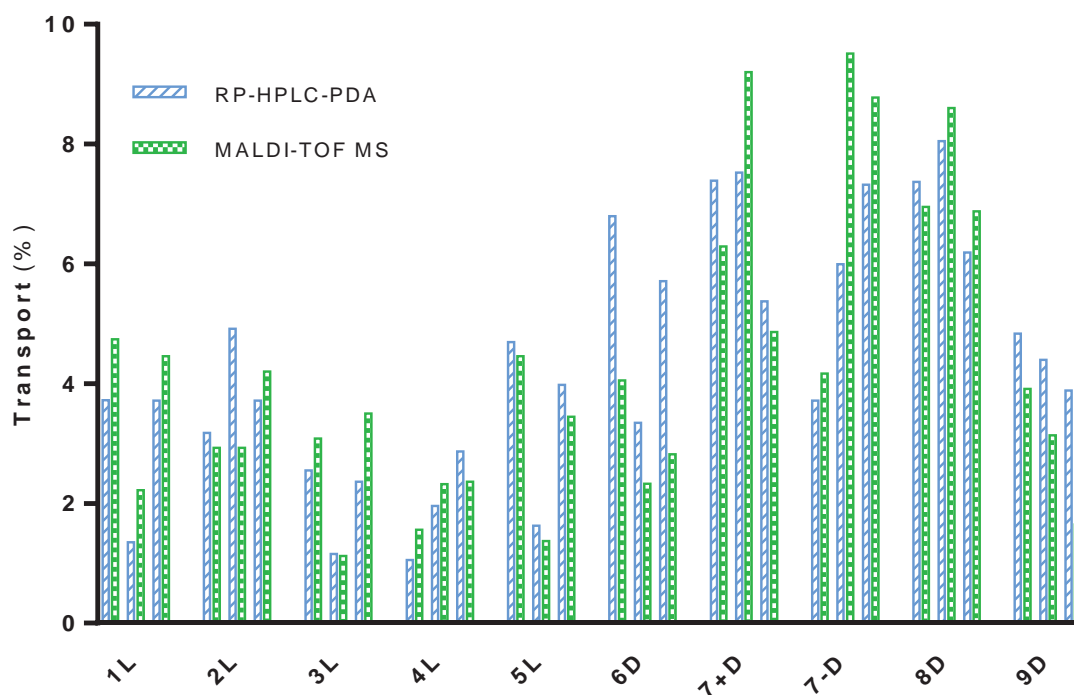


Figure 2.13. Transport (replicates) from the *in vitro* bovine BBB cell-based model assay, either quantified through RP-HPLC-PDA or by MALDI-TOF MS. Results are presented as transport (%). Created using GraphPad.

2.2.4.1. MALDI-TOF MS Limit of Quantification

Dilution series for three peptides 1L (HAI), 6D (*retro*-D-HAI) and 9D, ranging from 200 μM to 1.1 nM, were analyzed by MALDI-TOF MS (on an Applied Biosystems 4800 Plus MALDI-TOF spectrometer, using an ACH-based matrix). The initial dilution was prepared by mixing 20 μL of two solutions containing 400 or 800 μM of the light or heavy versions of the peptide, respectively. Consecutive dilutions 1/3 were then prepared by mixing 10 μL in 20 μL of H_2O . Finally, 1 μL of the sample and 1 μL of the ACH matrix were placed in a MALDI plate. The spectra were acquired and further analyzed to determine the limit of quantification. First, the experimental light/heavy ratio was determined for all the dilutions. The R_{LOQ} was then determined for all of them:

$$R_{\text{LOQ}} = \frac{R_i - \bar{R}}{\bar{R}} = \frac{R_i}{\bar{R}} - 1 \quad (2.6)$$

where, R_i and \bar{R} are the light/heavy ratio of each sample and the mean (*i.e.* $\bar{R} \equiv \sum_i^n \frac{R_i}{n}$, discarding the last dilution value), respectively. The deviation (%) is calculated as $R_{\text{LOQ}} \times 100$.

2.2.4.2. RP-HPLC-PDA Limit of Quantification

Dilution series for three peptides 1L (HAI), 6D (*retro*-D-HAI) and 9D, ranging from 200 μM to 1.1 nM, were analyzed by RP-HPLC-PDA. An initial solution at 200 μM was consecutively diluted 1/3 by mixing 100 μL in 200 μL of H_2O , up to a total of eleven dilutions. Finally, a specific volume of the sample, ranging from 5 to 100 μL , was injected to the HPLC system and then further analyzed (at 220 nm, the selected wavelength with the highest signal-to-noise; see **Table 2.5**) to determine the limit of quantification.

Table 2.5. Signal-to-noise ratio determined for the peptide HAI (not acetylated 1L) at diverse wavelengths: 200, 210 and 220 nm. The signal-to-noise ratio is higher at 220 nm than at the other two wavelengths.

Wavelength (nm)	Signal-to-Noise Ratio (normalized by the lowest value)
200	1.00
210	1.18
220	1.26

First, the total absorption corrected by the injected volume and dilution (R_i) was determined as:

$$R_i = \frac{A \times d}{V} \quad (2.7)$$

where, A , V and d are the total absorption area, the absorption area, the injected volume and the fold-dilution, respectively. Then, the R_{LOQ} was determined for all of them using **Eq. 2.6**.

In our MALDI-TOF MS method, we propose that two procedures can be followed in order to ensure that the concentration of the assayed peptide is above the LOQ. The most stringent one requires the determination of the LOQ for each peptide. The second one considers that similar molecules (our library of peptide analogs) have similar ionization properties. In our case, we first determined the LOQ for peptide 1L (HAI) and afterwards for 6D (*r*D-HAI) and 9D. Comparable results were obtained. We then assumed that all the peptide analogs had a similar LOQ since they all differed from the parent peptide in only one amino acid substitution and/or had a reversed sequence accompanied by an inverse configuration (**Figure 2.6c**).

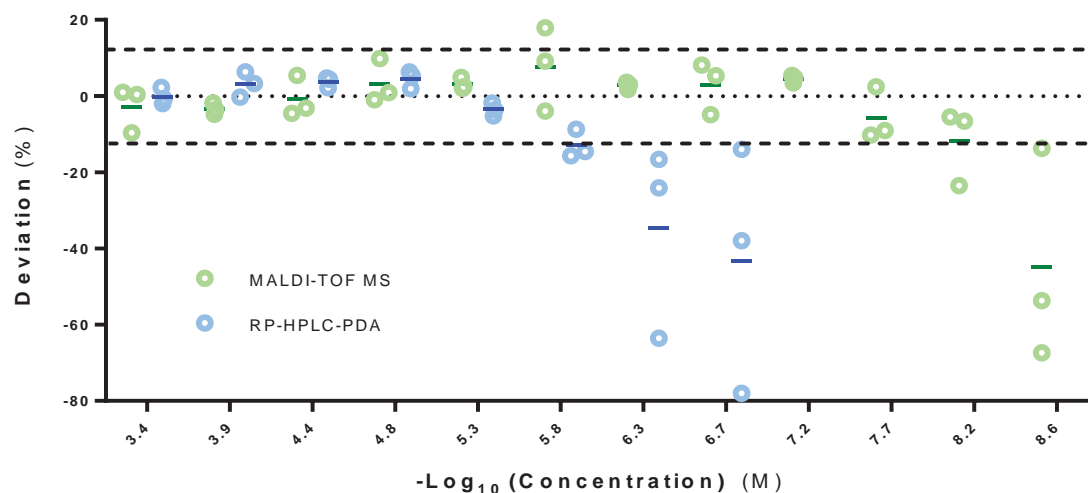


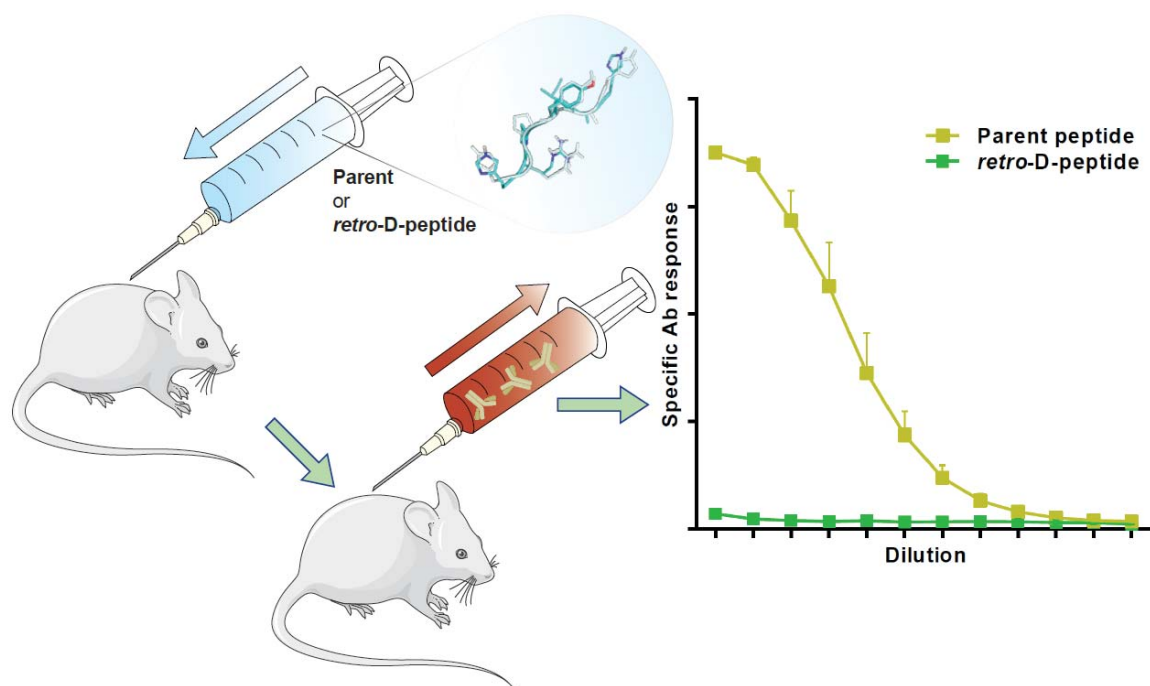
Figure 2.15. Determination of the limit of quantification of MALDI-TOF MS and RP-HPLC-PDA using the peptides 1L, 6D and 9D. Created using GraphPad.

To determine the LOQ of our MALDI-TOF MS approach, we analyzed consecutive dilutions (from 200 μ M to 1 nM) of samples of 1L (HAI), 6D (*r*D-HAI) and 9D, which contained light and heavy versions in similar concentrations (the latter double the

concentration of the former). Each dilution was analyzed by comparing the light/heavy ratio with the initial quantification before dilution. The LOQ remained around 3.4 nM in both cases when an average error of 8% was assumed (**Figure 2.15**). This value is much lower than the discrepancy between replicates in this type of assay (*e.g.* see **Figure 2.13**). Thus, MALDI-TOF MS allowed an increase in sensitivity of more than 3 orders of magnitude compared to RP-HPLC-PDA. Accordingly, all transport quantifications by MALDI-TOF MS fell within the LOQ.

Chapter 3

Study of Immunogenic Responses to BBB Shuttle Peptides



This chapter will give rise to the following article:

Arranz-Gibert, P.; Ciudad, S.; Seco, J.; García, J.; Giralt, E.; Teixidó, M. *Retro-D-peptides: The Phantom Therapeutics. Manuscript in preparation.*

During the last three decades, peptides have become privileged therapeutics²²⁴ and are now used in a broad range of applications. The relevant presence of these molecules in nature and accessible synthesis through well-established solid-phase peptide synthesis (SPPS)⁸² has facilitated their study and applicability in the pharma industry.^{225,226} Compared to therapeutics developed by classical medicinal chemistry (low molecular weight organic molecules), peptides display a better solubility profile, although this profile depends on the sequence.²²⁷ While the abundance of peptides in nature is advantageous from the perspective of toxicity, two principal drawbacks are intrinsic to their structure, namely protease degradation driven by proteolytic enzymes and eventual risk of immunogenicity.²²⁴ In addition, this class of therapeutics displays a short plasma half-life as a result of kidney clearance. Nevertheless, several approaches have partially resolved these issues. Recognition by proteases, and thus peptide degradation, can be avoided by using peptide derivatives like D-, β -²²⁸ or non-natural amino acid peptides, as well as other classes of peptidomimetics.²²⁹ Furthermore, PEGylation²³⁰ and other methodologies²³¹ can extend the plasma half-life of peptides by increasing their molecular weight (more precisely, their hydrodynamic radius).

The immunogenicity of peptides (as the native ligands of MHC class I/II) have been studied extensively.²³² While vaccine development requires activation of the immune response,²³³ other therapeutic treatments require not to elicit such type of response. Few approaches have reported effective reduction of immune system recognition/response. PEGylation²³⁰ is probably the most widely used method of choice to reduce immunogenicity, although adverse immunological effects, *i.e.* humoral responses, have been reported.²³⁴

Retro-D-peptides (containing *retro*-inverso- and *retro*-enantio-isomers of a parent peptide) are peptides derived from a parent peptide, made by L-amino acids, which sequence is inversed and made by D-amino acids. This rearrangement combines the properties of D-peptides, namely protease-resistance, and with the reversed amino acid sequence leads to an imperfect topology overlapping with that of the parent peptide but achieve good mimicry for short sequences.¹⁹⁸

We have applied the previously described strategy to a family of peptide BBB shuttles (H-HAIYPRH-NH₂ and H-THRPPMWSPVWP-NH₂,¹⁸⁸ namely HAI and THR peptides, respectively). BBB shuttles are molecular entities of diverse origin, *e.g.* synthetic or natural peptides, which have the capacity to cross the blood-brain barrier (BBB) and, when covalently conjugated to drugs unable to cross the BBB unaided, can deliver them into the central nervous system (CNS).²³⁵ Those that cross through receptor-mediated transcytosis are also included in the term ‘molecular Trojan horses’.^{119,236} Although only a few clinical trials on BBB shuttles have been reported,^{237,238} a huge number of these molecules effectively achieve their aim.^{84,239} While parent versions of both HAI and THR displayed efficient BBB permeability in several studies, our laboratory demonstrated the BBB shuttle capability and protease-resistance of *retro-D*-THR⁸⁴ and *retro-D*-HAI (BBB shuttle capacity studied previously, and protease-resistance tested in human serum shown in **Figure 3.1b**).

Here we conducted immunogenicity studies for several peptide BBB shuttles—two versions of HAI and THR peptides (**Fig 3.1a**), namely the parent and the respective *retro-D*-peptide. All peptides were obtained by manual SPPS using the Fmoc/*t*Bu strategy.

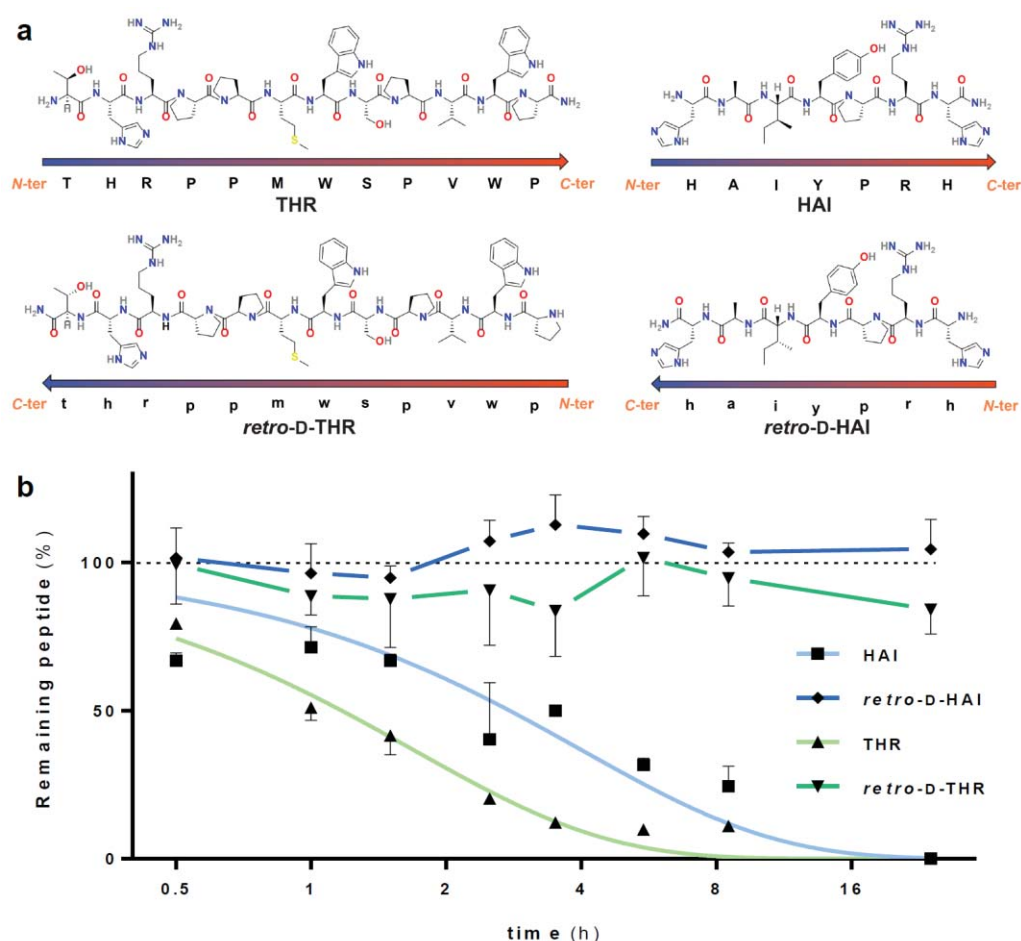


Figure 3.1. HAI, THR and the respective *retro*-D-versions; (a) peptide sequences and (b) stability assay in human serum. *Retro*-D-versions display a stable structural integrity over time while parent peptides display exponential degradation ($R^2 = 0.812$ and 0.970 , $t_{1/2} = 3.3$ and 1.0 h, HAI and THR, respectively). Data on THR and *retro*-D-THR extracted from Prades *et al.*⁸⁴ During the experiment (24 h) no significant differences were observed when *retro*-D-peptides were compared with the starting amount of peptide. Created using GraphPad, ChemBioDraw and Adobe InDesign.

The structural conformational arrangements of parent peptides and their respective *retro*-D-versions were initially studied by circular dichroism (CD) (**Figure 3.2b**), and later by nuclear magnetic resonance (NMR) spectroscopy (**Figure 3.2a**); NMR experiments conducted by Sonia Ciudad and Dr. Jesús García. While the coarse grain analysis by CD is consistent with similar conformational arrangements but not topologically exact, NMR adds further precision and shows how these peptides (both for HAI/ *retro*-D-HAI and THR/ *retro*-D-THR pairs) comprise several sets of thermodynamically stable conformational arrangements (analysis of NMR conformationally sensitive parameters such as chemical shifts, coupling constants, NH temperature coefficients and NOE pattern revealed

analogous results for the L-peptides and their *retro*-D-versions, thereby suggesting that they have similar conformational preferences).

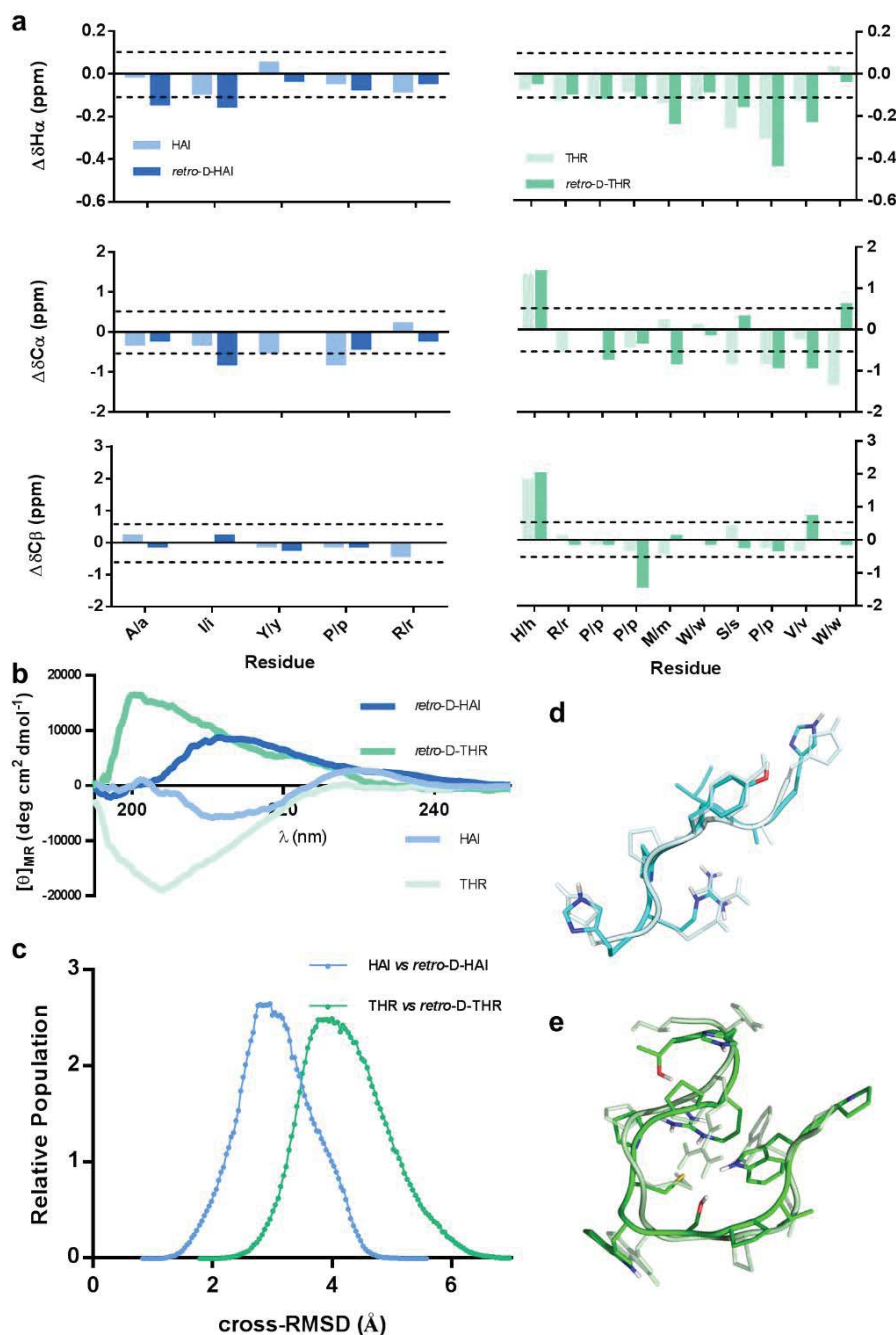


Figure 3.2. Structural analysis of the four peptides: (a) histograms showing the $^1H_\alpha$, $^{13}C_\alpha$ and $^{13}C_\beta$ chemical shift deviations (CSD) from random coil (RC)²⁴⁰ of the major species (of HAI (left) and THR (right), and their respective *retro*-D-versions, aligned by amino acid type), (b) the circular dichroism (CD) spectra, (c) the cross-RMSD derived from the comparison of the whole REMD structure sets of parent and *retro*-D-version peptides, and the three-dimensional superposition of one pairing obtained from the cross-RMSD matrix of (d) HAI and *retro*-D-HAI, and of (e) THR and *retro*-D-THR. Created using GraphPad, Microsoft PowerPoint and PyMOL.

Dr. Jesús Seco performed replica exchange molecular dynamics (REMD; **Figure 3.2c**) experiments. The overlapping of the two configurational isomers was analyzed. REMD allowed to determine how these peptides are topologically disposed. These results show that the two versions of the same peptide can adopt a similar three-dimensional arrangement (**Figure 2c-e**), in agreement with CD and NMR data.

To date, several studies have used D-peptides as tools for vaccine development. In these cases the peptides have been conjugated to large supramolecular entities, *e.g.* KLH and small unilamellar liposomes containing monophosphoryl lipid A.^{241,242} Nevertheless, the use of *retro*-D-peptides as therapeutics was controversial twenty years ago.^{243,244} Thus, to shed light on the immunogenicity of D-peptides and add further value to these compounds, we evaluated the immunological responses activated by *retro*-D-THR and *retro*-D-HAI peptides and compared them to that of their parent peptides. For this purpose, peptides (not conjugated) were *i.p.* administered to mice, and antibody titration was used as parameter to evaluate immunological (humoral) response by ELISA.

Unconjugated L-versions of both peptides displayed a moderate immunogenicity response (**Figure 3.4a**). Antibody titration of the first bleed showed a slightly higher signal for both peptides compared to the last bleeding. This signal was probably induced by the transition from IgM to IgG production in B cells. Thus, antibody titration decay is caused by a decrease in number, which is compensated by an increase in affinity and selectivity. In contrast, in the case of *retro*-D-peptides almost no signal was detected for specific antibodies (**Figure 3.4b**). Thus, *retro*-D-versions appear to be much less immunogenic than their corresponding parent peptides.

Nevertheless, in order to discard the possibility that antibody recognition was dependent on the terminus exposed in these cases (since *retro*-D-versions have them reversed—see **Figure 3.1a**), we tested the serum of mice immunized against *retro*-D-peptides by attaching these peptides to the other terminus on the ELISA plate (**Figure 3.3** and **3.4c**). In this regard, we evaluated the response of antibodies to the same peptide sequence but exposing the other terminus: the inversed order in *retro*-D-peptides (comparing with parent peptides) was corrected by displaying the opposite terminus. As an example, the HAI peptide attached to BSA (and subsequently to the plate) by the *N*-terminus displayed the sequence H₂NOC-H←R←P←Y←[...]-BSA-plate, and the peptide *retro*-D-HAI exposing the *N*-terminus showed H₂N-h→r→p→y→[...]-BSA-plate (see

header of Figure 3.4); compare Figure 3.4a,c, and see Figure 3.1a. Similar results were obtained as when *retro*-D-peptides exposed the C-terminus (Figure 3.4c), thereby confirming our hypothesis (antibody reactivity does not depend on the termini exposed).

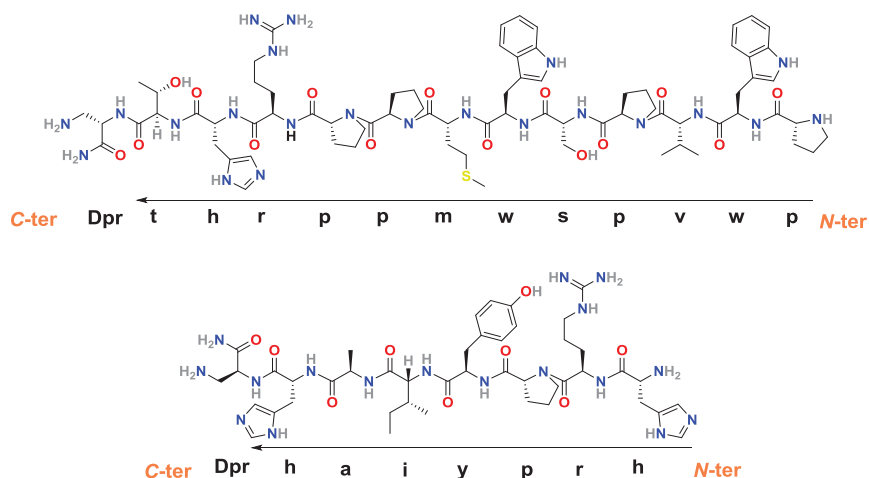


Figure 3.3. Peptide sequences of *retro*-D-versions containing the diaminopropionic acid (Dpr) residue at the C-terminus. Created using ChemBioDraw.

To the best of our knowledge, in all those immunological responses reported in the literature for either a *retro*-D-peptide or D-peptide (especially concerning vaccines), the parent one was derived from an existing sequence or even an immunodominant region of a viral protein.^{241,242} Thus, these D- or *retro*-D-versions could have generated a rapid and huge immune response when administered to animals (*e.g.* serum IgG and other neutralizing factors against adeno-associated virus are highly prevalent in the healthy population).²⁴⁵ In addition, a report describing D-proteins as entities exerting low immunogenicity was published 20 years ago.²⁴⁶ We therefore hypothesized that *retro*-D-peptides with a parent sequence not related to any existing protein would not be immunogenic *per se*. To exclude this possibility, we used a sequence similarity search tool (NCBI BLAST) to identify analogies between the parent peptides used and the whole data set of known peptide and protein sequences. No positive result was obtained, as previously described.¹²

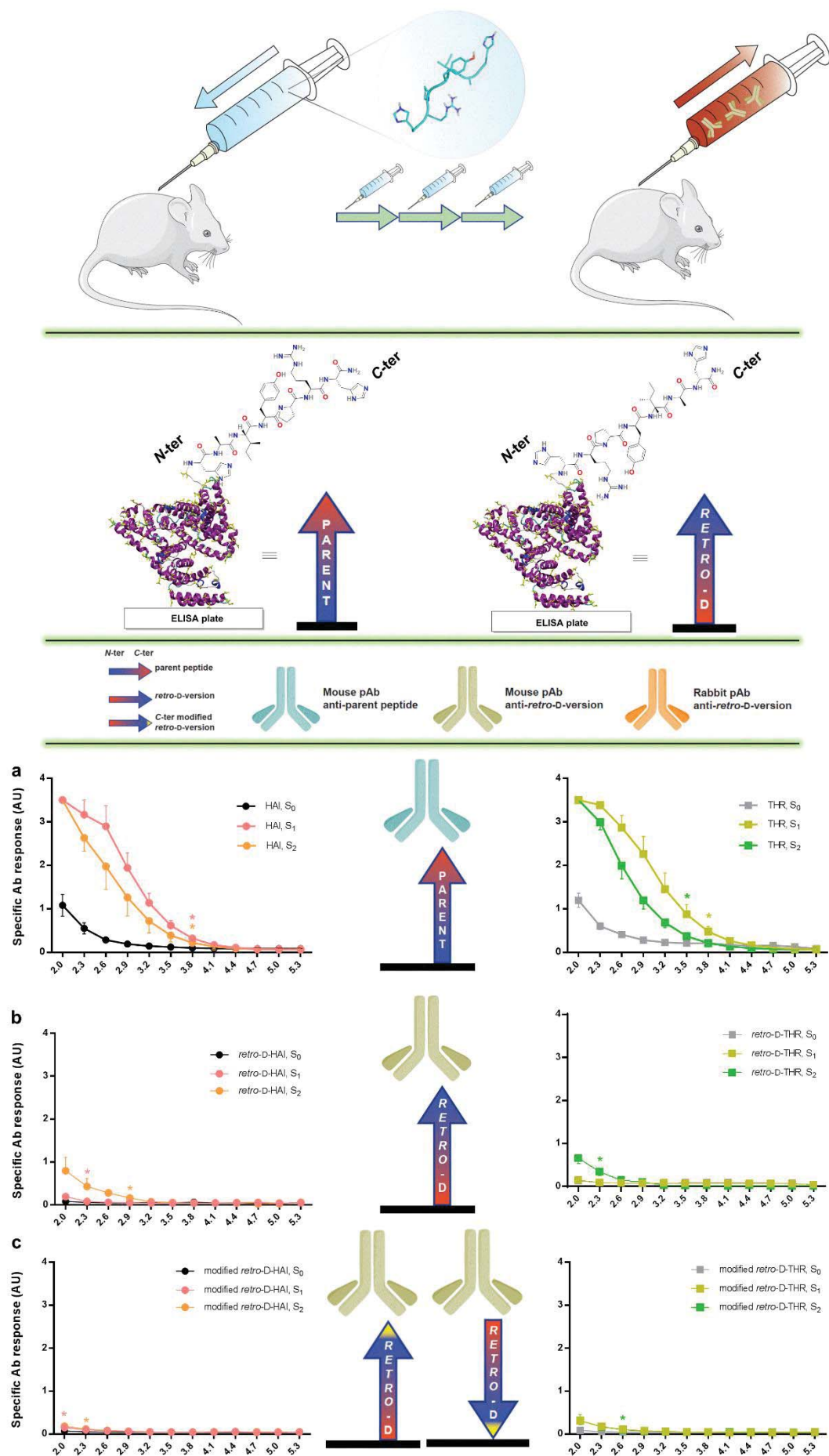


Figure 3.4. Titration of humoral response in mice by ELISA: (**header**) scheme of mice immunizations (shown with *retro*-D-HAI), ELISA evaluation of humoral response with peptide-BSA conjugates (HAI and *retro*-D-HAI shown), and the legend; (**a**) serum anti-parent peptides (HAI, THR), serum anti-*retro*-D-versions evaluated either with (**b**) C- or (**c**) N-terminus-exposed peptides. Initial consecutive significant differences between S_0 with S_1 or S_2 are labeled by asterisk/s (no asterisk, no significant differences in the whole dilution interval). Created using GraphPad, Adobe InDesign, ChemBioDraw, Microsoft PowerPoint and Servier Medical Art.

Although, as shown above, *retro*-D-HAI and *retro*-D-THR are not immunogenic *per se*, they could elicit an immunological response when conjugated to an immunogenic molecule. Thus, we conjugated these peptides to KLH and *s.c.* injected into rabbits. After the immunization, sera were tested by ELISA to identify antibodies displaying specific-peptide response. A strong increase in humoral response to these peptides (see **Figure 3.5**) was observed when compared to when they were used as unconjugated immunogens (**Figure 3.4b**). The peptide-specific antibodies generated for both *retro*-D-peptides seems to be an immunoresponse facilitated by the anchoring molecule (KHL in this case). Hence, in order to be able to use this class of peptide (*retro*-D) for vaccine development, they should be coupled to other immunogenic structures to facilitate recognition by the immune system. However, if these peptides are to have applications as other types of therapeutic agent (and an eventual immune response is undesirable), they must be used (1) as a single therapeutic, (2) attached directly (2a) to the therapeutic agent or (2b) to other non-immunogenic structures.

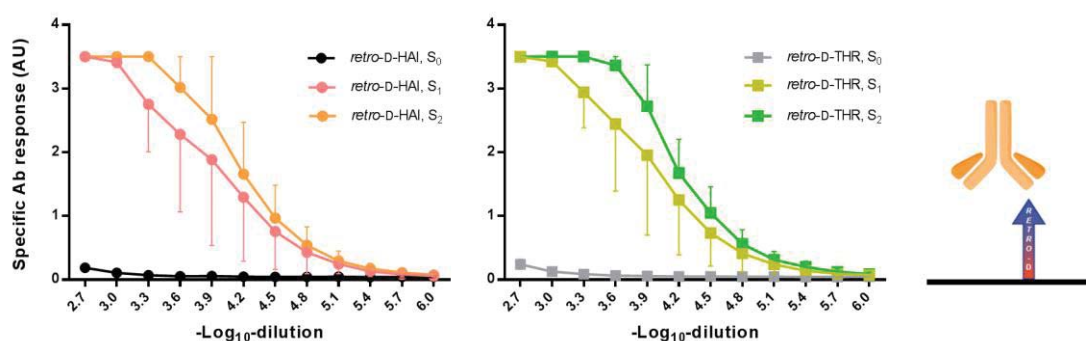


Figure 3.5. Titration of humoral response by ELISA in rabbit: serum anti-*retro*-D-peptides conjugated to KLH. Created using GraphPad, Adobe InDesign and Microsoft PowerPoint.

We have shown that *retro*-D-peptides, in addition to overcoming protease-sensitivity, can be a valuable tool to create therapeutics that do not sensitize the immune system, thus circumventing the intrinsic problems of L-peptides, derived from their backbone configuration, and leading to a new class of therapeutics that are not recognizable by the immune system—phantom therapeutics.

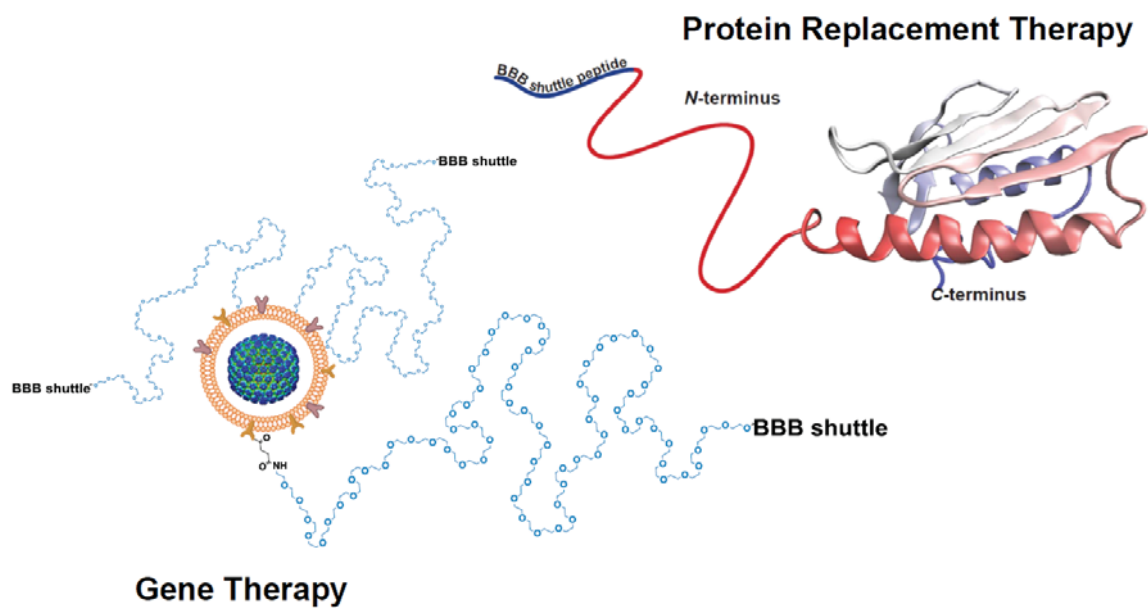
The B cell response (antibody production) in mice immunized with D- (precisely, *retro*-D) peptides that were not coupled to any molecule was markedly lower compared to those immunized with the L-versions. We postulate that both versions of the peptide may eventually be recognized by a B Cell Receptor (BCR/ membrane antibody); nevertheless, the D-version cannot be processed by peptidases and much less efficiently presented by the MCH-II to CD4⁺ T cells (T_H)—the left-handed polyproline II extended conformation adopted by peptides when loaded in the antigen-binding groove of MCH-II is not accessible for D-peptides (thus hydrogen bonding between the amide bond of the peptide and the MHC-II is hindered, although binding pockets for the side chains are preserved). Therefore, the survival and proliferative signals to the B cells recognizing D-peptides are much lower compared to those that recognize L-peptides. Thus, we propose that D-peptides have two mechanisms by which to silence the immune system, namely protease-resistance and the conformational arrangement of the backbone, both of which are consequences of the inversed α -carbon stereochemistry.

Since *retro*-D-peptides present good topological mimicry with their parent peptides, they are a simple solution for newly designed therapeutic peptides derived from diverse source of therapeutics with L-configuration, *e.g.* natural sources, phage display or computational design. Nevertheless, given the prior observations related to peptides composed by D-amino acids, we recommend a preliminary screening of the sequences of interest to test their prevalence and type of sources in nature in order to avoid eventual immune responses in advanced trials. In addition, we envisage the use of *retro*-D-peptides as protease-resistant variants to overcome immunological problems derived the intrinsic structure of drugs or vectors. As an example, viral vectors applied to gene therapy could be decorated with these peptides in order to allow them to escape from the immune system, either attached through a non-immunogenic linker or stand-alone, thereby avoiding systemic adverse reactions and neutralization by preexisting immunity.²⁴⁷ Furthermore, their cell-tropism could be modulated (*e.g.* by using *retro*-D-versions of cell-penetrating peptides (CPP), blood-brain barrier shuttles (BBB shuttles), homing peptides (HP)), in

order to target more effectively the diseased area and thus allowing the use of lower viral loads (*i.e.* reducing side effects and production costs).

Chapter 4

Attempts to Develop a Therapy for Friedreich's Ataxia at the CNS



Diseases with known simple genetic and metabolic causes are perfect targets for treatments involving the use of delivery tools to supply a therapeutic agent. In this regard, we considered Friedreich's Ataxia (FRDA), a neurodegenerative movement disorder, as a therapeutic condition in which to test our BBB shuttles, namely *retro-D-THR* (*rD-THR*) and *retro-D-HAI* (*rD-HAI*).

FRDA was first described by Nicholaus Friedreich in 1863,²⁴⁸ and it is currently the commonest inherited ataxia, with a prevalence of 1 case per 30,000 individuals (1:30,000) in Western Europe—²⁴⁹ the highest value is observed in the north of Spain (1:21,000) and a prevalence gradient is distributed from south-west to north-east in Europe.^{249,250} The annual cost of this disease per person in the United Kingdom is between £11,818 and £18,774, depending on whether the cost of long-term unemployment is included.²⁵¹ The onset of symptoms has been established to occur at 15.5 ± 8 years, and the mean time until the patient becomes confined to a wheelchair is 10.8 ± 6 years. The main signs and symptoms of this disease are gait and limb ataxia, dysarthria, lower-limb areflexia and axonal neuropathy, with a prevalence of more than 85%. In addition, cardiomyopathies, abnormal brainstem and visual evoked potentials, and impaired glucose tolerance (*e.g.* diabetes) show a prevalence ranging from 32–63%.²⁵²

FRDA is an autosomal recessive disease caused by a GAA trinucleotide (triplet) repeat (TNR) expansion located in an intronic region of chromosome 9q13—intron 1 of the frataxin (*FXN*) or *X25* gene.²⁵³ Repetitive sequences comprise 30% of the human genome.²⁵⁴ TNRs expand during progeny transmission, development and/or in somatic non-dividing cells when longer than a crucial threshold—*i.e.* pre-mutation length. In non-coding regions, like in FRDA, unstable parent-child transmissions initiate from the so-called pre-mutation allele length—between 31–100 units in FRDA. The repeat number in FRDA ranges from 70–1,000 units, while the normal repeat number ranges from 5–30 units.²⁵⁴ In this regard, a homopurine-homopyrimidine (GAA)_n•(TTC)_n repeat can adopt a triplex structure, called H-DNA, under negative supercoiling. For longer sequences, a similar structure is adopted, the so-called “sticky DNA” (**Figure 4.1**).²⁵⁵ This conformation is involved in the diverse mechanisms (replication or repair dependent) that give rise to the expansion of these repeats. TNRs instability in somatic cells, which also occurs in FRDA patients, is a repair-dependent mechanism.²⁵⁴ Although “sticky DNA” seems to be involved in the expansion of these repeats, more extensive DNA methylation and low levels of RNA polymerase II (RNAPII) and Histone H3 trimethylated at Lys 4 (and Lys 36 downstream of the repeat) lead to reduction in both transcription initiation and elongation—leading to a decrease in frataxin mRNA and thus low levels of protein expression.²⁵⁶ The length of alleles inversely correlates with age at onset of the disorder and directly correlates with disease severity.^{257,258} While 96% of the individuals affected by FRDA are homozygous with a GAA TNR expansion in intron 1, in other cases, allele dysfunction is caused by insertions, deletions or point mutations.²⁵⁹

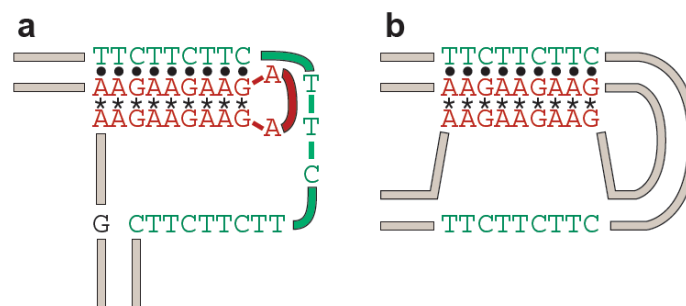


Figure 4.1. DNA structures formed by TNRs: (a) H-DNA and (b) sticky DNA formed by the (GAA)_n•(TTC)_n repeat. Only one possible isoform, in which the homopurine strand is donated to the triplex, is shown for the two structures. Watson-Crick and reverse Hoogsteen pairings are indicated by dots and asterisks, respectively. Adapted from Mirkin.²⁵⁵

Frataxin has five known isoforms. In 1996, Campuzano *et al.* first identified the *X25* gene as the critical region for the FRDA locus.²⁵³ This region (five exons, 1–4 & 5a) encodes a 210-amino acid protein, named frataxin²⁵³ (isoform A,²⁶⁰ “canonical”). An alternative product, isoform B,²⁶⁰ is obtained when exon 5b is transcribed instead of 5a (five exons, 1–4 & 5b).²⁵³ In 2002, Pianese *et al.* revealed a novel transcript of *X25*, so-called frataxin A1, which contains a 8-bp insertion between exons 4 and 5a (five exons, (1–4) & 8 bp & 5a).²⁶⁰ More recently, in 2012, Xia *et al.* observed two additional transcripts localized in the cerebellum and heart—isoforms II and III, respectively. These isoforms differ from the “canonical” one in the first exon (exon 1 \equiv 1A), which lacks the last 141 nucleotides (exon 1A Δ 141) or is substituted by another exon (exon 1B/1B Δ 18)—isoforms II and III, respectively.²⁶¹ They are localized in the cytosol (isoform II) and nucleus (isoform III),²⁶¹ whereas the rest of the isoforms are directed to the mitochondria, since they contain a mitochondrial localization signal (MLS).^{262–264} A summary of the diverse isoforms is shown in **Table 4.1**. Further work has continued studying isoforms B and A1,²⁶⁵ as well II and III.²⁶⁶

Table 4.1. Frataxin isoforms and their tissue and cellular expression patterns, splicing and residue length.

Isoform	Tissue Expression	Cellular Localization	Splicing (exons) ^e	Length (residues)
A ²⁵³ or I, ²⁶¹ “canonical”	ubiquitous	mitochondria	1–4 & 5a	210
B ²⁵³	ubiquitous/ rare	mitochondria	1–4 & 5b	171
A1 ²⁶⁰	ubiquitous/ rare	mitochondria	(1–4) & 8 bp & 5a	196
II ²⁶¹	cerebellum	cytosol	(1B/1B Δ 18)–4 & 5a	135
III ²⁶¹	heart	nucleus	(1A Δ 141)–4 & 5a	164

Although the relevance of several frataxin isoforms has been pointed out, the “canonical” one—hereinafter referred as FXN—is the most widely studied. Although the role of FXN in cellular metabolism is still unclear, it is accepted that it exerts a function in iron homeostasis by directly binding this ion: (1) serving as iron chaperone during iron-sulfur (Fe-S) cluster production; (2) participating in iron storage; (3) repairing oxidatively damaged aconitase Fe-S clusters; (4) regulating oxidative stress/ reactive oxygen species (ROS); and (5) participating in energy conversion and oxidative phosphorylation.^{267–270}

^e Exon 1 \equiv exon 1A, as discussed in Xia *et al.*²⁶¹

Interestingly, FXN orthologs have been observed throughout the diverse kingdoms of life, *e.g.* *Saccharomyces cerevisiae* (Yfh1), *Escherichia coli* (CyaY) and humans (HsFtx or FXN).²⁶⁷ In addition, frataxin has also been localized in hydrogenosomes—organelles with a common ancestry to mitochondria—of *Trichomonas vaginalis*, a unicellular eukaryote.²⁷¹ Recently, this protein has been shown to have dual localization in *Arabidopsis thaliana*, where chloroplasts and mitochondria contain AtFH, the frataxin homolog.²⁷² **Figure 4.2** shows the similarity between structures of Yfh1, CyaY and HsFtx.

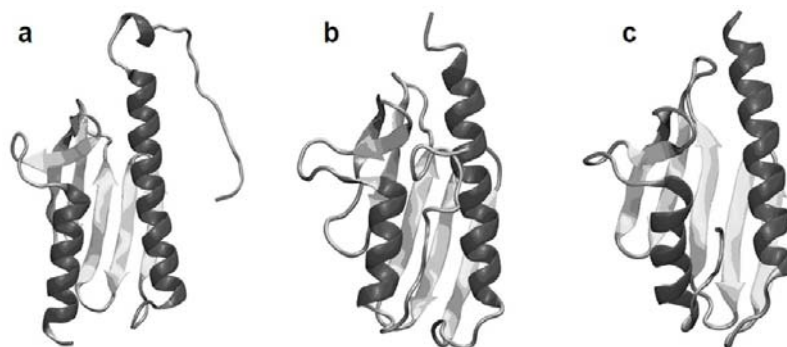


Figure 4.2. Structures of diverse frataxin orthologs: from (a) yeast (Yfh1, PDB ID# 2GA5), (b) human (HsFtx, PDB ID# 1LY7) and (c) bacteria (CyaY, PDB ID# 1SOY). Adapted from Bencze *et al.*²⁶⁷

FXN is expressed as pre-protein with the MLS (FXN^{1–210}, precursor, or *p*),²⁷³ and then cleaved between residues 41–42 and 55–56 by the mitochondrial processing peptidase (MPP), obtaining FXN^{42–210} (intermediate₄₂, or *i*₄₂) and FXN^{56–210} (mature₅₆, *m*₅₆), respectively.²⁷⁴ In addition to these proteolytic events, two C-terminal degradation products are observed.²⁷⁴ Later, in 2007, Yoon *et al.* identified a cleavage site between residues 77–78 promoted by iron to produce a truncated form (degraded₇₈, *d*₇₈).²⁷⁵ However, *in vivo* studies showed that the main mature form of FXN is produced after cleavage between residues 80–81 (mature₈₁, *m*₈₁),²⁷³ and it was reported to be the isoform with the highest rescue profile when lacking FXN.²⁷⁶ In this regard, the loss of the N-terminus is linked to a change in FXN functions,²⁷⁷ as longer sequences correlate with oligomerization, iron storage and stable interactions with NFS1•ISD11 (sulfur donor complex) and ISCU (iron-sulfur cluster assembly enzyme),²⁷⁸ while shorter ones are observed with monomeric configuration and are related to labile iron binding, and dynamic contacts with NFS1•ISD11 and ISCU.²⁷⁹ A summary of the main features of each metabolic isoform is shown in **Table 4.2**.

Table 4.2. Metabolic isoforms of FXN.

Isoform Name	Isoform Sequence	Proteolytic Event	Length (n° residues)
precursor, <i>p</i>	FXN ^{1–210}	-	210
intermediate ₄₂ , <i>i</i> ₄₂	FXN ^{42–210}	MPP ²⁷⁴	169
mature ₅₆ , <i>m</i> ₅₆	FXN ^{56–210}	MPP ²⁷⁴	155
degraded ₇₈ , <i>d</i> ₇₈	FXN ^{78–210}	Fe-mediated ²⁷⁵	133
mature ₈₁ , <i>m</i> ₈₁	FXN ^{81–210}	MPP ²⁷³	130

Recently, an European consortium—European Friedreich's Ataxia Consortium for Translational Studies (EFACTS)—has released data from a continuing study involving 592 FRDA patients, thus facilitating information on disease progression and clinical details.^{280,281} There is currently no US Food and Drug Administration (FDA)-approved treatment for FRDA; however, several strategies are under investigation and several in clinical trials.²⁸² These include symptomatic treatments, and temporal and permanent therapies (**Table 4.3**).^{282–286}

Table 4.3. Treatments currently being studied for FRDA.^f

Symptomatic Treatments	Temporal Therapies	Permanent Therapies
antioxidants	FXN stabilizers	excision of expanded repeats [‡]
iron chelators	FXN enhancers	expression induction using TALE [‡]
neurotrophic factors	RNA transcript therapy [‡]	gene therapy [‡]
	protein replacement therapy [‡]	cell therapy [‡]

Symptomatic treatments involve the use of the following: antioxidants, *e.g.* coenzyme Q10 (CoQ10) and idebenone, to counteract the oxidizing conditions experienced by cell metabolism in conditions of FXN deficit;^{249,287} iron chelators, *e.g.* deferiprone, to reduce the iron excess;^{288,289} neurotrophic factors, *e.g.* insulin/insulin-like growth factor 1 (IGF-1);²⁹⁰ and deuterated polyunsaturated fatty acids (PUFAs), *e.g.* linoleic acid deuterated at the peroxidation-prone *bis*-allylic positions,^{291,292} to slow down ROS-driven oxidation of PUFAs. Combinations of these drugs have also been tested.²⁹³ Temporal therapies include the use of FXN stabilizers—*e.g.* proteasome inhibitors—²⁹⁴ and enhancers—*e.g.* histone deacetylase (HDAC) inhibitors,^{295–300} interferon gamma-1b (IFN- γ)³⁰¹ and erythropoietin (EPO) derivatives.^{302–304} In addition, the delivery of mRNA (RNA transcript therapy) after

^f Therapies labeled with ‡ are specific for FRDA, others may cause general dysregulations.

intravenous injection showed a half-life greater than one week.³⁰⁵ On the other hand, the delivery of FXN (protein replacement therapy) using a TAT-FXN construct showed promise *in vivo* in a conditional mouse model for FRDA.³⁰⁶

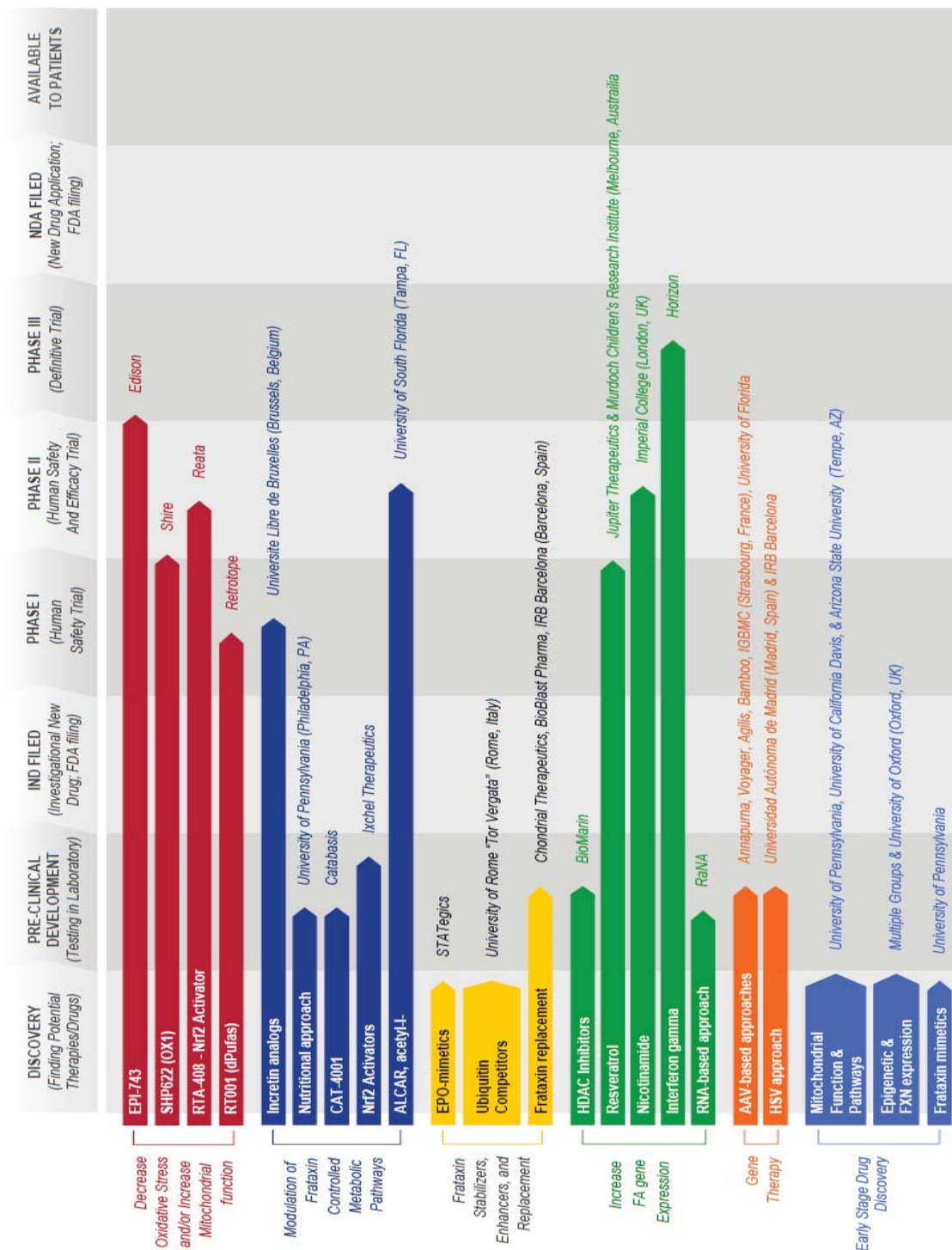


Figure 4.3. FRDA treatment pipeline (March 2016), from Friedreich's Ataxia Research Alliance (FARA).

On the other hand, permanent therapies offer a long-term solution without the need for a continuous treatment.³⁰⁷ In this regard, several studies proposed the use of methodologies to excise the expanded GAA repeats, like zinc finger nucleases,³⁰⁸ and also the use of transcription activator-like effector (TALE) proteins to increase the expression of FXN.^{309,310} The correction of this disease by means of gene therapy has been addressed using a bacterial artificial chromosome (BAC)³¹¹ and a yeast artificial chromosome (YAC),³¹² as well diverse viral vectors including lentiviral vectors,³¹³ adeno-associated viruses (AAVs),^{313,314} and herpes simplex virus type 1 (HSV-1) amplicon vectors.³¹⁵⁻³¹⁷ Cell therapies have also been studied using bone marrow stem cells, which induced FXN expression levels, resistance to oxidative stress and neuroprotection to FRDA cells;^{318,319} but induced pluripotent stem cells (iPSCs) from FRDA patients have also been successfully derived to neurons and cardiomyocytes with potential therapeutic applications.³²⁰⁻³²² Research funded by Friedreich's Ataxia Research Alliance (FARA) and the current stage is shown in **Figure 4.3**.

In this thesis, we explore the potential of a temporal and a permanent therapy for FRDA at the central nervous system (CNS), the former based on a protein replacement therapy and the latter on a gene therapy using HSV-1 amplicon vectors.

4.1. Protein Replacement Therapy for Friedreich's Ataxia at the CNS—Chemistry with Proteins

The year 1922 marked the use of the first protein drug, namely insulin. This hormone was purified from bovine and porcine pancreas and then used in patients with diabetes mellitus type I (DM-I).³²³ Later, the issues related to the use of insulin of animal origin, including immunological responses, were addressed by producing recombinant human insulin in *Escherichia coli*.³²⁴ Currently, more than 130 proteins are approved by the FDA for clinical use (over 95 of which are produced recombinantly), and many more are in development.³²⁴

Here we decided to study the viability of delivering FXN^{1–210} into the brain as the pre-protein isoform (precursor, *p*), since the MLS, not present in mature isoforms, was necessary to target the mitochondria. Therefore, we devised a therapeutic construct based on a BBB shuttle bioconjugated at the *N*-terminus of the protein. The processing of the MLS at any of the proteolytic sites would then give a native mature isoform (**Figure 4.4**).

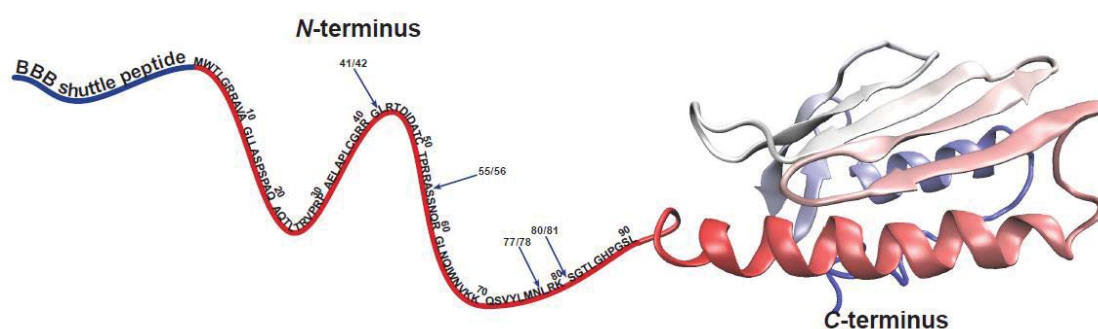


Figure 4.4. Construct designed for the protein replacement therapy for FRDA at the CNS: (BBB shuttle)-FXN^{1–210}. Proteolytic sites at the *N*-terminus are shown. Created with Visual Molecular Dynamics (VMD) and Adobe InDesign, using the structure PDB ID# 1LY7.

Both the BBB shuttle and protein can be ensembled through diverse methodologies, such as via bioconjugation to Cys,^{325,326} Lys^{327,328} or Tyr^{329–331} residues, but also Staudinger ligation,³³² or reactions between azides and alkynes—the so-called “click chemistry”.^{333,334} Native chemical ligation (NCL) methodologies enable bioconjugation at the *N*-terminus through the reaction of a thioester with an *N*-terminal Cys-containing protein.^{335,336} In addition, chemoenzymatic approaches are promising tools that allow the introduction of site-specific chemical modifications; however, they require the presence of relatively short

sequences or other chemical moieties in the protein.^{337,338} All the aforementioned approaches are carried out in buffered mild temperature and pH.

Here, we used (1) NCL, (2) the modification of the *N*-terminus through an oxime bond, and (3) a chemoenzymatic approach to bioconjugate the BBB shuttle peptides (*r*D-HAI and *r*D-THR) to the *N*-terminus of FXN. NCL is based on the *C*-terminal thioester reaction with the thiol group of an *N*-terminal Cys—reversible transesterification—, which after a *S*-to-*N*-acyl shift results in the formation of the final product, a native amide bond (**Figure 4.5**).

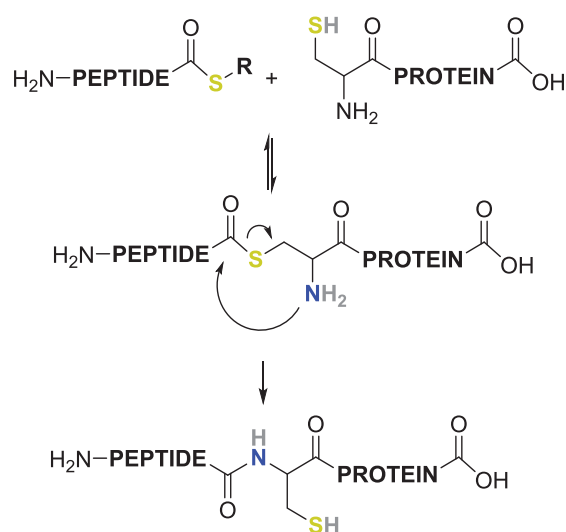


Figure 4.5. Bioconjugation/ ligation of a peptide to a protein through NCL. A first reversible step, a transthioesterification, is followed by a *S*→*N*-acyl transfer. Created using ChemBioDraw.

The second bioconjugation approach specifically modifies the *N*-terminal through a transamination reaction to afford a ketone or an aldehyde, still under mild conditions. The carbonyl group is then reacted with an aminooxy group to give an oxime bond (**Figure 4.6**). In more detail, the first step of this bioconjugation strategy—transamination—is based on the reaction between pyridoxal-5'-phosphate (PLP, a coenzyme) and the *N*-terminus of the protein, which yields a ketone or an aldehyde moiety (keto-protein).³³⁹⁻³⁴¹ The second step is the reaction between the keto-protein and the aminooxy moiety of the peptide in our case (R^2 -ONH₂) to give rise to an oxime bond, which is accelerated by aniline as nucleophilic catalyst.³⁴² Hydrazides can also be used; however, the hydrolysis rate of the hydrazone bond is in general much faster than for oximes—half-life of several minutes and ~25 days, respectively.³⁴³ The general conditions for each reaction are given in **Figure 4.6**.³⁴¹

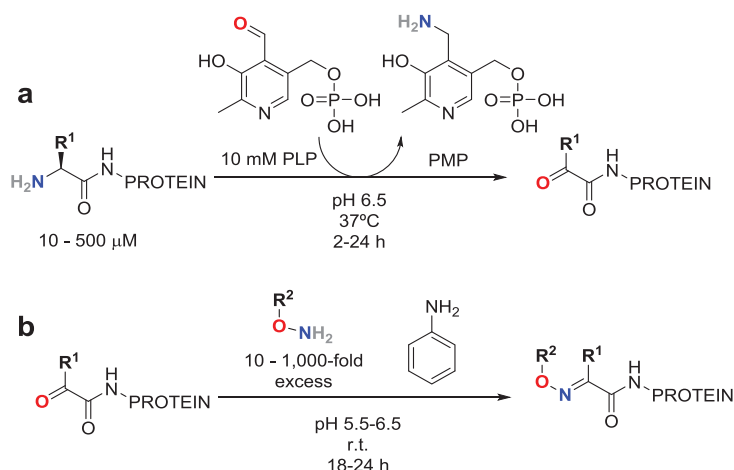


Figure 4.6. Bioconjugation reactions used for the *N*-terminal modification: (a) transamination and (b) oxime-linked protein bioconjugate reaction. $R^1 \equiv$ side-chain of the *N*-terminal residue, $R^2 \equiv$ molecule containing the aminoxy moiety. Created using ChemBioDraw.^g

However, this bioconjugation strategy may give rise to several products, the most relevant three being a keto-protein (intermediate), an oxime product (desired product), and a PLP covalent adduct (byproduct). Conversion to any of these products is dependent on the amino acid sequence, determined mainly by the *N*-terminal residue (**Figure 4.7**).³⁴¹

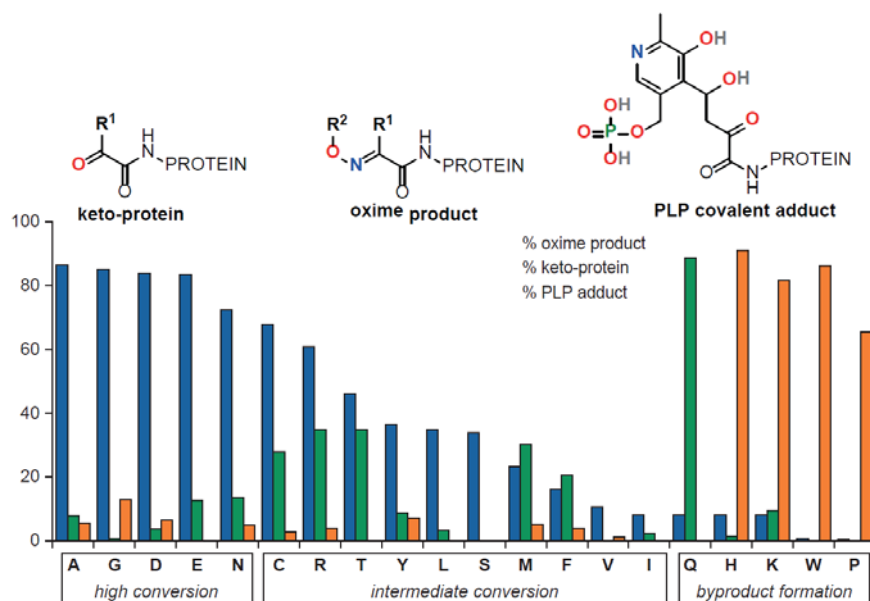


Figure 4.7. *N*-terminal bioconjugation efficiency and byproducts depending on the *N*-terminal amino acid. Study performed with the tetrapeptide sequence XKWA, where X is any of the 20 natural amino acids and an alkoxyamine probe, benzylalkoxyamine. Keto-protein, oxime product, and PLP aldol adduct (for an alanine-terminal) are shown. $R^1 \equiv$ side-chain of the *N*-terminal residue, $R^2 \equiv$ molecule containing the aminoxy moiety. Adapted from Witus *et al.*³⁴¹

^g PMP \equiv pyridoxamine-5'-phosphate.

Thus, we decided to use Gly as the terminal residue in our constructs (*i.e.* Gly-FXN¹⁻²¹⁰), since Gly—together with Ala, Asp and Glu—gives the best conversion to the oxime product (**Figure 4.7**), whereas the *N*-terminal residue found in the expressed protein (Met, or Trp after methionine aminopeptidases (MetAPs) cleavage)^{344,345} is not suitable for this bioconjugation strategy due to low oxime product conversion and/or byproduct formation (**Figure 4.7**).

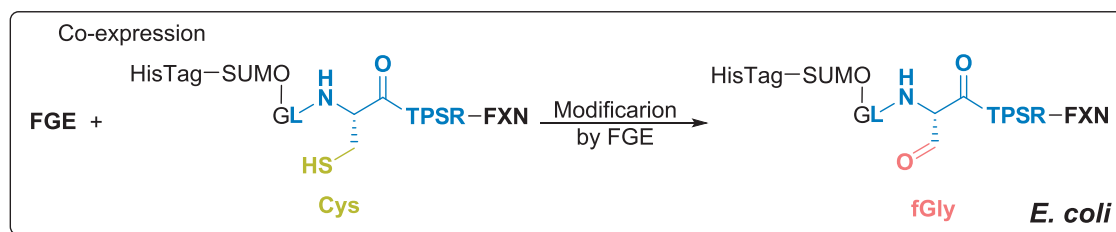


Figure 4.8. Co-expression of FGE and FXN construct (HisTag-SUMO-Gly-FGEsite-FXN). Both proteins are expressed together in *E. coli* and the FGE site-specific modification (6-mer tag, in blue) is modified within the cells (Cys to fGly conversion). Created using ChemBioDraw.

The third bioconjugation strategy we selected, the chemoenzymatic approach, is based on work by Bertozzi and co-workers,³³⁸ who showed that the co-expression of the protein of interest (containing a 6-mer tag (LCTPSR) at the *N*-terminus together) with the formylglycine-generating enzyme (FGE) enables the specific modification of the Cys residue in the tag to formylglycine (fGly)—a residue containing an aldehyde moiety that can be used for bioconjugation, as previously described. An additional Gly was added at the *N*-terminus to allow to work with the aforementioned bioconjugation strategy (**Figure 4.8**).

Each of these three approaches requires specific reactive moieties in the peptides and protein. FXN was expressed in *E. coli* as fusion protein, leaving the *N*-terminus of the final construct prepared to each bioconjugation strategy (**Table 4.4**). A HisTag was placed at the *N*-terminus, separated from the FXN construct by a SUMO (small ubiquitin-like modifier) protein, which then allows specific cleavage at its *C*-terminus (by using a SUMO protease), thus leaving the “clean” sequence of the desired protein.³⁴⁶⁻³⁴⁸ The fusion protein was then purified by immobilized metal affinity chromatography (IMAC) and cleaved using the SUMO protease, releasing the fragment MGSSH₆-SUMO. The final protein construct was purified using a reverse-IMAC followed by size-exclusion chromatography (SEC).

Table 4.4. The diverse FXN constructs expressed depending on the bioconjugation strategy followed.

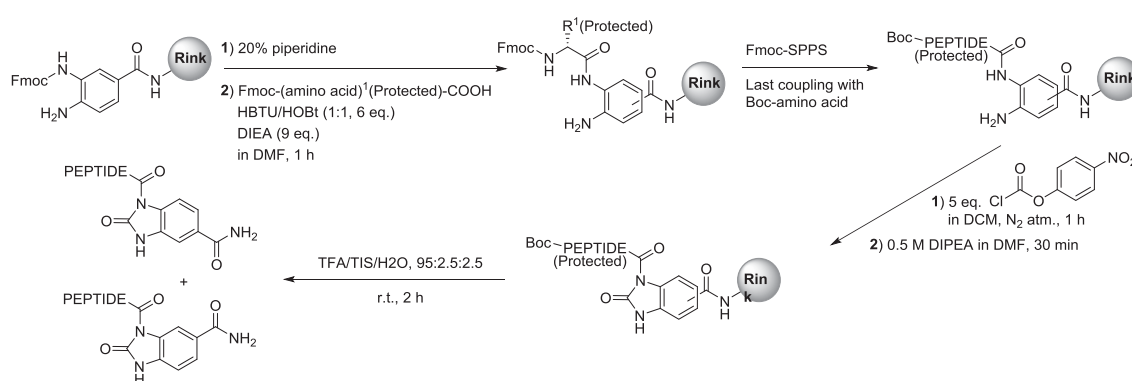
Chemical Approach	Protein Construct Expressed	Final Protein Construct
NCL	MGSSH ₆ -SUMO-Cys-FXN	Cys-FXN
N-terminal modification	MGSSH ₆ -SUMO-GlyLys-FXN	GlyLys-FXN
Chemoenzymatic approach	MGSSH ₆ -SUMO-Gly-FGEsite-FXN + FGE	Gly-FGEsite-FXN

The peptide BBB shuttles were also synthesized specifically for each bioconjugation approach (Table 4.5).

Table 4.5. The diverse peptides synthesized depending on the bioconjugation strategy followed.

Chemical Approach	Peptides Synthesized ^h
NCL	<i>r</i> D-HAI-Nbz and <i>r</i> D-THR-Nbz
N-terminal modification	AO- <i>r</i> D-HAI and AO- <i>r</i> D-THR
Chemoenzymatic approach	AO- <i>r</i> D-HAI and AO- <i>r</i> D-THR

Peptides-Nbz were synthesized following the Fmoc-SPPS approach reported by Blanco-Canosa *et al.*,³³⁵ where first diaminobenzoic acid (Dbz) is introduced in a resin terminated with a Rink linker. After the standard SPPS synthesis, the C-terminus is activated through acylation with *p*-nitrophenylchloroformate followed by the addition of a base. The peptide-Nbz is finally deprotected and cleaved by TFA treatment with scavengers (Figure 4.9).

**Figure 4.9.** Scheme for the synthesis of Nbz-peptides. Created using ChemBioDraw.ⁱ

^h Nbz ≡ *N*-acyl-benzimidazolinone, AO ≡ aminooxy moiety, *i.e.* aminooxyacetyl.

ⁱ Fmoc-SPPS ≡ 9-fluorenylmethyloxycarbonyl solid-phase peptide synthesis, R¹(Protected) ≡ side-chain of the first amino acid coupled to the resin protected for a Fmoc/*t*Bu strategy, DIPEA ≡ *N,N*-diisopropylethylamine, HBTU ≡ *O*-(benzotriazol-1-yl)-*N,N,N',N'*-tetramethyluronium hexafluorophosphate, HOBt ≡ 1-hydroxybenzotriazole, TIS ≡ triisopropylsilane, TFA ≡ trifluoroacetic acid.

AO-peptides were synthesized using the Fmoc/*t*Bu SPPS strategy. As final building block, Boc-(aminooxy)acetic acid was coupled by means of the same procedure used for the other residues. All the peptides shown in **Table 4.5** were obtained with high purity (>95%), as determined by reversed-phase high performance liquid chromatography (RP-HPLC), and identified by matrix-assisted laser desorption/ionization mass spectrometry (MALDI-TOF MS) and high-resolution MS (HRMS).

We initially started working with the chemoenzymatic approach; however, after several trials it was not possible to obtain the protein with the FGE-site modified (Cys to fGly). Nevertheless, the *N*-terminal Gly added to the design allowed us to work with the transamination reaction using PLP. Thus, we reacted Gly-FGEsite-FXN¹⁻²¹⁰ with PLP under similar conditions as those shown in **Figure 4.6** (50 mM phosphate buffer, pH 6.5, 21 μ M protein, 10 mM PLP, 18 – 24 h). However, we were not able to identify the modified protein (*i.e.* (2-oxoacetyl)-FGEsite-FXN¹⁻²¹⁰), not even after reacting with a tag (benzylhydroxylamine) to increase the mass difference and enable better discrimination by MS. The fluorescence detection in sodium dodecyl sulfate-polyacrylamide gel electrophoresis (SDS-PAGE) of the protein modified using fluorescein-5-thiosemicarbazide. In both cases similar conditions to those previously described in **Figure 4.6** (50 mM phosphate buffer, pH 5.5, protein 21 μ M, 10 eq. tag, 10 eq. aniline 2–20 h) were used. In addition, we used an improved version of the catalyst for the oxime bond forming reaction (aniline was substituted by *p*-phenylenediamine);³⁴⁹ however, the same negative results were obtained.

At this point, we suspected that the protein was being hydrolyzed, and we then decided to perform kinetic studies of the stability of FXN: (1) short-term stability at 37°C and (2) long-term stability at 4, -20 and -80°C—related to practical aspects for bioconjugation and storage, respectively.

Stability of FXN (using Gly-FXN¹⁻²¹⁰) at 37°C in phosphate buffer at pH 6.5 was studied over 21 h, taking samples at diverse time-points and freezing them in liquid nitrogen to stop possible degradation. It can be observed in **Figure 4.10** that the protein is being degraded at 37°C over time. The sample left for 21 h at 37°C is shown as a faint band in the gel, much less intense than the time zero sample.

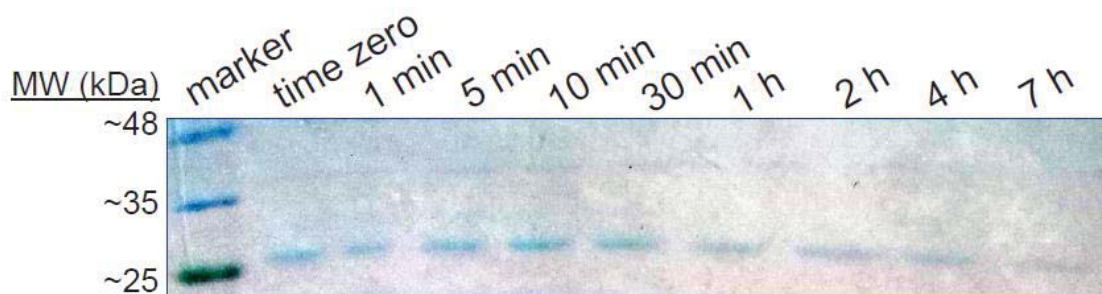


Figure 4.10. Stability of FXN at 37°C in phosphate buffer pH 6.5, observed by SDS-PAGE (marker: BlueStar Prestained Protein Marker, Nippon Genetics). No band observed after 21h (data not shown). Created with Adobe InDesign.

Regarding the long-term stability, the study was carried out over 6 months with the protein (Gly-FGEsite-FXN¹⁻²¹⁰) stored at 4, -20 and -80°C in 20 mM Tris buffer, pH 7.5, 50 mM NaCl and 5 mM EDTA (to chelate metal ions which might promote hydrolysis). At several time points (time zero, 1 and 4 weeks, and 3 and 6 months) the protein was characterized by MALDI-TOF MS, HPLC, HPLC-MS, SDS-PAGE, circular dichroism (CD) and HRMS (single time point, after two weeks). MALDI-TOF MS appeared to be not very useful to assess the stability of the protein since the protein signal was only detected for the sample at time zero—experimental mass: 23.99 kDa, vs. theoretical mass: 23.84 kDa (**Figure 4.11a**). RP-HPLC analysis revealed the rate of degradation increased from -80 to 4°C, as expected (**Figure 4.11b** and **Table 4.6**).^j HPLC-MS analysis revealed similar degradation pattern as observed by HPLC—spectra were more complex with degradation (**Figure 4.11c**). The deconvolution of the spectrum observed in **Figure 4.11c** (sample at -20°C) gives a mass of $23,843 \pm 2$ Da (theoretical mass = 23,850 Da). After one week, degradation was observed in the sample stored at 4°C by SDS-PAGE, and this becomes more evident over time (see **Figure 4.11d**, where a degradation band of ~11 kDa can be observed). In addition, dimers were formed in samples stored at -20 and -80°C (**Figure 4.11d**, where after 3 months a band of ~48 kDa is observed).

^j Analytical RP-HPLC was carried out using a C₁₈ column and a linear gradient from 0 to 100% of B. A ≡ H₂O 0.045% TFA, and B ≡ CH₃CN 0.036% TFA.

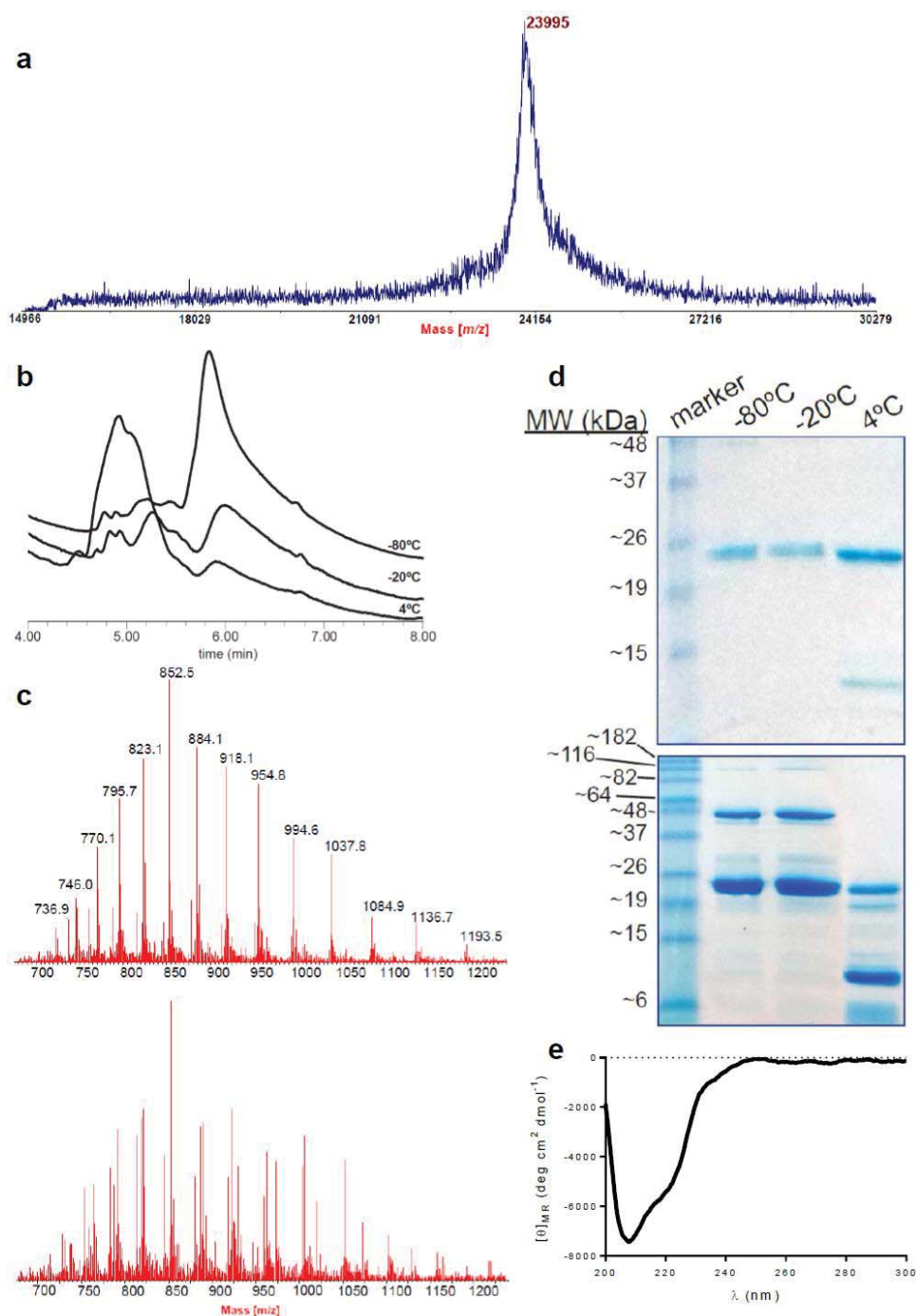


Figure 4.11. Data from the stability of FXN: (a) MALDI-TOF MS spectrum recorded from the sample of FXN at time zero; (b) RP-HPLC chromatograms of the samples stored during 6 months at 4, -20 and -80°C, showing an increase in degradation from -80 to 4°C (the peak at 6 min corresponds to FXN, and the other peaks at the front are degradation products); (c) spectra of HPLC-MS electrospray ionization (ESI) of samples preserved at (top) -20 and (bottom) 4°C during one week (sample at -80°C behaved similar to that at -20°C); (d) SDS-PAGE analysis after (top) 4 weeks and (bottom) 3 months (marker: BenchMark Pre-Stained Protein Ladder, Invitrogen); and (e) CD spectra of FXN in 50 mM phosphate buffer, pH 6.5. Created using GraphPad, Adobe Illustrator and InDesign.

Spectra from CD did not show differences between the diverse time points and temperatures (**Figure 4.11e**). In addition, the CD spectra were recorded in three buffers (20 mM Tris at pH 7.5, 50 mM phosphate at pH 6.5 and 50 mM ammonium acetate at pH 7.4) and the same profile was observed in all cases. HRMS enabled the identification of FXN in the three samples after two weeks, however the proportion quantified was higher in samples preserved at -20 and -80°C compared to 4°C.

Table 4.6. Long-term stability of FXN at diverse temperatures, showing the first time point where differences respect to the time zero were observed.

Method of Analysis	Temperature of Storage (°C)		
	4	-20	-80
MALDI-TOF ^k	<i>n.d.</i>	<i>n.d.</i>	<i>n.d.</i>
HPLC-PDA	1 week	3 months	6 months
HPLC-MS	1 week	4 weeks	6 months
SDS-PAGE	1 week	-	-
CD ^l	<i>n.c.</i>	<i>n.c.</i>	<i>n.c.</i>

The results are conclusive, preservation of FXN might be at 4°C for less than 24 h, at -20°C for up to 2 months, and for longer at -80°C. Therefore, we envisage a protein replacement therapy for the CNS based on the encapsulation of the full-length native protein (FXN¹⁻²¹⁰), in polymeric nanoparticles (NPs) conjugated with BBB shuttles. Hence, the stability of the protein might be increased by the shield provided by the organic polymer of the NPs. This strategy avoids the bioconjugation process which promotes the degradation process. To further increase the stability of the protein, the MLS might be redesigned.

^k *n.d.* ≡ not detected, only for time zero.

^l *n.c.* ≡ no change observed.

4.2. Gene Therapy for Friedreich's Ataxia at the CNS—Chemistry with Enveloped Viral Particles

Howard Temin concluded, in 1961, that stably inherited gene information could be transferred from a virus—he observed that chicken cells infected with the Rous sarcoma virus (RSV) stably inherited gene mutations containing the information for its progenies.³⁵⁰ A couple of years later, Rogers *et al.* demonstrated an initial proof-of-concept of virus mediated gene transfer.³⁵¹ Finally, in 1990s, the first gene therapy clinical trials started.³⁵² Nowadays, most of gene therapies are based on viral vectors, however other tools are being developed, such as organic NPs encapsulating the genetic material, liposomes, etc.—**Figure 4.12** shows the variety of vectors used in current clinical trials worldwide. Thus, gene therapy includes the use of nucleic acids for treatment, cure or prevention, regardless the vector used for transferring them.

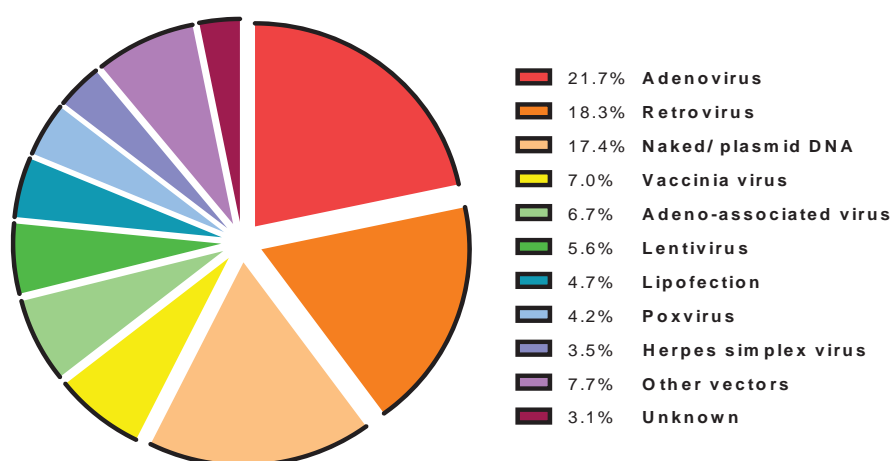


Figure 4.12. Vectors currently used in gene therapy clinical trials (total = 2409, of which 65% are for cancer diseases, 10% for monogenic diseases, 7.5% for infectious diseases, 7.4% for cardiovascular diseases and the rest of the percentage divided in various fields—only 1.8% are for neurological diseases). Data obtained from The Journal of Gene Medicine.^m Created using GraphPad.

Although other methodologies have been purposed as gene transfer vectors,³⁵³ viruses are specialized structures with high transfection efficiency. In addition, viral vectors are varied and each one might be suitable for specific purposes (examples currently used in clinical trials are shown in **Figure 4.12**). FRDA is characterized by three main genetic

^m The Journal of Gene Medicine, Wiley and Sons (<http://www.abedia.com/wiley/index.html>). Data updated on August 2016.

features: (1) recessive and (2) monogenic disease, and (3) it is caused by low expression of FXN and not by an increase in expression or a gain of new function. These three conditions make the treatment of this disease suitable by delivering a new copy of the gene—one copy (recessive) of one gene (monogenic) is enough. However, the packing capacity of viral vectors is limited, in general to several kb (*e.g.* adenoviruses, retroviruses and lentiviruses are limited to 8 kb³⁵⁴ whereas adeno-associated viruses (AAVs) to only 4.7 kb)³⁵⁵ and the complete *FRDA* genomic locus is about 80 kb (135 kb with the regulatory regions).^{253,260,316} In addition, frataxin is expressed in diverse isoforms with varied expression patterns depending on the tissue, as previously explained. In this regard, herpes simplex viruses—herpes simplex virus type 1 (HSV-1)—are associated to several desired features: (1) theoretically transgene capacity up to 150 kb,^{317,356} (2) ability to transduce a broad host range,³⁵⁶ (3) both dividing and non-dividing cells,³⁵⁶ and (4) very efficient with neuronal cells.³¹⁷ Furthermore, (4) these viruses can be obtained with relatively high titers.³⁵⁶ However, HSV-1 vectors do not cross the BBB.³⁵⁷

In this regard, the group of Prof. Díaz-Nido, at Centro de Biología Molecular Severo Ochoa (CBMSO), has been developing viral vectors based on HSV-1 amplicons. They express the 80 kb *FRDA* genomic locus, including all introns, and regulated by the endogenous promoter contained in a bacterial artificial chromosome (BAC). The effectiveness of these infectious BACs was proven both *in vitro*³¹⁶ and *in vivo* (mouse).³¹⁷ In addition, they recently proved the delivery of these viruses gives rise to the expression of three isoforms (I, II, III). BACs are double stranded DNA vectors (as the viral family of *Herpesviridae*, which genome length ranges from 125 to 230 kb)³⁵⁸ based on the *E. coli* fertility factor (F-factor) replicon. They are maintained as a circular supercoiled extrachromosomal single copy plasmid in the bacterial host,^{359,360} which can allocate up to 300 kb, and are more stable and easy to use compared with yeast artificial chromosomes (YACs).^{361,362} Briefly, these genomes are created by means of genetic engineering tools and then encapsidated in HSV-1-like particles through transfecting Vero2-2 cells with the components required. These components are the BAC containing the gene of interest; the *ICP27*-deleted packaging BAC plasmid with *pac* and *oris*,ⁿ and an oversized *pac*-(fHSVΔ*pac*Δ27 0+); and a small plasmid containing the *ICP27*—both plasmids supplemented in *trans*.^{316,363-366}

ⁿ Non-coding viral sequences *oris* and *pac* are the origin of DNA replication and DNA cleavage/packaging signal, respectively.

We envisaged the delivery of these viral particles to the CNS using BBB shuttle peptides. The chemistry on the surface of these viral particles and physicochemical characterization would be performed by the group of Prof. Giralt (IRB Barcelona), and the production of viruses and biological evaluation by the group of Prof. Díaz-Nido (CBMSO). The initial step was to establish a methodology to modify HSV-1 vectors and the subsequent characterization. We then designed strategies to modify covalently the outer structure of HSV-1 particles through a mild, clean and fast chemical method. These viruses are composed by an envelope made up with a membrane derived from the *trans* Golgi network (TGN) with the glycoproteins required for the cell entry (**Figure 4.14**). Thus, chemically modifying these viral particles is more similar to performing chemistry at the cellular surface than at viral capsids (protein-based superstructures).³⁶⁷

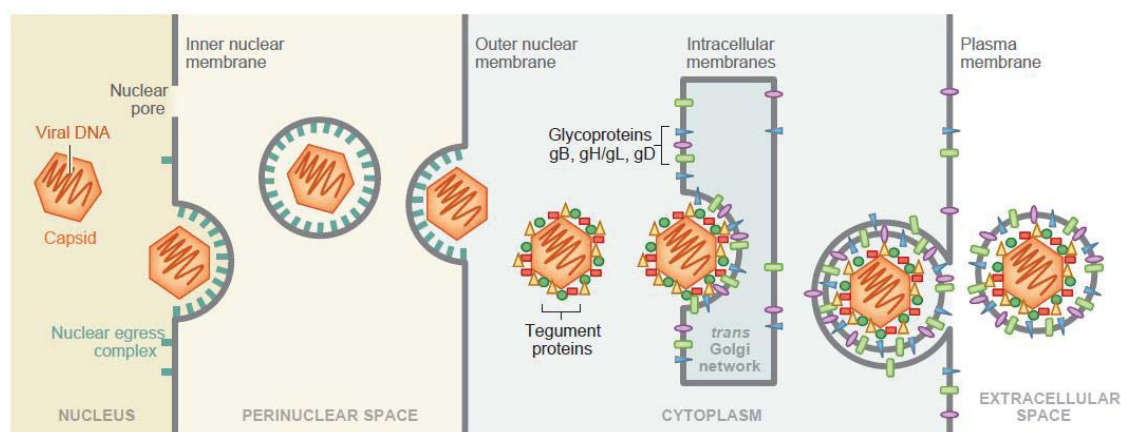


Figure 4.14. Scheme of herpesvirus egress. Herpesviruses replicate and encapsidate in cell nucleus and then bud at the nuclear envelope to egress from the nucleus; in the cytoplasm, viral capsids mature acquiring tegument proteins (16–35 proteins),³⁶⁸ and bud again in the TGN where the membrane contains the glycoproteins required for cell entry; finally, these viruses are released into the extracellular space. Adapted from Bigalke *et al.*³⁶⁹

Recently, Loret *et al.* characterized the mature virions of HSV-1 by MS, identifying 8 viral capsid proteins, 23 potential tegument proteins and 13 viral glycoproteins. In addition, 49 proteins from the host were identified in these virions.³⁷⁰ We identified in our HSV-1 vectors, using a bottom-up proteomics approach, 7 tegument proteins (UL13, UL16, UL36, UL47, UL48, UL49, UL50), 3 capsid proteins (UL17, UL18, UL38) and 3 envelope glycoproteins (gI, gB and gD) and a late protein (UL45)—both gB and UL45 are required for cell fusion.³⁷¹

We classified the strategies for envelope modification depending on the component where the BBB shuttles are attached: (1) lipid bilayer, (2) sugars of glycoproteins, and (3) directly to a protein residue (**Figure 4.15**). The bioconjugation into the lipid bilayer using the large surface available in the viral envelope could be performed using peptide-lipid conjugates through a non-covalent modification, which preserve the native structure of proteins. However, the display of BBB shuttles might be hindered by the surrounding glycoproteins and the use detergents might be required, which may distort the viral envelope. In addition, the synthesis of peptide-lipid conjugates might be hard due to the dual chemical character, namely amphiphilicity.

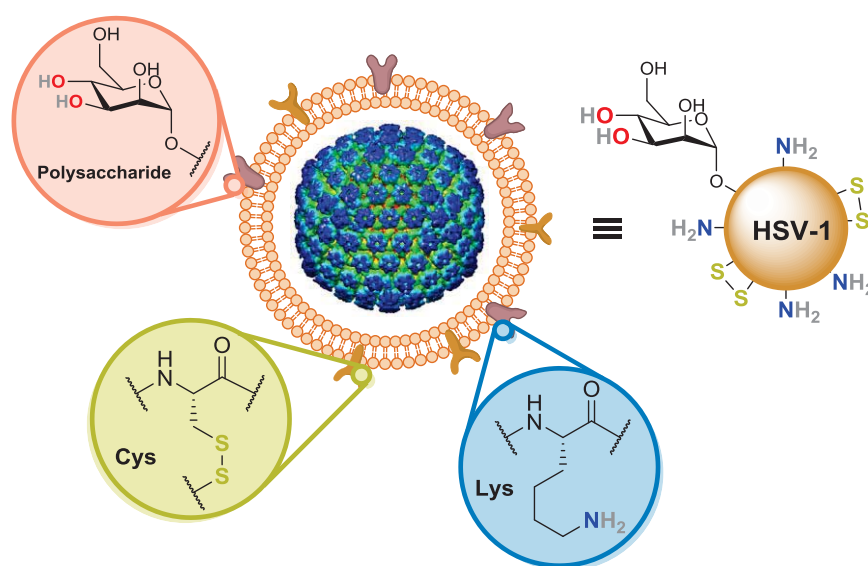


Figure 4.15. Simplified structure of HSV-1, showing reactive groups for bioconjugation: polysaccharides, cysteines (Cys) forming disulfide bridges and lysines (Lys). Created using ChemBioDraw, with the structure of HSV-1 C-capsid,^o EMD ID# EMD-5659.

Chemical modification of proteins might lead to change their structure and thus their biological activity; however, the methodology is more straightforward. Sugars of glycoproteins can be oxidized (*e.g.* with NaIO₄),³⁷³ and the generated aldehyde moieties then reacted with peptides functionalized with aminooxy groups (**Figure 4.16a**).³⁷⁴ Nevertheless, the oxidation reaction is not specific and might affect other chemical groups.³⁷⁵ Chemoenzymatic approaches have been tried with success in glycoproteins of cell surfaces;³⁷⁶ however, the polysaccharide composition of HSV-1 is complex,^{377,378} being hard to predict the effectiveness of the bioconjugation process.

^o The C-capsids are the closest in form to those encapsidated into mature virions.³⁷²

Strategies facing bioconjugation into protein side-chains are varied. Here, we selected two straightforward methodologies to covalently modify cysteine and lysine residues. Thiol reactive maleimides enable specific modification of cysteines (**Figure 4.16c**). However, this methodology entails a two-step process, since it requires the reduction of Cys-Cys disulfide bridges prior to reaction with maleimide groups. This increases the sample manipulation, and the reduction of disulfide bridges may induce conformational changes on proteins and thus alter their function.³⁷⁹

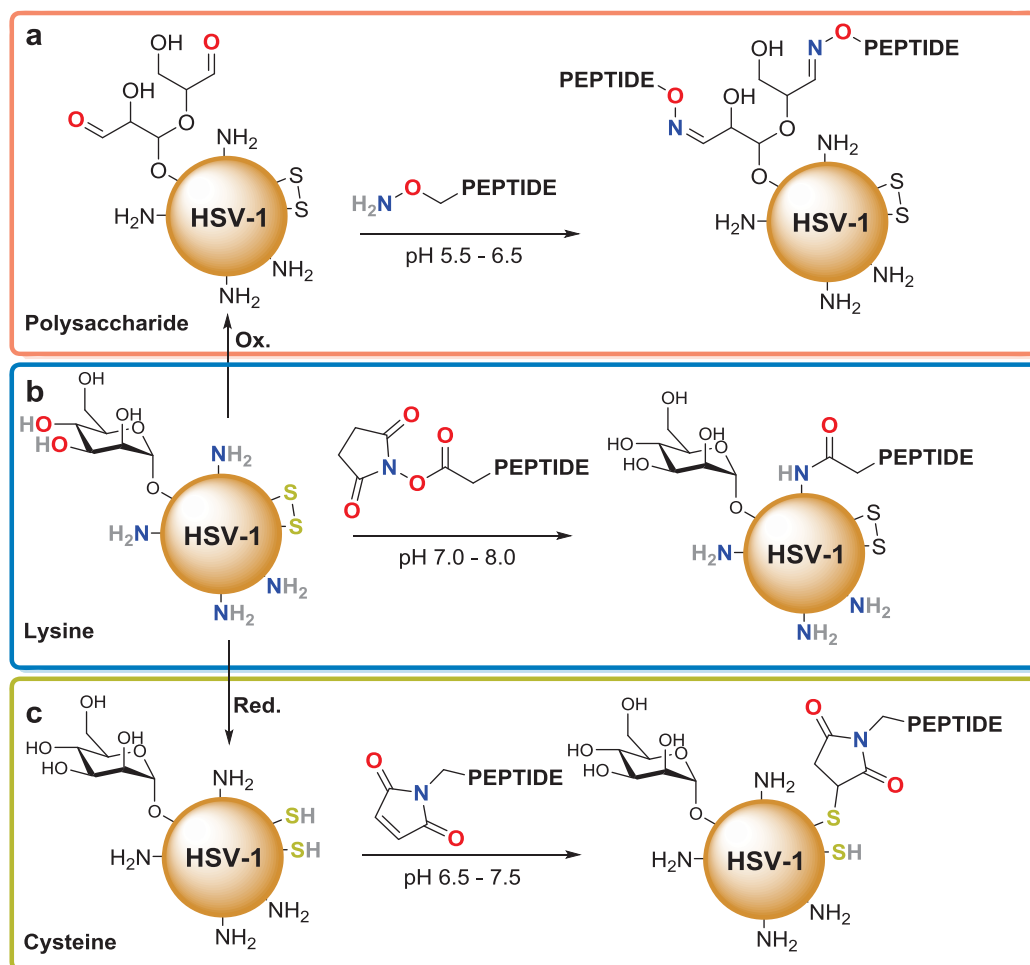


Figure 4.16. HSV-1 bioconjugation strategies: (a) oxidation of polysaccharides and reaction of aminoxy-peptides with the generated aldehydes; (b) reaction of lysine residues with peptides containing an NHS-ester; and (c) reaction of maleimide-peptides with thiol-free cysteines prior reduction of disulfide bridges. Created using ChemBioDraw.

Lysine bioconjugation is based on the reaction of nucleophiles with carboxylic acids activated with good leaving groups—*e.g.* *N*-hydroxysuccinimide (NHS). These reactions are performed in neutral/mild basic pH since primary amines—like in Lys side-chains—

are good nucleophiles but hydrolysis of NHS-esters in water is still acceptable (half-life of several hours at neutral pH, whereas at pH 8.0 and 8.6 half-life decreases to around 1 h and 10 min, respectively).³⁸⁰⁻³⁸² Lysine residues are abundant in proteins and thus it is likely to produce a variety of modifications that may not influence excessively the viability (infectivity) of HSV-1 particles. In addition, bioconjugation can be carried out in a single step if the peptide is synthesized containing an NHS-ester (**Figure 4.16b**).

A common issue is present in all these strategies: the BBB shuttle peptide could be hidden by the surrounding proteins or even by the conformation of the envelope lipid bilayer/ glycoprotein forming spikes (8 – 24 nm).³⁸³ We therefore added a spacer between the peptide and the reactive moiety to allow the peptide be more solvent-accessible. Polyethylene glycol (PEG) was selected for this purpose, since it has several key features: (1) water-soluble polymer, (2) FDA approved and (3) non-immunogenic³⁸⁴—although there is controversy on the last point.³⁸⁵ A PEG spacer of an average molecular weight of 3,500 Da (~20 nm) was incorporated in the design (**Figure 4.17**).

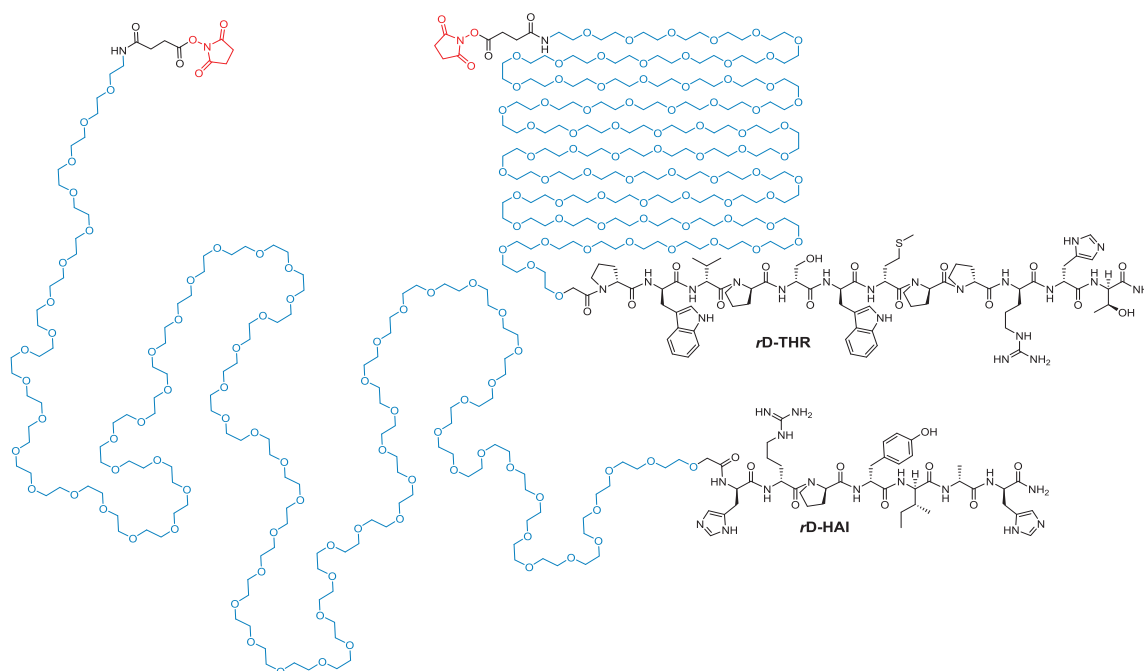


Figure 4.17. BBB shuttle peptide conjugates (NHS-PEG₃₅₀₀-peptide), highlighting NHS in red and PEG₃₅₀₀ in blue. A semi-extended and compressed conformations of PEG are shown for *rD*-HAI and *rD*-THR conjugates, respectively. Created using ChemBioDraw.

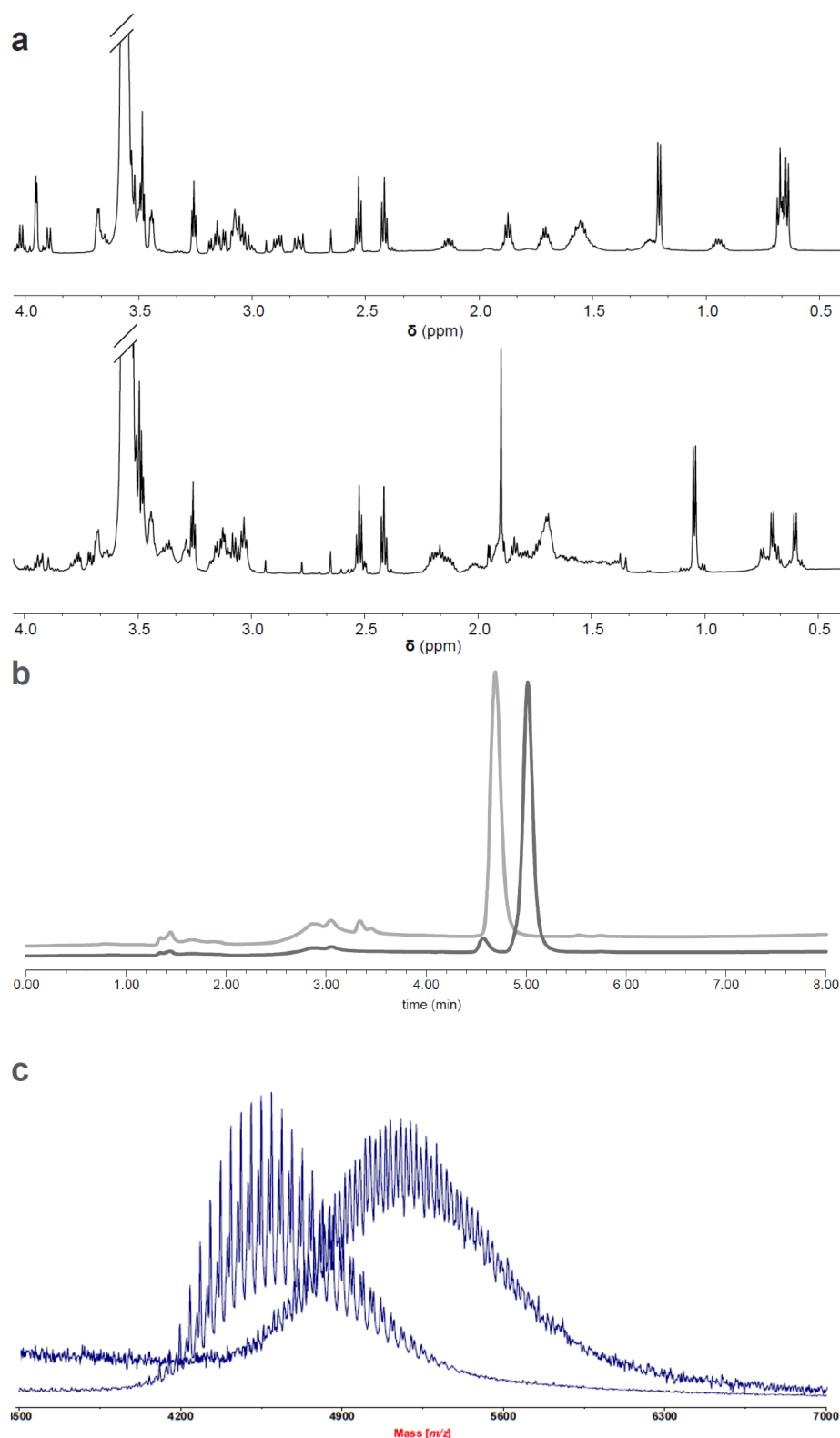


Figure 4.18. Characterization of NHS-PEG₃₅₀₀-rD-HAI and -rD-THR: (a) ^1H -NMR spectrum (top and bottom, respectively), (b) RP-HPLC chromatograms using a C₁₈ column and a linear gradient from 0 to 100% of CH₃CN (light and strong grey, respectively) and (c) MALDI-TOF MS spectra (left and right shifted mass distributions, respectively). Created using Adobe Illustrator and InDesign.

NHS-PEG-peptides were synthesized through Fmoc/*t*Bu SPPS strategy. Briefly, the PEG was incorporated as *N*-protected with Fmoc and *C*-terminated as carboxylic acid (only 1.2 eq.) using PyBOP as coupling agent and DIPEA (2 and 4 eq., respectively) in DMF/DCM 9:1 (v/v) for 3 h. Then, succinic anhydride (4 eq.) was coupled to the *N*-terminus prior deprotection with piperidine. DMAP (8 eq.) was added in DCM/DMF 9:1 and left for 2 h. NHS was then coupled by using 40 eq. using DIPCDI and DMAP (40 and 10 eq., respectively) in DCM/DMF 9:1 for 2 h.^p

These conjugates were always dissolved in 0.1% TFA in H₂O to avoid hydrolysis of the NHS-ester. Purification was performed by semi-preparative RP-HPLC. Purity of conjugates was >95% as observed by analytical RP-HPLC, and their identity was determined by ¹H-NMR and MALDI-TOF MS (**Figure 4.18**). HRMS software was unable to deconvolute the complexity of the diverse *m/z* distributions.

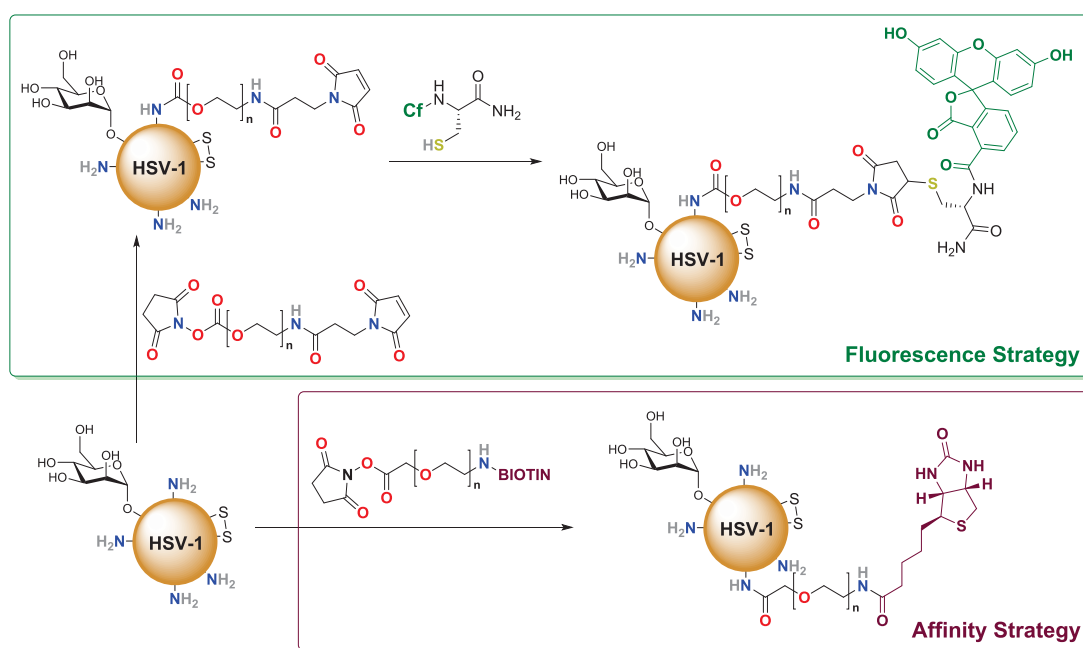


Figure 4.19. Bioconjugation reporter strategies. All reactions were performed in Hank's balanced salt solution (HBSS) at pH 7.4. Created using ChemBioDraw.

At the same time, a reporter molecule was selected. Initially, we envisaged the detection of modified viral particles through a fluorescence reporter (**Figure 4.19**). However, this strategy was not suitable since we were unable to detect any fluorescence signal—although lysates analyzed by SDS-PAGE (see method in **Figure 4.20**) showed less

^p DCM \equiv dichloromethane, DMAP \equiv 4-dimethylaminopyridine, DMF \equiv dimethylformamide, PyBOP \equiv benzotriazol-1-yl-oxytripyrrolidinophosphonium hexafluorophosphate.

staining compared to unmodified sample—and it required to perform two reactions. Thus, we decided to pursue with a new strategy based on affinity detection using a commercial NHS-PEG₃₅₀₀-biotin (**Figure 4.19**). This strategy, in addition to quantification, would also allow the selective capture of modified proteins using streptavidin-coated magnetic nanoparticles and posterior identification by HRMS—affinity selection of proteins coupled to MS (ASMS) (**Figure 4.20**). Nevertheless, several attempts failed, identifying only the streptavidin derived from the magnetic nanoparticles.

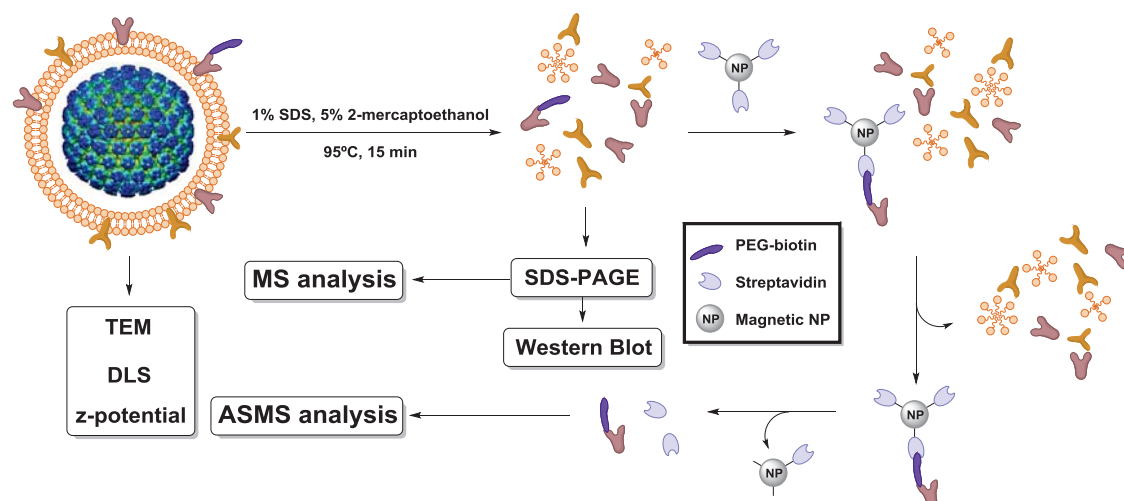


Figure 4.20. Methodologies used for characterization of HSV-1 viral particles: transmission electron microscopy (TEM), dynamic light scattering (DLS) and ζ -potential of native or modified samples; SDS-PAGE, western blot and MS analysis of lysates; and affinity selection of proteins coupled to MS (ASMS). Created using ChemBioDraw, with the structure of HSV-1 C-capsid, EMD ID# EMD-5659.

Other methodologies were used to characterize the native and modified HSV-1 particles (**Figure 4.20**). Lysates were analyzed by SDS-PAGE after treatment under denaturing conditions (1% SDS, 5% 2-mercaptoethanol, at 95°C for 15 min). Silver staining was used to reveal protein bands since sensitivity is higher compared to that obtained using Coomassie blue, which did not result in a band pattern when initially used (sensitivity of Coomassie blue and silver staining is about 0.3–1 μg and 2–5 ng/protein band, respectively).³⁸⁶ Bioconjugation of NHS-PEG-peptide conjugates resulted in a decrease in staining; however, the band pattern of native samples did not change (**Figure 4.21a**), expected upon covalent addition of one or more ~5 kDa molecules (PEG-peptides). The same event was also observed for pure proteins (human transferrin (hTf) and bovine serum albumin (BSA)) modified with NHS-PEG₃₅₀₀-biotin, thus showing that PEG moieties may

interfere during the staining process but also the complexity of the sample increased enormously. This complexity is derived from the combination of three factors: (1) the sample contains several proteins, (2) each bioconjugated protein is likely to be modified in a different residue and (3) the PEG moiety is polydispersed—*e.g.* a sample containing 50 different proteins, each with 10 solvent-accessible lysine residues, modified with a polydispersed PEG with 10 major products would give rise to 5,000 potential products.

Analysis by western blot (WB) using polyclonal antibodies (pAbs) against wild type (WT) HSV-1 revealed a drop in recognition upon bioconjugation (**Figure 4.21a**). This implies a decrease in antigenicity (to be recognized by adaptive immunity, *e.g.* B- or T-cell receptors and Abs), and then probably in immunogenicity (to produce humoral or cell-mediated immune responses)—both interesting features for human therapy. However, this could be driven by highly functionalized proteins that would not have accessible those antigens recognized by antibodies. Modified viral particles were titrated,^q by the group of Prof. Díaz-Nido, and compared with those unmodified (**Figure 4.21b**). The infectivity was preserved. Hence, these modified viruses are less recognized by Abs while at the same time keep the original infectivity.

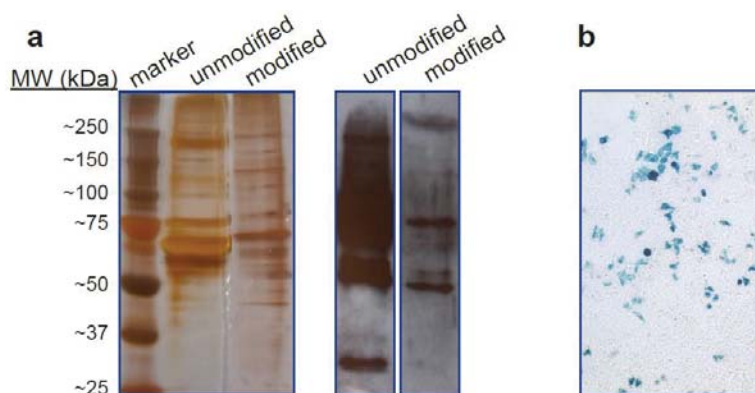


Figure 4.21. Characterization of HSV-1 samples by: (a) SDS-PAGE revealed using silver staining (marker: Precision Plus Protein Dual Xtra Standards, Bio-Rad) and WB using a goat pAb anti-HSV-1 (ab156292, Abcam) and an anti-goat HRP-conjugated secondary Ab (viruses modified using 2,000 eq. of NHS-PEG₃₅₀₀-biotin per viral particle); and (b) infectivity titration of viral particles (transfection of G16-9 cells, X-Gal^r staining and counting of blue cells).^s Created using Adobe InDesign.

^q Briefly, 150,000 G16-9 cells/well were seeded in a 24-well plate and left for 24 h. Then, diverse dilutions of the HSV-1 sample—these viral particles contained pHSVlac, coding for β -galactosidase—were added and left for 48 h. Finally, X-Gal staining (revealing β -galactosidase activity) was performed and blue cells were counted.

^r X-Gal \equiv 5-bromo-4-chloro-3-indolyl- β -D-galactopyranoside.

^s From Iván Fernández-Frías (group of Prof. Díaz-Nido, CBMSO).

Attempts to characterize HSV-1 particles by transmission electron microscopy (TEM) were not successful. We were not able to recognize any viral particle using negative staining; however, immuno-TEM using the same pAb against HSV-1 used in WB and an anti-goat 18-nm gold-conjugated Ab helped in the identification of unmodified HSV-1 particles. Low-resolution images were obtained—we are currently improving these results for both modified and unmodified particles.

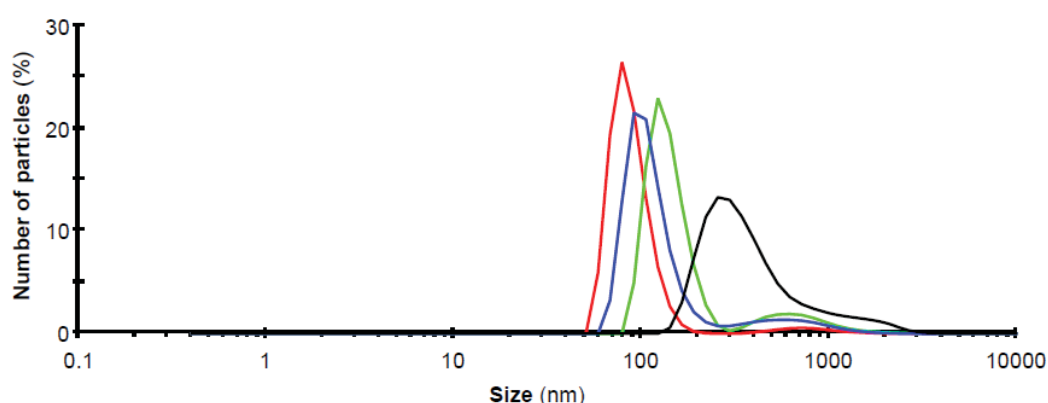


Figure 4.22. Size (nm) distribution per number of particles: (**red**) unmodified sample, and samples (**black**) 1, (**blue**) 2 and (**green**) 3. Created using Adobe Illustrator.

Size-distribution of both bioconjugated or not HSV-1 samples was assessed by dynamic light scattering (DLS). We decided to test diverse reaction conditions using NHS-ester-PEG₃₅₀₀-biotin: (sample 1) adding EDC, (sample 2) adding EDC and concentrating the sample 10-times and (sample 3) without adding EDC but concentrating the sample 10-times.[†] A huge increase in size for sample 1 was observed, whereas samples 2 and 3 maintained roughly the same size distribution (**Figure 4.22**).

Table 4.7. Relationship between reaction conditions and ζ -potential. Bioconjugation reactions were performed using 2,000 eq. of NHS-PEG₃₅₀₀-biotin in HBSS buffer at pH 7.4 for 2 h.

Sample ID	Reaction Conditions		ζ -Potential (mV)
	Relative Conc. ^u	Additional Reagents	
Unmodified	-	-	-11.2 ± 0.2
1	×1	EDC	-10.9 ± 0.5
2	×10	EDC	-15.2 ± 1.1
3	×10	-	-13.7 ± 0.6

[†] EDC ≡ 1-ethyl-3-(3-dimethylaminopropyl)carbodiimide.

^u Concentration of HSV-1 particles: (× 1) ≡ 400 TU/μL; (× 10) ≡ 4,000 TU/μL.

In addition, bioconjugation of these samples was numerically evaluated by means of ζ -potential. Whereas sample 1 maintained the same value as the unmodified particles, samples 2 and 3 showed an increase in the negativity of that parameter (**Table 4.7**). Reaction of NHS-esters made up with no charged moieties (PEG-biotin) may lead to a reduction in the net surface charge, since amino groups (from the side-chains of Lys residues, with a pK_a of ~ 10.0)³⁸⁷ react to form a neutral amide bond. Following this rationale, sample 1 could have suffered a crosslinking process between viral particles (reaction between side-chains containing carboxylic acid and amines promoted by EDC) which may produce the apparent aggregation shown in **Figure 4.22**; whereas concentrated viral samples would be modified with NHS-ester moieties, producing a decrease in the ζ -potential and preserving the same size as the unmodified viruses. In addition, EDC apparently did not produce crosslinking between viral particles.

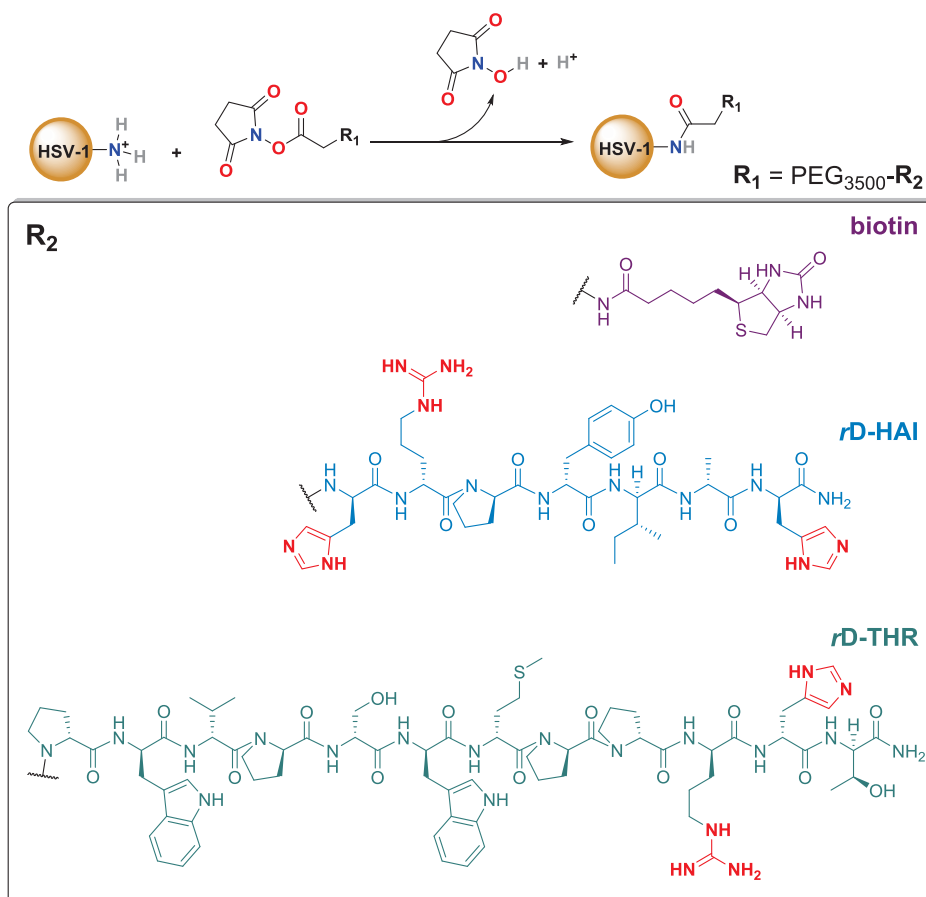


Figure 4.23. HSV-1 bioconjugation at Lys residues. pK_as: Lys (in general, ~10.0;³⁸⁷ however, it depends on solvent exposure and ranges from 5.3 to 10.4),³⁸⁸ Arg (~13.8),³⁸⁹ His (5.8–7.9),³⁹⁰⁻³⁹² NHS (6.0).³⁹³ Created using ChemBioDraw.

We then decided to continue working without adding EDC, since it still produced a ζ -potential shift, whereas we observed side-effects of EDC in sample 1. Contrary to samples modified with NHS-PEG₃₅₀₀-biotin, reaction of viral particles with NHS-PEG₃₅₀₀-*rD*-THR showed a positive increase in ζ -potential (**Table 4.8**). Here, the neutral biotin moiety is replaced by *rD*-THR, which has one positively charged residue (Arg with a very basic pK_a of 13.8)³⁸⁹ and a His residue which might be slightly positive at pH 7.4 (pK_a of 5.8–7.9).³⁹⁰⁻³⁹² Therefore, it was expected to reduce the negative ζ -potential value, although producing a smaller shift (in absolute value) compared with NHS-PEG₃₅₀₀-biotin bioconjugation. Same result can be expected for *rD*-HAI—only positive charges from two His and one Arg residues (**Figure 4.23**).

Table 4.8. Relationship between reaction conditions and ζ -potential. Bioconjugation reactions were performed using 2,000 eq. of NHS-PEG-*rD*-THR in HBSS buffer at pH 7.4 for 2 h.

Sample ID	Reaction Conditions		ζ -Potential (mV)
	Relative Conc.	Additional Reagents	
Unmodified	-	-	-15.8 ± 1.4
Modified	×10	-	-14.5 ± 0.2

Although changes in ζ -potential after bioconjugation shifted consistently in the same direction (negative and positive for NHS-PEG-biotin and NHS-PEG-*rD*-THR, respectively), these results will be confirmed by using radioactive analysis—briefly, labeling NHS-PEG-*rD*-THR with a radioisotope, bioconjugating it to HSV-1 particles and then determining the radioactive signal. In addition, both ζ -potential and radioactive assessment of NHS-PEG-*rD*-HAI will be performed. Finally, *in vivo* studies will be performed to evaluate both infectivity and transport through the BBB—stereotaxic and intravenous injections of modified viral particles, respectively.

The methodology here presented can be used to modify other viral particles, enveloped or not, but also cells—the surface of HSV-1 viruses is more similar to cell surfaces than to viral capsids.^v

^v The complete description of the characterization and bioconjugation performed per each sample is shown in the Experimental Section (Product Characterization).

CONCLUSIONS

1. A hybrid design combining the “gold standard” passive diffusion BBB shuttle (NMePhe)₄ and the water-soluble amino acid proline increases water-solubility by three orders of magnitude—low millimolar range—compared to (NMePhe)₄.
2. The transport of (PhPro)₄ carrying a cargo (NIP and L-DOPA) is around 7-fold higher compared to that of the (NMePhe)₄ shuttle. Furthermore, (PhPro)₄ maintains the permeability when a cargo is attached, whereas (NMePhe)₄ shows a marked reduction.
3. The analysis of the transport of the 16-stereoisomer library revealed that stereochemistry plays a significant role in passive diffusion through biological membranes.
4. Three analogs from the *retro*-D-version of HAI, sharing a substitution in the same proline residue, show a 2-fold increase in transport compared to the parent peptide. Two of them show 4- and 8-fold increase in transport when assayed in cell culture medium instead of buffer.
5. Using a subtle modification (*i.e.* N-terminal acetylation), a novel method combining *in vitro* cell-based BBB models and MALDI-TOF MS allows an increase in sensitivity by three orders of magnitude compared with a standard method (RP-HPLC-PDA), and the use of cell culture medium during these assays.
6. The injection of BBB shuttles made with L-amino acids (HAI and THR) in mice elicit a low immune (humoral) response, which are even lower for their *retro*-D-versions made with D-amino acids.
7. Attempts to bioconjugate the N-terminus of frataxin (FXN) failed due to the lack of stability of the N-terminal region of this protein by proteolytic degradation.

8. The attachment of BBB shuttles on HSV-1 particles using Lys bioconjugation enables the modification of these viral particles in a single step, reducing the sample manipulation and thus preserving their structural integrity better. In addition, the use of PEG₃₅₀₀ as spacer between the virus and the BBB shuttle peptide hampers antibody recognition while preserving infectivity of viral bioconjugates.
9. The combination of methods from molecular biology (SDS-PAGE, western blot) with proteomics (mass spectrometry) and biophysical tools (TEM, DLS and ζ -potential) enables the characterization of the bioconjugated viruses.

EXPERIMENTAL SECTION

Materials and Methods

Solid-Phase Synthesis of Compounds

Reagents and Solvents. Protected amino acids and resins were supplied by Luxembourg Industries (Tel-Aviv, Israel), Neosystem (Strasbourg, France), Calbiochem-Novabiochem AG (Laüfelfingen, Switzerland), PolyPeptide Laboratories (Torrance, CA USA), Bachem AG (Bubendorf, Switzerland), PCAS BioMatrix Inc. (St-Jean-sur-Richelieu, Quebec, Canada) and Iris Biotech (Marktredwitz, Germany). PyBOP, COMU and Oxyma were provided by Calbiochem-Novabiochem AG. Acetic acid-1-¹³C,_{d4} was obtained from Aldrich (Milwaukee, WI, USA). DIEA and ninhydrin were from Fluka Chemika (Buchs, Switzerland). HOAt was purchased from GL Biochem Shanghai Ltd. (Shanghai, China). Solvents for peptide synthesis and RP-HPLC were from Scharlau or SDS (Barcelona, Spain). Trifluoroacetic acid was purchased from KaliChemie (Bad Wimpfen, Germany). The other chemicals used were from Aldrich (Milwaukee) and were of the highest purity commercially available.

General Protocol for SPPS. Standard solid-phase peptide elongation and other solid-phase manipulations were done manually in polypropylene syringes, each fitted with a polyethylene porous disk at the bottom. Solvents and soluble reagents were removed by suction. Between couplings and deprotections, the resin was washed with DMF (5 × 1 min), DCM (5 × 1 min), and DMF (5 × 1 min), using 5 mL of solvent/g of resin each time. During couplings, the syringe was left under automatic stirring. Intermittent manual stirring was applied during deprotections.

In each chapter of this thesis the syntheses were performed using diverse resins and coupling conditions, here specified.

Identification Tests. After each reaction, the Kaiser test³⁹⁴ was used to identify primary amines on the *N*-terminus of the elongating peptide on the solid support. The chloranil test³⁹⁵ was used to identify secondary amines.

Initial Conditioning of Resin. The Sieber Amide and Fmoc-Rink-Amide AM resins were conditioned by washing with DMF (5 × 1 min), DCM (5 × 1 min), and DMF (5 × 1 min), followed by 20% piperidine in DMF (1 × 1 min, 2 × 10 min) to remove the Fmoc group. Finally, resins were washed with DMF (5 × 1 min). H-Rink Amide-ChemMatrix resin was conditioned by washing with CH₃OH (5 × 1 min), DMF (5 × 1 min), DCM (5 × 1 min), 1% TFA in DCM (5 × 1 min), DCM (5 × 1 min), DMF (5 × 1 min), DCM (5 × 1

min), 5% DIPEA in DCM (5×1 min), DCM (5×1 min) and finally DMF (5×1 min). The resins used in each chapter of this thesis are specified below:

Chapter	Resin
1	Sieber ³⁹⁶ Amide
2	Fmoc-Rink-Amide AM ^{394,395}
3	H-Rink ³⁹⁷ Amide-ChemMatrix
4	H-Rink Amide-ChemMatrix, and Dawson Dbz AM resin ³³⁵

Fmoc Group Removal. Fmoc group was removed by treating the resin with 20% piperidine in DMF (3–4 mL/g of resin; 1×1 min, 2×10 min). For secondary amine Fmoc deprotection, resin was additionally treated with DBU, toluene, and piperidine in DMF (5:5:20:70, v/v) (1×10 min).

Coupling of the First Amino Acid onto the Resin and Following Couplings. For the syntheses of HAI analogs, were added sequentially to the resin in DMF (minimal volume to allow the complete dissolution of the reagents), with the appropriate coupling reagents. The mixture was allowed to react under stirring in an orbital shaker for 1 h. Afterwards, the solvent was removed by filtration, and the resin was washed with DMF (5×1 min) and DCM (5×1 min). The extent of coupling was checked by the appropriate colorimetric test. When required, a recoupling step was performed using the same previous conditions but for longer (2 h).

Chapter	Coupling Conditions
1	<i>N</i> -protected Fmoc-amino acid, Fmoc-NIP-OH or Fmoc-L-DOPA-OH (4 eq.), PyBOP (4 eq.) and HOAt (12 eq.), followed by DIPEA (12 eq.)
2	<i>N</i> -protected Fmoc-amino acid (4 eq.), COMU ³⁹⁸ (4 eq.), and Oxyma Pure ³⁹⁹ (4 eq.), followed by DIPEA (8 eq.).
3	<i>N</i> -protected Fmoc-amino acids (4 eq.) were activated by Cl-HOBt ⁴⁰⁰ (4 eq.) with DIPCDI (4 eq.)
4	<i>N</i> -protected Fmoc-amino acids (4 eq.) or Boc-(aminooxy)acetic acid (for AO-peptides) were activated by Cl-HOBt (4 eq.) with DIPCDI (4 eq.) for the couplings on H-Rink Amide-ChemMatrix resin, as well for the second and subsequent couplings on Dawson Dbz AM resin <i>N</i> -protected Fmoc-amino acids (4 eq.) were activated by HBTU/HOBt (6 eq.) with DIPEA (9 eq.) for the first coupling on Dawson Dbz AM resin

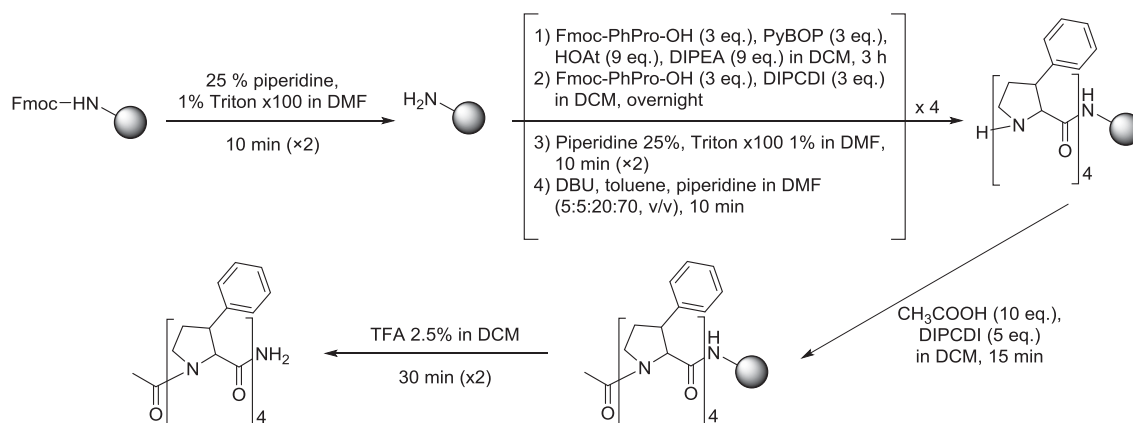
N-Terminal Capping. The anhydride of the acetic acid (4 eq.) was prepared by mixing acetic acid (8 eq.) with DIPCDI (2:1) and adding 1 mL of DCM. Two minutes of agitation was applied. Afterwards, the solvent was added to the SPPS syringe, and the precipitate (*N,N'*-diisopropylurea) was discarded. DCM was added until all the resin was covered, and DIPEA (4 eq.) was then added. After 30 min with stirring in the orbital shaker, the solvent was removed by filtration, and the resin was washed with DCM (5×1 min), DMF (5×1 min) and DCM (5×1 min). The extent of coupling was checked by the appropriate colorimetric test.

Peptide Cleavage. In order to cleave the peptides from the resin, the cleavage cocktail (TFA/TIS/H₂O, 95:2.5:2.5, v/v; except for peptides synthesized in chapter 1, where TFA/DCM, 2.5:97.5, v/v was used) was added to each syringe. Intermittent manually agitation was applied for 30–60 min. The solvent was collected in the same plastic tube and evaporated by a N₂ flow.

Work-Up. After evaporation of the cleavage cocktail, 20 mL of methyl *tert*-butyl ether (MTBE) was added to the plastic tube containing the dry residue. This tube was centrifuged at $2,000 \times g$ for 10 min. The solvent was then discarded by decantation. This process was repeated two more times. After the last washing with MTBE, the final residue was dissolved in H₂O/CH₃CN (1:1) and then lyophilized.

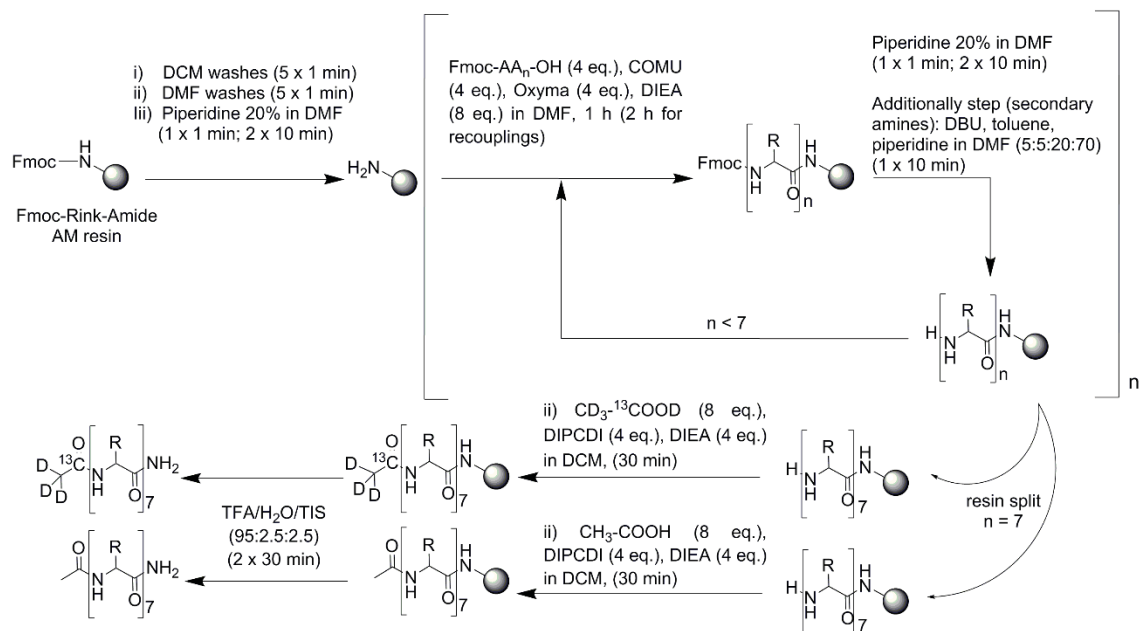
Special Considerations. For the synthesis of the 16 stereoisomers of (PhPro)₄, resin was placed in *tea bags*, which were labeled and then heat-sealed, according to the procedure developed by Houghten and coworkers (1985).¹⁶⁷ Solvents were removed by decantation after taking the *tea bags* out of the reaction pot. Washings between synthetic steps were done with DMF (2×1 min), isopropanol (1×1 min), DMF (2×1 min), using a solvent volume that covered the bags entirely. In order to use the same solvent for washing steps as in the synthetic steps, an initial or final washing with DCM (2×1 min) was performed. During couplings the mixture was allowed to react with continuous stirring. One pot was used per type of coupling/deprotection/colorimetric test. The colorimetric test was done using a pH indicator, bromophenol blue.^{401,402} After deprotections and couplings, 1 drop of 1% bromophenol blue in DMF was placed in the DMF volume containing the *tea bags*. A positive result is given by an intense blue staining of the resin, which results from the free amines occurring in the growing peptide (higher pH) after a decoupling step. The lack of resin staining (natural color of the resin under DMF solvation) is due to the absence of free

amines, expected after a coupling step. The Fmoc group was removed by treating the resin with 25% piperidine and 1% Triton x100 in DMF (using the minimal volume to cover all *tea bags*; 2×10 min). In all cases, resin was additionally treated with DBU, toluene, and piperidine in DMF (5:5:20:70, v/v) (1×10 min). A diagram of the synthetic strategy for the 16 stereoisomers of (PhPro)₄ is shown in **Scheme M.1**.



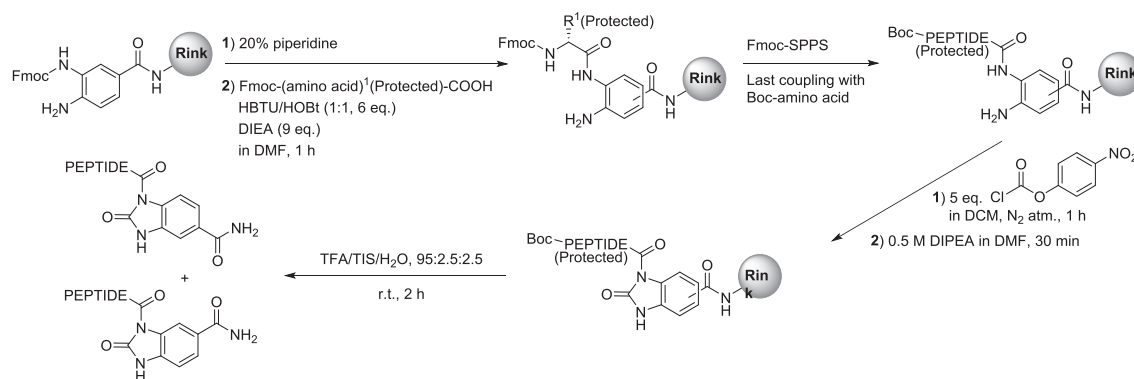
Scheme M.1. Synthetic strategy for the 16 stereoisomers of (PhPro)₄.

A diagram of the synthetic strategy for HAI analogs is shown in **Scheme M.2**. Importantly, each peptide was differentially acetylated using CD₃-¹³COOD or CH₃-COOH.



Scheme M.2. Strategy for the synthesis of the complete set of HAI analogs with a final splitting step that allows differential isotopic labeling by means of acetylation.

Peptides-Nbz were synthesized following a Fmoc-SPPS approach reported by Blanco-Canosa *et al.*,³³⁵ where first diaminobenzoic acid (Dbz) is incorporated in a resin terminated with a Rink linker. After the standard SPPS synthesis, the C-terminus is activated through acylation with *p*-nitrophenylchloroformate followed by the addition of a base. The peptide-Nbz is finally deprotected and cleaved by TFA treatment with scavengers (**Scheme M.3**).



Scheme M.3. Scheme for the synthesis of Nbz-peptides. Created using ChemBioDraw.

NHS-PEG-peptides were synthesized through Fmoc/*t*Bu SPPS strategy. PEG was incorporated as *N*-protected with Fmoc and *C*-terminated as carboxylic acid (Fmoc-PEG₃₅₀₀-COOH; JenKem Technology USA, Plano, TX, USA), using only 1.2 eq.; PyBOP and DIPEA (2 and 4 eq., respectively) were added and the reaction was then left in DMF/DCM 9:1 (v/v) for 3 h with continuous stirring. Then, succinic anhydride (4 eq.) was coupled to the *N*-terminus prior desprotection with piperidine (1 × 1 min and 2 × 15 min). DMAP (8 eq.) was added in DCM/DMF 9:1 and left for 2 h with continuous stirring. NHS was then coupled by using 40 eq. and, DIPCDI and DMAP (40 and 10 eq., respectively) in DCM/DMF 9:1 for 2 h. Finally, the resin was cleaved with TFA/TIS/H₂O for 2 h, and lyophilized in H₂O/CH₃CN prior evaporation with N₂ flow.

Peptide and Amino Acid Purification and Characterization

RP-HPLC Purification. The peptides were purified by reverse-phase HPLC using a Sunfire C₁₈ column (150 × 10 mm × 5 μm, 100 Å; Waters, Milford, CT, USA); solvents: H₂O (0.1% TFA) and CH₃CN (0.1% TFA); and flow rate of 3 mL/min. Fmoc-PhPro-OH amino acid enantiomers were separated using a chiral Lux Cellulose-2 column (150 × 21.2 mm, 5 μm, 1,000 Å, cellulose tris(3-chloro-4-methylphenylcarbamate) stationary phase; Phenomenex Inc., Torrance, CA, USA); solvents: CH₃OH and CH₃CN (0.1% TFA); and flow rate of 3 mL/min.

General Characterization. Compound identity was confirmed using MALDI-TOF MS (Applied Biosystems 4700 MALDI-TOF spectrometer; PE Applied Biosystems, Foster City, CA, USA), RP-HPLC-MS (Alliance 2796 with photodiode array (PDA) detector 2998, ESI-MS model Micromass ZQ and Masslynx version 4.0 software; Waters) and HRMS in a Synapt HDMS (Waters) or LTQ-FT Ultra (Thermo Scientific, Waltham, MA, USA). Peptide purity was checked by RP-HPLC (Alliance 2695 with PDA detector 2998 and software EmpowerPro 2; Waters) using a Sunfire C₁₈ column (150 × 4.6 mm × 5 μm, 100 Å, Waters); solvents: H₂O (0.045% TFA) and CH₃CN (0.036% TFA); flow rate of 1 mL/min.

The purity of the Fmoc-PhPro-OH enantiomers was checked by RP-HPLC using a chiral Lux Cellulose-2 column (150 × 4.6 mm analytical, 5 μm, 1,000 Å, cellulose tris(3-chloro-4-methylphenylcarbamate) stationary phase; Phenomenex Inc.); solvents: CH₃OH and CH₃CN (0.1% TFA); and flow rate of 1 mL/min.

Additionally, ¹H-NMR (600 MHz) experiments confirmed the identity and purity of the set of pure HAI analogs (as well the proper isotopic labeling between pairs of peptides (either acetylated with acetic acid or with acetic acid-1-¹³C,d₄)) and of PEG-peptide conjugates. Samples were prepared by dissolving peptides or PEG-peptide conjugates in H₂O/ D₂O 80:20 (v/v) or D₂O, respectively. Suppression of the water signal was achieved by WATERGATE W5.⁴⁰³ For PEG-peptide conjugates, d1 = 10 s was used. All experiments were performed at 298 K.

Specific Rotation. Specific rotation of the PhPro amino acid enantiomers was determined with the polarimeter P-2000 (Jasco, Easton, MD, USA). Cells with a pathlength of 1 dm were used. The parameters used during measurements were as follows:

accumulations (3), and wavelength (589 nm). Samples were dissolved in CH₃OH at a final concentration of 0.0008 g/mL. The values of α_D were calculated as shown in **Eq. M.1**:

$$\alpha_D = \frac{\alpha}{l \cdot c} \quad (\text{M.1})$$

where α is the value returned by the instrument, l is the pathlength, c is the concentration, and α_D is the specific rotation.

Amino Acid Analysis. Peptide content and amino acid ratio were determined by chromatographic separation and quantification of the hydrolyzed product. Peptide samples were hydrolyzed in 6 M HCl at 110°C for 16 h. The solvent was then evaporated to dryness under reduced pressure. The residue was dissolved in 20 mM HCl and derivatized using the AccQ·Tag protocol (Waters) using 6-aminoquinolyl-*N*-hydroxysuccinimidyl carbamate. Finally, samples were analyzed by HPLC.

Water-Solubility. Solubility of peptides was determined by weighing an amount of the peptide in a vial and dissolving it in a certain volume of water, taking care to ensure saturation. The vials were then left for 1 h at 37°C under soft agitation. Afterwards, they were left for 20 min at room temperature and centrifuged to precipitate any non-dissolved particle. From that solution, a volume (not higher than 70% of the total volume) was passed through a 400- μ m filter and moved to a weighed glass vial. Finally, the vials were lyophilized for one day and weighed. Solubility was calculated as the difference of mass between the glass vials with and without peptide divided by the volume taken.

Structural Data

Circular Dichroism. Circular dichroism spectra were obtained with a J-715 or an 810 UV-Vis spectropolarimeter (Jasco), with a Peltier CDF 426S/426L. Parameters used: sensitivity (standard (100 mdeg)), start (250 nm), end (190 nm), data pitch (0.1 nm), scanning mode (continuous), scanning speed (10 nm/min), response (4 sec), band width (1.0 nm), and accumulation (3). Molar ellipticity was calculated using the **Eq. M.2**:

$$\theta_{MR} = \frac{\theta}{10 \cdot l \cdot C \cdot n} \quad (\text{M.2})$$

where θ_{MR} is the molar ellipticity in $\text{deg} \cdot \text{cm}^2 \cdot \text{dmol}^{-1}$, θ is the measured ellipticity value in mdeg, l is the optical path in cm, C is the concentration of the peptide/protein in mol/L, and n is the number of residues in the peptide/protein.

NMR. NMR experiments were performed on a Bruker Avance III 600 MHz spectrometer equipped with a TCI cryoprobe. Samples were prepared by dissolving peptides (5 mM) in 50 mM NaCl, 25 mM sodium phosphate buffer, H₂O/D₂O 90:10, at pH 7.4, containing 0.02% NaN₃. Chemical shifts were referenced to internal sodium-3-(trimethylsilyl)propanesulfonate (DSS). Water signal suppression was achieved by excitation sculpting⁴⁰⁴. Residue specific assignments were obtained from 2D total correlated spectroscopy (TOCSY) and correlation spectroscopy (COSY) experiments, while 2D nuclear Overhauser effect spectroscopy (NOESY) permitted sequence specific assignments. ¹³C resonances were assigned from 2D ¹H-¹³C HSQC spectra. All experiments were performed at 298 K, except NOESY spectra, which were acquired at 278 K. Amide proton temperature coefficients were determined from a series of one-dimensional spectra acquired between 278 and 308K. TOCSY and NOESY mixing times were 70 and 250 ms, respectively. Relative populations of the *cis/trans* isomers were estimated from integration of amide protons in the 1D ¹H-NMR spectra or alternatively, when ¹H integration was precluded by signal overlap, from the relative intensities of ¹H-¹³C-HSQC crosspeaks corresponding to the Pro C δ resonances. In those cases that ¹H integration was possible, both methods provided identical results.

Protease-Resistance in Human Serum. Peptides at a final concentration of 150 μM in Hank's balanced solution salt were incubated at 37°C in the presence of 90% human serum (from human male AB plasma). At pre-established time points, aliquots of 200 μL were extracted, and serum proteins were precipitated by addition of 200 μL of acetonitrile

at 4°C to stop degradation. After 30 min at 4°C, samples were centrifuged at 10,000 rpm for 30 min at 4°C. The supernatant was analyzed by RP-HPLC and MALDI-TOF mass spectrometry.

Computational Analysis of the Peptide Conformations. The preferential conformation adopted by each peptide system was evaluated by replica exchange molecular dynamics Simulations (REMD).⁴⁰⁵ Simulations started from a linearly extended peptide conformation built with XLEaP program module from the AMBER14 molecular mechanics package.⁴⁰⁶ The Amber ff99SB force field, together with the reoptimized proline omega-bond angle parameters,⁴⁰⁷ was used. The initial extended peptide structure was first subjected to minimization protocol consisting of 1,000 steps of steep decent method followed by 500 steps of conjugate gradient method. Optimized structures were gradually heated to 300 K in 200 ps. The final state was chosen as the initial structure for all the 16 replicas. Temperatures were set in a range from 300 to 500 K.⁴⁰⁸ Generalized Born model⁴⁰⁹ with an effective salt concentration of 0.2 M was deployed to mimic the solvation effect. Nonpolar solvation term was approximately represented by surface area term.⁴¹⁰ Integral time step was set to 1 fs. Temperature was regulated using Berendsen thermostat⁴¹¹ with a coupling time constant of 1 ps. SHAKE algorithm⁴¹² was used to constrain all the covalent bonds involving hydrogen atoms. Swaps between replicas were attempted every 2 ps, and ~35% acceptance probability was obtained. Each replica was simulated during 150 ns. Snapshots were saved every 2 ps. To evaluate the degree of overlap between parent peptides and their *retro-D*-version forms, a non-symmetric RMSD distance matrix was built using the ptraj module of the Amber package. To preserve the correct alignment between the parent peptide and their *retro-D*-version, distances were computed between analog amino acids (*i.e.*, the *N*-terminal amino acid of the parent peptide corresponds to *C*-terminal amino acid in its *retro-D*-version, and *vice versa*). The resulting RMSD matrix, composed of 1,000 equally spaced snapshots of the equilibrated part (100 ns) of the parent peptide and of its *retro-D*-version, was subjected to histogram analysis. R software⁴¹³ was used in all statistical analyses. Additionally, 2D RMSD plots (mass weighted) for the same 1,000 equally spaced snapshots of each simulation were computed to visually determine the number of clusters visited by each peptide system during the replica exchange simulation. In order to further compute the similarity between the conformational space sampled by the trajectories of the parent peptide and *retro-D*-version, essential dynamics techniques^{414,415} were used.

In Vitro Assays

Parallel Artificial Membrane Permeability Assay (PAMPA): The PAMPA assay was used to determine passive diffusion capacity across the BBB. The standard parameter that quantifies transport independently of time and concentrations is the effective permeability (P_e), shown in the **Eq. M.3**:

$$P_e = \frac{-218.3}{t} \text{Log} \left(1 - \frac{2C_A(t)}{C_D(t_0)} \right) \cdot 10^{-6} \text{cm/s} \quad (\text{M.3})$$

where t is the running time (4 h), $C_A(t)$ is the concentration of the compound in the acceptor well at time t , and $C_D(t_0)$ is the compound concentration in the donor well before running the PAMPA assay ($t_0 = 0$ h). Transport (%) values were obtained by dividing the amount in the acceptor well at time t , $C_A(t)$, and in the donor well at time zero, $C_D(t_0)$, multiplied by 100. Membrane retention was calculated from the difference between the initial amount, $C_D(t_0)$, and the amounts in donor, $C_D(t)$, and acceptor, $C_A(t)$, compartments at the end of the experiment ($t = 4$ h).

The buffer (System Solution) was prepared from the commercial concentrated solution from pION (Woburn, MA, USA) by dissolving 5 mL with 200 mL of water. The pH (2.4) was adjusted to 7.4 by using a 0.5 M NaOH solution. Then, 1-propanol (20%) was added to the solution.

The samples were dissolved with the System Solution containing 20% 1-propanol (1 mL). Peptides were assayed at concentrations adjusted to allow the best quantification by RP-HPLC. Propranolol was used as a positive control.

The PAMPA sandwich (96-transwell plate, pION) was separated into the donor and acceptor plates, and the stirring magnets were added to the donor compartments. Next, 4 μL of a phospholipid mixture supplied by Avantis Polar Lipids (Alabaster, AL, USA) (porcine brain polar lipid extract; 20 mg/mL in dodecane) was added to the membrane, located at the bottom of the acceptor compartments. This phospholipid mixture comprised phosphatidylcholine (PC; 12.6%), phosphatidylethanolamine (PE; 33.1%), phosphatidylserine (PS; 18.5%), phosphatidylinositol (PI; 4.1%), phosphatidic acid (0.8%), and other compounds (30.9%).

Samples containing the peptides (195 μL) were added to the donor compartments, (three replicates). Afterwards, acceptor wells were placed above the donor plate and filled with 200 μL of System Solution (20% 1-propanol).

The PAMPA plate was placed into a GUTBOX (containing wet sponges) for 4 h at room temperature. Agitation was maintained in 25 μm of unstirred water layer (UWL). After the incubation time, the donor and the acceptor plates were separated, and the samples were collected from both and placed into separate tubes. The integrity of the samples (donor and acceptor wells and time zero solutions) was identified by MALDI-TOF spectroscopy. The samples were also analyzed by RP-HPLC, and P_e was calculated from the integrated chromatographic peaks.

***In Vitro* Bovine BBB Cell-Based Model Assay.** This assay was an adapted model⁸⁴ of the method previously published by Gaillard and de Boer.⁴¹⁶ Bovine brain endothelial cells were purchased from Cell applications (San Diego, CA, USA), and astrocytes were obtained from rat pups (Wistar rats from Charles River, Wilmington, MA, USA). Before performing the assay, TEER was measured in all transwells (TEER > 100 $\Omega\cdot\text{cm}^2$). Transwell plates (Corning Costar 24-well plate, 0.33 cm^2 membrane well insert and 0.4 μm pore size) were purchased from Corning (Corning, NY, USA). Peptides were prepared at a concentration of 200 μM in Ringer-HEPES buffer containing 20 μM Lucifer yellow (LY) lithium salt (Sigma-Aldrich) as control ($P_{\text{app}} < 17 \cdot 10^{-6} \text{ cm/s}$). The apical compartment was filled with 200 μL of the solution containing the peptide, and 800 μL of Ringer-HEPES was poured into the basal well. Three replicates of each peptide were assayed. The plate was left for 2 h in the incubator at 37°C. Finally, the samples were collected and analyzed or frozen until analysis. LY fluorescence was measured in a 96-well plate with a Fluoroskan Ascent Microplate Fluorometer (Thermo Fisher Scientific).

Finally, in order to evaluate the *in vitro* transport of the peptides, two parameters were determined, namely transport (T), expressed as a percentage, and apparent permeability (P_{app}), described by **Eq. M.4** and **M.5**, respectively.

$$T = \frac{Q_A(t)}{Q_D(t_0)} \times 100 (\%) \quad (\text{M.4})$$

$$P_{\text{app}} = \frac{dQ_A(t)}{dt} \frac{1}{A} \frac{1}{Q_D(t_0)} V_D \approx \frac{Q_A(t)}{t} \frac{1}{A} \frac{1}{Q_D(t_0)} V_D = \frac{V_D}{t} \frac{1}{A} \frac{Q_A(t)}{Q_D(t_0)} = \frac{V_D}{t} \frac{1}{A} \frac{T}{100} (\text{cm/s}) \quad (\text{M.5})$$

where, $Q_A(t)$ is the amount (mass or mole) of peptide in the acceptor well at the end of the experiment (at time t); $Q_D(t_0)$ accounts for the amount of peptide initially evaluated (in the donor well at time $t = 0$). $\frac{dQ_A(t)}{dt}$ is the permeability rate of the peptide; A is the area (in cm^2) of the membrane delimiting the two wells, donor and acceptor; V_D is the volume in the donor well (in cm^3); and t is the time length of the experiment (2 h) in seconds. $Q_A(t)$ and $Q_D(t_0)$ values were obtained from those recorded by RP-HPLC-PDA (220 nm) and MALDI-TOF MS, and thus these two equations are adapted in each case (see next section). The apparent permeability was obtained from the transport (T) values expressed in percentage (shown in the last step of **Eq. M.5**).

***In Vitro* Human BBB Cell-Based Model Assay.** This assay was performed using the model published by Prof. Cecchelli in 2014.⁴¹⁷ Endothelial cells and pericytes were defrosted in gelatin-coated Petri dishes (Corning). Pericytes and endothelial cells were cultured in DMEM pH 6.8 or in supplemented endothelial cell growth medium (Sciencells), respectively. After 48 h, pericytes (50,000 cells/well) and endothelial cells (80,000 cells/well) were seeded in gelatin-coated 12-well plates or in Matrigel-coated 12-well transwell inserts, respectively. Transwell plates (Corning Costar 12-well plate, 1.13 cm^2 membrane well insert and 0.4 μm pore size) were purchased from Corning. BD matrigel matrix was from Corning. Medium (endothelial cell medium, ECM from Innoprot, Derio, Spain) was changed every 2–3 days and assays were performed 7–8 days after seeding. Lucifer Yellow (50 μM) was used as internal control ($P_{app} < 15 \cdot 10^{-6} \text{ cm/s}$). LY fluorescence was measured in a 96-well plate with a Fluoroskan Ascent Microplate Fluorometer (Thermo Fisher Scientific).

Compounds were dissolved in Ringer-HEPES at a concentration of 200 μM . Then, 500 μL of the compound and 1,500 μL of Ringer-HEPES alone were introduced in the apical or in the basolateral compartments, respectively. The plates were set on at 37 $^\circ\text{C}$ for 2 h. The solutions from both compartments were then recovered and quantified by HPLC and identified by MALDI-TOF.

RP-HPLC Coupled to PDA Quantification. This method determined peptide transport by applying the ratio between the peak areas integrated in the chromatograms from the acceptor and donor wells further correction by the injected volumes and those contained in each well (**Eq. M.4** and **M.6**).

$$T = \frac{Q_A^I(t)}{Q_D^I(t_0)} \times \frac{V_D^I}{V_A^I} \times \frac{V_A^W}{V_D^W} \times 100 (\%) \quad (\text{M.6})$$

where $Q_A^I(t)$ and $Q_D^I(t_0)$ account for the integrated area in the HPLC chromatograms of acceptor (at time $t = 2\text{h}$) and donor (at time $t_0 = 0$) wells, respectively; V_D^I and V_A^I are the injected volumes from donor and acceptor wells, respectively; and V_A^W and V_D^W are the volumes in each acceptor and donor well, respectively.

MALDI-TOF MS Quantification. Quantitative MS data were recorded on an Applied Biosystems 4800 Plus MALDI-TOF spectrometer, using an ACH-based matrix.

Transport quantification by MALDI-TOF MS was performed by mixing 10 μL of the sample of the *in vitro* cell-based model and another 10 μL from the heavy peptide as internal standard at a similar concentration as the light one. Then, 1 μL of this mixture was placed on the MALDI plate, together with 1 μL of the freshly prepared solution of the selected matrix (ACH). This MALDI matrix was prepared by dissolving 15 mg of α -cyano-4-hydroxycinnamic acid (ACH) in 1 mL of $\text{H}_2\text{O}/\text{CH}_3\text{CN}$ 1:1 (v/v) containing 0.1% TFA. MS spectra were recorded and transport was calculated. This parameter was obtained from the intensity ratios *light/heavy* for acceptor and donor wells further corrected by the volumes of each well (detailed in **Eq. M.7**).

$$T = \frac{Q_A^{\text{Light}}(t)/Q^{\text{Heavy}}}{Q_D^{\text{Light}}(t_0)/R \times Q^{\text{Heavy}}} \times \frac{V_A^W}{V_D^W} \times 100 (\%) \quad (\text{M.7})$$

$Q_A^{\text{Light}}(t)/Q^{\text{Heavy}}$ accounts for the relative amount of the light peptide in the acceptor well (at time t) compared with a prepared dilution of the heavy isomer (at 2 μM). $Q_D^{\text{Light}}(t_0)/R \times Q^{\text{Heavy}}$ determines the relative amount of light peptide in donor well (at time $t = 0$) compared with a prepared dilution of the heavy isomer (at 200 μM ; *i.e.* in our case $R = 100$).

RP-HPLC-PDA Limit of Quantification. Dilution series for three peptides 1L (HAI), 6D (*retro*-D-HAI) and 9D, ranging from 200 μM to 1.1 nM, were analyzed by RP-HPLC-PDA. An initial solution at 200 μM was consecutively diluted 1/3 by mixing 100 μL in 200 μL of H_2O , up to a total of eleven dilutions. Finally, a specific volume of the sample, ranging from 5 to 100 μL , was injected to the HPLC system and then further analyzed to determine the limit of quantification. First, the total absorption corrected by the injected volume and dilution (R_i) was determined as:

$$R_i = \frac{A \times d}{V} \quad (\text{M.8})$$

where, A , V and d are the total absorption area, the absorption area, the injected volume and the fold-dilution, respectively. Then, the R_{LOQ} was determined for all of them:

$$R_{LOQ} = \frac{R_i - \bar{R}}{\bar{R}} = \frac{R_i}{\bar{R}} - 1 \quad (\text{M.9})$$

where, \bar{R} is the mean (*i.e.* $\bar{R} \equiv \sum_i^n \frac{R_i}{n}$; last five dilutions discarded). The deviation (%) is calculated as $R_{LOQ} \times 100$.

MALDI-TOF MS Limit of Quantification. Dilution series for three peptides 1L (HAI), 6D (*retro*-D-HAI) and 9D, ranging from 200 μM to 1.1 nM, were analyzed by MALDI-TOF MS (on an Applied Biosystems 4800 Plus MALDI-TOF spectrometer, using an ACH-based matrix). The initial dilution was prepared by mixing 20 μL of two solutions containing 400 or 800 μM of the light or heavy versions of the peptide, respectively. Consecutive dilutions 1/3 were then prepared by mixing 10 μL in 20 μL of H_2O . Finally, 1 μL of the sample and 1 μL of the ACH matrix were placed in a MALDI plate. The spectra were acquired and further analyzed to determine the limit of quantification. First, the experimental light/heavy ratio was determined for all the dilutions. The R_{LOQ} was then determined for all of them:

$$R_{LOQ} = \frac{R_i - \bar{R}}{\bar{R}} = \frac{R_i}{\bar{R}} - 1 \quad (\text{M.10})$$

where, R_i and \bar{R} are the light/heavy ratio of each sample and the mean (*i.e.* $\bar{R} \equiv \sum_i^n \frac{R_i}{n}$, discarding the last dilution value), respectively. The deviation (%) is calculated as $R_{LOQ} \times 100$.

Protein Expression, Purification, Bioconjugation and Characterization

Plasmid Constructs. The plasmids pOPINS-Gly-FGEsite-FXN, pOPINS-Gly-Lys-FXN and pOPINS-Cys-FXN used were generated in the IRB Protein Expression Core Facility.

Expression. Protein expressions were performed by the IRB Protein Expression Core Facility. Co-expression of the frataxin fusion protein (HisTag-SUMO-Gly-FGEsite-FXN¹⁻²¹⁰) with formylglycine-generating enzyme (FGE) was performed as described by Bertozzi and co-workers.³³⁸ MGSSH₆-SUMO-GlyLys-FXN and MGSSH₆-SUMO-Cys-FXN were expressed in auto-induction⁴¹⁸ conditions in B834(DE3) cells. Briefly, a single colony containing the appropriate plasmid was cultured overnight in 10 mL of Overnight Express Terrific Broth (Merck, Darmstadt, Germany) with kanamycin and 1% glucose (w/v) at 37°C. The overnight culture is diluted into 2 L of Overnight Express Terrific Broth and 500 mL are placed in 2 L shake-flasks and incubated at 37°C with orbital shaking for 4h. The temperature is then decreased to 25°C and cultures are left for 24 h more. The cultures are pelleted by centrifugation using a rotor JLA-8.1000 (Beckman Coulter, Pasadena, CA, USA) at $8,000 \times g$ for 20 min. The cell pellets are then frozen at -80°C or re-suspended in 30 mL of cell lysis buffer (50 mM Tris at pH 7.5, 500 mM NaCl, 20 mM imidazole and 0.2% Tween; supplemented with protease inhibitor tablets (Complete EDTA, Roche Diagnostics, Indianapolis, IN, USA) and DNase I) per 10 g of sample. Samples are passed through the basic Z cell disruptor (Constant Systems Ltd., Daventry, United Kingdom) at 20 Kpsi and centrifuged at $30,000 \times g$ for 30 min at 4°C. The cleared lysate is ready for purification.

Purification. Three purification procedures were performed using an ÄKTAexplorer (GE Healthcare) fast protein liquid chromatography (FPLC) system: immobilized metal affinity chromatography (IMAC) and reverse-IMAC both using a 5 mL HiTrap HP column (GE Healthcare, Little Chalfont, United Kingdom) and size-exclusion chromatography (SEC) using a HiPrep 26/10 Desalting column (GE Healthcare). Samples (cleared lysates) were loaded into the IMAC column pre-equilibrated with 50 mM NaH₂PO₄ at pH 8.0, 300 mM NaCl, 20 mM imidazole with 0.02% Tween, washed with 50 mM Tris at pH 8.0, 500 mM NaCl, 40 mM imidazole, and eluted in the same buffer with 300 mM imidazole Tween. Fractions containing the correct protein construct were diluted with five parts of 20 mM Tris at pH 8.0, 200 mM NaCl, 1 mM EDTA, and supplemented with protease inhibitor

tablets (Complete EDTA, Roche Diagnostics). SUMO protease was then added at a SUMO:SUMO-FXN construct ratio of 1/50 (w/w) and left overnight at 4°C. Sample was incubated in 100 mM EDTA and 0.1 mM TCEP for 4 h. It was then buffer exchanged to 50 mM MES at pH 6.0, 300 mM NaCl and 1 mM EDTA. The sample was later diluted in 100 mM Tris at pH 8.0, 5 mM imidazole and 200 mM NaCl, filtered through a 0.2 μ m filter and loaded into the IMAC column pre-equilibrated with 50 mM Tris at pH 8.0, 1 mM EDTA and 500 mM NaCl, 30 mM imidazole, and eluted with the same buffer containing 500 mM imidazole. The protein sample was then buffer exchanged in 20 mM Tris at pH 7.5, 50 mM NaCl, 5 mM EDTA, supplemented with protease inhibitor tablets (Complete EDTA, Roche Diagnostics).

Bioconjugation. The protein Gly-FGEsite-FXN¹⁻²¹⁰ (21 μ M) was reacted with PLP in phosphate buffer 50 mM, pH 6.5, PLP 10 mM, for 18–24 h and subsequently characterized by SDS-PAGE and HPLC-MS. The buffer exchanged product (21 μ M) was further reacted with benzylhydroxylamine or fluorescein-5-thiosemicarbazide (to facilitate the detection by MS or fluorescence, respectively) in phosphate buffer 50 mM, pH 5.5, 10 eq. tag, 10 eq. aniline (or *p*-phenylenediamine)³⁴⁹ during 2–20 h. Removal of reagents after reaction times and buffer exchanges were performed by using SEC gravity columns (NAP-5, PD MidiTrap G-25 or PD-10; GE Healthcare).

Characterization. Protein quantification was performed by absorption measure at 280 nm using NanoDrop. SDS-PAGE, RP-HPLC, RP-HPLC-MS, MALDI-TOF MS and HRMS were used to determine the purity and identity of protein samples.

SDS-PAGE was performed in a Mini-PROTEAN cell (BioRad, Hercules, CA, USA) connected to a PowerPac power supply (BioRad) and using Tris-glycine-SDS gels of 10–15% acrylamide to analyze denatured proteins. Gels were visualized using Coomassie blue staining (10% AcOH, 0.25 g brilliant blue in H₂O) and then discolored (20% CH₃OH, 3% glacial AcOH).

RP-HPLC was used with the same purpose using analogous conditions to those used for peptides, but using a Sunfire column (150 \times 4.6 mm \times 5 μ m, 100 Å, Waters) and two additional columns for proteins (BioSuite pC₁₈, 4.6 \times 150 mm \times 7 μ m, 500 Å, Waters; Widepore XB-C₁₈, 150 \times 2.10 mm \times 3.6 μ m, 200 Å, Phenomenex).

MALDI-TOF MS was carried out similarly as for peptides but using linear mode.

HRMS (LTQ-FT Ultra, Thermo Scientific) of intact protein (1 mg protein/mL, 20 mM Tris buffer, 50 mM NaCl, 5 mM EDTA at pH 7.5) were performed by the IRB Mass Spectrometry and Proteomics Core Facility. Samples diluted to 5 μ M with 1% formic acid aqueous solution were injected. LC-MS coupling was performed with the Advion Triversa Nanomate (Advion BioSciences, Ithaca, NY, USA) as the nanoESI source performing nanoelectrospray through chip technology. The Nanomate was attached to an LTQ-FT Ultra mass spectrometer and operated at a spray voltage of 1.7 kV and a delivery pressure of 0.5 psi in positive mode (capillary temperature, 200°C; tube lens, 100 V; and m/z range of 400 – 2,000 amu).

HSV-1 Bioconjugation and Characterization

Bioconjugation. The bioconjugation of HSV-1 particles was performed by using 2,000 eq. of NHS-PEG₃₅₀₀-maleimide (JenKem Technology USA), -biotin (JenKem Technology USA) or -peptide (*r*D-HAI or *r*D-THR) in HBSS buffer pH 7.4 at r.t.; in general, the concentration of these particles per μ L ranged from 400 to 4,000 (if samples $\times 1$) or ten times higher if samples $\times 10$. To concentrate or wash the viruses from the reaction, a centrifugation step was performed ($100,000 \times g$, 2 h; using a sucrose cushion). Finally, they were resuspended in HBSS buffer pH 7.4. The infectivity of these particles was analyzed by the group of professor Díaz-Nido (CBMSO).

Characterization. A combination of diverse techniques was used to assess the bioconjugation process and characterize the unmodified HSV-1 particles (SDS-PAGE, western blot, bottom-up MS, ASMS, TEM (negative staining and immuno-TEM), DLS and ζ -potential).

SDS-PAGE was performed in a Mini-PROTEAN cell (BioRad) connected to a PowerPac power supply (BioRad) and using Tris-glycine-SDS gels of 10-15% acrylamide to analyze denatured proteins (boiled 5 min at 95°C and with loading buffer, and 2% β -mercaptoethanol or dithiothreitol (DTT)). Gels were visualized using coomassie blue staining (10% AcOH, 0.25 g brilliant blue in H₂O) and then discolored (20% CH₃OH, 3% glacial AcOH), or by silver staining (using 0.75 mm gels) following five steps: fixation (50 mL CH₃OH, 12 mL AcOH, MilliQ H₂O up to 100 mL; addition of 50 μ L 37% formaldehyde at the last moment), pretreatment (19.12 mg sodium thiosulfate (Na₂S₂O₃) in 150 mL MilliQ H₂O), impregnation (0.2 g silver nitrate (AgNO₃), MilliQ H₂O up to 100 mL; keeping it wrapped in aluminum foil and adding 74.8 μ L 37% formaldehyde at the last moment), revealing (6 g sodium carbonate (Na₂CO₃), 2 mL pretreatment solution, MilliQ H₂O up to 100 mL; addition of 50 μ L 37% formaldehyde at the last moment) and stop revealing (50 mL CH₃OH, 15 mL AcOH, MilliQ H₂O up to 100 mL).

Western blots (WB) were initiated by transferring gels into nitrocellulose membranes o/n, at 4°C and using a power supply E802 (Consort, Turnhout, Belgium) with a voltage of 30V. Membranes were then blocked with 5% milk in H₂O for 2h at r.t., incubated with the primary antibody (goat pAb to HSV-1, 4 mg/mL; ab156292, batch GR179872-1; Abcam, Cambridge, United Kingdom; dilution 1/500) in TBST buffer (50 mM Tris buffer at pH 7.5, 190 mM NaCl, 0.1% Tween 20) 5% milk overnight at 4°C, washed with TBST buffer

10-15 min at r.t., incubated with the secondary antibody (anti-goat-HRP conjugate; dilution 1/40,000) in TBST buffer for 1 h at r.t., washed with TBST buffer 10-15 min at r.t., revealed with ECL substrate (EMD Millipore Immobilon western chemiluminescent HRP substrate (ECL), Merck Millipore, Billerica, MA, USA) and recorded using Amersham Hyperfilm ECL (GE Healthcare).

MS bottom-up approach for the characterization of HSV-1 particles was performed by the IRB Mass Spectrometry and Proteomics Core Facility. Samples were digested directly in polyacrylamide gel slices with trypsin (10 ng/ μ L) in 50 mM NH_4HCO_3 at 37°C overnight, prior reduction with 10 mM DTT for 45 min at 56°C and alkylation for 30 min in the dark with 50 mM iodoacetic acid (IAA). Samples were then desalted with C_{18} tips (PolyLC, Columbia, MD, USA) and reconstituted in 1% formic acid aqueous solution. LC-MS coupling was performed with the Advion Triversa Nanomate (Advion BioSciences, Ithaca, NY, USA) with the nanoESI source performing nanoelectrospray through chip technology. The Nanomate was attached to an Orbitrap Fusion Lumos Tribrid (Thermo Scientific) mass spectrometer and operated at a spray voltage of 1.7 kV and a delivery pressure of 0.5 psi in positive mode (ion transfer tube temperature, 275°C; RF lens, 30%; and m/z range of 400 – 1,600 amu). Data processing: Xcalibur software version 2.0SR2 (Thermo Scientific) and Proteome Discoverer software version 1.4 (Thermo Scientific) with SEQUEST HT algorithm, the UniProt database (HSV release 2016_06 with contaminants database), and using trypsin digestion (full) with two missed cleavages, carbamidomethyl in cysteine as static modification and methionine oxidation as dynamic modification, 10 ppm for precursor mass tolerance and 0.6 Da of MS/MS tolerance.

Affinity selection of proteins coupled to MS (ASMS) was applied to samples modified with NHS-PEG₃₅₀₀-biotin. Samples (containing ~20,000 HSV-1 particles) were initially denaturated by adding 1% SDS, 5% 2-mercaptoethanol and leaving at 95°C for 15 min. Samples were then left 5 min at r.t. and then incubated with streptavidin-coated magnetic particles (100 μ L of streptavidin-coated magnetic microparticles (1 μ m) ref. 49532 (1% solid); Sigma-Aldrich) at r.t. for 2 h, prior washing of these microparticles with 50 mM ammonium acetate buffer at pH 7.5. The magnetic microparticles were then washed 3 times with 50 mM ammonium acetate buffer at pH 7.5, resuspended in the same buffer (45 μ L) and left at 95°C for 15 min to release the captured biotin moieties. Samples (supernatants) were processed and analyzed in the IRB Mass Spectrometry and Proteomics Core Facility. They were reduced with 100 mM DTT for 1 h and carbamidomethylated for 10 min in the

dark with 50 mM IAA. Proteins were then digested with trypsin (2%, w/w) at 37°C overnight. The digestion was stopped by adding formic acid to a final concentration of 1% (v/v). LC-MS coupling was performed with the Advion Triversa Nanomate (Advion BioSciences) with the nanoESI source performing nanoelectrospray through chip technology. The Nanomate was attached to an LTQ-FT Ultra (Thermo Scientific) mass spectrometer and operated at a spray voltage of 1.7 kV and a delivery pressure of 0.5 psi in positive mode (capillary temperature, 200°C; tube lens, 120 V; and m/z range of 350 – 2,000 amu). Data processing: Xcalibur software version 2.0SR2 (Thermo Scientific) and Proteome Discoverer software version 1.4 (Thermo Scientific) with SEQUEST algorithm, the SwissProt database (HSV1 + BSA + cRAP, release 2014_11), and using trypsin digestion with two missed cleavages, carbamidomethyl in cysteine as static modification and methionine oxidation as dynamic modification, 10 ppm for precursor mass tolerance and 0.6 Da of MS/MS tolerance.

Transmission electron microscopy (TEM) was used to visualize unmodified HSV-1 particles using two labeling procedures, negative staining and immunogold labeling, prior fixation with 2% paraformaldehyde. Negative staining was performed by placing formvar (or carbon) coated copper 200 mesh grid (prior treatment with CTA005 Glow Discharger Unit, Bal-tec, Los Angeles, CA, USA) onto a drop containing the HSV-1 sample for 60 s, and then the grid is passed through five drops of uranyl acetate, 10 s in each one. Immunogold labeling is initiated blocking the grids with 5% BSA in PBS 0.01 M (3×5 min) and 1% BSA in PBS 0.01 M (1×5 min). The grids are then incubated with the primary antibody (goat pAb to HSV-1, 4 mg/mL; ab156292, batch GR179872-1; Abcam; dilution 1/500) in 1% BSA in PBS 0.01 M for 30 min, washed with 1% BSA in PBS 0.01 M (5×5 min), incubated with the secondary antibody (18 nm colloidal gold-AffinityPure donkey anti-goat IgG (H+L) minimal cross-reaction; Jackson ImmunoResearch, West Grove, PA, USA) for 30 min, and washed with PBS (5×5 min), glutaraldehyde (2% in 10 mM PBS) for 5 min and water (3×1 min). The treated grids are incubated with uranyl oxalate (2% in 10 mM PBS) for 1min. Finally, the grids from both procedures are dried and left for 2 h before visualizing in the TEM instrument (JEM-1010, JEOL, Tokyo, Japan).

Dynamic light scattering (DLS) and ζ -potential were measured in disposable capillary cells (DTS1070 from Malvern Instruments, Malvern, United Kingdom) containing viral samples using a Zsizer Nano-S (Malvern Instruments) with the Zsizer software (Malvern Instruments). Default parameter values were used, at 25°C and refractive index of 1.41.⁴¹⁹

***In Vivo* Experiments**

Experiments for the evaluation of immunogenic responses to peptides were designed by our group and performed by AntibodyBCN.

Peptide Conjugation to BSA or KLH. Each peptide (1 mg) was conjugated using either 1 mg of BSA ($\geq 98\%$) or KLH (premium quality) obtained from Sigma-Aldrich. For each peptide sample, proteins were dissolved in 0.2 mL of MES buffer (0.1 M, pH 5) and 0.9 mg of EDC dissolved in 0.1 mL of MilliQ water was added. After mixing for 10 min, 1 mg of the corresponding peptide dissolved in 0.55 mL of MES buffer was added and the mixture was left at room temperature for 3 h. Afterwards, it was filtered using Amicon Ultra-3K centrifugal filter devices at 5,000 rpm for 30 min, the residue was washed with MilliQ water and filtered again. Finally, this residue was dissolved in MilliQ water and freeze-dried in a vial for lyophilization. The lyophilized products were the corresponding conjugates. Peptide-BSA conjugates were identified through an UltrafleXtreme MALDI-TOF mass spectrometer (Bruker Daltonics), using a 2,6,-dihydroxyacetophenone (DHAP) matrix.

Mouse Immunization, Bleedings, and Serum Analysis by ELISA. Four groups of four BALB/c mice were treated with either one of the parent peptides or their *retro*-D-version. Each mouse received seven doses *i.p.* of 50 μg of peptide. Complete Freund's⁴²⁰ adjuvant (CFA) was administered in the first dose, incomplete Freund's adjuvant (IFA) in the subsequent five booster injections, and PBS in the last one. Bleedings for the titration of specific antibody production were performed before the first dose (time zero bleeding) and five days after the fourth and last dose. The peptide-specific humoral response was quantified by ELISA. MaxiSorp plates (Nunc) were treated with 0.1 mL of the corresponding peptide-BSA conjugate (1 μg) per well in carbonate buffer, overnight at 4°C. Afterwards, plates were blocked with 0.2 mL PBS-Tween 20 (T20) containing 2% of milk powder for 2 h at 37°C. Each sample serum was consecutively diluted 1/2 (starting by dilution 1:100) in PBS-T20 and incubated for 1 h at 37°C. Incubation with a secondary antibody (dil. 1/5,000) anti-Mouse IgG-HRP (ref. R1253HRP; batch 26922; Acris) was left for 1 h at 37°C. Washes (x3) with PBST (300 μL /well) were applied after each antibody incubation. Finally, TMB (100 μL /well) was added and left for 30 min, when the stop solution (100 μL , HCl_{aq} 1N) blocked the colorimetric reaction. Plates were read at 450 nm.

Rabbit Immunization, Bleedings and Serum Analysis by ELISA. Each rabbit was immunized *s.c.* with five doses of 250 μg of the conjugate (peptide-KLH), each at different localization, altogether with CFA in the initial dose and IFA in the last four. Bleedings were obtained nine days after the third and the last dose. The peptide-specific humoral response was quantified by ELISA. Peptides were resuspended (8 mg/mL) in pre-adsorption buffer (23 mM NHS in DMF and 46 mM DCC in DMF, 1:1 (v/v)). MaxiSorp plates (Nunc) were treated with 0.1 mL of the corresponding peptide (1 μg), overnight at 4°C. Afterwards, plates were blocked with 0.2 mL PBS-T20 containing 2% of milk powder for 2 h at 37°C. Each sample serum was consecutively diluted 1/2 (starting by dilution 1:500) in PBS-T20 and incubated for 1 h at 37°C. Then, an incubation with a secondary antibody (dil. 1/10,000) anti-Rabbit IgG- HRP (ref. R1364HRP; batch 22489; Acris) was left for 1 h at 37°C. Washes (x3) with PBST (300 μl /well) were applied after each antibody incubation. Finally, TMB (100 μl /well) was added and left for 30 min, when the stop solution (100 μl , HCl_{aq} 1N) blocked the colorimetric reaction. Plates were read at 450.

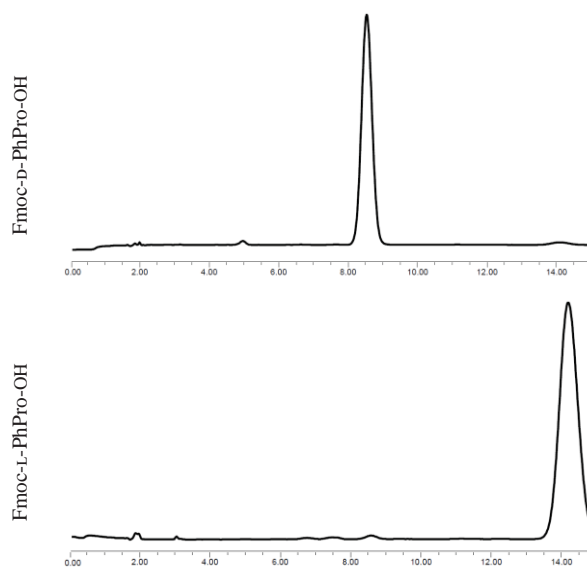
Rabbit Polyclonal Antibodies Purification and Characterization. Half the serum samples were purified through an affinity column of protein A (HiTrap Protein A HP, GE Healthcare), dialyzed against PBS \times 0.1 (membranes used: SnakeSkin Dialysis Tubing, 10K MWCO, 35 mm; Thermo Scientific) o/n at 4°C with stirring at 100 rpm, and further characterized. Antibody purity was checked by SDS-PAGE (12% acrylamide gel; denaturing conditions (sample treated for 5 min at 100°C in loading buffer 0.2 M DTT)), while ELISA was used to test the specificity of the response. ELISA was performed as before purification.

Product Characterization

Amino Acids**Chapter 1**

Amino Acid	MW (g/mol)	MALDI-TOF [M+Na] ⁺	Purity ^w (%)	HPLC t _R ^x (min)	α_{589}^{25} (0.8 mg/mL)	Absolute Configuration ^{163,164}
Fmoc-D-PhPro-OH	413.2	436.2	>99	14.2	41.6	<i>S, S</i>
Fmoc-L-PhPro-OH	413.2	436.2	>99	8.5	-38.6	<i>R, R</i>

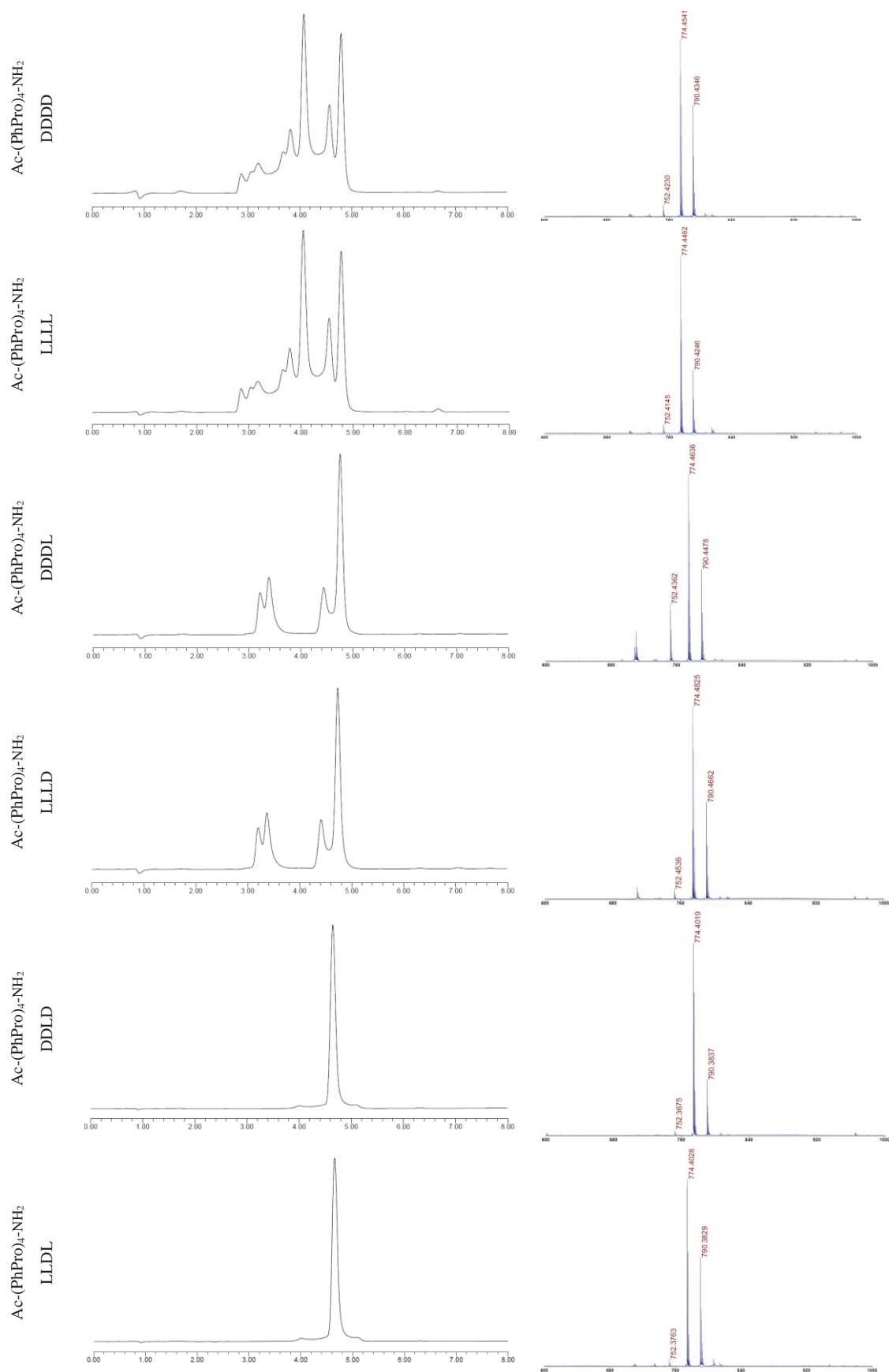
RP-HPLC characterization (x-axis in min)

^w After purification by RP-HPLC.^x Isocratic gradient with CH₃OH/CH₃CN (45:55) in 15 min (1 mL/min) using a Lux Cellulose-2 column (150 × 4.6 mm analytical, 5 μm, 1,000 Å, cellulose tris(3-chloro-4-methylphenylcarbamate) stationary phase; Phenomenex Inc.).

Peptides**Chapter 1**

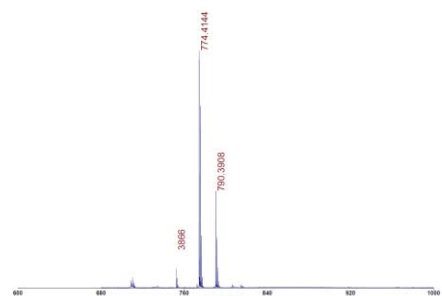
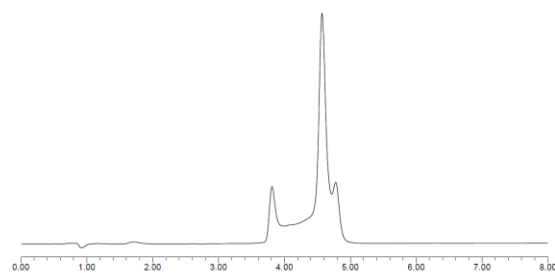
Peptide Absolute Configuration	HRMS calcd. [M+H] ⁺	FTMS ^y [M+H] ⁺	MALDI-TOF MS [M+Na] ⁺	Purity ^z (%)	HPLC t _R ^{aa} (min)	Yield (%)
Ac-(PhPro) ₄ -NH ₂ DDDD	752.3812	752.3841	774.5	>99	2.8 – 5.0	13
Ac-(PhPro) ₄ -NH ₂ DDDL	752.3812	752.3805	774.4	>99	3.0 – 5.0	13
Ac-(PhPro) ₄ -NH ₂ DDL D	752.3812	752.3832	774.4	>99	3.9 – 5.2	13
Ac-(PhPro) ₄ -NH ₂ DLDD	752.3812	752.3834	774.4	>99	3.7 – 5.0	8
Ac-(PhPro) ₄ -NH ₂ LDDD	752.3812	752.3795	774.4	>99	3.0 – 5.3	11
Ac-(PhPro) ₄ -NH ₂ DDL L	752.3812	752.3826	774.4	>99	3.2 – 4.6	2.7
Ac-(PhPro) ₄ -NH ₂ DLDL	752.3812	752.3835	774.4	>99	4.8 – 6.2	13
Ac-(PhPro) ₄ -NH ₂ LDDL	752.3812	752.3835	774.4	>99	3.0 – 5.4	13
Ac-(PhPro) ₄ -NH ₂ DLLD	752.3812	752.3825	774.4	>99	3.2 – 5.6	13
Ac-(PhPro) ₄ -NH ₂ LDLD	752.3812	752.3813	774.4	>99	4.8 – 6.2	13
Ac-(PhPro) ₄ -NH ₂ LLDD	752.3812	752.3799	774.4	>99	3.3 – 4.6	29
Ac-(PhPro) ₄ -NH ₂ DLLL	752.3812	752.3812	774.4	>99	2.9 – 5.2	11
Ac-(PhPro) ₄ -NH ₂ LDLL	752.3812	752.3814	774.4	>99	3.7 – 5.0	8
Ac-(PhPro) ₄ -NH ₂ LLDL	752.3812	752.3813	774.4	>99	3.9 – 5.2	13
Ac-(PhPro) ₄ -NH ₂ LLLL	752.3812	752.3800	774.4	>99	2.9 – 5.0	13
Ac-(PhPro) ₄ -NH ₂ LLLL	752.3812	752.3816	774.4	>99	2.8 – 5.0	13
Ac-(PhPro) ₄ -NH ₂ 16-stereoisomer mixture	752.3812	752.3823	774.4	n.a.	n.a.	69
L-DOPA-(PhPro) ₄ -NH ₂ 16-stereoisomer mixture	889.42833	889.42820	911.5	n.a.	n.a.	18
NIP-(PhPro) ₄ -NH ₂ 16-stereoisomer mixture	821.43850	821.43785	843.4	n.a.	n.a.	18
Ac-(Pro) ₄ -NH ₂ LLLL	448.2555	448.2552	470.2	>99	3.92	100

^y LTQ-FT Ultra/Synapt HDMS.^z n.a. ≡ not applicable. After purification by RP-HPLC.^{aa} Gradient from 0 to 100% or 50 to 80% CH₃CN in 8 min (1 mL/min) using a Sunfire C₁₈ column (150 × 4.6 mm × 5 μm, 100 Å, Waters) for Pro- or PhPro-based peptides, respectively.

RP-HPLC chromatograms and MALDI-TOF spectra (x-axis in min and m/z , respectively)

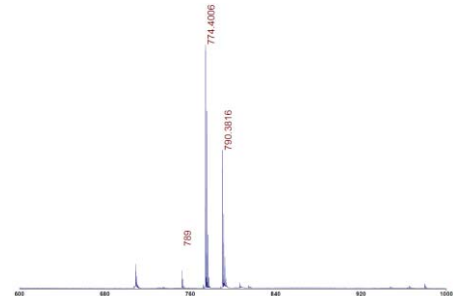
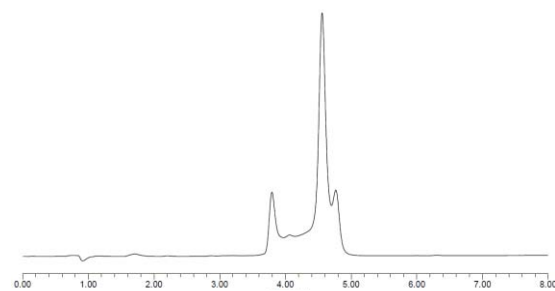
Ac-(PhPro)₄-NH₂

DLDD



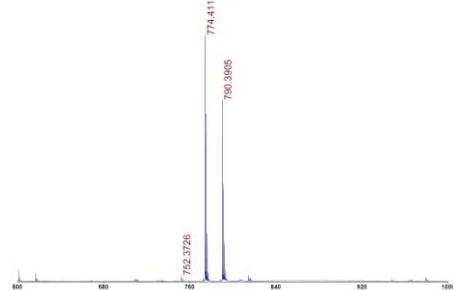
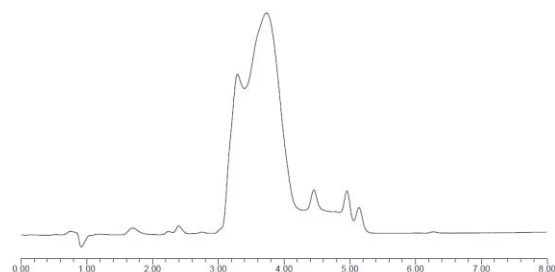
Ac-(PhPro)₄-NH₂

LDLL



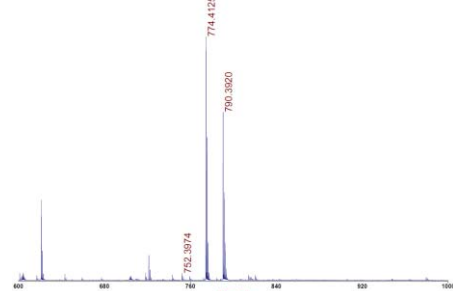
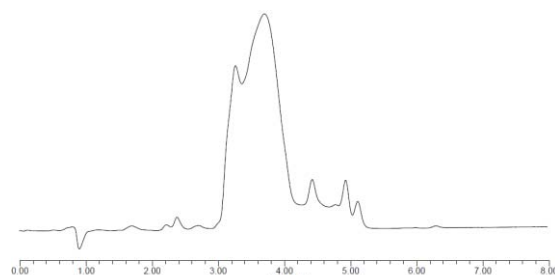
Ac-(PhPro)₄-NH₂

DLLL



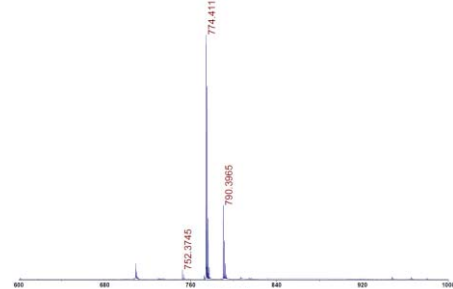
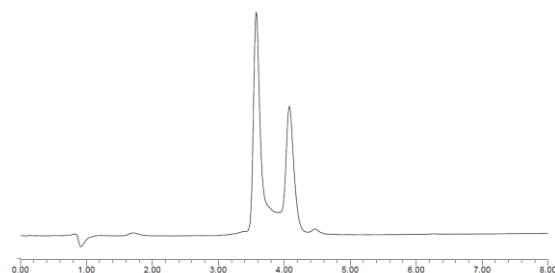
Ac-(PhPro)₄-NH₂

LLDD



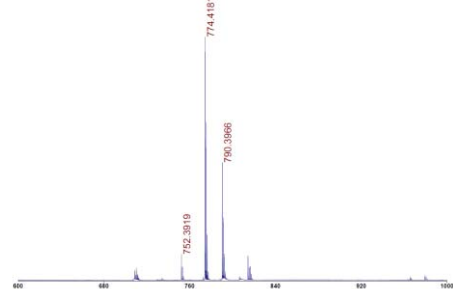
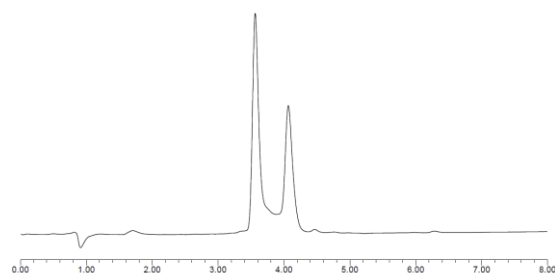
Ac-(PhPro)₄-NH₂

DDLL



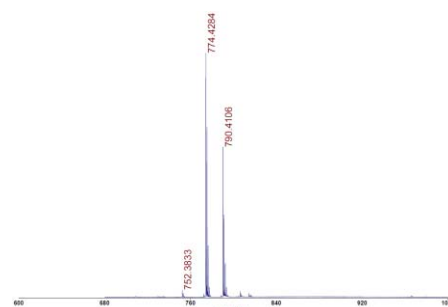
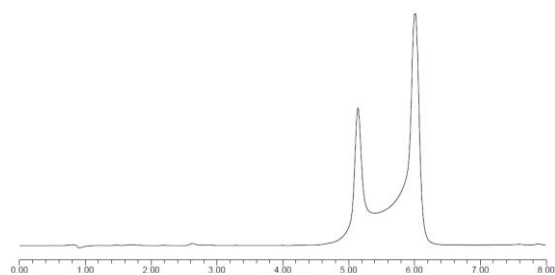
Ac-(PhPro)₄-NH₂

LLDD

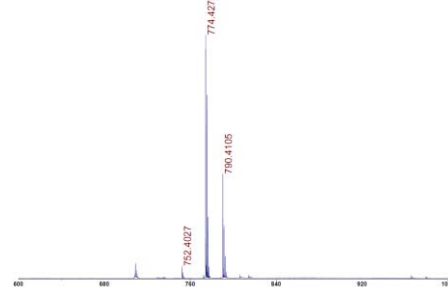
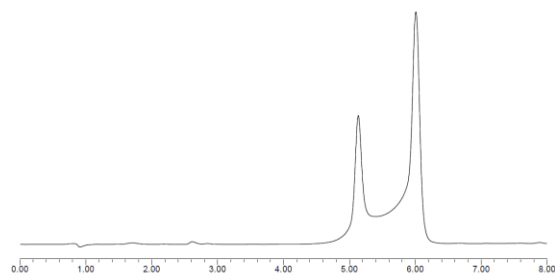


Ac-(PhPro)₄-NH₂

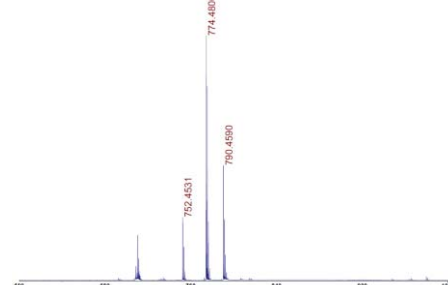
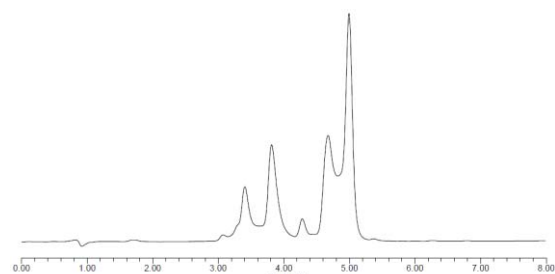
DLDL

Ac-(PhPro)₄-NH₂

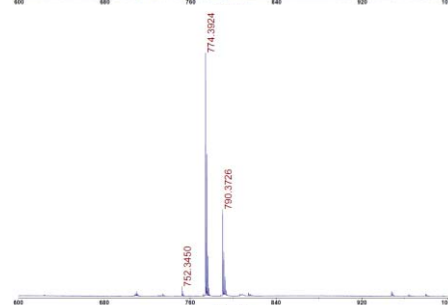
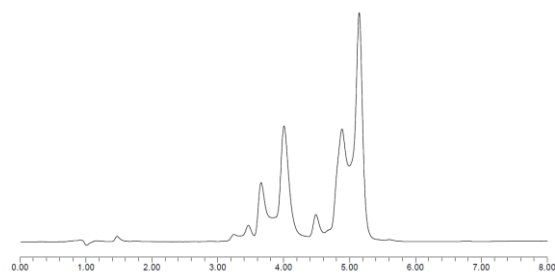
LLDL

Ac-(PhPro)₄-NH₂

LDDL

Ac-(PhPro)₄-NH₂

DLLD



Chapter 2

Peptide (light/heavy) ^{bb}	HRMS calcd. [M+H] ⁺	FTMS ^{cc} [M+H] ⁺	MALDI-TOF [M+H] ⁺	Purity ^{dd} (%)	HPLC t _R ^{ee} (min)	Yield (%)
Ac-HAIYPRH-NH ₂ (1L)	934.5006/ 938.5228	934.5010/ 938.5236	934.4/ 938.4	97/ 97	3.60/ 3.69	11/15
Ac-HA(hCha)YPRH-NH ₂ (2L)	988.5475/ 992.5697	988.5482/ 992.5690	988.5/ 992.5	100/ 100	3.87/ 3.84	15/16
Ac-HAI(Tic)PRH-NH ₂ (3L)	946.5006/ 950.5227	946.5027/ 950.5231	946.4/ 950.4	100/ 100	3.72/ 3.72	12/8
Ac-HAI(aPhe)PRH-NH ₂ (4L)	933.5166/ 937.5388	933.5200/ 937.5429	933.4/ 937.7	94/ 94	3.41/ 3.45	69/54
Ac-HAI(FPhe)PRH-NH ₂ (5L)	936.4963/ 940.5184	936.5001/ 940.5162	936.6/ 940.6	95/ 96	4.03/ 4.00	55/48
Ac-hrpyiah-NH ₂ (6D)	934.5006/ 938.5228	934.5046/ 938.5210	934.6/ 938.6	95/ 94	3.38/ 3.37	58/63
Ac-hr(L-PhPro)yah-NH ₂ (7+D)	1010.5319/ 1014.5541	1010.5290/ 1014.5558	1010.6/ 1014.6	95/ 95	3.74/ 3.73	53/77
Ac-hr(D-PhPro)yah-NH ₂ (7-D)	1010.5319/ 1014.5541	1010.5325/ 1014.5559	1010.6/ 1014.6	94/ 95	3.80/ 3.79	70/66
Ac-hr(D-Pip)yah-NH ₂ (8D)	948.5162/ 952.5384	948.5162/ 952.5397	948.6/ 952.6	99/ 99	3.47/ 3.46	10/5
Ac-(D-Tha)rpyiah-NH ₂ (9D)	951.4618/ 955.4840	951.4603/ 955.4844	951.6/ 955.5	98/ 97	3.65/ 3.64	29/12

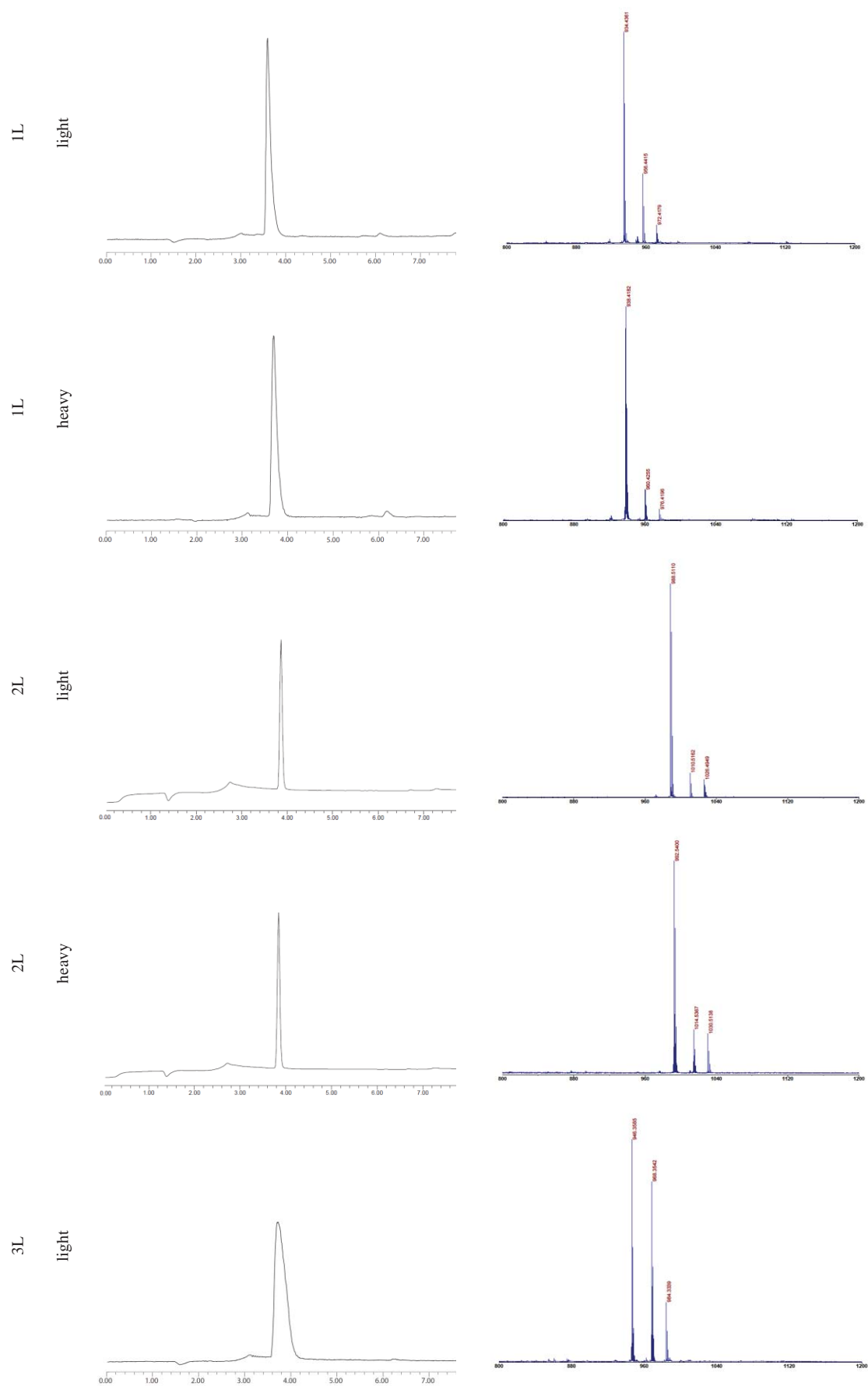
^{bb} hCha ≡ homocyclohexyl-L-alanine; Tic ≡ 7-hydroxy-(S)-1.2.3.4-tetrahydroisoquinoline-3-carboxylic acid; aPhe ≡ 4-amino-L-phenylalanine; FPhe ≡ 4-fluoro-L-phenylalanine; L-PhPro ≡ (2S, 3S)-3-phenylpyrrolidine-2-carboxylic acid; D-PhPro ≡ (2R, 3R)-3-phenylpyrrolidine-2-carboxylic acid; D-Pip ≡ D-pipecolic acid; D-Tha ≡ 4-thiazoyl-D-alanine; lowercase letter means D-amino acid.

^{cc} LTQ-FT Ultra/Synapt HDMS.

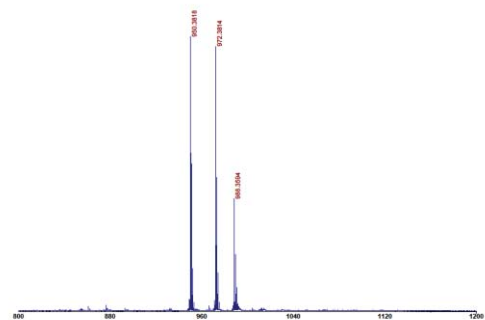
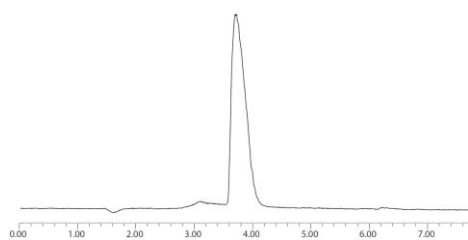
^{dd} After purification by RP-HPLC.

^{ee} Gradient from 0 to 100% CH₃CN in 8 min (1 mL/min) using a Sunfire C₁₈ column (150 × 4.6 mm × 5 μm, 100 Å, Waters).

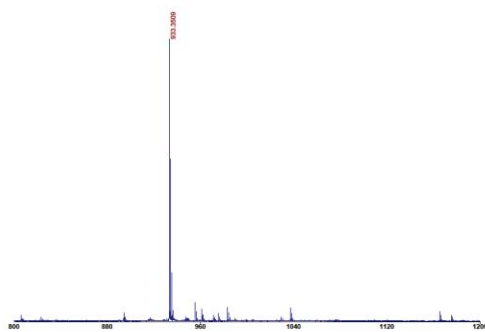
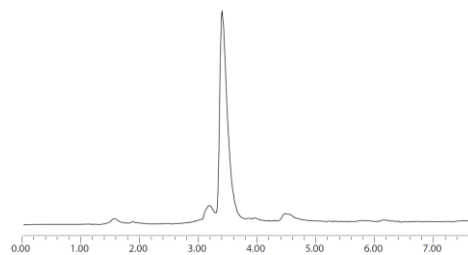
RP-HPLC chromatograms and MALDI-TOF spectra (x-axis in min and m/z , respectively)



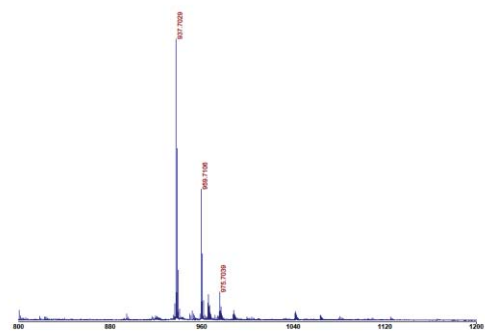
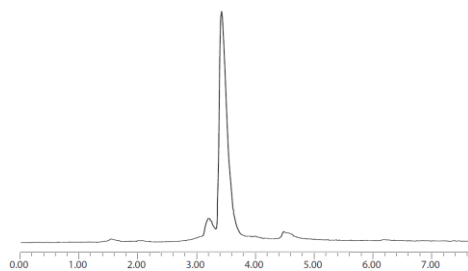
3L
heavy



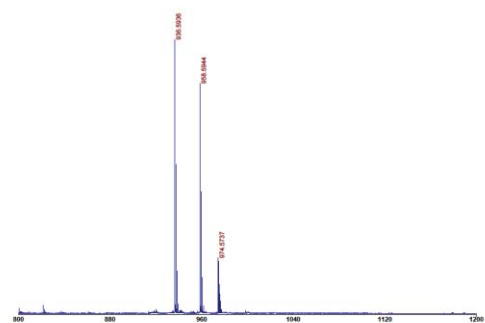
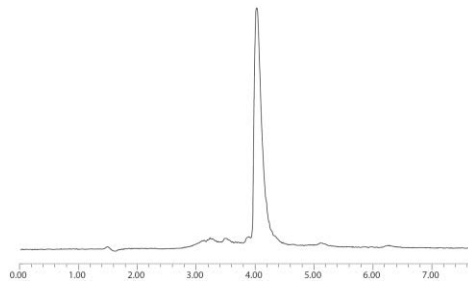
4L
light



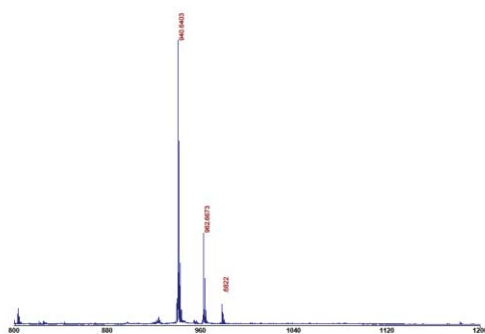
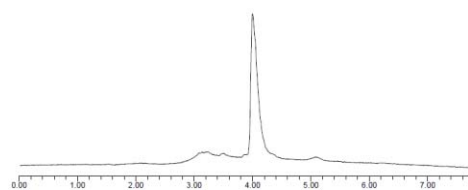
4L
heavy



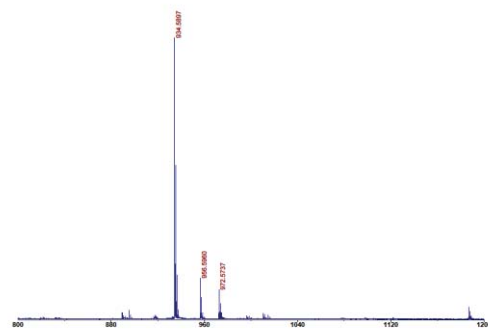
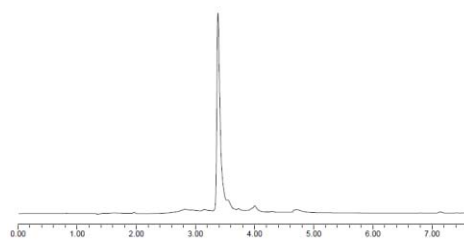
5L
light



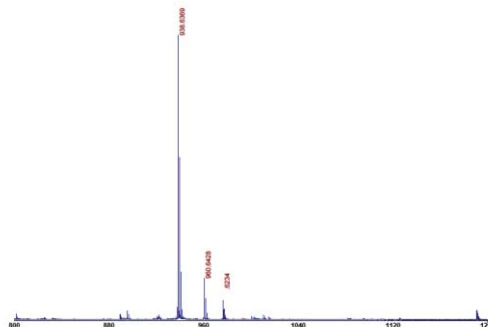
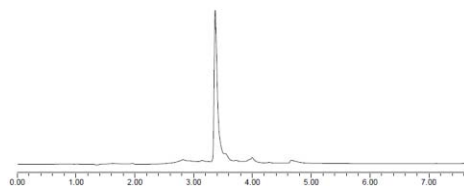
5L
heavy



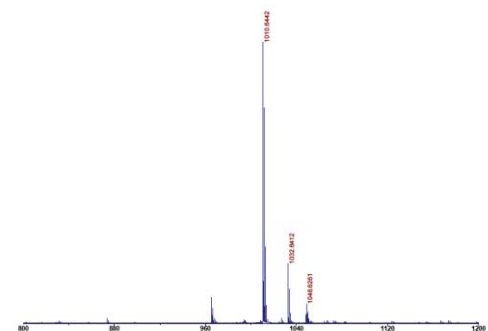
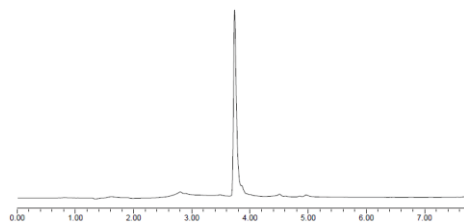
6D light



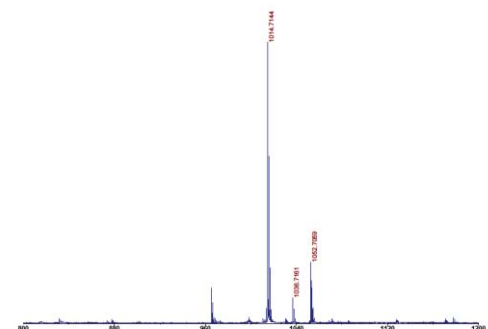
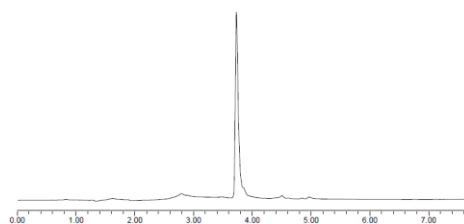
6D heavy



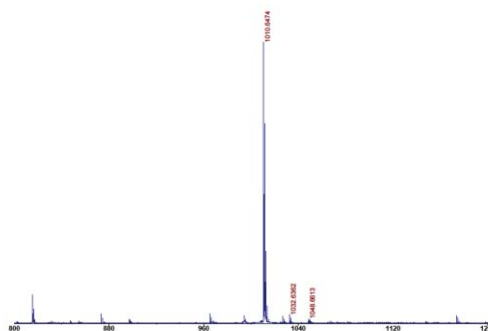
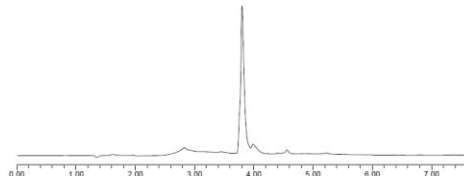
7+D light



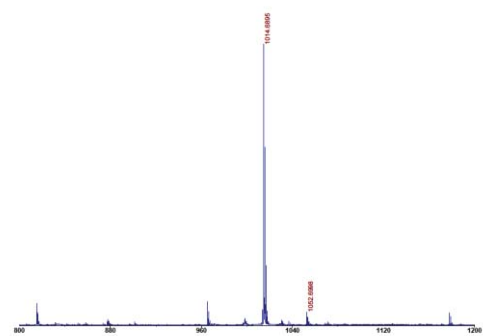
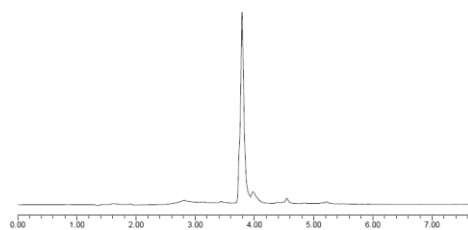
7+D heavy



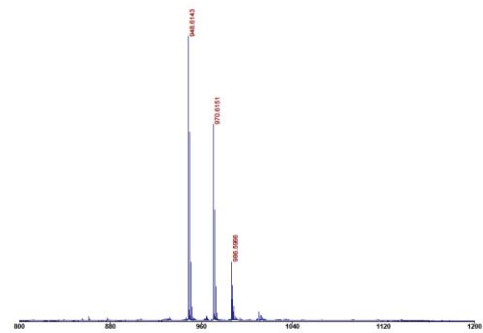
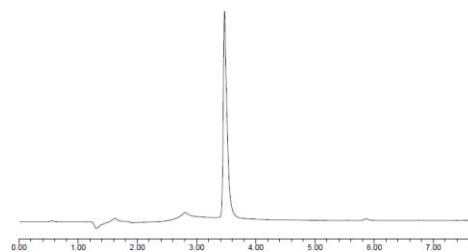
7-D light



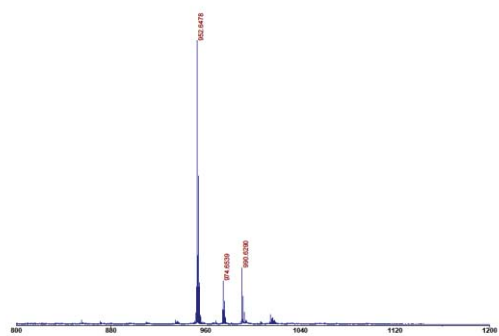
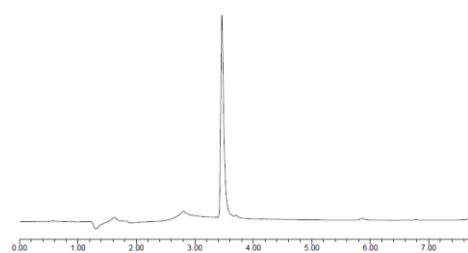
7-D heavy



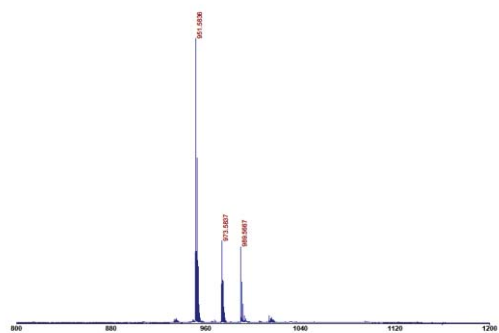
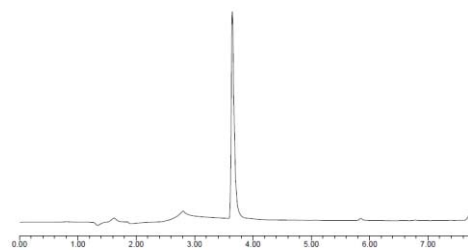
8D light



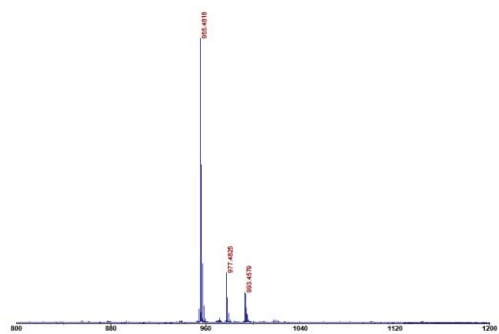
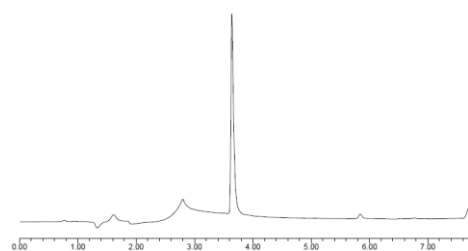
8D heavy

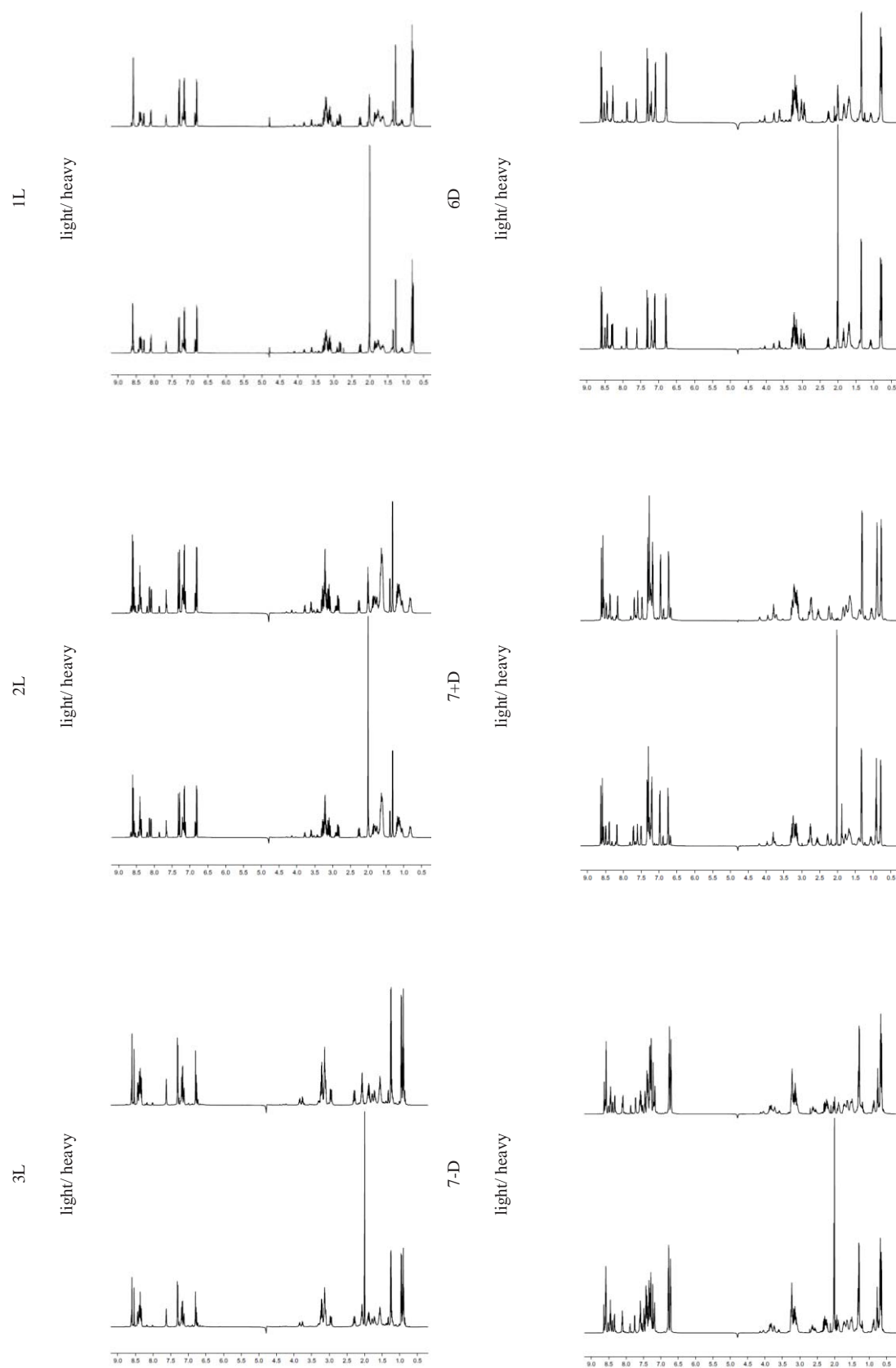


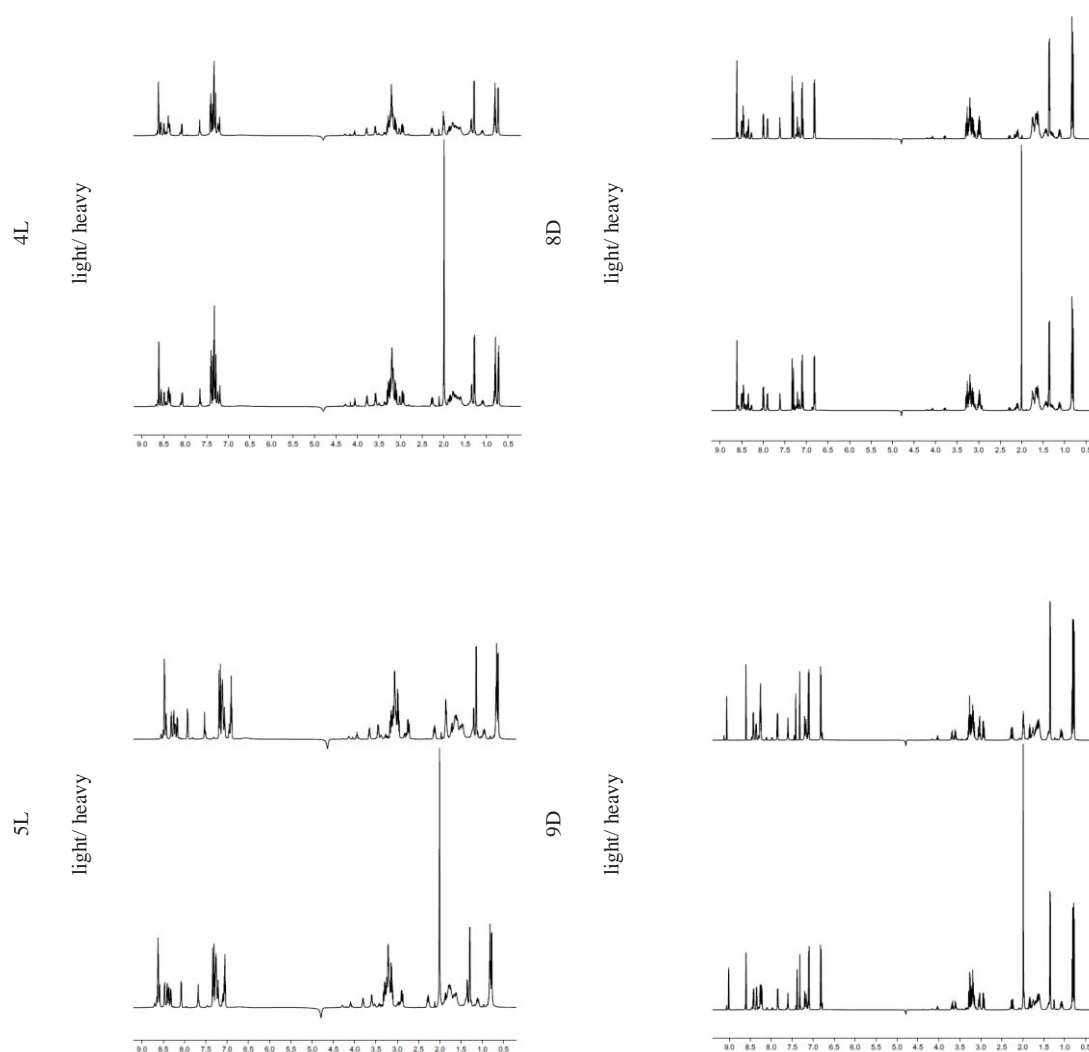
9D light



9D heavy



^1H -NMR spectra (x-axis in ppm)

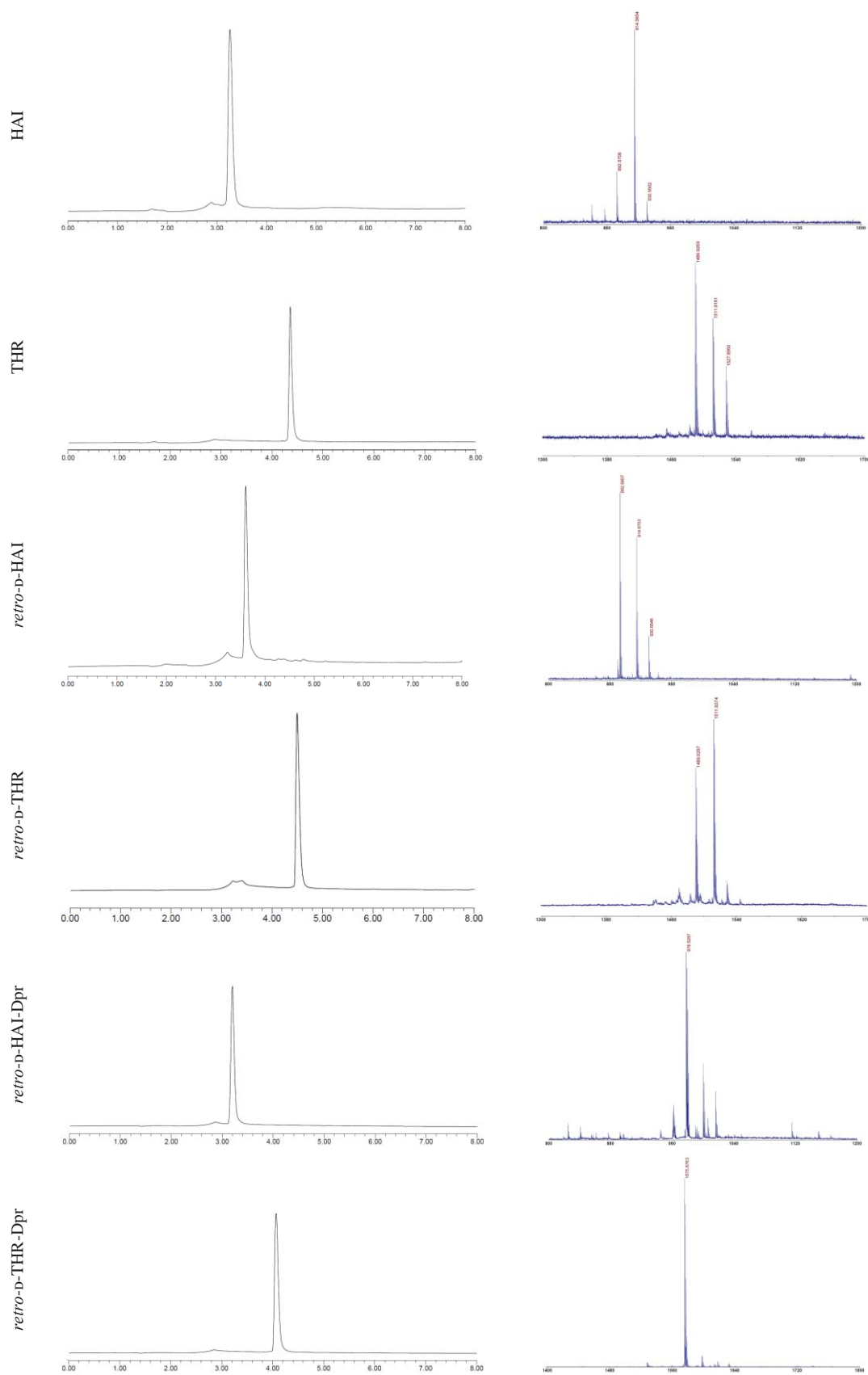


Chapter 3

Peptide	HRMS calcd. [M]	FTMS ^{ff} [M]	MALDI-TOF [M+H] ⁺	Purity ^{gg} (%)	HPLC t _R ^{hh} (min)
HAI	891.48275	891.48155	892.6	>99	3.26
THR	1488.74486	1488.74256	1489.9	>99	4.36
<i>retro</i> -D-HAI	891.48275	891.48244	892.7	>99	3.61
<i>retro</i> -D-THR	1488.74486	1488.74466	1489.9	>99	4.50
<i>retro</i> -D-HAI-Dpr	977.53077	977.52875	978.5	>99	3.20
<i>retro</i> -D-THR-Dpr	1574.79287	1574.79039	1575.9	>99	4.07

^{ff} LTQ-FT Ultra/Synapt HDMS.^{gg} After purification by RP-HPLC.^{hh} Gradient from 0 to 100% CH₃CN in 8 min (1 mL/min) using a Sunfire C₁₈ column (150 × 4.6 mm × 5 μm, 100 Å, Waters).

RP-HPLC chromatograms and MALDI-TOF spectra (x-axis in min and m/z , respectively)

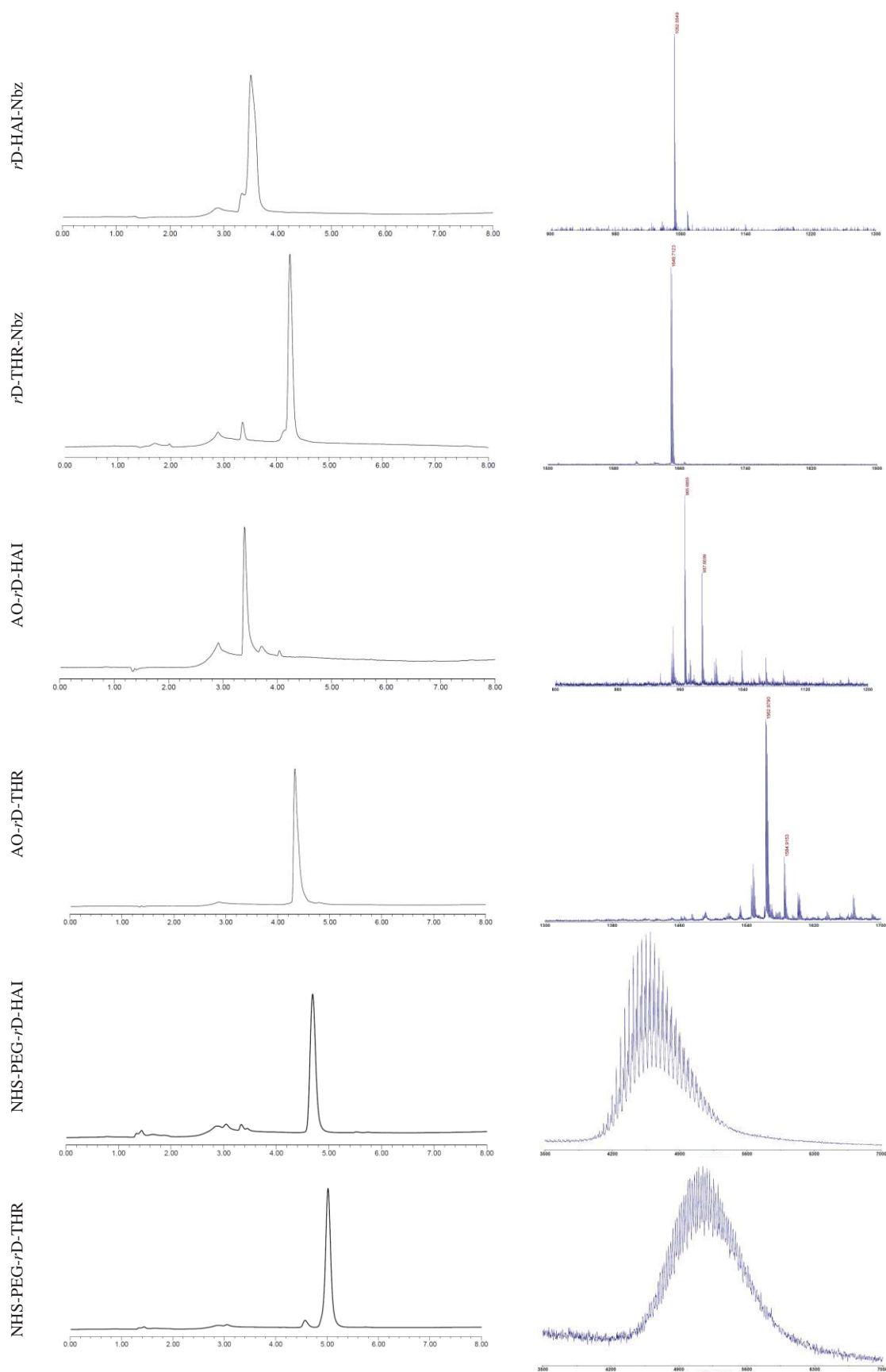


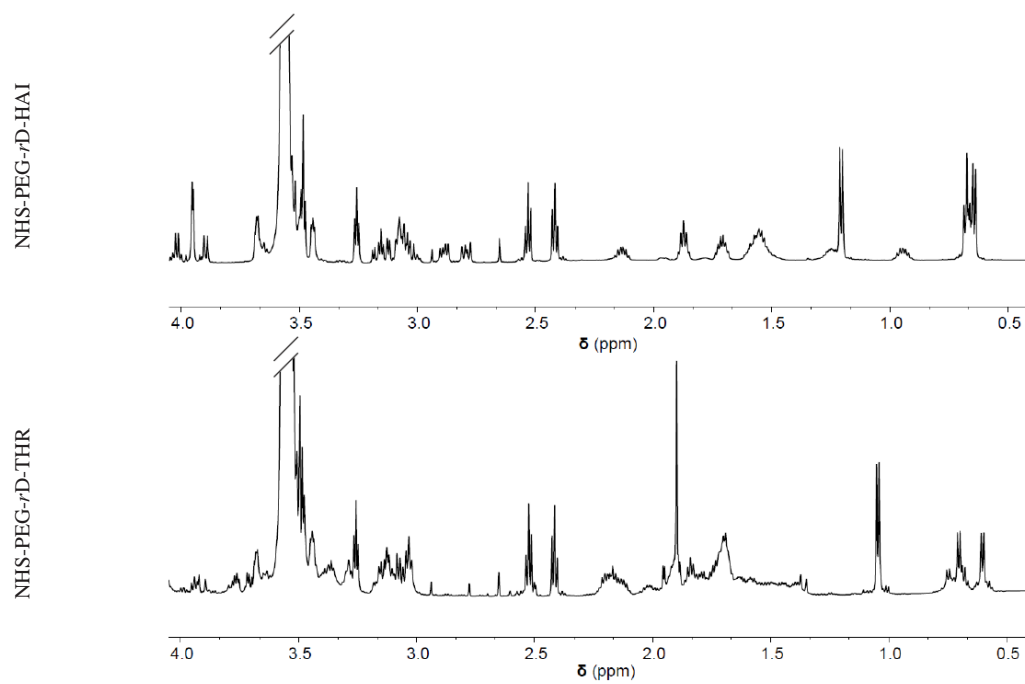
Chapter 4

Peptide	HRMS calcd. [M+H] ⁺	FTMS ⁱⁱ [M+H] ⁺	MALDI-TOF [M+H] ⁺	Purity ^{jj} (%)	HPLC t _R ^{kk} (min)
<i>r</i> D-HAI-Nbz	1052.5173	1052.5158	1052.6	94	3.50
<i>r</i> D-THR-Nbz ^{ll}	1648.77214	1648.77002	1649.7	92	4.25
AO- <i>r</i> D-HAI	965.50605	965.50641	965.7	93	3.40
AO- <i>r</i> D-THR	1562.76787	1562.76851	1563.0	100	4.33
NHS-PEG- <i>r</i> D-HAI	n.a. ^{mm}	n.a.	n.a.	96	4.69
NHS-PEG- <i>r</i> D-THR	n.a.	n.a.	n.a.	96	5.02

ⁱⁱ LTQ-FT Ultra/Synapt HDMS.^{jj} After purification by RP-HPLC.^{kk} Gradient from 0 to 100% CH₃CN in 8 min (1 mL/min) using a Sunfire C₁₈ column (150 × 4.6 mm × 5 μm, 100 Å, Waters).^{ll} HRMS calcd. and FTMS as [M].^{mm} n.a. ≡ not applicable.

RP-HPLC chromatograms and MALDI-TOF spectra (x-axis in min and m/z , respectively)

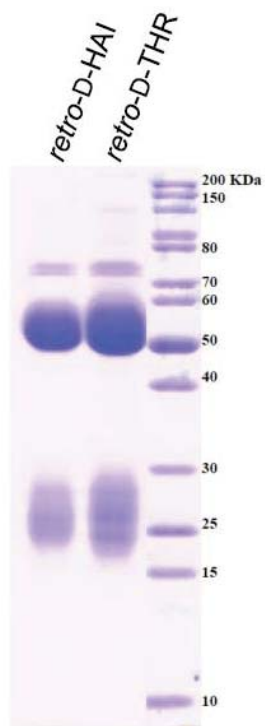


^1H -NMR spectra

Biologics

Chapter 3

SDS-PAGE of pAbs against *retro*-D-peptides produced in rabbit after affinity purification



Chapter 4

HSV-1 bioconjugation and characterization by batch

PEG compound	HSV-1 batch	Bioconjugation method ⁿⁿ	Characterization
NHS-PEG-MAL	2	NHS-PEG-MAL, 6,000 eq.; 2 h Cf-Cys 6,000 eq.; 1 h at r.t. on o/n at 4°C	TEM (neg. stain.), DLS, SDS-PAGE, Fluorescence
NHS-PEG-MAL	2	NHS-PEG-MAL, 50 eq.; 2 h Cf-Cys 50 eq.; 1h at r.t. and o/n at 4°C	TEM (neg. stain.), DLS, SDS-PAGE, Fluorescence
NHS-PEG-MAL	3	NHS-PEG-MAL, 2,000 eq.; 2 h Cf-Cys 2,000 eq.; 4 h	TEM (neg. stain.), DLS, SDS-PAGE, Fluorescence
NHS-PEG-MAL	3	NHS-PEG-MAL, 1 mM; 2 h Cf-Cys 1 mM; 4 h	TEM (neg. stain.), DLS, SDS-PAGE, Fluorescence
NHS-PEG-biotin	1	NHS-PEG-biotin, 2,000 eq.; 2 h	SDS-PAGE
NHS-PEG-biotin	6	NHS-PEG-biotin, 2,000 eq.; 2 h	SDS-PAGE, WB
NHS-PEG-biotin	6	NHS-PEG-biotin, 100 eq.; 2 h	SDS-PAGE, WB
NHS-PEG-biotin	8	NHS-PEG-biotin, 2,000 eq.; vol. 1/10, 2 h	SDS-PAGE, WB DLS, ζ-potential
NHS-PEG-biotin	8	NHS-PEG-biotin, 2,000 eq.; EDC, 2,000 eq.; conc. ×10, 2 h	SDS-PAGE, WB DLS, ζ-potential, ASMS
NHS-PEG-biotin	8	NHS-PEG-biotin, 2,000 eq.; EDC, 2,000 eq.; conc. ×1, 2 h	SDS-PAGE, WB DLS, ζ-potential
NHS-PEG-biotin	10	NHS-PEG-biotin, 2,000 eq.; conc. ×10, 2 h	Only infectivity
NHS-PEG-biotin	10	NHS-PEG-biotin, 2,000 eq.; EDC, 2,000 eq.; conc. ×10, 2 h	Only infectivity
-	11	-	MS
NHS-PEG-rD-THR	15	NHS-PEG-rD-THR, 2,000 eq.; conc. ×10, 2 h	DLS, ζ-potential
NHS-PEG-rD-THR	19	NHS-PEG-rD-THR, 2,000 eq.; conc. ×10, 2 h	DLS, ζ-potential
NHS-PEG-rD-THR	20	NHS-PEG-rD-THR, 2,000 eq.; conc. ×10, 2 h	DLS, ζ-potential
NHS-PEG-rD-THR	22	NHS-PEG-rD-THR, 2,000 eq.; conc. ×10, 2 h	SDS-PAGE, DLS, ζ-potential

ⁿⁿ Unless specified, reactions performed at room temperature.

REFERENCES

- (1) Miller, G. On the origin of the nervous system. *Science* **2009**, *325*, 24.
- (2) Nakanishi, N.; Yuan, D.; Jacobs, D. K.; Hartenstein, V. Early development, pattern, and reorganization of the planula nervous system in Aurelia (Cnidaria, Scyphozoa). *Dev. Genes Evol.* **2008**, *218*, 511.
- (3) Martindale, M. Q. The evolution of metazoan axial properties. *Nat. Rev. Genet.* **2005**, *6*, 917.
- (4) Dunn, C. W.; Hejnol, A.; Matus, D. Q.; Pang, K.; Browne, W. E.; Smith, S. A.; Seaver, E.; Rouse, G. W.; Obst, M.; Edgecombe, G. D.; Sorensen, M. V.; Haddock, S. H. D.; Schmidt-Rhaesa, A.; Okusu, A.; Kristensen, R. M.; Wheeler, W. C.; Martindale, M. Q.; Giribet, G. Broad phylogenomic sampling improves resolution of the animal tree of life. *Nature* **2008**, *452*, 745.
- (5) Ryan, J. F.; Pang, K.; Schnitzler, C. E.; Nguyen, A. D.; Moreland, R. T.; Simmons, D. K.; Koch, B. J.; Francis, W. R.; Havlak, P.; Program, N. C. S.; Smith, S. A.; Putnam, N. H.; Haddock, S. H.; Dunn, C. W.; Wolfsberg, T. G.; Mullikin, J. C.; Martindale, M. Q.; Baxevanis, A. D. The genome of the ctenophore *Mnemiopsis leidyi* and its implications for cell type evolution. *Science* **2013**, *342*, 1242592.
- (6) Moroz, L. L.; Kocot, K. M.; Citarella, M. R.; Dosung, S.; Norekian, T. P.; Povolotskaya, I. S.; Grigorenko, A. P.; Dailey, C.; Berezikov, E.; Buckley, K. M.; Ptitsyn, A.; Reshetov, D.; Mukherjee, K.; Moroz, T. P.; Bobkova, Y.; Yu, F.; Kapitonov, V. V.; Jurka, J.; Bobkov, Y. V.; Swore, J. J.; Girardo, D. O.; Fodor, A.; Gusev, F.; Sanford, R.; Bruders, R.; Kittler, E.; Mills, C. E.; Rast, J. P.; Derelle, R.; Solovyev, V. V.; Kondrashov, F. A.; Swalla, B. J.; Sweedler, J. V.; Rogaev, E. I.; Halanych, K. M.; Kohn, A. B. The ctenophore genome and the evolutionary origins of neural systems. *Nature* **2014**, *510*, 109.
- (7) Nakanishi, N.; Sogabe, S.; Degnan, B. M. Evolutionary origin of gastrulation: Insights from sponge development. *BMC Biol.* **2014**, *12*, 26.
- (8) Solnica-Krezel, L.; Sepich, D. S. Gastrulation: Making and shaping germ layers. *Annu. Rev. Cell Dev. Biol.* **2012**, *28*, 687.
- (9) Lu, C. C.; Brennan, J.; Robertson, E. J. From fertilization to gastrulation: Axis formation in the mouse embryo. *Curr. Opin. Genet. Dev.* **2001**, *11*, 384.
- (10) Wozniak, M. A.; Chen, C. S. Mechanotransduction in development: A growing role for contractility. *Nat. Rev. Mol. Cell Biol.* **2009**, *10*, 34.
- (11) Lowe, C. J.; Wu, M.; Salic, A.; Evans, L.; Lander, E.; Stange-Thomann, N.; Gruber, C. E.; Gerhart, J.; Kirschner, M. Anteroposterior patterning in Hemichordates and the origins of the Chordate nervous system. *Cell* **2003**, *113*, 853.
- (12) Knecht, A. K.; Bronner-Fraser, M. Induction of the neural crest: A multigene process. *Nat. Rev. Genet.* **2002**, *3*, 453.
- (13) Murry, C. E.; Keller, G. Differentiation of embryonic stem cells to clinically relevant populations: Lessons from embryonic development. *Cell* **2008**, *132*, 661.
- (14) Evseenko, D.; Zhu, Y.; Schenke-Layland, K.; Kuo, J.; Latour, B.; Ge, S.; Scholes, J.; Dravid, G.; Li, X.; MacLellan, W. R.; Crooks, G. M. Mapping the first stages of mesoderm commitment during differentiation of human embryonic stem cells. *Proc. Natl. Acad. Sci. U. S. A.* **2010**, *107*, 13742.
- (15) Stemple, D. L. Structure and function of the notochord: An essential organ for chordate development. *Development* **2005**, *132*, 2503.
- (16) Grapin-Botton, A.; Melton, D. A. Endoderm development: From patterning to organogenesis. *Trends Genet.* **1996**, *12*, 124.
- (17) Halton, D. W.; Gustafsson, M. K. S. Functional morphology of the platyhelminth nervous system. *Parasitology* **1996**, *113*, S47.
- (18) Telford, M. J. Animal phylogeny. *Curr. Biol.* **2006**, *16*, R981.
- (19) Telford, Maximilian J.; Budd, Graham E.; Philippe, H. Phylogenomic insights into animal evolution. *Curr. Biol.* **2015**, *25*, R876.
- (20) Rankin, C. H. From gene to identified neuron to behaviour in *Caenorhabditis elegans*. *Nat. Rev. Genet.* **2002**, *3*, 622.
- (21) Jorgensen, E. M.; Mango, S. E. The art and design of genetic screens: *Caenorhabditis elegans*. *Nat. Rev. Genet.* **2002**, *3*, 356.
- (22) Bishop, N. A.; Guarente, L. Two neurons mediate diet-restriction-induced longevity in *C. elegans*. *Nature* **2007**, *447*, 545.
- (23) Hobert, O.; Johnston, R. J.; Chang, S. Left-right asymmetry in the nervous system: The *Caenorhabditis elegans* model. *Nat. Rev. Neurosci.* **2002**, *3*, 629.
- (24) Chatterjee, N.; Sinha, S. Understanding the mind of a worm: hierarchical network structure underlying nervous system function in *C. elegans*. *Prog. Brain Res.* **2007**, *168*, 145.
- (25) Shubin, N.; Tabin, C.; Carroll, S. Deep homology and the origins of evolutionary novelty. *Nature* **2009**, *457*, 818.
- (26) Benito-Gutiérrez, È.; Arendt, D. CNS evolution: New insight from the mud. *Curr. Biol.* **2009**, *19*, R640.

- (27) Mineta, K.; Nakazawa, M.; Cebrià, F.; Ikeo, K.; Agata, K.; Gojobori, T. Origin and evolutionary process of the CNS elucidated by comparative genomics analysis of planarian ESTs. *Proc. Natl. Acad. Sci. U. S. A.* **2003**, *100*, 7666.
- (28) Le Douarin, N. M.; Dupin, E. The neural crest in vertebrate evolution. *Curr. Opin. Genet. Dev.* **2012**, *22*, 381.
- (29) Abbott, N. J. Dynamics of CNS barriers: Evolution, differentiation, and modulation. *Cell. Mol. Neurobiol.* **2005**, *25*, 5.
- (30) Abbott, N. J. In *Physiology and Pharmacology of the Blood-Brain Barrier*; Bradbury, M. W. B., Ed.; Springer: Berlin-Heidelberg, Germany, 1992; Vol. 103, p 371.
- (31) Banerjee, S.; Bhat, M. A. Neuron-glia interactions in blood-brain barrier formation. *Annu. Rev. Neurosci.* **2007**, *30*, 235.
- (32) Matter, K.; Balda, M. S. Signalling to and from tight junctions. *Nat. Rev. Mol. Cell Biol.* **2003**, *4*, 225.
- (33) Kniesel, U.; Wolburg, H. Tight junctions of the blood–brain barrier. *Cell. Mol. Neurobiol.* **2000**, *20*, 57.
- (34) Wolburg, H.; Lippoldt, A. Tight junctions of the blood–brain barrier: Development, composition and regulation. *Vascul. Pharmacol.* **2002**, *38*, 323.
- (35) Rubin, L. L.; Staddon, J. M. The cell biology of the blood-brain barrier. *Annu. Rev. Neurosci.* **1999**, *22*, 11.
- (36) Lun, M. P.; Monuki, E. S.; Lehtinen, M. K. Development and functions of the choroid plexus-cerebrospinal fluid system. *Nat. Rev. Neurosci.* **2015**, *16*, 445.
- (37) Vorbrodt, A. W.; Dobrogowska, D. H. Molecular anatomy of intercellular junctions in brain endothelial and epithelial barriers: electron microscopist's view. *Brain Res. Rev.* **2003**, *42*, 221.
- (38) Brown, P. D.; Davies, S. L.; Speake, T.; Millar, I. D. Molecular mechanisms of cerebrospinal fluid production. *Neuroscience* **2004**, *129*, 955.
- (39) Del Bigio, M. R. The ependyma: A protective barrier between brain and cerebrospinal fluid. *Glia* **1995**, *14*, 1.
- (40) Nabeshima, S.; Reese, T. S.; Landis, D. M. D.; Brightman, M. W. Junctions in the meninges and marginal glia. *J. Comp. Neurol.* **1975**, *164*, 127.
- (41) Saunders, N. R.; Ek, C. J.; Habgood, M. D.; Dziegielewska, K. M. Barriers in the brain: A renaissance? *Trends Neurosci.* **2008**, *31*, 279.
- (42) Gaillard, P. J.; Visser, C. C.; de Boer, A. G. Targeted delivery across the blood–brain barrier. *Expert Opin. Drug Deliv.* **2005**, *2*, 299.
- (43) Pardridge, W. M. The blood-brain barrier: Bottleneck in brain drug development. *NeuroRx* **2005**, *2*, 3.
- (44) Hynynen, K. Ultrasound for drug and gene delivery to the brain. *Adv. Drug Del. Rev.* **2008**, *60*, 1209.
- (45) Obermeier, B.; Daneman, R.; Ransohoff, R. M. Development, maintenance and disruption of the blood-brain barrier. *Nat. Med.* **2013**, *19*, 1584.
- (46) Banks, W. A. From blood-brain barrier to blood-brain interface: New opportunities for CNS drug delivery. *Nat. Rev. Drug Discov.* **2016**, *15*, 275.
- (47) Armulik, A.; Genove, G.; Mae, M.; Nisancioglu, M. H.; Wallgard, E.; Niaudet, C.; He, L.; Norlin, J.; Lindblom, P.; Strittmatter, K.; Johansson, B. R.; Betsholtz, C. Pericytes regulate the blood-brain barrier. *Nature* **2010**, *468*, 557.
- (48) Daneman, R.; Zhou, L.; Kebede, A. A.; Barres, B. A. Pericytes are required for blood-brain barrier integrity during embryogenesis. *Nature* **2010**, *468*, 562.
- (49) Abbott, N. J.; Ronnback, L.; Hansson, E. Astrocyte-endothelial interactions at the blood-brain barrier. *Nat. Rev. Neurosci.* **2006**, *7*, 41.
- (50) Persidsky, Y.; Ramirez, S. H.; Haorah, J.; Kanmogne, G. D. Blood–brain barrier: Structural components and function under physiologic and pathologic conditions. *J. Neuroimmune Pharmacol.* **2006**, *1*, 223.
- (51) Hawkins, B. T.; Davis, T. P. The blood-brain barrier/neurovascular unit in health and disease. *Pharmacol. Rev.* **2005**, *57*, 173.
- (52) Huber, J. D.; Egleton, R. D.; Davis, T. P. Molecular physiology and pathophysiology of tight junctions in the blood–brain barrier. *Trends Neurosci.* **2001**, *24*, 719.
- (53) Harris, T. J. C.; Tepass, U. Adherens junctions: From molecules to morphogenesis. *Nat. Rev. Mol. Cell Biol.* **2010**, *11*, 502.
- (54) Patabendige, A.; Skinner, R. A.; Morgan, L.; Joan Abbott, N. A detailed method for preparation of a functional and flexible blood–brain barrier model using porcine brain endothelial cells. *Brain Res.* **2013**, *1521*, 16.

- (55) Chaitali, G.; Vikram, P.; Jorge, G.-M.; Damir, J.; Nicola, M. Blood-brain barrier P450 enzymes and multidrug transporters in drug resistance: A synergistic role in neurological diseases. *Curr. Drug Metab.* **2011**, *12*, 742.
- (56) Saunders, N. R.; Dreifuss, J. J.; Dziegielewska, K. M.; Johansson, P. A.; Habgood, M. D.; Mollgard, K.; Bauer, H. C. The rights and wrongs of blood-brain barrier permeability studies: A walk through 100 years of history. *Front. Neurosci.* **2014**, *8*, 404.
- (57) Lipinski, C. A.; Lombardo, F.; Dominy, B. W.; Feeney, P. J. Experimental and computational approaches to estimate solubility and permeability in drug discovery and development settings. *Adv. Drug Del. Rev.* **2012**, *64*, Supplement, 4.
- (58) Davis, J. T.; Okunola, O.; Quesada, R. Recent advances in the transmembrane transport of anions. *Chem. Soc. Rev.* **2010**, *39*, 3843.
- (59) Wei, L. Adsorptive-mediated brain delivery systems. *Curr. Pharm. Biotechnol.* **2012**, *13*, 2340.
- (60) Qian, Z. M.; Li, H.; Sun, H.; Ho, K. Targeted drug delivery via the transferrin receptor-mediated endocytosis pathway. *Pharmacol. Rev.* **2002**, *54*, 561.
- (61) Mayor, S.; Pagano, R. E. Pathways of clathrin-independent endocytosis. *Nat. Rev. Mol. Cell Biol.* **2007**, *8*, 603.
- (62) Bareford, L. M.; Swaan, P. W. Endocytic mechanisms for targeted drug delivery. *Adv. Drug Del. Rev.* **2007**, *59*, 748.
- (63) May, R. C.; Machesky, L. M. Phagocytosis and the actin cytoskeleton. *J. Cell Sci.* **2001**, *114*, 1061.
- (64) Özen, I.; Deierborg, T.; Miharada, K.; Padel, T.; Englund, E.; Genové, G.; Paul, G. Brain pericytes acquire a microglial phenotype after stroke. *Acta Neuropathol.* **2014**, *128*, 381.
- (65) Balabanov, R.; Washington, R.; Wagnerova, J.; Dore-Duffy, P. CNS microvascular pericytes express macrophage-like function, cell surface integrin α M, and macrophage marker ED-2. *Microvasc. Res.* **1996**, *52*, 127.
- (66) Tomás-Camardiel, M.; Venero, J. L.; Herrera, A. J.; De Pablos, R. M.; Pintor-Toro, J. A.; Machado, A.; Cano, J. Blood–brain barrier disruption highly induces aquaporin-4 mRNA and protein in perivascular and parenchymal astrocytes: Protective effect by estradiol treatment in ovariectomized animals. *J. Neurosci. Res.* **2005**, *80*, 235.
- (67) Pratten, M. K.; Lloyd, J. B. Pinocytosis and phagocytosis: The effect of size of a particulate substrate on its mode of capture by rat peritoneal macrophages cultured *in vitro*. *BBA-Gen. Subjects* **1986**, *881*, 307.
- (68) Merrifield, C. J.; Moss, S. E.; Ballestrem, C.; Imhof, B. A.; Giese, G.; Wunderlich, I.; Almers, W. Endocytic vesicles move at the tips of actin tails in cultured mast cells. *Nat. Cell Biol.* **1999**, *1*, 72.
- (69) Lajoie, J. M.; Shusta, E. V. Targeting receptor-mediated transport for delivery of biologics across the blood-brain barrier. *Annu. Rev. Pharmacol. Toxicol.* **2015**, *55*, 613.
- (70) McMahon, H. T.; Boucrot, E. Molecular mechanism and physiological functions of clathrin-mediated endocytosis. *Nat. Rev. Mol. Cell Biol.* **2011**, *12*, 517.
- (71) Greenwood, J.; Heasman, S. J.; Alvarez, J. I.; Prat, A.; Lyck, R.; Engelhardt, B. Review: Leucocyte–endothelial cell crosstalk at the blood–brain barrier: A prerequisite for successful immune cell entry to the brain. *Neuropathol. Appl. Neurobiol.* **2011**, *37*, 24.
- (72) Pachter, J. S.; de Vries, H. E.; Fabry, Z. The blood-brain barrier and its role in immune privilege in the central nervous system. *J. Neuropathol. Exp. Neurol.* **2003**, *62*, 593.
- (73) Engelhardt, B.; Ransohoff, R. M. Capture, crawl, cross: The T cell code to breach the blood–brain barriers. *Trends Immunol.* **2012**, *33*, 579.
- (74) Del Maschio, A.; De Luigi, A.; Martin-Padura, I.; Brockhaus, M.; Bartfai, T.; Fruscella, P.; Adorini, L.; Martino, G.; Furlan, R.; De Simoni, M. G.; Dejana, E. Leukocyte recruitment in the cerebrospinal fluid of mice with experimental meningitis is inhibited by an antibody to junctional adhesion molecule (Jam). *J. Exp. Med.* **1999**, *190*, 1351.
- (75) Millan, J.; Hewlett, L.; Glyn, M.; Toomre, D.; Clark, P.; Ridley, A. J. Lymphocyte transcellular migration occurs through recruitment of endothelial ICAM-1 to caveola- and F-actin-rich domains. *Nat. Cell Biol.* **2006**, *8*, 113.
- (76) Miner, J. J.; Diamond, M. S. Mechanisms of restriction of viral neuroinvasion at the blood–brain barrier. *Curr. Opin. Immunol.* **2016**, *38*, 18.
- (77) Kim, K. S. Mechanisms of microbial traversal of the blood-brain barrier. *Nat. Rev. Micro.* **2008**, *6*, 625.
- (78) Ley, K.; Laudanna, C.; Cybulsky, M. I.; Nourshargh, S. Getting to the site of inflammation: The leukocyte adhesion cascade updated. *Nat. Rev. Immunol.* **2007**, *7*, 678.
- (79) Gustavsson, A.; Svensson, M.; Jacobi, F.; Allgulander, C.; Alonso, J.; Beghi, E.; Dodel, R.; Ekman, M.; Faravelli, C.; Fratiglioni, L.; Gannon, B.; Jones, D. H.; Jennum, P.; Jordanova, A.; Jönsson, L.; Karampampa, K.; Knapp, M.; Kobelt, G.; Kurth, T.; Lieb, R.; Linde, M.; Ljungcrantz, C.; Maercker, A.; Melin, B.; Moscarelli, M.; Musayev, A.; Norwood, F.; Preisig, M.; Pugliatti, M.; Rehm, J.; Salvador-Carulla,

- L.; Schlehofer, B.; Simon, R.; Steinhausen, H.-C.; Stovner, L. J.; Vallat, J.-M.; den Bergh, P. V.; van Os, J.; Vos, P.; Xu, W.; Wittchen, H.-U.; Jönsson, B.; Olesen, J. Cost of disorders of the brain in Europe 2010. *Eur. Neuropsychopharmacol.* **2011**, *21*, 718.
- (80) Olesen, J.; Gustavsson, A.; Svensson, M.; Wittchen, H. U.; Jönsson, B.; study group, C.; European Brain, C. The economic cost of brain disorders in Europe. *Eur. J. Neurol.* **2012**, *19*, 155.
- (81) DiLuca, M.; Olesen, J. The cost of brain diseases: A burden or a challenge? *Neuron* **2014**, *82*, 1205.
- (82) Merrifield, R. B. Solid phase peptide synthesis. I. The synthesis of a tetrapeptide. *J. Am. Chem. Soc.* **1963**, *85*, 2149.
- (83) Getz, J. A.; Rice, J. J.; Daugherty, P. S. Protease-resistant peptide ligands from a knottin scaffold library. *ACS Chem. Biol.* **2011**, *6*, 837.
- (84) Prades, R.; Oller-Salvia, B.; Schwarzmaier, S. M.; Selva, J.; Moros, M.; Balbi, M.; Grazu, V.; de La Fuente, J. M.; Egea, G.; Plesnila, N.; Teixido, M.; Giralt, E. Applying the *retro*-enantio approach to obtain a peptide capable of overcoming the blood-brain barrier. *Angew. Chem. Int. Ed.* **2015**, *54*, 3967.
- (85) Kastin, A. J.; Akerstrom, V. Nonsaturable entry of neuropeptide Y into brain. *Am. J. Physiol. Endocrinol. Metab.* **1999**, *276*, E479.
- (86) Kastin, A. J.; Akerstrom, V. Orexin A but not Orexin B rapidly enters brain from blood by simple diffusion. *J. Pharmacol. Exp. Ther.* **1999**, *289*, 219.
- (87) Kannan, R.; Kuhlenskamp, J. F.; Jeandidier, E.; Trinh, H.; Ookhtens, M.; Kaplowitz, N. Evidence for carrier-mediated transport of glutathione across the blood-brain barrier in the rat. *J. Clin. Invest.* **1990**, *85*, 2009.
- (88) Bachhawat, A. K.; Thakur, A.; Kaur, J.; Zulkifli, M. Glutathione transporters. *BBA-Gen. Subjects* **2013**, *1830*, 3154.
- (89) Banks, W. A.; Kastin, A. J.; Fischman, A. J.; Coy, D. H.; Strauss, S. L. Carrier-mediated transport of enkephalins and N-Tyr-MIF-1 across blood-brain barrier. *Am. J. Physiol. Endocrinol. Metab.* **1986**, *251*, E477.
- (90) Barrera, C. M.; Banks, W. A.; Kastin, A. J. Passage of Tyr-MIF-1 from blood to brain. *Brain Res. Bull.* **1989**, *23*, 439.
- (91) Banks, W. A.; Kastin, A. J. Peptide transport systems for opiates across the blood-brain barrier. *Am. J. Physiol. Endocrinol. Metab.* **1990**, *259*, E1.
- (92) Drin, G.; Rousselle, C.; Scherrmann, J.-M.; Rees, A. R.; Temsamani, J. Peptide delivery to the brain via adsorptive-mediated endocytosis: Advances with SynB vectors. *AAPS PharmSci* **2002**, *4*, 61.
- (93) Frankel, A. D.; Pabo, C. O. Cellular uptake of the tat protein from human immunodeficiency virus. *Cell* **1988**, *55*, 1189.
- (94) Vivès, E.; Brodin, P.; Lebleu, B. A truncated HIV-1 Tat protein basic domain rapidly translocates through the plasma membrane and accumulates in the cell nucleus. *J. Biol. Chem.* **1997**, *272*, 16010.
- (95) Hervé, F.; Ghinea, N.; Scherrmann, J.-M. CNS delivery via adsorptive transcytosis. *The AAPS Journal* **2008**, *10*, 455.
- (96) Ruan, G.; Agrawal, A.; Marcus, A. I.; Nie, S. Imaging and tracking of Tat peptide-conjugated quantum dots in living cells: New insights into nanoparticle uptake, intracellular transport, and vesicle shedding. *J. Am. Chem. Soc.* **2007**, *129*, 14759.
- (97) Derossi, D.; Joliot, A. H.; Chassaing, G.; Prochiantz, A. The third helix of the Antennapedia homeodomain translocates through biological membranes. *J. Biol. Chem.* **1994**, *269*, 10444.
- (98) Derossi, D.; Calvet, S.; Trembleau, A.; Brunissen, A.; Chassaing, G.; Prochiantz, A. Cell Internalization of the third helix of the Antennapedia homeodomain is receptor-independent. *J. Biol. Chem.* **1996**, *271*, 18188.
- (99) Boissguérin, P.; Deshayes, S.; Gait, M. J.; O'Donovan, L.; Godfrey, C.; Betts, C. A.; Wood, M. J. A.; Lebleu, B. Delivery of therapeutic oligonucleotides with cell penetrating peptides. *Adv. Drug Del. Rev.* **2015**, *87*, 52.
- (100) Koren, E.; Torchilin, V. P. Cell-penetrating peptides: Breaking through to the other side. *Trends Mol. Med.* **2012**, *18*, 385.
- (101) Milletti, F. Cell-penetrating peptides: classes, origin, and current landscape. *Drug Discov. Today* **2012**, *17*, 850.
- (102) Hussain, M. M.; Strickland, D. K.; Bakillah, A. The mammalian low-density lipoprotein receptor family. *Annu. Rev. Nutr.* **1999**, *19*, 141.
- (103) Zensi, A.; Begley, D.; Pontikis, C.; Legros, C.; Mihoreanu, L.; Wagner, S.; Büchel, C.; von Briesen, H.; Kreuter, J. Albumin nanoparticles targeted with Apo E enter the CNS by transcytosis and are delivered to neurones. *J. Control. Release* **2009**, *137*, 78.
- (104) Re, F.; Cambianica, I.; Sesana, S.; Salvati, E.; Cagnotto, A.; Salmons, M.; Couraud, P.-O.; Moghimi, S. M.; Masserini, M.; Sancini, G. Functionalization with ApoE-derived peptides enhances the interaction with

- brain capillary endothelial cells of nanoliposomes binding amyloid-beta peptide. *J. Biotechnol.* **2011**, *156*, 341.
- (105) Wang, D.; El-Amouri, S. S.; Dai, M.; Kuan, C.-Y.; Hui, D. Y.; Brady, R. O.; Pan, D. Engineering a lysosomal enzyme with a derivative of receptor-binding domain of apoE enables delivery across the blood–brain barrier. *Proc. Natl. Acad. Sci. U. S. A.* **2013**, *110*, 2999.
- (106) Agnello, V.; Ábel, G.; Elfahal, M.; Knight, G. B.; Zhang, Q.-X. Hepatitis C virus and other Flaviviridae viruses enter cells via low density lipoprotein receptor. *Proc. Natl. Acad. Sci. U. S. A.* **1999**, *96*, 12766.
- (107) Abbruscato, T. J.; Lopez, S. P.; Mark, K. S.; Hawkins, B. T.; Davis, T. P. Nicotine and cotinine modulate cerebral microvascular permeability and protein expression of ZO-1 through nicotinic acetylcholine receptors expressed on brain endothelial cells. *J. Pharm. Sci.* **2002**, *91*, 2525.
- (108) Zhan, C.; Li, B.; Hu, L.; Wei, X.; Feng, L.; Fu, W.; Lu, W. Micelle-based brain-targeted drug delivery enabled by a nicotine acetylcholine receptor ligand. *Angew. Chem. Int. Ed.* **2011**, *50*, 5482.
- (109) Schnell, M. J.; McGettigan, J. P.; Wirblich, C.; Papaneri, A. The cell biology of rabies virus: Using stealth to reach the brain. *Nat. Rev. Micro.* **2010**, *8*, 51.
- (110) Kumar, P.; Wu, H.; McBride, J. L.; Jung, K.-E.; Hee Kim, M.; Davidson, B. L.; Kyung Lee, S.; Shankar, P.; Manjunath, N. Transvascular delivery of small interfering RNA to the central nervous system. *Nature* **2007**, *448*, 39.
- (111) Liu, Y.; Huang, R.; Han, L.; Ke, W.; Shao, K.; Ye, L.; Lou, J.; Jiang, C. Brain-targeting gene delivery and cellular internalization mechanisms for modified rabies virus glycoprotein RVG29 nanoparticles. *Biomaterials* **2009**, *30*, 4195.
- (112) Dautry-Varsat, A.; Ciechanover, A.; Lodish, H. F. pH and the recycling of transferrin during receptor-mediated endocytosis. *Proc. Natl. Acad. Sci. U. S. A.* **1983**, *80*, 2258.
- (113) Aisen, P. Entry of iron into cells: A new role for the transferrin receptor in modulating iron release from transferrin. *Ann. Neurol.* **1992**, *32*, S62.
- (114) Jefferies, W. A.; Brandon, M. R.; Hunt, S. V.; Williams, A. F.; Gatter, K. C.; Mason, D. Y. Transferrin receptor on endothelium of brain capillaries. *Nature* **1984**, *312*, 162.
- (115) Rouault, T. A. Iron metabolism in the CNS: Implications for neurodegenerative diseases. *Nat. Rev. Neurosci.* **2013**, *14*, 551.
- (116) Moos, T.; Morgan, E. H. Transferrin and transferrin receptor function in brain barrier systems. *Cell. Mol. Neurobiol.* **2000**, *20*, 77.
- (117) Wiley, D. T.; Webster, P.; Gale, A.; Davis, M. E. Transcytosis and brain uptake of transferrin-containing nanoparticles by tuning avidity to transferrin receptor. *Proc. Natl. Acad. Sci. U. S. A.* **2013**, *110*, 8662.
- (118) Thorstensen, K.; Romslo, I. The role of transferrin in the mechanism of cellular iron uptake. *Biochem. J.* **1990**, *271*, 1.
- (119) Pardridge, W. M. Drug and gene targeting to the brain with molecular trojan horses. *Nat. Rev. Drug Discov.* **2002**, *1*, 131.
- (120) Pardridge, W. M. Molecular Trojan horses for blood–brain barrier drug delivery. *Curr. Opin. Pharmacol.* **2006**, *6*, 494.
- (121) Pardridge, W. M. Blood–brain barrier drug delivery of IgG fusion proteins with a transferrin receptor monoclonal antibody. *Expert Opin. Drug Deliv.* **2015**, *12*, 207.
- (122) Afergan, E.; Epstein, H.; Dahan, R.; Koroukhov, N.; Rohekar, K.; Danenberg, H. D.; Golomb, G. Delivery of serotonin to the brain by monocytes following phagocytosis of liposomes. *J. Control. Release* **2008**, *132*, 84.
- (123) Prades, R.; Guerrero, S.; Araya, E.; Molina, C.; Salas, E.; Zurita, E.; Selva, J.; Egea, G.; López-Iglesias, C.; Teixidó, M.; Kogan, M. J.; Giralt, E. Delivery of gold nanoparticles to the brain by conjugation with a peptide that recognizes the transferrin receptor. *Biomaterials* **2012**, *33*, 7194.
- (124) Wei, X.; Zhan, C.; Chen, X.; Hou, J.; Xie, C.; Lu, W. *Retro*-inverso isomer of Angiopep-2: A stable d-peptide ligand inspires brain-targeted drug delivery. *Mol. Pharm.* **2014**, *11*, 3261.
- (125) Gao, H.; Zhang, S.; Cao, S.; Yang, Z.; Pang, Z.; Jiang, X. Angiopep-2 and activatable cell-penetrating peptide dual-functionalized nanoparticles for systemic glioma-targeting delivery. *Mol. Pharm.* **2014**, *11*, 2755.
- (126) Teixidó, M.; Zurita, E.; Malakoutikhah, M.; Tarragó, T.; Giralt, E. Diketopiperazines as a tool for the study of transport across the blood–brain barrier (BBB) and their potential use as BBB-shuttles. *J. Am. Chem. Soc.* **2007**, *129*, 11802.
- (127) Arranz-Gibert, P.; Guixar, B.; Malakoutikhah, M.; Muttenthaler, M.; Guzmán, F.; Teixidó, M.; Giralt, E. Lipid bilayer crossing—The gate of symmetry. Water-soluble phenylproline-based blood-brain barrier shuttles. *J. Am. Chem. Soc.* **2015**, *137*, 7357.

- (128) Abbott, N. J. Blood–brain barrier structure and function and the challenges for CNS drug delivery. *J. Inherited Metab. Dis.* **2013**, *36*, 437.
- (129) Pardridge, W. M. Blood–brain barrier delivery. *Drug Discov. Today* **2007**, *12*, 54.
- (130) Träuble, H. The movement of molecules across lipid membranes: A molecular theory. *J. Membr. Biol.* **1971**, *4*, 193.
- (131) Lieb, W.; Stein, W. Non-stokesian nature of transverse diffusion within human red cell membranes. *J. Membr. Biol.* **1986**, *92*, 111.
- (132) Pardridge, W. M. CNS drug design based on principles of blood-brain barrier transport. *J. Neurochem.* **1998**, *70*, 1781.
- (133) Wager, T. T.; Hou, X.; Verhoest, P. R.; Villalobos, A. Moving beyond rules: The development of a central nervous system multiparameter optimization (CNS MPO) approach to enable alignment of druglike properties. *ACS Chem. Neurosci.* **2010**, *1*, 435.
- (134) Spector, M. S.; Selinger, J. V.; Singh, A.; Rodriguez, J. M.; Price, R. R.; Schnur, J. M. Controlling the morphology of chiral lipid tubules. *Langmuir* **1998**, *14*, 3493.
- (135) Selinger, J. V.; Schnur, J. M. Theory of chiral lipid tubules. *Phys. Rev. Lett.* **1993**, *71*, 4091.
- (136) Lalitha, S.; Sampath Kumar, A.; Stine, K. J.; Covey, D. F. Chirality in membranes: First evidence that enantioselective interactions between cholesterol and cell membrane lipids can be a determinant of membrane physical properties. *J. Supramol. Chem.* **2001**, *1*, 53.
- (137) Cruciani, O.; Borocci, S.; Lamanna, R.; Mancini, G.; Segre, A. L. Chiral recognition of dipeptides in phosphatidylcholine aggregates. *Tetrahedron: Asymmetry* **2006**, *17*, 2731.
- (138) Bombelli, C.; Borocci, S.; Cruciani, O.; Mancini, G.; Monti, D.; Segre, A. L.; Sorrenti, A.; Venanzi, M. Chiral recognition of dipeptides in bio-membrane models: The role of amphiphile hydrophobic chains. *Tetrahedron: Asymmetry* **2008**, *19*, 124.
- (139) Bombelli, C.; Borocci, S.; Lupi, F.; Mancini, G.; Mannina, L.; Segre, A. L.; Viel, S. Chiral recognition of dipeptides in a biomembrane model. *J. Am. Chem. Soc.* **2004**, *126*, 13354.
- (140) Chikhale, E.; Ng, K.-Y.; Burton, P.; Borchardt, R. Hydrogen bonding potential as a determinant of the *in vitro* and *in situ* blood–brain barrier permeability of peptides. *Pharm. Res.* **1994**, *11*, 412.
- (141) Malakoutikhah, M.; Teixidó, M.; Giralt, E. Toward an optimal blood–brain barrier shuttle by synthesis and evaluation of peptide libraries. *J. Med. Chem.* **2008**, *51*, 4881.
- (142) Malakoutikhah, M.; Prades, R.; Teixidó, M.; Giralt, E. *N*-methyl phenylalanine-rich peptides as highly versatile blood–brain barrier shuttles. *J. Med. Chem.* **2010**, *53*, 2354.
- (143) Malakoutikhah, M.; Guixer, B.; Arranz-Gibert, P.; Teixido, M.; Giralt, E. 'A la carte' peptide shuttles: tools to increase their passage across the blood-brain barrier. *ChemMedChem* **2014**, *9*, 1594.
- (144) Di, L.; Kerns, E. H.; Fan, K.; McConnell, O. J.; Carter, G. T. High throughput artificial membrane permeability assay for blood–brain barrier. *Eur. J. Med. Chem.* **2003**, *38*, 223.
- (145) Chiang, Y.-C.; Lin, Y.-J.; Horng, J.-C. Stereoelectronic effects on the transition barrier of polyproline conformational interconversion. *Protein Sci.* **2009**, *18*, 1967.
- (146) MacArthur, M. W.; Thornton, J. M. Influence of proline residues on protein conformation. *J. Mol. Biol.* **1991**, *218*, 397.
- (147) Pujals, S.; Giralt, E. Proline-rich, amphipathic cell-penetrating peptides. *Adv. Drug Del. Rev.* **2008**, *60*, 473.
- (148) Ghose, A. K.; Herbertz, T.; Hudkins, R. L.; Dorsey, B. D.; Mallamo, J. P. Knowledge-based, central nervous system (CNS) lead selection and lead optimization for CNS drug discovery. *ACS Chem. Neurosci.* **2011**, *3*, 50.
- (149) Kansy, M.; Senner, F.; Gubernator, K. Physicochemical high throughput screening: Parallel artificial membrane permeation assay in the description of passive absorption processes. *J. Med. Chem.* **1998**, *41*, 1007.
- (150) Katzenschlager, R.; Poewe, W. Parkinson disease: Intestinal levodopa infusion in PD - The first randomized trial. *Nat. Rev. Neurol.* **2014**, *10*, 128.
- (151) Olanow, C. W.; Obeso, J. A.; Stocchi, F. Continuous dopamine-receptor treatment of Parkinson's disease: scientific rationale and clinical implications. *Lancet Neurol.* **2006**, *5*, 677.
- (152) Vossler, D. G.; Morris Iii, G. L.; Harden, C. L.; Montouris, G.; Faught, E.; Kanner, A. M.; Fix, A.; French, J. A. Tiagabine in clinical practice: Effects on seizure control and behavior. *Epilepsy Behav.* **2013**, *28*, 211.
- (153) Del Amo, E. M.; Urtti, A.; Yliperttula, M. Pharmacokinetic role of L-type amino acid transporters LAT1 and LAT2. *Eur. J. Pharm. Sci.* **2008**, *35*, 161.
- (154) Tomlinson, C. L.; Stowe, R.; Patel, S.; Rick, C.; Gray, R.; Clarke, C. E. Systematic review of levodopa dose equivalency reporting in Parkinson's disease. *Mov. Disord.* **2010**, *25*, 2649.
- (155) Cannazza, G.; Di Stefano, A.; Mosciatti, B.; Braghiroli, D.; Baraldi, M.; Pinnen, F.; Sozio, P.; Benatti, C.; Parenti, C. Detection of levodopa, dopamine and its metabolites in rat striatum dialysates

- following peripheral administration of L-DOPA prodrugs by mean of HPLC–EC. *J. Pharm. Biomed. Anal.* **2005**, *36*, 1079.
- (156) Di Stefano, A.; Carafa, M.; Sozio, P.; Pinnen, F.; Braghiroli, D.; Orlando, G.; Cannazza, G.; Ricciutelli, M.; Marianecchi, C.; Santucci, E. Evaluation of rat striatal L-Dopa and DA concentration after intraperitoneal administration of l-dopa prodrugs in liposomal formulations. *J. Control. Release* **2004**, *99*, 293.
- (157) Hawkins, R. A.; Mokashi, A.; Simpson, I. A. An active transport system in the blood–brain barrier may reduce levodopa availability. *Exp. Neurol.* **2005**, *195*, 267.
- (158) Di Stefano, A.; Sozio, P.; Cerasa, L. Antiparkinson prodrugs. *Molecules* **2008**, *13*, 46.
- (159) Pinnen, F.; Cacciatore, I.; Cornacchia, C.; Sozio, P.; Iannitelli, A.; Costa, M.; Pecci, L.; Nasuti, C.; Cantalamessa, F.; Di Stefano, A. Synthesis and study of L-Dopa–glutathione codrugs as new anti-Parkinson agents with free radical scavenging properties. *J. Med. Chem.* **2007**, *50*, 2506.
- (160) Barrett-Jolley, R. Nipecotinic acid directly activates GABAA-like ion channels. *Br. J. Pharmacol.* **2001**, *133*, 673.
- (161) Ali, F. E.; Bondinell, W. E.; Dandridge, P. A.; Frazee, J. S.; Garvey, E.; Girard, G. R.; Kaiser, C.; Ku, T. W.; Lafferty, J. J.; Moonsammy, G. I.; et al. Orally active and potent inhibitors of gamma-aminobutyric acid uptake. *J. Med. Chem.* **1985**, *28*, 653.
- (162) Krosgaard-Larsen, P.; Johnston, G. A. R. Inhibition of GABA uptake in rat brain slices by nipecotinic acid, various isoxazoles and related compounds. *J. Neurochem.* **1975**, *25*, 797.
- (163) Flamant-Robin, C.; Wang, Q.; Chiaroni, A.; Sasaki, N. A. An efficient method for the stereoselective synthesis of *cis*-3-substituted prolines: Conformationally constrained α -amino acids. *Tetrahedron* **2002**, *58*, 10475.
- (164) Belokon, Y. N.; Bulychev, A. G.; Pavlov, V. A.; Fedorova, E. B.; Tsyryapkin, V. A.; Bakhmutov, V. A.; Belikov, V. M. Synthesis of enantio- and diastereoisomerically pure substituted prolines via condensation of glycine with olefins activated by a carbonyl group. *J. Chem. Soc., Perkin Trans. 1* **1988**, 2075.
- (165) Fields, G. B.; Noble, R. L. Solid phase peptide synthesis utilizing 9-fluorenylmethoxycarbonyl amino acids. *Int. J. Pept. Protein Res.* **1990**, *35*, 161.
- (166) Carpino, L. A.; El-Faham, A.; Minor, C. A.; Albericio, F. Advantageous applications of azabenzotriazole (triazolopyridine)-based coupling reagents to solid-phase peptide synthesis. *J. Chem. Soc., Chem. Commun.* **1994**, 201.
- (167) Houghten, R. A. General method for the rapid solid-phase synthesis of large numbers of peptides: Specificity of antigen-antibody interaction at the level of individual amino acids. *Proc. Natl. Acad. Sci. U. S. A.* **1985**, *82*, 5131.
- (168) Houghten, R. A.; Pinilla, C.; Blondelle, S. E.; Appel, J. R.; Dooley, C. T.; Cuervo, J. H. Generation and use of synthetic peptide combinatorial libraries for basic research and drug discovery. *Nature* **1991**, *354*, 84.
- (169) Houghten, R. A. Parallel array and mixture-based synthetic combinatorial chemistry: Tools for the next millennium. *Annu. Rev. Pharmacol. Toxicol.* **2000**, *40*, 273.
- (170) Bochicchio, B.; Tamburro, A. M. Polyproline II structure in proteins: Identification by chiroptical spectroscopies, stability, and functions. *Chirality* **2002**, *14*, 782.
- (171) Goodman, M.; Chorev, M. On the concept of linear modified *retro*-peptide structures. *Acc. Chem. Res.* **1979**, *12*, 1.
- (172) Freidinger, R. M.; Veber, D. F. Peptides and their *retro* enantiomers are topologically nonidentical. *J. Am. Chem. Soc.* **1979**, *101*, 6129.
- (173) Li, C.; Pazgier, M.; Li, J.; Li, C.; Liu, M.; Zou, G.; Li, Z.; Chen, J.; Tarasov, S. G.; Lu, W.-Y.; Lu, W. Limitations of peptide *retro*-inverso isomerization in molecular mimicry. *J. Biol. Chem.* **2010**, *285*, 19572.
- (174) Spector, A. A.; Yorek, M. A. Membrane lipid composition and cellular function. *J. Lipid Res.* **1985**, *26*, 1015.
- (175) Lingwood, D.; Simons, K. Lipid rafts as a membrane-organizing principle. *Science* **2010**, *327*, 46.
- (176) Yechiel, E.; Barenholz, Y. Relationships between membrane lipid composition and biological properties of rat myocytes. Effects of aging and manipulation of lipid composition. *J. Biol. Chem.* **1985**, *260*, 9123.
- (177) Boesze-Battaglia, K.; Schimmel, R. Cell membrane lipid composition and distribution: implications for cell function and lessons learned from photoreceptors and platelets. *J. Exp. Biol.* **1997**, *200*, 2927.
- (178) Edidin, M. The state of lipid rafts: From model membranes to cells. *Annu. Rev. Biophys. Biomol. Struct.* **2003**, *32*, 257.
- (179) Simons, K.; Ikonen, E. Functional rafts in cell membranes. *Nature* **1997**, *387*, 569.
- (180) Kummerow, F. A. Modification of cell membrane composition by dietary lipids and its implications for atherosclerosis. *Ann. N.Y. Acad. Sci.* **1983**, *414*, 29.

- (181) SoOderberg, M.; Edlund, C.; Alafuzoff, I.; Kristensson, K.; Dallner, G. Lipid composition in different regions of the brain in Alzheimer's disease/senile dementia of Alzheimer's type. *J. Neurochem.* **1992**, *59*, 1646.
- (182) Norton, W. T.; Abe, T.; Poduslo, S. E.; DeVries, G. H. The lipid composition of isolated brain cells and axons. *J. Neurosci. Res.* **1975**, *1*, 57.
- (183) Santos, C. R.; Schulze, A. Lipid metabolism in cancer. *FEBS J.* **2012**, *279*, 2610.
- (184) Maxfield, F. R.; Tabas, I. Role of cholesterol and lipid organization in disease. *Nature* **2005**, *438*, 612.
- (185) van Meer, G.; Voelker, D. R.; Feigenson, G. W. Membrane lipids: Where they are and how they behave. *Nat. Rev. Mol. Cell Biol.* **2008**, *9*, 112.
- (186) Li, Y. C.; Park, M. J.; Ye, S.-K.; Kim, C.-W.; Kim, Y.-N. Elevated levels of cholesterol-rich lipid rafts in cancer cells are correlated with apoptosis sensitivity induced by cholesterol-depleting agents. *Am. J. Pathol.* **2006**, *168*, 1107.
- (187) Oller-Salvia, B.; Sanchez-Navarro, M.; Giralte, E.; Teixido, M. Blood-brain barrier shuttle peptides: An emerging paradigm for brain delivery. *Chem. Soc. Rev.* **2016**, *45*, 4690.
- (188) Lee, J. H.; Engler, J. A.; Collawn, J. F.; Moore, B. A. Receptor mediated uptake of peptides that bind the human transferrin receptor. *Eur. J. Biochem.* **2001**, *268*, 2004.
- (189) Zong, T.; Mei, L.; Gao, H.; Cai, W.; Zhu, P.; Shi, K.; Chen, J.; Wang, Y.; Gao, F.; He, Q. Synergistic dual-ligand doxorubicin liposomes improve targeting and therapeutic efficacy of brain glioma in animals. *Mol. Pharm.* **2014**, *11*, 2346.
- (190) Du, W.; Fan, Y.; Zheng, N.; He, B.; Yuan, L.; Zhang, H.; Wang, X.; Wang, J.; Zhang, X.; Zhang, Q. Transferrin receptor specific nanocarriers conjugated with functional 7peptide for oral drug delivery. *Biomaterials* **2013**, *34*, 794.
- (191) Kuang, Y.; Jiang, X.; Zhang, Y.; Lu, Y.; Ma, H.; Guo, Y.; Zhang, Y.; An, S.; Li, J.; Liu, L.; Wu, Y.; Liang, J.; Jiang, C. Dual functional peptide-driven nanoparticles for highly efficient glioma-targeting and drug codelivery. *Mol. Pharm.* **2016**, *13*, 1599.
- (192) Han, L.; Huang, R.; Liu, S.; Huang, S.; Jiang, C. Peptide-conjugated PAMAM for targeted doxorubicin delivery to transferrin receptor overexpressed tumors. *Mol. Pharm.* **2010**, *7*, 2156.
- (193) Prades, R. *Towards a universal blood-brain barrier shuttle: Protease-resistant peptide shuttles with capacity to deliver cargos into the central nervous system*, Universitat de Barcelona, 2012.
- (194) Aday, S.; Cecchelli, R.; Hallier-Vanuxeem, D.; Dehouck, M.; Ferreira, L. Stem cell-based human blood–brain barrier models for drug discovery and delivery. *Trends Biotechnol.* **2016**, *34*, 382.
- (195) Abbott, N. J.; Dolman, D. E. M.; Yusof, S. R.; Reichel, A. In *Drug Delivery to the Brain*; Hammarlund-Udenaes, M., de Lange, E. C. M., Thorne, R. G., Eds.; Springer: New York, NY, USA, 2014; Vol. 10, p 163.
- (196) Mandal, H. S.; Kraatz, H.-B. Effect of the surface curvature on the secondary structure of peptides adsorbed on nanoparticles. *J. Am. Chem. Soc.* **2007**, *129*, 6356.
- (197) Khlebtsov, N.; Dykman, L. Biodistribution and toxicity of engineered gold nanoparticles: a review of *in vitro* and *in vivo* studies. *Chem. Soc. Rev.* **2011**, *40*, 1647.
- (198) Fletcher, M. D.; Campbell, M. M. Partially modified *retro-inverso* peptides: Development, synthesis, and conformational behavior. *Chem. Rev.* **1998**, *98*, 763.
- (199) Chatterjee, J.; Rechenmacher, F.; Kessler, H. *N*-methylation of peptides and proteins: An important element for modulating biological functions. *Angew. Chem. Int. Ed.* **2013**, *52*, 254.
- (200) Miller, S. C.; Scanlan, T. S. Site-selective *N*-methylation of peptides on solid support. *J. Am. Chem. Soc.* **1997**, *119*, 2301.
- (201) Artursson, P.; Palm, K.; Luthman, K. Caco-2 monolayers in experimental and theoretical predictions of drug transport. *Adv. Drug Del. Rev.* **2012**, *64*, Supplement, 280.
- (202) Patani, G. A.; LaVoie, E. J. Bioisosterism: A rational approach in drug design. *Chem. Rev.* **1996**, *96*, 3147.
- (203) Cramer, R. D.; Clark, R. D.; Patterson, D. E.; Ferguson, A. M. Bioisosterism as a molecular diversity descriptor: Steric fields of single “topomeric” conformers. *J. Med. Chem.* **1996**, *39*, 3060.
- (204) Leach, A. R.; Gillet, V. J.; Lewis, R. A.; Taylor, R. Three-dimensional pharmacophore methods in drug discovery. *J. Med. Chem.* **2010**, *53*, 539.
- (205) Markt, P.; Feldmann, C.; Rollinger, J. M.; Raduner, S.; Schuster, D.; Kirchmair, J.; Distinto, S.; Spitzer, G. M.; Wolber, G.; Laggner, C.; Altmann, K.-H.; Langer, T.; Gertsch, J. Discovery of novel CB2 receptor ligands by a pharmacophore-based virtual screening workflow. *J. Med. Chem.* **2009**, *52*, 369.
- (206) Cecchelli, R.; Berezowski, V.; Lundquist, S.; Culot, M.; Renftel, M.; Dehouck, M.-P.; Fenart, L. Modelling of the blood-brain barrier in drug discovery and development. *Nat. Rev. Drug Discov.* **2007**, *6*, 650.

- (207) Balimane, P. V.; Chong, S. Cell culture-based models for intestinal permeability: A critique. *Drug Discov. Today* **2005**, *10*, 335.
- (208) Wilhelm, I.; Krizbai, I. A. *In vitro* models of the blood–brain barrier for the study of drug delivery to the brain. *Mol. Pharm.* **2014**, *11*, 1949.
- (209) Mensch, J.; Melis, A.; Mackie, C.; Verreck, G.; Brewster, M. E.; Augustijns, P. Evaluation of various PAMPA models to identify the most discriminating method for the prediction of BBB permeability. *Eur. J. Pharm. Biopharm.* **2010**, *74*, 495.
- (210) Zhou, Y.; Yoon, J. Recent progress in fluorescent and colorimetric chemosensors for detection of amino acids. *Chem. Soc. Rev.* **2012**, *41*, 52.
- (211) Tang, F.; Ouyang, H.; Yang, J. Z.; Borchardt, R. T. Bidirectional transport of rhodamine 123 and Hoechst 33342, fluorescence probes of the binding sites on P-glycoprotein, across MDCK–MDR1 cell monolayers. *J. Pharm. Sci.* **2004**, *93*, 1185.
- (212) Burlina, F.; Sagan, S.; Bolbach, G.; Chassaing, G. Quantification of the cellular uptake of cell-penetrating peptides by MALDI-TOF mass spectrometry. *Angew. Chem. Int. Ed.* **2005**, *44*, 4244.
- (213) Burlina, F.; Sagan, S.; Bolbach, G.; Chassaing, G. A direct approach to quantification of the cellular uptake of cell-penetrating peptides using MALDI-TOF mass spectrometry. *Nat. Protocols* **2006**, *1*, 200.
- (214) Uchida, Y.; Ito, K.; Ohtsuki, S.; Kubo, Y.; Suzuki, T.; Terasaki, T. Major involvement of Na(+)-dependent multivitamin transporter (SLC5A6/SMVT) in uptake of biotin and pantothenic acid by human brain capillary endothelial cells. *J. Neurochem.* **2015**, *134*, 97.
- (215) Delehanty, J.; Mattoussi, H.; Medintz, I. Delivering quantum dots into cells: Strategies, progress and remaining issues. *Anal. Bioanal. Chem.* **2009**, *393*, 1091.
- (216) Fenart, L.; Cecchelli, R. In *The Blood-Brain Barrier*; Nag, S., Ed.; Humana Press: Totowa, NJ, USA, 2003; Vol. 89, p 277.
- (217) Lundquist, S.; Renftel, M.; Brillault, J.; Fenart, L.; Cecchelli, R.; Dehouck, M.-P. Prediction of drug transport through the blood-brain barrier *in vivo*: A comparison between two *in vitro* cell models. *Pharm. Res.* **2002**, *19*, 976.
- (218) Poller, B.; Wagenaar, E.; Tang, S. C.; Schinkel, A. H. Double-transduced MDCKII cells to study Human P-glycoprotein (ABCB1) and breast cancer resistance protein (ABCG2) interplay in drug transport across the blood–brain barrier. *Mol. Pharm.* **2011**, *8*, 571.
- (219) Pardridge, W. M. Drug transport across the blood-brain barrier. *J. Cereb. Blood Flow Metab.* **2012**, *32*, 1959.
- (220) Domon, B.; Aebersold, R. Mass spectrometry and protein analysis. *Science* **2006**, *312*, 212.
- (221) Aigner, A.; Wolf, S.; Gassen, H. G. Transport and detoxication: Principles, approaches, and perspectives for research on the blood-brain barrier. *Angew. Chem. Int. Ed.* **1997**, *36*, 24.
- (222) Hitchcock, S. A.; Pennington, L. D. Structure–brain exposure relationships. *J. Med. Chem.* **2006**, *49*, 7559.
- (223) Wängler, C.; Chowdhury, S.; Höfner, G.; Djurova, P.; Purisima, E. O.; Bartenstein, P.; Wängler, B.; Fricker, G.; Wanner, K. T.; Schirmacher, R. Shuttle–cargo fusion molecules of transport peptides and the hD2/3 receptor antagonist fallypride: A feasible approach to preserve ligand–receptor binding? *J. Med. Chem.* **2014**, *57*, 4368.
- (224) Vlieghe, P.; Lisowski, V.; Martinez, J.; Khrestchatsky, M. Synthetic therapeutic peptides: Science and market. *Drug Discov. Today* **2010**, *15*, 40.
- (225) Recent patent applications relating to peptide therapeutics. *Nat. Biotech.* **2006**, *24*, 656.
- (226) Bray, B. L. Large-scale manufacture of peptide therapeutics by chemical synthesis. *Nat. Rev. Drug Discov.* **2003**, *2*, 587.
- (227) Antosova, Z.; Mackova, M.; Kral, V.; Macek, T. Therapeutic application of peptides and proteins: Parenteral forever? *Trends Biotechnol.* **2009**, *27*, 628.
- (228) Cheloha, R. W.; Maeda, A.; Dean, T.; Gardella, T. J.; Gellman, S. H. Backbone modification of a polypeptide drug alters duration of action *in vivo*. *Nat. Biotech.* **2014**, *32*, 653.
- (229) Avan, I.; Hall, C. D.; Katritzky, A. R. Peptidomimetics via modifications of amino acids and peptide bonds. *Chem. Soc. Rev.* **2014**, *43*, 3575.
- (230) Harris, J. M.; Chess, R. B. Effect of pegylation on pharmaceuticals. *Nat. Rev. Drug Discov.* **2003**, *2*, 214.
- (231) Schellenberger, V.; Wang, C.-w.; Geething, N. C.; Spink, B. J.; Campbell, A.; To, W.; Scholle, M. D.; Yin, Y.; Yao, Y.; Bogin, O.; Cleland, J. L.; Silverman, J.; Stemmer, W. P. C. A recombinant polypeptide extends the *in vivo* half-life of peptides and proteins in a tunable manner. *Nat. Biotech.* **2009**, *27*, 1186.
- (232) Neefjes, J.; Jongsma, M. L. M.; Paul, P.; Bakke, O. Towards a systems understanding of MHC class I and MHC class II antigen presentation. *Nat. Rev. Immunol.* **2011**, *11*, 823.
- (233) Purcell, A. W.; McCluskey, J.; Rossjohn, J. More than one reason to rethink the use of peptides in vaccine design. *Nat. Rev. Drug Discov.* **2007**, *6*, 404.

- (234) Ishida, T.; Ichihara, M.; Wang, X.; Yamamoto, K.; Kimura, J.; Majima, E.; Kiwada, H. Injection of PEGylated liposomes in rats elicits PEG-specific IgM, which is responsible for rapid elimination of a second dose of PEGylated liposomes. *J. Control. Release* **2006**, *112*, 15.
- (235) Malakoutikhah, M.; Teixidó, M.; Giralt, E. Shuttle-mediated drug delivery to the brain. *Angew. Chem. Int. Ed.* **2011**, *50*, 7998.
- (236) Chen, Y.; Liu, L. Modern methods for delivery of drugs across the blood–brain barrier. *Adv. Drug Del. Rev.* **2012**, *64*, 640.
- (237) Kurzrock, R.; Gabrail, N.; Chandhasin, C.; Moulder, S.; Smith, C.; Brenner, A.; Sankhala, K.; Mita, A.; Elian, K.; Bouchard, D.; Sarantopoulos, J. Safety, pharmacokinetics, and activity of GRN1005, a novel conjugate of Angiopep-2, a peptide facilitating brain penetration, and paclitaxel, in patients with advanced solid tumors. *Mol. Cancer Ther.* **2012**, *11*, 308.
- (238) Steeg, P. S.; Camphausen, K. A.; Smith, Q. R. Brain metastases as preventive and therapeutic targets. *Nat. Rev. Cancer* **2011**, *11*, 352.
- (239) Liu, S.; Guo, Y.; Huang, R.; Li, J.; Huang, S.; Kuang, Y.; Han, L.; Jiang, C. Gene and doxorubicin co-delivery system for targeting therapy of glioma. *Biomaterials* **2012**, *33*, 4907.
- (240) Wishart, D. S.; Bigam, C. G.; Holm, A.; Hodges, R. S.; Sykes, B. D. ¹H, ¹³C and ¹⁵N random coil NMR chemical shifts of the common amino acids. I. Investigations of nearest-neighbor effects. *J. Biomol. NMR* **1995**, *5*, 67.
- (241) Guichard, G.; Benkirane, N.; Zeder-Lutz, G.; van Regenmortel, M. H.; Briand, J. P.; Muller, S. Antigenic mimicry of natural L-peptides with *retro*-inverso-peptidomimetics. *Proc. Natl. Acad. Sci. U. S. A.* **1994**, *91*, 9765.
- (242) Briand, J.-P.; Benkirane, N.; Guichard, G.; Newman, J. F. E.; Van Regenmortel, M. H. V.; Brown, F.; Muller, S. A *retro*-inverso peptide corresponding to the GH loop of foot-and-mouth disease virus elicits high levels of long-lasting protective neutralizing antibodies. *Proc. Natl. Acad. Sci. U. S. A.* **1997**, *94*, 12545.
- (243) Guichard, G.; Muller, S.; van Regenmortel, M.; Briand, J. P.; Mascagni, P.; Giralt, E. Structural limitations to antigenic mimicry achievable with *retroinverso* (all-D-*retro*) peptides. *Trends Biotechnol.* **1996**, *14*, 44.
- (244) Hervé, M.; Maillére, B.; Mourier, G.; Texier, C.; Leroy, S.; Ménez, A. On the immunogenic properties of *retro*-inverso peptides. Total *retro*-inversion of T-cell epitopes causes a loss of binding to MHC II molecules. *Mol. Immunol.* **1997**, *34*, 157.
- (245) Boutin, S.; Monteilhet, V.; Veron, P.; Leborgne, C.; Benveniste, O.; Montus, M. F.; Masurier, C. Prevalence of serum IgG and neutralizing factors against adeno-associated virus (AAV) types 1, 2, 5, 6, 8, and 9 in the healthy population: Implications for gene therapy using AAV vectors. *Hum. Gene Ther.* **2010**, *21*, 704.
- (246) Dintzis, H. M.; Symer, D. E.; Dintzis, R. Z.; Zawadzke, L. E.; Berg, J. M. A comparison of the immunogenicity of a pair of enantiomeric proteins. *Proteins: Struct., Funct., Bioinf.* **1993**, *16*, 306.
- (247) Nayak, S.; Herzog, R. W. Progress and prospects: Immune responses to viral vectors. *Gene Ther.* **2010**, *17*, 295.
- (248) Friedreich, N. Ueber degenerative Atrophie der spinalen Hinterstränge. *Archiv für pathologische Anatomie und Physiologie und für klinische Medizin* **1863**, *26*, 391.
- (249) Schulz, J. B.; Boesch, S.; Burk, K.; Durr, A.; Giunti, P.; Mariotti, C.; Pousset, F.; Schols, L.; Vankan, P.; Pandolfo, M. Diagnosis and treatment of Friedreich Ataxia: A European perspective. *Nat. Rev. Neurol.* **2009**, *5*, 222.
- (250) Vankan, P. Prevalence gradients of Friedreich's Ataxia and R1b haplotype in Europe co-localize, suggesting a common Palaeolithic origin in the Franco-Cantabrian ice age refuge. *J. Neurochem.* **2013**, *126*, 11.
- (251) Giunti, P.; Greenfield, J.; Stevenson, A. J.; Parkinson, M. H.; Hartmann, J. L.; Sandtmann, R.; Piercy, J.; O'Hara, J.; Casas, L. R.; Smith, F. M. Impact of Friedreich's ataxia on health-care resource utilization in the United Kingdom and Germany. *Orphanet J. Rare Dis.* **2013**, *8*, 38.
- (252) Dürr, A.; Cossee, M.; Agid, Y.; Campuzano, V.; Mignard, C.; Penet, C.; Mandel, J.-L.; Brice, A.; Koenig, M. Clinical and genetic abnormalities in patients with Friedreich's Ataxia. *New Engl. J. Med.* **1996**, *335*, 1169.
- (253) Campuzano, V.; Montermini, L.; Moltò, M. D.; Pianese, L.; Cossée, M.; Cavalcanti, F.; Monros, E.; Rodius, F.; Duclos, F.; Monticelli, A.; Zara, F.; Cañizares, J.; Koutnikova, H.; Bidichandani, S. I.; Gellera, C.; Brice, A.; Trouillas, P.; De Michele, G.; Filla, A.; De Frutos, R.; Palau, F.; Patel, P. I.; Di Donato, S.; Mandel, J.-L.; Coccozza, S.; Koenig, M.; Pandolfo, M. Friedreich's Ataxia: Autosomal recessive disease caused by an intronic GAA triplet repeat expansion. *Science* **1996**, *271*, 1423.
- (254) McMurray, C. T. Mechanisms of trinucleotide repeat instability during human development. *Nat. Rev. Genet.* **2010**, *11*, 786.
- (255) Mirkin, S. M. Expandable DNA repeats and human disease. *Nature* **2007**, *447*, 932.

- (256) Kumari, D.; Biacsi, R. E.; Usdin, K. Repeat expansion affects both transcription initiation and elongation in Friedreich Ataxia cells. *J. Biol. Chem.* **2011**, *286*, 4209.
- (257) Filla, A.; De Michele, G.; Cavalcanti, F.; Pianese, L.; Monticelli, A.; Campanella, G.; Coccozza, S. The relationship between trinucleotide (GAA) repeat length and clinical features in Friedreich Ataxia. *Am. J. Hum. Genet.* **1996**, *59*, 554.
- (258) Schöls, L.; Amoiridis, G.; Przuntek, H.; Frank, G.; Epplen, J. T.; Epplen, C. Friedreich's Ataxia. Revision of the phenotype according to molecular genetics. *Brain* **1997**, *120*, 2131.
- (259) Galea, C. A.; Huq, A.; Lockhart, P. J.; Tai, G.; Corben, L. A.; Yiu, E. M.; Gurrin, L. C.; Lynch, D. R.; Gelbard, S.; Durr, A.; Pousset, F.; Parkinson, M.; Labrum, R.; Giunti, P.; Perlman, S. L.; Delatycki, M. B.; Evans-Galea, M. V. Compound heterozygous FXN mutations and clinical outcome in Friedreich Ataxia. *Ann. Neurol.* **2016**, *79*, 485.
- (260) Pianese, L.; Tammara, A.; Turano, M.; De Biase, I.; Monticelli, A.; Coccozza, S. Identification of a novel transcript of X25, the human gene involved in Friedreich Ataxia. *Neurosci. Lett.* **2002**, *320*, 137.
- (261) Xia, H.; Cao, Y.; Dai, X.; Marelja, Z.; Zhou, D.; Mo, R.; Al-Mahdawi, S.; Pook, M. A.; Leimkühler, S.; Rouault, T. A.; Li, K. Novel frataxin isoforms may contribute to the pathological mechanism of Friedreich Ataxia. *PLoS One* **2012**, *7*, e47847.
- (262) Koutnikova, H.; Campuzano, V.; Foury, F.; Dolle, P.; Cazzalini, O.; Koenig, M. Studies of human, mouse and yeast homologues indicate a mitochondrial function for frataxin. *Nat. Genet.* **1997**, *16*, 345.
- (263) Babcock, M.; de Silva, D.; Oaks, R.; Davis-Kaplan, S.; Jiralerspong, S.; Montermini, L.; Pandolfo, M.; Kaplan, J. Regulation of mitochondrial iron accumulation by Yfh1p, a putative homolog of frataxin. *Science* **1997**, *276*, 1709.
- (264) Priller, J.; Scherzer, C. R.; Faber, P. W.; MacDonald, M. E.; Yong, A. B. Frataxin gene of Friedreich's Ataxia is targeted to mitochondria. *Ann. Neurol.* **1997**, *42*, 265.
- (265) Abruzzo, P. M.; Marini, M.; Bolotta, A.; Malisardi, G.; Manfredini, S.; Ghezzi, A.; Pini, A.; Tasco, G.; Casadio, R. Frataxin mRNA isoforms in FRDA patients and normal subjects: Effect of tocotrienol supplementation. *BioMed Res. Int.* **2013**, *2013*, 9.
- (266) Pérez-Luz, S.; Gimenez-Cassina, A.; Fernández-Frías, I.; Wade-Martins, R.; Díaz-Nido, J. Delivery of the 135 kb human frataxin genomic DNA locus gives rise to different frataxin isoforms. *Genomics* **2015**, *106*, 76.
- (267) Bencze, K. Z.; Kondapalli, K. C.; Cook, J. D.; McMahon, S.; Millán-Pacheco, C.; Pastor, N.; Stemmler, T. L. The structure and function of frataxin. *Crit. Rev. Biochem. Mol. Biol.* **2006**, *41*, 269.
- (268) Pastore, A.; Puccio, H. Frataxin: A protein in search for a function. *J. Neurochem.* **2013**, *126*, 43.
- (269) Colin, F.; Martelli, A.; Clémancey, M.; Latour, J.-M.; Gambarelli, S.; Zepieri, L.; Birck, C.; Page, A.; Puccio, H.; Ollagnier de Choudens, S. Mammalian frataxin controls sulfur production and iron entry during *de novo* Fe4S4 cluster assembly. *J. Am. Chem. Soc.* **2013**, *135*, 733.
- (270) Parent, A.; Elduque, X.; Cornu, D.; Belot, L.; Le Caer, J.-P.; Grandas, A.; Toledano, M. B.; D'Autréaux, B. Mammalian frataxin directly enhances sulfur transfer of NFS1 persulfide to both ISCU and free thiols. *Nature Communications* **2015**, *6*, 5686.
- (271) Dolezal, P.; Dancis, A.; Lesuisse, E.; Sutak, R.; Hrdý, I.; Embley, T. M.; Tachezy, J. Frataxin, a conserved mitochondrial protein, in the hydrogenosome of *Trichomonas vaginalis*. *Eukaryot. Cell* **2007**, *6*, 1431.
- (272) Turowski, V. R.; Akin, C.; Maliandi, M. V.; Buchensky, C.; Leaden, L.; Peralta, D. A.; Busi, M. V.; Araya, A.; Gomez-Casati, D. F. Frataxin is localized to both the chloroplast and mitochondrion and is involved in chloroplast Fe-S protein function in *Arabidopsis*. *PLoS One* **2015**, *10*, e0141443.
- (273) Condò, I.; Ventura, N.; Malisan, F.; Rufini, A.; Tomassini, B.; Testi, R. *In vivo* maturation of human frataxin. *Hum. Mol. Genet.* **2007**, *16*, 1534.
- (274) Cavadini, P.; Adamec, J.; Taroni, F.; Gakh, O.; Isaya, G. Two-step processing of human frataxin by mitochondrial processing peptidase: Precursor and intermediate forms are cleaved at different rates. *J. Biol. Chem.* **2000**, *275*, 41469.
- (275) Yoon, T.; Dizin, E.; Cowan, J. A. N-terminal iron-mediated self-cleavage of human frataxin: Regulation of iron binding and complex formation with target proteins. *J. Biol. Inorg. Chem.* **2007**, *12*, 535.
- (276) Schmucker, S.; Argentini, M.; Carelle-Calmels, N.; Martelli, A.; Puccio, H. The *in vivo* mitochondrial two-step maturation of human frataxin. *Hum. Mol. Genet.* **2008**, *17*, 3521.
- (277) Faraj, S. E.; Venturutti, L.; Roman, E. A.; Marino-Buslje, C. B.; Mignone, A.; Tosatto, S. C. E.; Delfino, J. M.; Santos, J. The role of the N-terminal tail for the oligomerization, folding and stability of human frataxin. *FEBS Open Bio* **2013**, *3*, 310.
- (278) Gakh, O.; Ranatunga, W.; Smith, D. Y. t.; Ahlgren, E. C.; Al-Karadaghi, S.; Thompson, J. R.; Isaya, G. Architecture of the Human Mitochondrial Iron-Sulfur Cluster Assembly Machinery. *J. Biol. Chem.* **2016**, *291*, 21296.

- (279) Gakh, O.; Bedekovics, T.; Duncan, S. F.; Smith, D. Y.; Berkholtz, D. S.; Isaya, G. Normal and Friedreich Ataxia cells express different isoforms of frataxin with complementary roles in iron-sulfur cluster assembly. *J. Biol. Chem.* **2010**, *285*, 38486.
- (280) Reetz, K.; Dogan, I.; Costa, A. S.; Dafotakis, M.; Fedosov, K.; Giunti, P.; Parkinson, M. H.; Sweeney, M. G.; Mariotti, C.; Panzeri, M.; Nanetti, L.; Arpa, J.; Sanz-Gallego, I.; Durr, A.; Charles, P.; Boesch, S.; Nachbauer, W.; Klopstock, T.; Karin, I.; Depondt, C.; vom Hagen, J. M.; Schöls, L.; Giordano, I. A.; Klockgether, T.; Bürk, K.; Pandolfo, M.; Schulz, J. B. Biological and clinical characteristics of the European Friedreich's Ataxia consortium for translational studies (EFACTS) cohort: A cross-sectional analysis of baseline data. *Lancet Neurol.* **2015**, *14*, 174.
- (281) De Michele, G.; Filla, A. Movement disorders: Friedreich Ataxia today - preparing for the final battle. *Nat. Rev. Neurol.* **2015**, *11*, 188.
- (282) Aranca, T. V.; Jones, T. M.; Shaw, J. D.; Staffetti, J. S.; Ashizawa, T.; Kuo, S.-H.; Fogel, B. L.; Wilmot, G. R.; Perlman, S. L.; Onyike, C. U.; Ying, S. H.; Zesiewicz, T. A. Emerging therapies in Friedreich's Ataxia. *Neurodegener. Dis. Manag.* **2016**, *6*, 49.
- (283) Anzovino, A.; Lane, D. J. R.; Huang, M. L. H.; Richardson, D. R. Fixing frataxin: 'Ironing out' the metabolic defect in Friedreich's Ataxia. *Br. J. Pharmacol.* **2014**, *171*, 2174.
- (284) Richardson, T. E.; Kelly, H. N.; Yu, A. E.; Simpkins, J. W. Therapeutic strategies in Friedreich's Ataxia. *Brain Res.* **2013**, *1514*, 91.
- (285) Strawser, C. J.; Schadt, K. A.; Lynch, D. R. Therapeutic approaches for the treatment of Friedreich's ataxia. *Expert Rev. Neurother.* **2014**, *14*, 947.
- (286) Pandolfo, M. Treatment of Friedreich's Ataxia. *Expert Opin. Orphan Drugs* **2013**, *1*, 221.
- (287) Parkinson, M. H.; Schulz, J. B.; Giunti, P. Co-enzyme Q10 and idebenone use in Friedreich's Ataxia. *J. Neurochem.* **2013**, *126*, 125.
- (288) Pandolfo, M.; Arpa, J.; Delatycki, M. B.; Le Quan Sang, K. H.; Mariotti, C.; Munnich, A.; Sanz-Gallego, I.; Tai, G.; Tarnopolsky, M. A.; Taroni, F.; Spino, M.; Tricta, F. Deferiprone in Friedreich Ataxia: A 6-Month randomized controlled trial. *Ann. Neurol.* **2014**, *76*, 509.
- (289) Pandolfo, M.; Hausmann, L. Deferiprone for the treatment of Friedreich's Ataxia. *J. Neurochem.* **2013**, *126*, 142.
- (290) Sanz-Gallego, I.; Torres-Aleman, I.; Arpa, J. IGF-1 in Friedreich's Ataxia – Proof-of-concept trial. *Cerebellum Ataxias* **2014**, *1*, 10.
- (291) Cotticelli, M. G.; Crabbe, A. M.; Wilson, R. B.; Shchepinov, M. S. Insights into the role of oxidative stress in the pathology of Friedreich Ataxia using peroxidation resistant polyunsaturated fatty acids. *Redox Biol.* **2013**, *1*, 398.
- (292) Abeti, R.; Uzun, E.; Renganathan, I.; Honda, T.; Pook, M. A.; Giunti, P. Targeting lipid peroxidation and mitochondrial imbalance in Friedreich's Ataxia. *Pharmacol. Res.* **2015**, *99*, 344.
- (293) Arpa, J.; Sanz-Gallego, I.; Rodríguez-de-Rivera, F. J.; Domínguez-Melcón, F. J.; Prefasi, D.; Oliva-Navarro, J.; Moreno-Yanguela, M. Triple therapy with deferiprone, idebenone and riboflavin in Friedreich's Ataxia – open-label trial. *Acta Neurol. Scand.* **2014**, *129*, 32.
- (294) Rufini, A.; Fortuni, S.; Arcuri, G.; Condò, I.; Serio, D.; Incani, O.; Malisan, F.; Ventura, N.; Testi, R. Preventing the ubiquitin–proteasome-dependent degradation of frataxin, the protein defective in Friedreich's Ataxia. *Hum. Mol. Genet.* **2011**, *20*, 1253.
- (295) Jacoby, D.; Rusche, J.; Iudicello, M.; De Mercanti, S.; Clerico, M.; Gibbin, M.; Longo, F.; Miao, W.; Rai, M.; Piga, A.; Pandolfo, M.; Durelli, L. Epigenetic therapy for Friedreich's Ataxia: A phase I clinical trial (PL1.003). *Neurology* **2014**, *82*.
- (296) Soragni, E.; Miao, W.; Iudicello, M.; Jacoby, D.; De Mercanti, S.; Clerico, M.; Longo, F.; Piga, A.; Ku, S.; Campau, E.; Du, J.; Penalver, P.; Rai, M.; Madara, J. C.; Nazor, K.; O'Connor, M.; Maximov, A.; Loring, J. F.; Pandolfo, M.; Durelli, L.; Gottesfeld, J. M.; Rusche, J. R. Epigenetic therapy for Friedreich Ataxia. *Ann. Neurol.* **2014**, *76*, 489.
- (297) Gottesfeld, J. M.; Rusche, J. R.; Pandolfo, M. Increasing frataxin gene expression with histone deacetylase inhibitors as a therapeutic approach for Friedreich's Ataxia. *J. Neurochem.* **2013**, *126*, 147.
- (298) Chan, P. K.; Torres, R.; Yandim, C.; Law, P. P.; Khadayate, S.; Mauri, M.; Grosan, C.; Chapman-Rothe, N.; Giunti, P.; Pook, M.; Festenstein, R. Heterochromatinization induced by GAA-repeat hyperexpansion in Friedreich's Ataxia can be reduced upon HDAC inhibition by vitamin B3. *Hum. Mol. Genet.* **2013**, *22*, 2662.
- (299) Libri, V.; Yandim, C.; Athanasopoulos, S.; Loyse, N.; Natisvili, T.; Law, P. P.; Chan, P. K.; Mohammad, T.; Mauri, M.; Tam, K. T.; Leiper, J.; Piper, S.; Ramesh, A.; Parkinson, M. H.; Huson, L.; Giunti, P.; Festenstein, R. Epigenetic and neurological effects and safety of high-dose nicotinamide in patients with Friedreich's Ataxia: an exploratory, open-label, dose-escalation study. *Lancet* **2014**, *384*, 504.
- (300) Soragni, E.; Gottesfeld, J. M. Translating HDAC inhibitors in Friedreich's ataxia. *Expert Opin. Orphan Drugs* **2016**, *4*, 961.

- (301) Seyer, L.; Greeley, N.; Foerster, D.; Strawser, C.; Gelbard, S.; Dong, Y.; Schadt, K.; Cotticelli, M. G.; Brocht, A.; Farmer, J.; Wilson, R. B.; Lynch, D. R. Open-label pilot study of interferon gamma-1b in Friedreich Ataxia. *Acta Neurol. Scand.* **2015**, *132*, 7.
- (302) Sturm, B.; Stupphann, D.; Kaun, C.; Boesch, S.; Schranzhofer, M.; Wojta, J.; Goldenberg, H.; Scheiber-Mojdehkar, B. Recombinant human erythropoietin: Effects on frataxin expression *in vitro*. *Eur. J. Clin. Invest.* **2005**, *35*, 711.
- (303) Boesch, S.; Nachbauer, W.; Mariotti, C.; Sacca, F.; Filla, A.; Klockgether, T.; Klopstock, T.; Schöls, L.; Jacobi, H.; Büchner, B.; vom Hagen, J. M.; Nanetti, L.; Manicom, K. Safety and tolerability of carbamylated erythropoietin in Friedreich's Ataxia. *Mov. Disord.* **2014**, *29*, 935.
- (304) Egger, K.; Clemm von Hohenberg, C.; Schocke, M. F.; Guttmann, C. R. G.; Wassermann, D.; Wigand, M. C.; Nachbauer, W.; Kremser, C.; Sturm, B.; Scheiber-Mojdehkar, B.; Kubicki, M.; Shenton, M. E.; Boesch, S. White matter changes in patients with Friedreich's Ataxia after treatment with erythropoietin. *J. Neuroimaging* **2014**, *24*, 504.
- (305) Nabhan, J. F.; Wood, K. M.; Rao, V. P.; Morin, J.; Bhamidipaty, S.; LaBranche, T. P.; Gooch, R. L.; Bozal, F.; Bulawa, C. E.; Guild, B. C. Intrathecal delivery of frataxin mRNA encapsulated in lipid nanoparticles to dorsal root ganglia as a potential therapeutic for Friedreich's ataxia. *Sci. Rep.* **2016**, *6*, 20019.
- (306) Vyas, P. M.; Tomamichel, W. J.; Pride, P. M.; Babbey, C. M.; Wang, Q.; Mercier, J.; Martin, E. M.; Payne, R. M. A TAT-frataxin fusion protein increases lifespan and cardiac function in a conditional Friedreich's Ataxia mouse model. *Hum. Mol. Genet.* **2012**, *21*, 1230.
- (307) Evans-Galea, M. V.; Pébay, A.; Dottori, M.; Corben, L. A.; Ong, S. H.; Lockhart, P. J.; Delatycki, M. B. Cell and gene therapy for Friedreich Ataxia: Progress to date. *Hum. Gene Ther.* **2014**, *25*, 684.
- (308) Li, Y.; Polak, U.; Bhalla, A. D.; Rozwadowska, N.; Butler, J. S.; Lynch, D. R.; Dent, S. Y. R.; Napierala, M. Excision of expanded GAA repeats alleviates the molecular phenotype of Friedreich's Ataxia. *Mol. Ther.* **2015**, *23*, 1055.
- (309) Tremblay, J. P.; Chapdelaine, P.; Coulombe, Z.; Rousseau, J. Transcription activator-like effector proteins induce the expression of the frataxin gene. *Hum. Gene Ther.* **2012**, *23*, 883.
- (310) Chapdelaine, P.; Coulombe, Z.; Chikh, A.; Gerard, C.; Tremblay, J. P. A potential new therapeutic approach for Friedreich Ataxia: Induction of frataxin expression with TALE proteins. *Mol Ther Nucleic Acids* **2013**, *2*, e119.
- (311) Sarsero, J. P.; Li, L.; Holloway, T. P.; Voullaire, L.; Gazeas, S.; Fowler, K. J.; Kirby, D. M.; Thorburn, D. R.; Galle, A.; Cheema, S.; Koenig, M.; Williamson, R.; Ioannou, P. A. Human BAC-mediated rescue of the Friedreich Ataxia knockout mutation in transgenic mice. *Mamm. Genome* **2004**, *15*, 370.
- (312) Pook, M. A.; Al-Mahdawi, S.; Carroll, C. J.; Cossée, M.; Puccio, H.; Lawrence, L.; Clark, P.; Lowrie, M. B.; Bradley, J. L.; Cooper, M. J.; Koenig, M.; Chamberlain, S. Rescue of the Friedreich's Ataxia knockout mouse by human YAC transgenesis. *Neurogenetics* **2001**, *3*, 185.
- (313) Fleming, J.; Spinoulas, A.; Zheng, M.; Cunningham, S. C.; Ginn, S. L.; McQuilty, R. C.; Rowe, P. B.; Alexander, I. E. Partial correction of sensitivity to oxidant stress in Friedreich Ataxia patient fibroblasts by frataxin-encoding adeno-associated virus and lentivirus vectors. *Hum. Gene Ther.* **2005**, *16*, 947.
- (314) Perdomini, M.; Belbellaa, B.; Monassier, L.; Reutenauer, L.; Messaddeq, N.; Cartier, N.; Crystal, R. G.; Aubourg, P.; Puccio, H. Prevention and reversal of severe mitochondrial cardiomyopathy by gene therapy in a mouse model of Friedreich's Ataxia. *Nat. Med.* **2014**, *20*, 542.
- (315) Lim, F.; Palomo, G. M.; Mauritz, C.; Gimenez-Cassina, A.; Illana, B.; Wandosell, F.; Diaz-Nido, J. Functional recovery in a Friedreich's Ataxia mouse model by frataxin gene transfer using an HSV-1 amplicon vector. *Mol. Ther.* **2007**, *15*, 1072.
- (316) Gomez-Sebastian, S.; Gimenez-Cassina, A.; Diaz-Nido, J.; Lim, F.; Wade-Martins, R. Infectious delivery and expression of a 135 kb human FRDA genomic DNA locus complements Friedreich's Ataxia deficiency in human cells. *Mol. Ther.* **2007**, *15*, 248.
- (317) Gimenez-Cassina, A.; Wade-Martins, R.; Gomez-Sebastian, S.; Corona, J. C.; Lim, F.; Diaz-Nido, J. Infectious delivery and long-term persistence of transgene expression in the brain by a 135-kb iBAC-FXN genomic DNA expression vector. *Gene Ther.* **2011**, *18*, 1015.
- (318) Kemp, K.; Mallam, E.; Hares, K.; Witherick, J.; Scolding, N.; Wilkins, A. Mesenchymal stem cells restore frataxin expression and increase hydrogen peroxide scavenging enzymes in Friedreich Ataxia fibroblasts. *PLoS One* **2011**, *6*, e26098.
- (319) Jones, J.; Estirado, A.; Redondo, C.; Bueno, C.; Martínez, S. Human adipose stem cell-conditioned medium increases survival of Friedreich's Ataxia cells submitted to oxidative stress. *Stem Cells Dev.* **2012**, *21*, 2817.
- (320) Ku, S.; Soragni, E.; Campau, E.; Thomas, E. A.; Altun, G.; Laurent, L. C.; Loring, J. F.; Napierala, M.; Gottesfeld, J. M. Friedreich's Ataxia induced pluripotent stem cells model intergenerational GAA-TC triplet repeat instability. *Cell Stem Cell* **2010**, *7*, 631.

- (321) Liu, J.; Verma, P. J.; Evans-Galea, M. V.; Delatycki, M. B.; Michalska, A.; Leung, J.; Crombie, D.; Sarsero, J. P.; Williamson, R.; Dottori, M.; Pébay, A. Generation of induced pluripotent stem cell lines from Friedreich Ataxia patients. *Stem Cell Rev.* **2011**, *7*, 703.
- (322) Hick, A.; Wattenhofer-Donzé, M.; Chintawar, S.; Tropel, P.; Simard, J. P.; Vaucamps, N.; Gall, D.; Lambot, L.; André, C.; Reutenauer, L.; Rai, M.; Teletin, M.; Messaddeq, N.; Schiffmann, S. N.; Viville, S.; Pearson, C. E.; Pandolfo, M.; Puccio, H. Neurons and cardiomyocytes derived from induced pluripotent stem cells as a model for mitochondrial defects in Friedreich's ataxia. *Dis. Model. Mech.* **2013**, *6*, 608.
- (323) Banting, F. G.; Best, C. H.; Collip, J. B.; Campbell, W. R.; Fletcher, A. A. Pancreatic extracts in the treatment of diabetes mellitus. *Can. Med. Assoc. J.* **1922**, *12*, 141.
- (324) Leader, B.; Baca, Q. J.; Golan, D. E. Protein therapeutics: A summary and pharmacological classification. *Nat. Rev. Drug Discov.* **2008**, *7*, 21.
- (325) Chalker, J. M.; Bernardes, G. J. L.; Lin, Y. A.; Davis, B. G. Chemical modification of proteins at cysteine: Opportunities in chemistry and biology. *Chem. Asian J.* **2009**, *4*, 630.
- (326) Hoyle, C. E.; Lowe, A. B.; Bowman, C. N. Thiol-click chemistry: A multifaceted toolbox for small molecule and polymer synthesis. *Chem. Soc. Rev.* **2010**, *39*, 1355.
- (327) Chen, X.; Muthoosamy, K.; Pfisterer, A.; Neumann, B.; Weil, T. Site-selective lysine modification of native proteins and peptides via kinetically controlled labeling. *Bioconjugate Chem.* **2012**, *23*, 500.
- (328) Ráindlová, V.; Pohl, R.; Hocek, M. Synthesis of aldehyde-linked nucleotides and DNA and their bioconjugations with lysine and peptides through reductive amination. *Chem. Eur. J.* **2012**, *18*, 4080.
- (329) Joshi, N. S.; Whitaker, L. R.; Francis, M. B. A three-component Mannich-type reaction for selective tyrosine bioconjugation. *J. Am. Chem. Soc.* **2004**, *126*, 15942.
- (330) Jones, M. W.; Mantovani, G.; Blindauer, C. A.; Ryan, S. M.; Wang, X.; Brayden, D. J.; Haddleton, D. M. Direct peptide bioconjugation/PEGylation at tyrosine with linear and branched polymeric diazonium salts. *J. Am. Chem. Soc.* **2012**, *134*, 7406.
- (331) Ban, H.; Nagano, M.; Gavriluk, J.; Hakamata, W.; Inokuma, T.; Barbas, C. F. Facile and stable linkages through tyrosine: Bioconjugation strategies with the tyrosine-click reaction. *Bioconjugate Chem.* **2013**, *24*, 520.
- (332) van Berkel, S. S.; van Eldijk, M. B.; van Hest, J. C. M. Staudinger ligation as a method for bioconjugation. *Angew. Chem. Int. Ed.* **2011**, *50*, 8806.
- (333) Moses, J. E.; Moorhouse, A. D. The growing applications of click chemistry. *Chem. Soc. Rev.* **2007**, *36*, 1249.
- (334) Lutz, J.-F.; Zarafshani, Z. Efficient construction of therapeutics, bioconjugates, biomaterials and bioactive surfaces using azide-alkyne "click" chemistry. *Adv. Drug Del. Rev.* **2008**, *60*, 958.
- (335) Blanco-Canosa, J. B.; Dawson, P. E. An efficient Fmoc-SPPS approach for the generation of thioester peptide precursors for use in native chemical ligation. *Angew. Chem. Int. Ed.* **2008**, *47*, 6851.
- (336) Dawson, P. E.; Kent, S. B. H. Synthesis of native proteins by chemical ligation. *Annu. Rev. Biochem.* **2000**, *69*, 923.
- (337) Rabuka, D. Chemoenzymatic methods for site-specific protein modification. *Curr. Opin. Chem. Biol.* **2010**, *14*, 790.
- (338) Carrico, I. S.; Carlson, B. L.; Bertozzi, C. R. Introducing genetically encoded aldehydes into proteins. *Nat. Chem. Biol.* **2007**, *3*, 321.
- (339) Scheck, R. A.; Dedeo, M. T.; Iavarone, A. T.; Francis, M. B. Optimization of a biomimetic transamination reaction. *J. Am. Chem. Soc.* **2008**, *130*, 11762.
- (340) Gilmore, J. M.; Scheck, R. A.; Esser-Kahn, A. P.; Joshi, N. S.; Francis, M. B. N-terminal protein modification through a biomimetic transamination reaction. *Angew. Chem. Int. Ed.* **2006**, *45*, 5307.
- (341) Witus, L. S.; Francis, M. Site-specific protein bioconjugation via a pyridoxal 5'-phosphate-mediated N-terminal transamination reaction. *Curr. Protoc. Chem. Biol.* **2009**, *2*, 125.
- (342) Dirksen, A.; Hackeng, T. M.; Dawson, P. E. Nucleophilic catalysis of oxime ligation. *Angew. Chem. Int. Ed.* **2006**, *45*, 7581.
- (343) Kalia, J.; Raines, R. T. Hydrolytic stability of hydrazones and oximes. *Angew. Chem. Int. Ed.* **2008**, *47*, 7523.
- (344) Xiao, Q.; Zhang, F.; Nacev, B. A.; Liu, J. O.; Pei, D. Protein N-terminal processing: Substrate specificity of *Escherichia coli* and Human methionine aminopeptidases. *Biochemistry* **2010**, *49*, 5588.
- (345) Frottin, F.; Martinez, A.; Peynot, P.; Mitra, S.; Holz, R. C.; Giglione, C.; Meinel, T. The proteomics of N-terminal methionine cleavage. *Mol. Cell. Proteomics* **2006**, *5*, 2336.
- (346) Mukhopadhyay, D.; Dasso, M. Modification in reverse: The SUMO proteases. *Trends Biochem. Sci.* **2007**, *32*, 286.
- (347) Malakhov, M. P.; Mattern, M. R.; Malakhova, O. A.; Drinker, M.; Weeks, S. D.; Butt, T. R. SUMO fusions and SUMO-specific protease for efficient expression and purification of proteins. *J. Struct. Funct. Genomics* **2004**, *5*, 75.

- (348) Wang, H.; Xiao, Y.; Fu, L.; Zhao, H.; Zhang, Y.; Wan, X.; Qin, Y.; Huang, Y.; Gao, H.; Li, X. High-level expression and purification of soluble recombinant FGF21 protein by SUMO fusion in *Escherichia coli*. *BMC Biotechnol.* **2010**, *10*, 14.
- (349) Rashidian, M.; Mahmoodi, M. M.; Shah, R.; Dozier, J. K.; Wagner, C. R.; Distefano, M. D. A highly efficient catalyst for oxime ligation and hydrazone–oxime exchange suitable for bioconjugation. *Bioconjugate Chem.* **2013**, *24*, 333.
- (350) Temin, H. M. Mixed infection with two types of Rous sarcoma virus. *Virology* **1961**, *13*, 158.
- (351) Rogers, S.; Pfuderer, P. Use of viruses as carriers of added genetic information. *Nature* **1968**, *219*, 749.
- (352) Wirth, T.; Parker, N.; Ylä-Herttuala, S. History of gene therapy. *Gene* **2013**, *525*, 162.
- (353) Yin, H.; Kanasty, R. L.; Eltoukhy, A. A.; Vegas, A. J.; Dorkin, J. R.; Anderson, D. G. Non-viral vectors for gene-based therapy. *Nat. Rev. Genet.* **2014**, *15*, 541.
- (354) Thomas, C. E.; Ehrhardt, A.; Kay, M. A. Progress and problems with the use of viral vectors for gene therapy. *Nat. Rev. Genet.* **2003**, *4*, 346.
- (355) Kotterman, M. A.; Schaffer, D. V. Engineering adeno-associated viruses for clinical gene therapy. *Nat. Rev. Genet.* **2014**, *15*, 445.
- (356) Sena-Estevés, M.; Saeki, Y.; Fraefel, C.; Breakefield, X. O. HSV-1 amplicon vectors—Simplicity and versatility. *Mol. Ther.* **2000**, *2*, 9.
- (357) During, M. J. In *Viral Vectors*; Loewy, A. D., Ed.; Academic Press: San Diego, CA, USA, 1995, p 89.
- (358) Roizmann, B.; Desrosiers, R. C.; Fleckenstein, B.; Lopez, C.; Minson, A. C.; Studdert, M. J. The family Herpesviridae: an update. The Herpesvirus study group of the international committee on taxonomy of viruses. *Arch. Virol.* **1992**, *123*, 425.
- (359) Shizuya, H.; Birren, B.; Kim, U. J.; Mancino, V.; Slepak, T.; Tachiiri, Y.; Simon, M. Cloning and stable maintenance of 300-kilobase-pair fragments of human DNA in *Escherichia coli* using an F-factor-based vector. *Proc. Natl. Acad. Sci. U. S. A.* **1992**, *89*, 8794.
- (360) Connor, M.; Peifer, M.; Bender, W. Construction of large DNA segments in *Escherichia coli*. *Science* **1989**, *244*, 1307.
- (361) Monaco, A. P.; Larin, Z. YACs, BACs, PACs and MACs: Artificial chromosomes as research tools. *Trends Biotechnol.* **1994**, *12*, 280.
- (362) Kim, U.-J.; Birren, B. W.; Slepak, T.; Mancino, V.; Boysen, C.; Kang, H.-L.; Simon, M. I.; Shizuya, H. Construction and characterization of a human bacterial artificial chromosome library. *Genomics* **1996**, *34*, 213.
- (363) Saeki, Y.; Fraefel, C.; Ichikawa, T.; Breakefield, X. O.; Chiocca, E. A. Improved helper virus-free packaging system for HSV amplicon vectors using an ICP27-deleted, oversized HSV-1 DNA in a bacterial artificial chromosome. *Mol. Ther.* **2001**, *3*, 591.
- (364) Hibbitt, O. C.; Wade-Martins, R. Delivery of large genomic DNA inserts >100 kb using HSV-1 amplicons. *Curr. Gene Ther.* **2006**, *6*, 325.
- (365) Kasai, K.; Saeki, Y. DNA-based methods to prepare helper virus-free Herpes amplicon vectors and versatile design of amplicon vector plasmids. *Curr. Gene Ther.* **2006**, *6*, 303.
- (366) Saeki, Y.; Breakefield, X. O.; Chiocca, E. A. In *Viral Vectors for Gene Therapy: Methods and Protocols*; Machida, C. A., Ed.; Humana Press: Totowa, NJ, USA, 2003; Vol. 76, p 51.
- (367) Kellam, B.; De Bank, P. A.; Shakesheff, K. M. Chemical modification of mammalian cell surfaces. *Chem. Soc. Rev.* **2003**, *32*, 327.
- (368) Johnson, D. C.; Baines, J. D. Herpesviruses remodel host membranes for virus egress. *Nat. Rev. Micro.* **2011**, *9*, 382.
- (369) Bigalke, J. M.; Heldwein, E. E. Nuclear exodus: Herpesviruses lead the way. *Annu. Rev. Virol.* **2016**, *3*, 387.
- (370) Loret, S.; Guay, G.; Lippé, R. Comprehensive characterization of extracellular Herpes simplex virus type 1 virions. *J. Virol.* **2008**, *82*, 8605.
- (371) Haanes, E. J.; Nelson, C. M.; Soule, C. L.; Goodman, J. L. The UL45 gene product is required for herpes simplex virus type 1 glycoprotein B-induced fusion. *J. Virol.* **1994**, *68*, 5825.
- (372) Tandon, R.; Mocarski, E.; Conway, J. The A, B, Cs of Herpesvirus capsids. *Viruses* **2015**, *7*, 899.
- (373) Amer, H.; Nypelö, T.; Sulaeva, I.; Bacher, M.; Henniges, U.; Potthast, A.; Rosenau, T. Synthesis and characterization of periodate-oxidized polysaccharides: Dialdehyde xylan (DAX). *Biomacromolecules* **2016**, *17*, 2972.
- (374) Agarwal, P.; Bertozzi, C. R. Site-specific antibody–drug conjugates: The nexus of bioorthogonal chemistry, protein engineering, and drug development. *Bioconjugate Chem.* **2015**, *26*, 176.

- (375) Huang, J.; Qin, H.; Sun, Z.; Huang, G.; Mao, J.; Cheng, K.; Zhang, Z.; Wan, H.; Yao, Y.; Dong, J.; Zhu, J.; Wang, F.; Ye, M.; Zou, H. A peptide N-terminal protection strategy for comprehensive glycoproteome analysis using hydrazide chemistry based method. *Sci. Rep.* **2015**, *5*, 10164.
- (376) Mercer, N.; Ramakrishnan, B.; Boeggeman, E.; Verdi, L.; Qasba, P. K. Use of novel mutant galactosyltransferase for the bioconjugation of terminal N-acetylglucosamine (GlcNAc) residues on live cell surface. *Bioconjugate Chem.* **2013**, *24*, 144.
- (377) Mårdberg, K.; Nyström, K.; Tarp, M. A.; Trybala, E.; Clausen, H.; Bergström, T.; Olofsson, S. Basic amino acids as modulators of an O-linked glycosylation signal of the herpes simplex virus type 1 glycoprotein gC: Functional roles in viral infectivity. *Glycobiology* **2004**, *14*, 571.
- (378) Biller, M.; Mårdberg, K.; Hassan, H.; Clausen, H.; Bolmstedt, A.; Bergström, T.; Olofsson, S. Early steps in O-linked glycosylation and clustered O-linked glycans of herpes simplex virus type 1 glycoprotein C: effects on glycoprotein properties. *Glycobiology* **2000**, *10*, 1259.
- (379) Bulaj, G. Formation of disulfide bonds in proteins and peptides. *Biotechnol. Adv.* **2005**, *23*, 87.
- (380) Mattson, G.; Conklin, E.; Desai, S.; Nielander, G.; Savage, M. D.; Morgensen, S. A practical approach to crosslinking. *Mol. Biol. Rep.* **1993**, *17*, 167.
- (381) Brinkley, M. A brief survey of methods for preparing protein conjugates with dyes, haptens and crosslinking reagents. *Bioconjugate Chem.* **1992**, *3*, 2.
- (382) Cline, G. W.; Hanna, S. B. Kinetics and mechanisms of the aminolysis of N-hydroxysuccinimide esters in aqueous buffers. *J. Org. Chem.* **1988**, *53*, 3583.
- (383) Stannard, L. M.; Fuller, A. O.; Spear, P. G. Herpes simplex virus glycoproteins associated with different morphological entities projecting from the virion envelope. *J. Gen. Virol.* **1987**, *68*, 715.
- (384) Roberts, M. J.; Bentley, M. D.; Harris, J. M. Chemistry for peptide and protein PEGylation. *Adv. Drug Del. Rev.* **2002**, *54*, 459.
- (385) Schellekens, H.; Hennink, W. E.; Brinks, V. The immunogenicity of polyethylene glycol: Facts and fiction. *Pharm. Res.* **2013**, *30*, 1729.
- (386) Sasse, J.; Gallagher, S. R. Staining proteins in gels. *Curr. Protoc. Mol. Biol.* **2009**, *Supplement 85*, 10.6.1.
- (387) Zhang, M.; Vogel, H. J. Determination of the side chain pKa values of the lysine residues in calmodulin. *J. Biol. Chem.* **1993**, *268*, 22420.
- (388) Isom, D. G.; Castañeda, C. A.; Cannon, B. R.; García-Moreno E., B. Large shifts in pKa values of lysine residues buried inside a protein. *Proc. Natl. Acad. Sci. U. S. A.* **2011**, *108*, 5260.
- (389) Fitch, C. A.; Platzer, G.; Okon, M.; Garcia-Moreno E, B.; McIntosh, L. P. Arginine: Its pKa value revisited. *Protein Sci.* **2015**, *24*, 752.
- (390) Sali, D.; Bycroft, M.; Fersht, A. R. Stabilization of protein structure by interaction of α -helix dipole with a charged side chain. *Nature* **1988**, *335*, 740.
- (391) Tanokura, M.; Tasumi, M.; Miyazawa, T. ¹H Nuclear magnetic resonance studies of histidine-containing di- and tripeptides. Estimation of the effects of charged groups on the pKa value of the imidazole ring. *Biopolymers* **1976**, *15*, 393.
- (392) Sancho, J.; Serrano, L.; Fersht, A. R. Histidine residues at the N- and C-termini of α -helices: Perturbed pKas and protein stability. *Biochemistry* **1992**, *31*, 2253.
- (393) Ames, D. E.; Grey, T. F. The synthesis of some N-hydroxyimides. *J. Chem. Soc.* **1955**, 631.
- (394) Kaiser, E.; Colescott, R. L.; Bossinger, C. D.; Cook, P. I. Color test for detection of free terminal amino groups in the solid-phase synthesis of peptides. *Anal. Biochem.* **1970**, *34*, 595.
- (395) Vojtkovsky, T. Detection of secondary amines on solid phase. *Pept. Res.* **1995**, *8*, 236.
- (396) Sieber, P. A new acid-labile anchor group for the solid-phase synthesis of C-terminal peptide amides by the Fmoc method. *Tetrahedron Lett.* **1987**, *28*, 2107.
- (397) Rink, H. Solid-phase synthesis of protected peptide fragments using a trialkoxy-diphenyl-methylester resin. *Tetrahedron Lett.* **1987**, *28*, 3787.
- (398) El-Faham, A.; Funosas, R. S.; Prohens, R.; Albericio, F. COMU: A safer and more effective replacement for benzotriazole-based uronium coupling reagents. *Chem. Eur. J.* **2009**, *15*, 9404.
- (399) Subirós-Funosas, R.; Prohens, R.; Barbas, R.; El-Faham, A.; Albericio, F. Oxyma: An efficient additive for peptide synthesis to replace the benzotriazole-based HOBt and HOAt with a lower risk of explosion. *Chem. Eur. J.* **2009**, *15*, 9394.
- (400) Albericio, F. Developments in peptide and amide synthesis. *Curr. Opin. Chem. Biol.* **2004**, *8*, 211.
- (401) Krchňák, V.; Vágner, J.; Šafář, P.; Lebl, M. Noninvasive continuous monitoring of solid-phase peptide synthesis by acid-base indicator. *Collect. Czech. Chem. Commun.* **1988**, *53*, 2542.
- (402) Cho, J. K.; White, P. D.; Klute, W.; Dean, T. W.; Bradley, M. Self-indicating resins: Sensor beads and in situ reaction monitoring. *J. Comb. Chem.* **2003**, *5*, 632.
- (403) Liu, M.; Mao, X.-a.; Ye, C.; Huang, H.; Nicholson, J. K.; Lindon, J. C. Improved WATERGATE pulse sequences for solvent suppression in NMR spectroscopy. *J. Magn. Reson.* **1998**, *132*, 125.

- (404) Hwang, T. L.; Shaka, A. J. Water suppression that works. Excitation sculpting using arbitrary waveforms and pulsed-field gradients. *J. Magn. Reson., Series A* **1995**, *112*, 275.
- (405) Sugita, Y.; Okamoto, Y. Replica-exchange molecular dynamics method for protein folding. *Chem. Phys. Lett.* **1999**, *314*, 141.
- (406) Case, D. A.; Berryman, J. T.; Betz, R. M.; Cerutti, D. S.; Cheatham, T. E.; III; Darden, T. A.; Duke, R. E.; Giese, T. J.; Gohlke, H.; Goetz, A. W.; Homeyer, N.; Izadi, S.; Janowski, P.; Kaus, J.; Kovalenko, A.; Lee, T. S.; LeGrand, S.; Li, P.; Luchko, T.; Luo, R.; Madej, B.; Merz, K. M.; Monard, G.; Needham, P.; Nguyen, H.; Nguyen, H. T.; Omelyan, I.; Onufriev, A.; Roe, D. R.; Roitberg, A.; Salomon-Ferrer, R.; Simmerling, C. L.; Smith, W.; Swails, J.; Walker, R. C.; Wang, J.; Wolf, R. M.; Wu, X.; York, D. M.; Kollman, P. A. *AMBER 2015*; University of California: San Francisco, CA, USA, 2015.
- (407) Doshi, U.; Hamelberg, D. Reoptimization of the AMBER force field parameters for peptide bond (omega) torsions using accelerated molecular dynamics. *The Journal of Physical Chemistry B* **2009**, *113*, 16590.
- (408) Patriksson, A.; van der Spoel, D. A temperature predictor for parallel tempering simulations. *Phys. Chem. Chem. Phys.* **2008**, *10*, 2073.
- (409) Mongan, J.; Simmerling, C.; McCammon, J. A.; Case, D. A.; Onufriev, A. Generalized born model with a simple, robust molecular volume correction. *J. Chem. Theory Comput.* **2007**, *3*, 156.
- (410) Weiser, J.; Shenkin, P. S.; Still, W. C. Approximate atomic surfaces from linear combinations of pairwise overlaps (LCPO). *J. Comput. Chem.* **1999**, *20*, 217.
- (411) Berendsen, H. J. C.; Postma, J. P. M.; van Gunsteren, W. F.; DiNola, A.; Haak, J. R. Molecular dynamics with coupling to an external bath. *J. Chem. Phys.* **1984**, *81*, 3684.
- (412) Ryckaert, J.-P.; Ciccotti, G.; Berendsen, H. J. C. Numerical integration of the cartesian equations of motion of a system with constraints: Molecular dynamics of n-alkanes. *J. Comput. Phys.* **1977**, *23*, 327.
- (413) R Development Core Team *R: A language and environment for statistical computing*; R Foundation for Statistical Computing: Vienna, Austria, 2010.
- (414) Rueda, M.; Ferrer-Costa, C.; Meyer, T.; Pérez, A.; Camps, J.; Hospital, A.; Gelpí, J. L.; Orozco, M. A consensus view of protein dynamics. *Proc. Natl. Acad. Sci. U. S. A.* **2007**, *104*, 796.
- (415) Van Aalten, D. M. F.; De Groot, B. L.; Findlay, J. B. C.; Berendsen, H. J. C.; Amadei, A. A comparison of techniques for calculating protein essential dynamics. *J. Comput. Chem.* **1997**, *18*, 169.
- (416) Gaillard, P.; de Boer, A. In *Drug Delivery Systems*; Jain, K., Ed.; Humana Press: Totowa, NJ, USA, 2008; Vol. 437, p 161.
- (417) Cecchelli, R.; Aday, S.; Sevin, E.; Almeida, C.; Culot, M.; Dehouck, L.; Coisne, C.; Engelhardt, B.; Dehouck, M.-P.; Ferreira, L. A stable and reproducible human blood-brain barrier model derived from hematopoietic stem cells. *PLoS One* **2014**, *9*, e99733.
- (418) Studier, F. W. Protein production by auto-induction in high-density shaking cultures. *Protein Expr. Purif.* **2005**, *41*, 207.
- (419) Ymeti, A.; Greve, J.; Lambeck, P. V.; Wink, T.; van, H.; Beumer, Wijn, R. R.; Heideman, R. G.; Subramaniam, V.; Kanger, J. S. Fast, ultrasensitive virus detection using a Young interferometer sensor. *Nano Lett.* **2007**, *7*, 394.
- (420) Freund, J.; McDermott, K. Sensitization to horse serum by means of adjuvants. *Exp. Biol. Med.* **1942**, *49*, 548.

SUMMARY IN CATALAN

INTRODUCCIÓ

Evolutivament, el sistema nerviós s'ha anat tornant més complex, esdevenint imprescindible el seu correcte funcionament per a la supervivència. Per això, van aparèixer el crani i les vèrtebres en alguns animals (craniats i vertebrats, respectivament), per protegir l'encèfal i la medul·la espinal de forces mecàniques. Per una altra banda, també van aparèixer barreres cel·lulars que l'aïllaven de la resta del cos per tal de regular selectivament el transport de metabòlits, però també de possibles toxines o intrusions de microorganismes. Quatre són aquestes barreres (**Figura R.1**): meninges, plexe coroideo, epèndima i barrera hematoencefàlica (BHE).

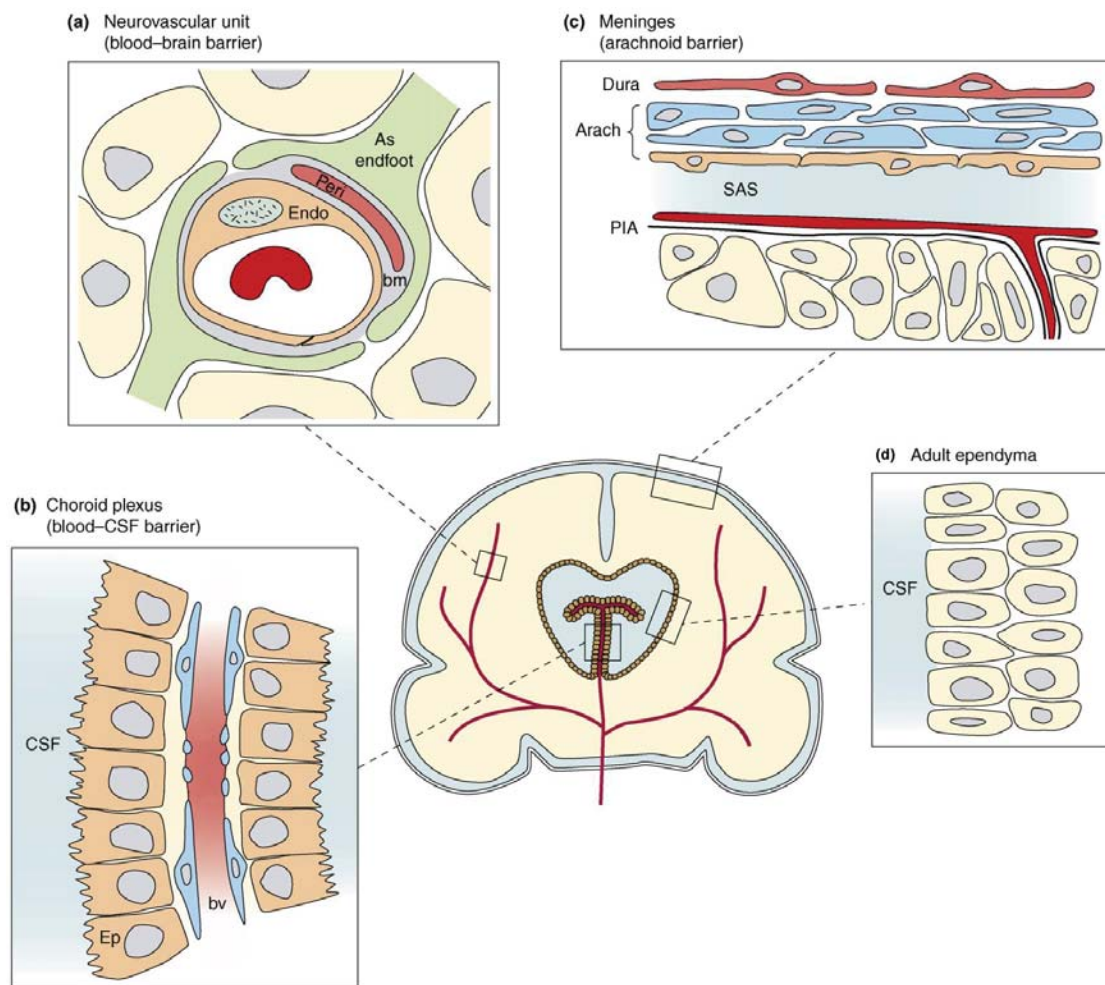


Figura R.1. Barreres del sistema nerviós central (SNC): (a) barrera hematoencefàlica, (b) plexe coroideo, (b) meninges i (d) epèndima. Abreviacions: Endo, cèl·lula endotelial; Peri, pericit; bm, membrana basal; As, astròcit; Ep, cèl·lula epitelial; bv, vas sanguini; Dura, duramàter; Arach, aracnoide; SAS, espai subaracnoïdal; PIA, superfície pial; CSF, fluid cerebroespinal. Adaptat de Saunders *et al.*

La BHE és la barrera que es troba en els capil·lars del cervell, i està formada per diversos tipus cel·lulars (incloent cèl·lules endotelials, perícits, astròcits i neurones) i la matriu extracel·lular (**Figura R.2**). En aquests capil·lars, les cèl·lules endotelials tenen unes unions cèl·lula-cèl·lula especials, anomenades unions estretes, que deixen menys espai intercel·lular. A més, també formen una barrera enzimàtica, i selectiva a través de diversos mecanismes de transport.

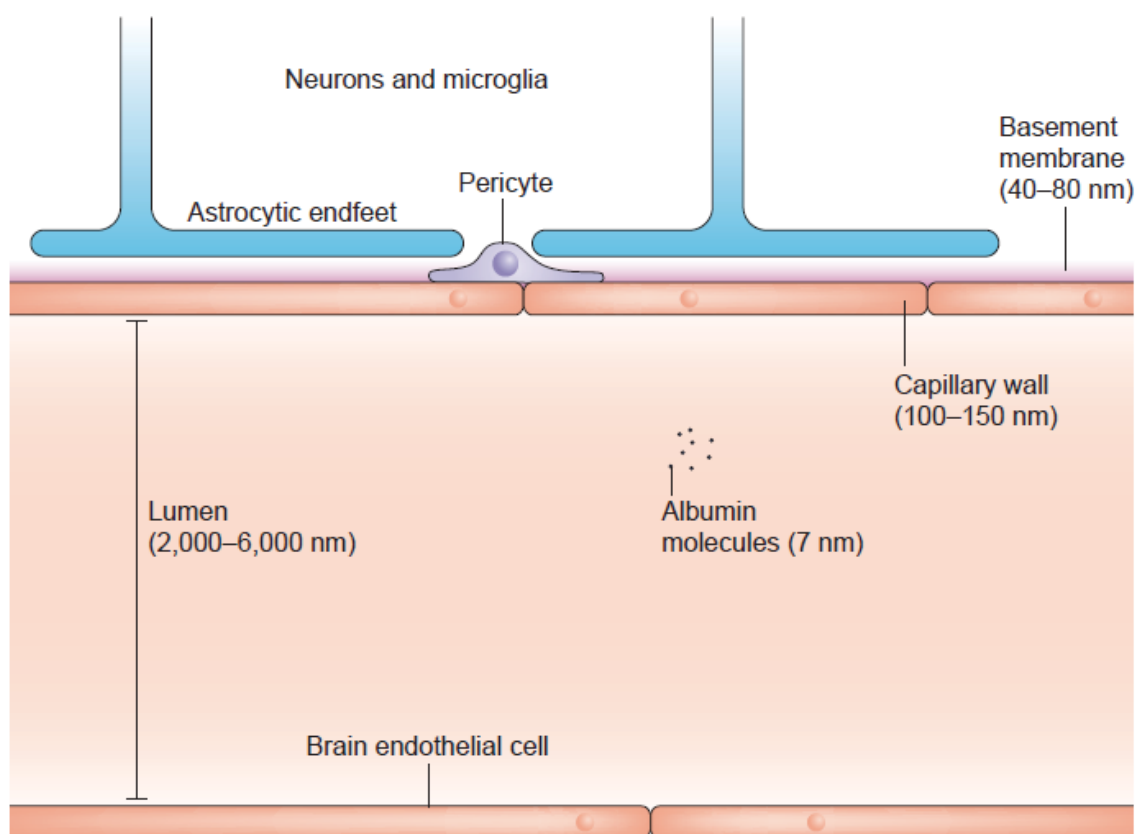


Figura R.2. Estructura de la barrera hematoencefàlica: cèl·lules endotelials, perícits, astròcits i neurones i membrana basal (matriu extracel·lular). Adaptat de Banks.

Aquesta barrera suposa un impediment per al desenvolupament de tractaments per malalties que afecten al sistema nerviós central (SNC), ja que impedeix que més del 98% dels fàrmacs de baix pes molecular no la puguin creuar, tal com gairebé el 100% dels d'alt pes molecular. En aquest sentit, els costos pels tractaments de les malalties que afecten al SNC a Europa van assolir els 798.000 milions d'euros, uns 1.550 € per càpita. Per això, la investigació de mètodes per poder enviar fàrmacs al cervell s'ha anat incrementant exponencialment en els darrers anys.

Diversos mecanismes permeten el transport a través de la BHE. El transport passiu, que no involucra l'ús de la maquinària cel·lular i per tant d'energia, conté dos mecanismes: hidrofílic o paracel·lular, i lipofílic o transcel·lular. El primer, restringit al transport entre cèl·lules, està molt impedit per la presència de les unions estretes. El segon depèn de les característiques fisicoquímiques de compost, que li permetran ser transportat a través de la membrana plasmàtica (5 normes de Lipinski).

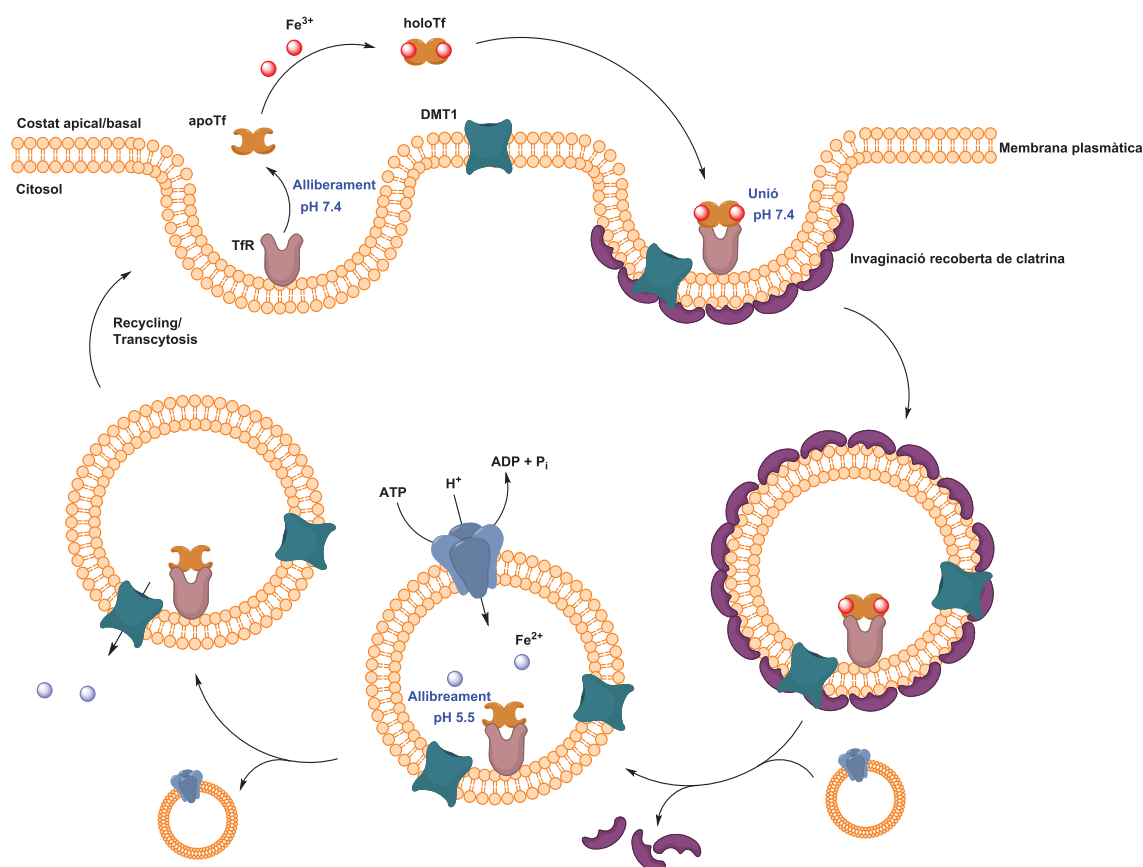


Figura R.3. Entrada de ferro a través de transferrina (Tf) i el seu receptor (TfR). A pH 7.4—exterior cel·lular—, la Tf difèrrica (holoTf) s'uneix al TfR, mentre que no ho fa la apoTf; i a pH 5.5—vesícula endocítica—el ferro és dissociat (després de reduir-lo la NADH:ferricianur oxidoreductasa) i transportat al citosol per la DMT1, però la apoTf es manté unida al TfR; finalment, la apoTf és retornada a la membrana cel·lular i dissociada a pH 7.4. Creada usant ChemBioDraw.

Per una altra banda, hi ha els mecanismes de transport actiu que comprenen els transportadors proteics i el transport endocític. L'últim és interessant des d'un punt de vista terapèutic, ja que permet transportar entitats moleculars més grans. Dins dels mecanismes endocítics s'hi troben la endocitosi mediada per adsorció (EMA) o per receptor (EMR). La EMA es basa en les interaccions més o menys inespecífiques entre molècules carregades

positivament i les membranes plasmàtiques carregades negativament. Per altra banda, la EMR involucra interaccions amb un receptor de la membrana, el qual és endocitat i posteriorment retornat a la membrana. En el cas de les cèl·lules polaritzades, com les endotelials, aquest procés es pot produir d'un costat a l'altre (apical, basal), anomenat transitosi (veure el procés per la transferrina i el seu receptor en la **Figura R.3**).

Durant les últimes dècades s'ha anat veient que gairebé tots els mecanismes de transport cel·lular, amb algunes excepcions, eren usats per algun pèptid o proteïna natural (toxines, lligands de receptors, etc.). Per això, aquestes molècules són avantatjoses per al disseny de llançadores que permetin el transport de fàrmacs al cervell creuant la BHE, anomenats pèptids llançadora.

OBJECTIUS

Aquesta tesi està dividida en quatre capítols que es corresponen als objectius principals. Els primers tres objectius estan centrats en recerca bàsica de pèptids llançadora, mentre que el quart té un caràcter més aplicat.

Objectiu 1: Dissenyar, sintetitzar i avaluar una nova família de pèptids llançadora que creuen a través de transport passiu.

- 1.1. Millorar la baixa solubilitat dels pèptids llançadora basats en (NMePhe)₄.
- 1.2. Millorar la seva capacitat com a llançadores (mantenir el transport un cop s'hi incorpora la molècula terapèutica).
- 1.3. Estudiar el rol de l'estereoquímica en el transport per difusió passiva.

Objectiu 2: Estudiar una nova família de pèptids llançadora que creuen per transcitosi mitjançada per receptor i desenvolupar una metodologia basada en la combinació de l'ús d'espectrometria de masses MALDI-TOF i models *in vitro* (cel·lulars) per avaluar el transport a través de la BHE.

Objectiu 3: Estudiar i comparar les respostes immunogèniques produïdes per pèptids llançadora fets d'aminoàcids L i les seves respectives versions *retro-D*, formats per aminoàcids D.

Objectiu 4: Realitzar uns estudis preliminars amb l'objectiu final de desenvolupar una teràpia per Atàxia de Friedreich (AF) al sistema nerviós central (SNC).

- 4.1. Estudiar la viabilitat d'una teràpia de reemplaçament proteic per AF basada en la conjugació directa de pèptids llançadora a frataxina (FXN).
- 4.2. Millorar els mètodes de bioconjugació per modificar herpesvirus amb pèptids llançadora per desenvolupar una teràpia gènica per AF al SNC.
- 4.3. Caracteritzar fisicoquímicament i biològicament les partícules virals abans i després de modificar-les.

RESULTATS I DISCUSSIÓ

Capítol 1. Estudi de pèptids llançadora que creuen per difusió passiva

El transport de molècules al SNC a través de difusió passiva es fa per la via transcel·lular, ja que la paracel·lular està molt impedida. Per a poder creuar usant la via lipofílica (transcel·lular), les molècules han de tenir unes característiques fisicoquímiques concretes, tals com tenir limitats els grups polars i el pes molecular (més detallat en les 5 normes de Lipinski).

Anteriorment, al laboratori s'havien desenvolupat uns pèptids llançadora basats en (NMePhe)₄ que presentaven un molt bon transport a través de difusió passiva, però la baixa solubilitat (submicromolar) impedia l'ús més pràctic d'aquests compostos. Per això, es va dissenyar un pèptid llançadora en que els seus aminoàcids fossin híbrids entre NMePhe i l'aminoàcid natural *N*-alquilat, amb gran solubilitat en aigua, prolina. Així, el disseny final va ser la fenilprolina (PhPro) (veure **Figura R.4**).

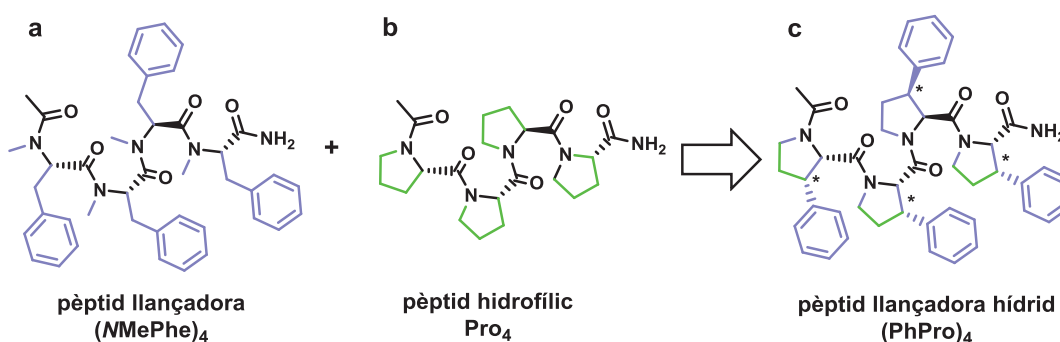


Figura R.4. Estructura del (a) pèptid llançadora (NMePhe)₄, (b) poliprolina hidrofílica Pro₄, i (c) el pèptid llançadora híbrid (PhPro)₄; *homo*-L, C-terminal amida, i N-terminal acetilat. Creada amb ChemBioDraw.

Un cop fet el disseny es va avaluar el transport del pèptid (PhPro)₄, fent servir un model *in vitro* fisicoquímic de transport passiu (PAMPA), i posteriorment es va comparar amb l'anterior pèptid llançadora (NMePhe)₄. El disseny híbrid va mostrar propietats de transport similars a (NMePhe)₄, mentre que la Pro₄ pràcticament no va poder creuar (**Figura R.5**).

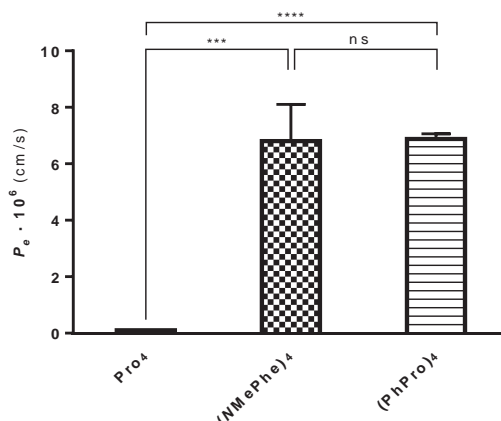


Figura R.5. Transport en PAMPA: *homo*-L Pro₄, *homo*-L (NMePhe)₄ i barreja dels 16 estereoisòmers de (PhPro)₄ (n = 3; mitjana ± SD; significació: ns ≡ no significatiu ($p \geq 0.05$), ** ≡ molt significatiu ($0.001 \leq p < 0.01$), *** ≡ extremadament significatiu ($0.0001 \leq p < 0.001$), **** ≡ extremadament significatiu ($p < 0.0001$)). Creada amb GraphPad.

Adicionalment, també es volia avaluar la capacitat de transportar altres molècules amb rellevància terapèutica. Anteriorment, s'havia demostrat que la (NMePhe)₄ era capaç de transportar NIP i L-DOPA, així que es va avaluar la (PhPro)₄ en PAMPA. Es va observar que el disseny híbrid no només era millor que la (NMePhe)₄ (7 vegades superior), sinó que també mantenia el transport inicial sense portar cap molècula—a diferència de la (NMePhe)₄ que veia el seu transport bastant reduït (**Figura R.6**).

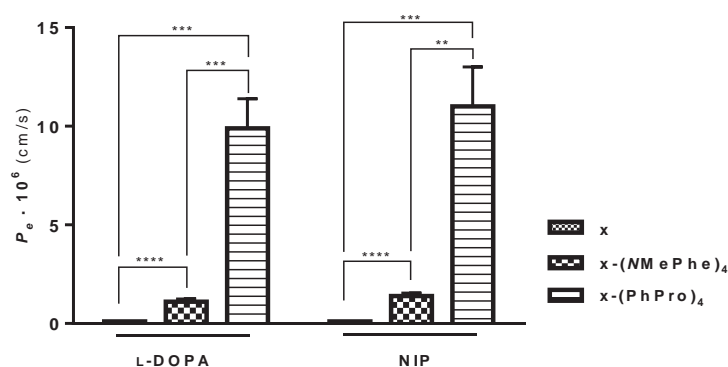


Figura R.6. Transport en PAMPA de L-DOPA i NIP sols o transportats per *homo*-L (NMePhe)₄ o barreja dels 16 estereoisòmers de (PhPro)₄ (n = 3; mitjana ± SD; significació: ns ≡ no significatiu ($p \geq 0.05$), ** ≡ molt significatiu ($0.001 \leq p < 0.01$), *** ≡ extremadament significatiu ($0.0001 \leq p < 0.001$), **** ≡ extremadament significatiu ($p < 0.0001$)). Creada amb GraphPad.

L'objectiu principal d'aquest disseny híbrid era la millora de la solubilitat i per tant es va determinar la solubilitat en aigua del tetrapèptid (PhPro)₄. El valor obtingut va ser intermedi entre la de (NMePhe)₄ (submicromolar) i la de Pro₄ (300 mM), en el rang mil·limolar baix. Això suposa una millora de tres ordres de magnitud respecte al disseny anterior.

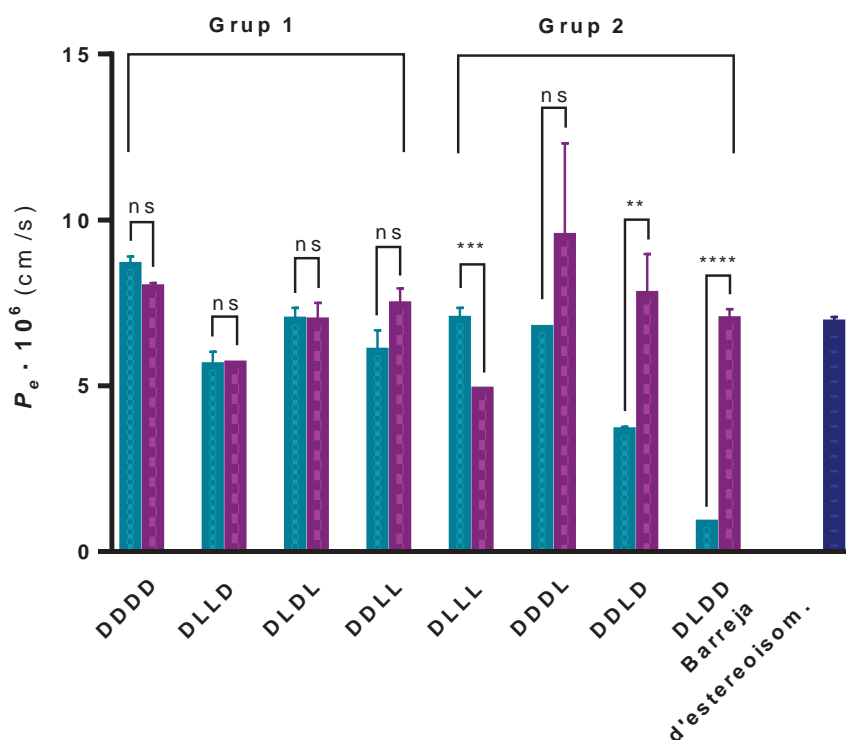


Figura R.7. Transport en PAMPA dels 16 estereoisòmers individuals, aparellats per enantiòmers, i la barreja dels 16 estereoisòmers (columna blau fosc). La columna blau clar correspon a la configuració mostrada en el gràfic (primera columna = DDDD); la columna lila representa l'enantiòmer de la configuració mostrada en el gràfic (primera columna = LLLL) ($n = 3$; mitjana \pm SD; significació: ns \equiv no significantiu ($p \geq 0.05$), ** \equiv molt significantiu ($0.001 \leq p < 0.01$), *** \equiv extremadament significantiu ($0.0001 \leq p < 0.001$), **** \equiv extremadament significantiu ($p < 0.0001$)). Creada amb GraphPad.

Finalment, es va estudiar el rol de l'estereoquímica en el transport per difusió passiva a través de membranes biològiques aprofitant que l'aminoàcid PhPro té dues configuracions *cis* possibles, (*S,S*) i (*R,R*). Així, es va sintetitzar la biblioteca de 16 estereoisòmers de la (PhPro)₄ i es va avaluar per PAMPA. Es va observar que hi havia discriminació enantiomèrica, i que aquesta era més important com més asimètrics eren els pèptids (Grup 2) (**Figura R.7**).

Capítol 2. Estudi de pèptids llançadora que creuen la BHE a través de transcitosi mitjançada per receptor

El descobriment i posterior desenvolupament tant de pèptids llançadora com d'altres compostos que creuin la BHE per transport actiu requereix l'ús de models *in vitro* cel·lulars que simulen aquesta barrera. Tan mateix, es requereix una millora dels mètodes analítics de quantificació per a poder avaluar el transport de compostos assajats a menor concentració, així permetent estudis mecanístics, i condicions més semblants a les fisiològiques.

Es va dissenyar inicialment una biblioteca de 10 anàlegs d'un pèptid llançadora (HAI), el qual s'havia estudiat i desenvolupat prèviament en el laboratori (**Figura R.8**). El propòsit d'aquesta peptidoteca era doble: per una banda, estudiar les diferències de transport segons quin residu s'ha substituït per un aminoàcid anàleg no natural, i per l'altra, fer-la servir per validar i desenvolupar un mètode de quantificació basat en marcatge isotòpic i espectrometria de masses MALDI-TOF.

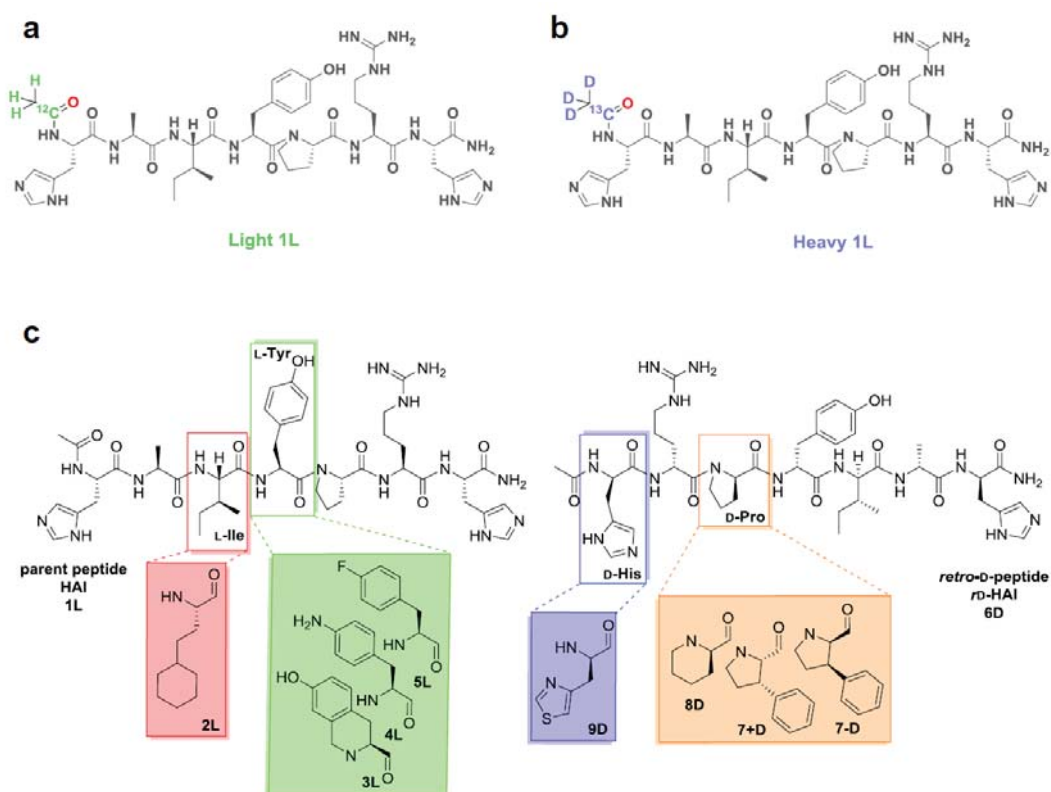


Figura R.8. Pèptid llançadora H-HAIYPRH-NH₂ (1L): versions (a) lleugera, i (b) pesada, ambdues marcades isotòpicament amb un grup acetil; i (c) biblioteca d'anàlegs de HAI (1L) a la esquerra, i de la versió *retro*-D (*rD*-HAI o 6D) a la dreta. Creada amb ChemBioDraw i Microsoft PowerPoint.

El mètode es basa en marcar isotòpicament de manera diferencial cada pèptid, una versió amb un grup acetil sense marcatge (versió lleugera), i una altra amb marcatge (quatre deuteris i un carboni 13; versió pesada) que resulta en un increment de massa de +4 unitats de massa atòmiques (**Figura R.9**). Un dels pèptids és avaluat, i l'altre s'usa com a patró intern per quantificar usant espectrometria de masses MALDI-TOF.

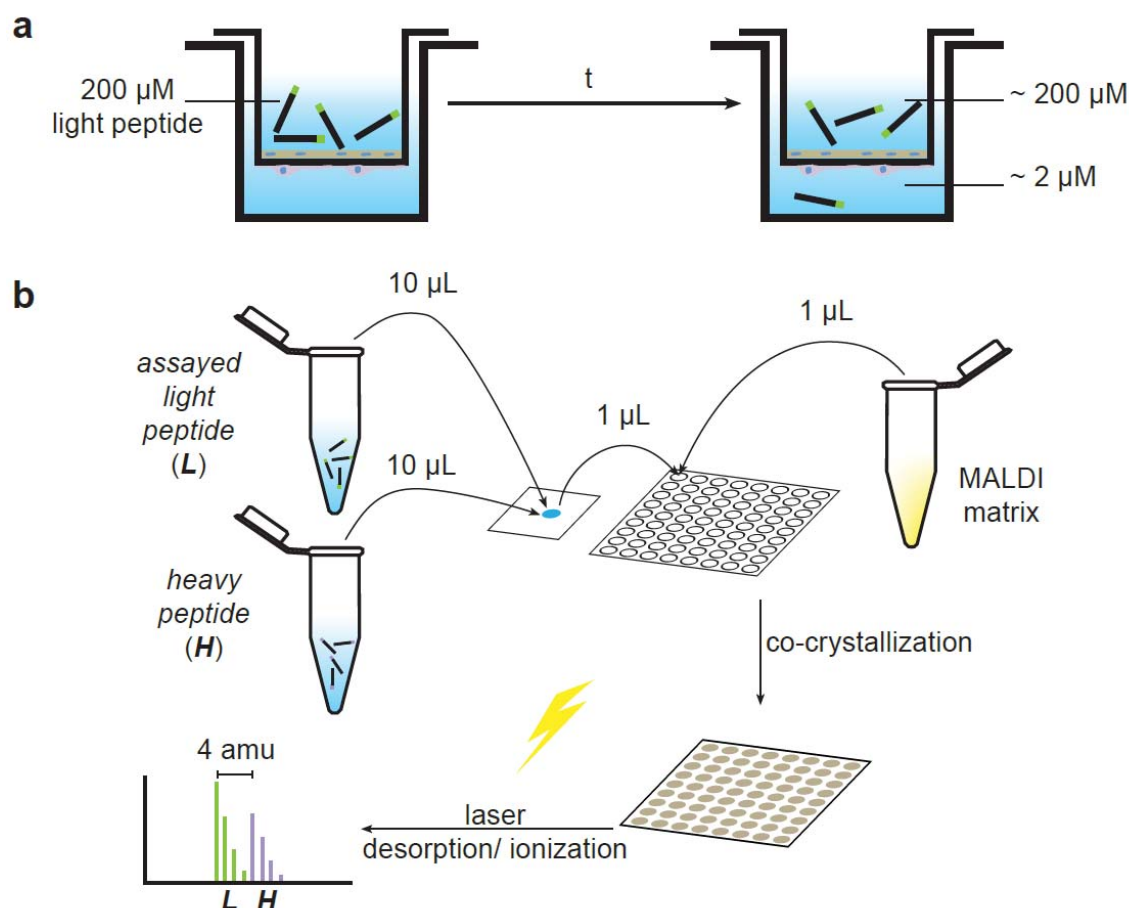


Figura R.9. Esquema del mètode quantificació del transport usant espectrometria de masses MALDI-TOF. El model *in vitro* cel·lular de BHE (a) és preparat en un sistema de pouets on cèl·lules endotelials són cultivades en una membrana que separa dos compartiments (donador i acceptor). Abans de l'experiment, el donador conté el pèptid lleuger a assajar; al final de l'experiment, una quantitat del pèptid haurà passat al pouet acceptor (si s'assaja el pèptid a 200 µM en el compartiment donador, aproximadament una concentració de 2 µM s'ha de quantificar en el pouet acceptor al final de l'experiment). Així, (b) dues al·lotes de la versió pesada es preparen, una a 200 µM i la altra a 2 µM; 10 µL del pèptid lleuger (dels compartiments acceptor i donador) i 10 µL de la versió pesada a una concentració similar són barrejats. Seguidament, 1 µL d'aquesta barreja i 1 µL d'una matriu de MALDI apropiada (per exemple ACH) són col·locats en la placa de MALDI. Finalment, els espectres són adquirits. Creada usant Adobe InDesign.

Al comparar l'anàlisi de les mostres quantificades per RP-HPLC-PDA o utilitzant el nou mètode basat en espectrometria de masses es van observar petites diferències. Tot i això, l'anàlisi conjunt dels resultats amb un mateix mètode mostra que les diferències estadísticament significatives no són iguals pels resultats obtinguts amb cadascun dels mètodes. El mètode de RP-HPLC-PDA mostra pràcticament només diferències entre els pèptids L i D, mentre que la metodologia d'espectrometria de masses revela que les diferències estadísticament significatives són només amb tres anàlegs, tots amb la substitució a la prolina (**Figura R.10**). En dos d'ells el reemplaçament de l'aminoàcid substituït és un dels enantiòmers de PhPro.

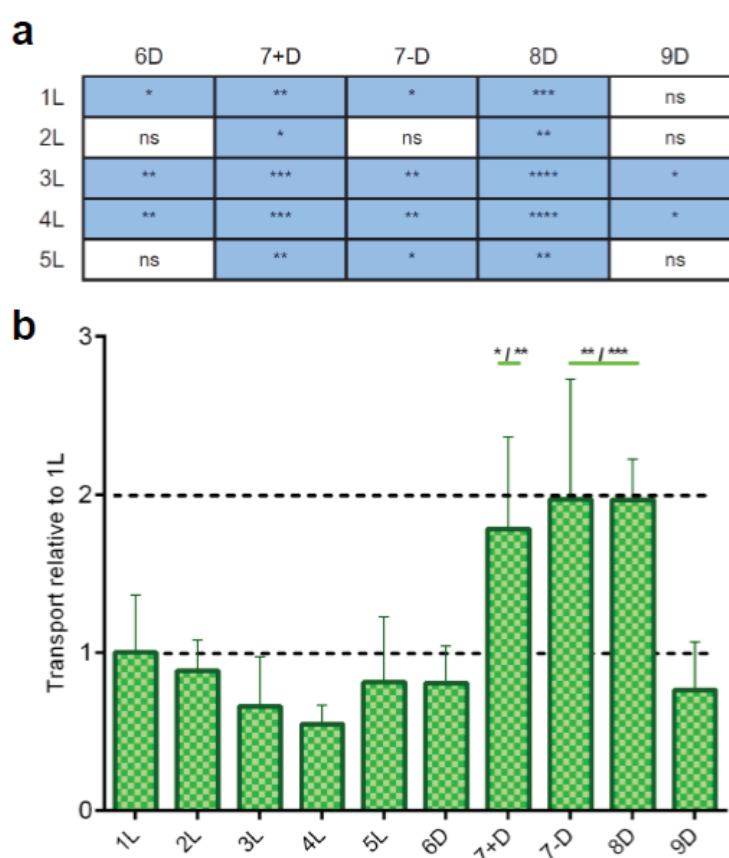


Figura R.10. Transport dels pèptids en el model boví *in vitro* de BHE analitzats per RP-HPLC-PDA (en **blau**) o espectrometria de masses MALDI-TOF (en **verd**); **(a)** quantificació del transport per RP-HPLC-PDA mostra diferències significatives entre pèptids L i D (i també, diferències significatives (*) entre el pèptid 9D amb el 7+D i el 8D); **(b)** significació de la quantificació del transport per MALDI-TOF MS. Significació: ns \equiv no significatiu ($p \geq 0.05$), * \equiv significatiu ($0.01 \leq p < 0.05$), ** \equiv molt significatiu ($0.001 \leq p < 0.01$), *** \equiv extremadament significatiu ($0.0001 \leq p < 0.001$), **** \equiv extremadament significatiu ($p < 0.0001$). Creada usant GraphPad i Adobe InDesign.

Addicionalment, dos d'ells (no s'avalua el pèptid amb la substitució de L-PhPro) s'assagen en un model *in vitro* cel·lular de BHE usant medi de cultiu, revelant que aquestes diferències de transport entre el pèptid origina (HAI) i els anàlegs encara és més gran (4 i 8 vegades) (veure **Figura R.11**).

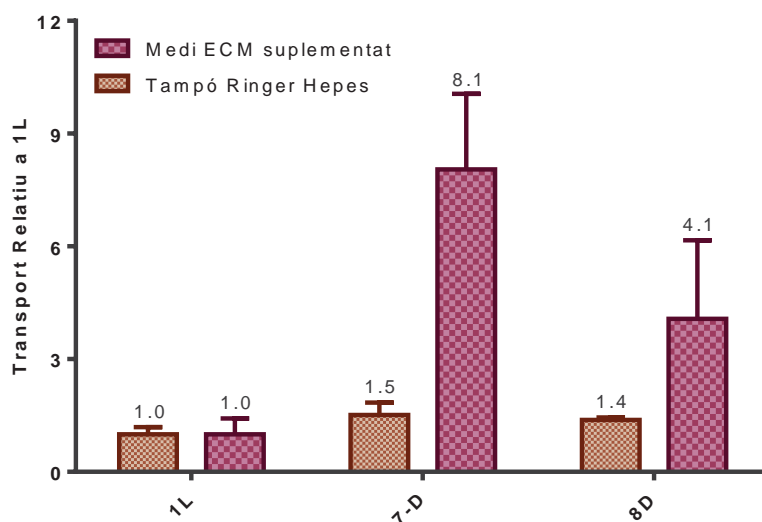


Figura R.11. Transport dels pèptids en el model humà *in vitro* de BHE (usant dissolució tamponada o medi cel·lular durant l'assaig): transport relatiu a 1L. Creada usant GraphPad.

El mètode de quantificació del transport per espectrometria de masses ha permès una millora de la sensibilitat de tres ordres de magnitud (de mil·limolar, pel mètode de RP-HPLC-PDA, a micromolar), i a més augmentar la versatilitat dels mètodes *in vitro* cel·lulars de BHE (permet la quantificació de mostres amb medi cel·lular).

Capítol 3. Estudi de les respostes immunogèniques produïdes per pèptids llançadora

La immunogenicitat dels pèptids, com a lligands nadius dels MHC de classe I i II, s'ha estudiat extensivament. Se sap que hi ha seqüències que produeixen una resposta immunogènica molt més forta que altres. Tanmateix, també s'han estudiat les respostes immunogèniques en front de pèptids D, trobant disparitat en els resultats obtinguts. Així, no es pot predir el grau de resposta immunogènica contra una seqüència d'aminoàcids D concreta.

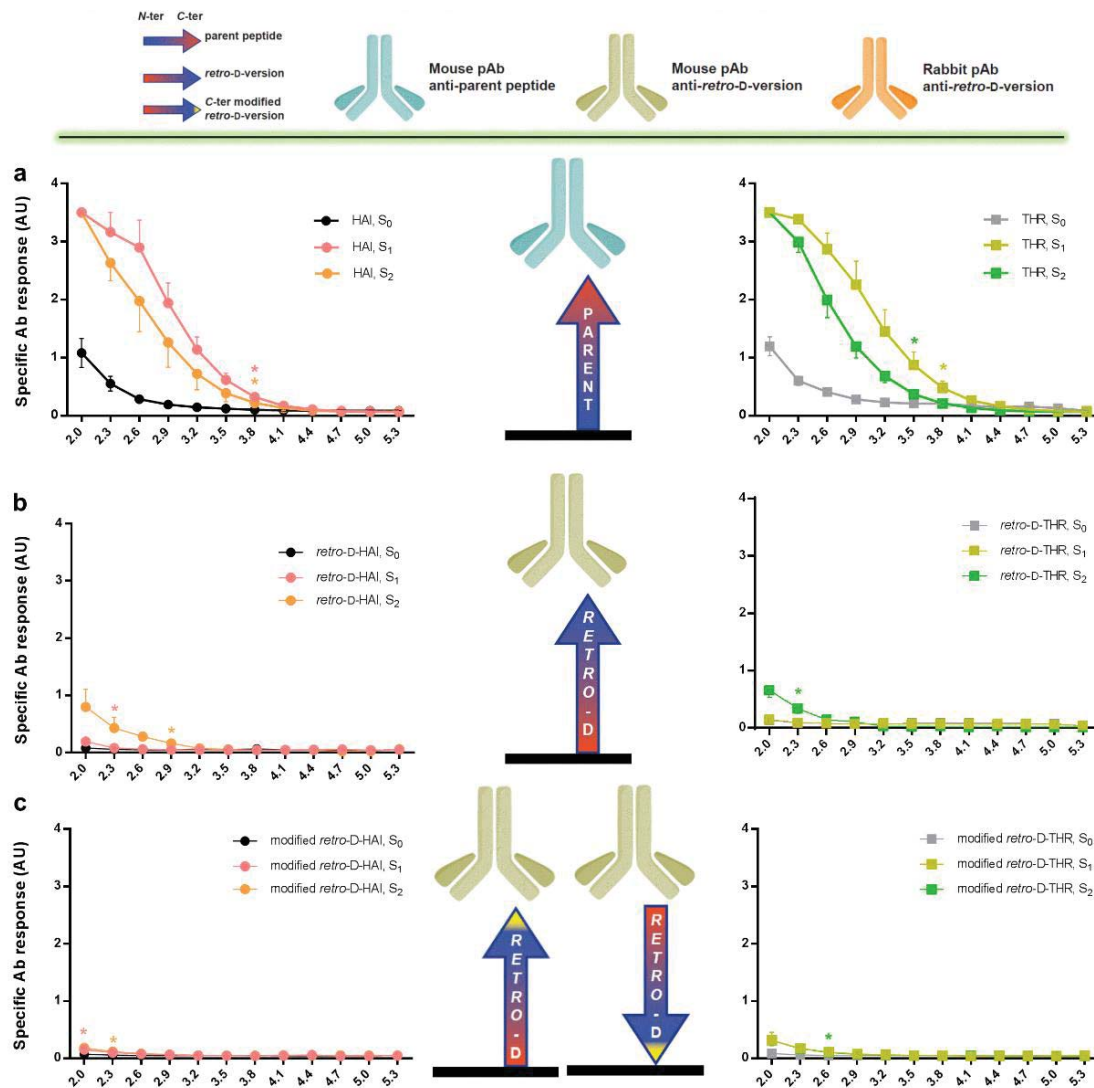


Figura R.12. Avaluació de la resposta immunològica (humoral) de diversos pèptids llançadora en ratolí: (a) sèrum anti-(HAI, THR), sèrum anti-versions *retro-D* avaluades amb els extrems (b) C- o (c) N-terminal exposats. Les primeres diferències significatives de manera consecutiva en les dilucions s'assenyala amb un asterisc. Creada amb GraphPad, Adobe InDesign, ChemBioDraw, Microsoft PowerPoint i Servier Medical Art.

Per tal d'obtenir un resultat quantitatiu de la immunogenicitat dels pèptids llançadora usats en el nostre laboratori (HAI, THR, i les respectives versions *retro-D*), es van immunitzar ratolins amb cadascun dels pèptids sense conjuguar a una altra molècula (**Figura R.12**). S'observa que tots els pèptids produeixen una resposta immunològica baixa, però les versions *retro-D* encara menor.

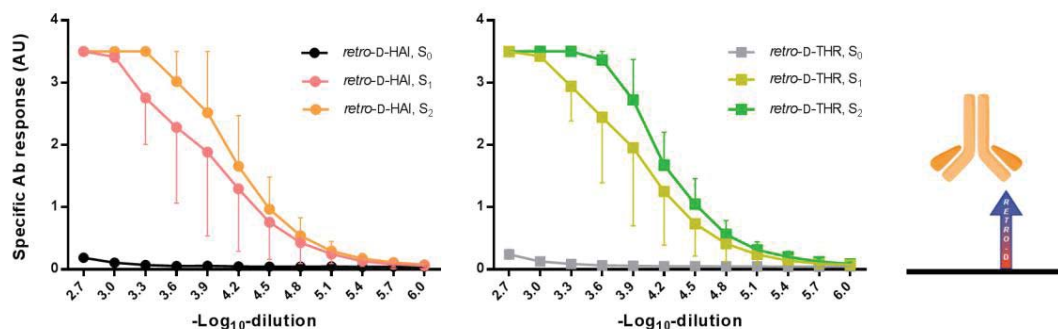


Figura R.13. Titulació de la resposta humoral (conill) en ELISA: sèrum anti-pèptids *retro-D* conjugats a KLH. Creada usant GraphPad, Adobe InDesign i Microsoft PowerPoint.

Per una altra banda, la resposta immunològica (humoral) en conills contra els pèptids *retro-D* conjugats a una molècula de KLH (proteïna que per si sola provoca una forta reacció immunològica) és molt diferent, i en aquest cas, sí que es poden arribar a aïllar els anticossos específics contra els pèptids. Pensem que el fet d'estar conjugats a una molècula que es pot processar és clau per al procés de la resposta immunològica.

Capítol 4. Intentos per desenvolupar una teràpia per Atàxia de Friedreich al SNC

L'atàxia de Friedreich (FRDA) és una malaltia neurodegenerativa de base genètica. La causa principal és una expansió de la repetició del triplet (GAA) localitzada en el primer intró del gen de la frataxina (FXN), una proteïna mitocondrial codificada en el nucli. Això produeix una reducció de l'expressió de FXN, el que provoca alteracions en el metabolisme cel·lular, sobretot en metabolisme del ferro i estat redox. Pel fet de que l'origen de la FRDA sigui una deficiència en la funció de la proteïna, i no un mal funcionament d'aquesta, la malaltia és recessiva. Això fa que una teràpia de reemplaçament proteic sigui, en principi, una opció adequada. Per una altra banda, com que només hi ha un gen implicat, és a dir que és monogènica, la teràpia gènica també es contempla com a opció, ja que n'hi ha prou amb tenir una còpia del gen que expressi la proteïna funcional.

Així, vam explorar inicialment el desenvolupament d'una teràpia de reemplaçament proteic. L'extrem *N*-terminal de la proteïna conté la senyal de localització mitocondrial, la qual es processa durant la translocació de la proteïna al mitocondri. Per això, es va dissenyar el constructe terapèutic amb el pèptid llançadora unit a l'extrem *N*-terminal de la frataxina (un cop processat, queda la proteïna madura).

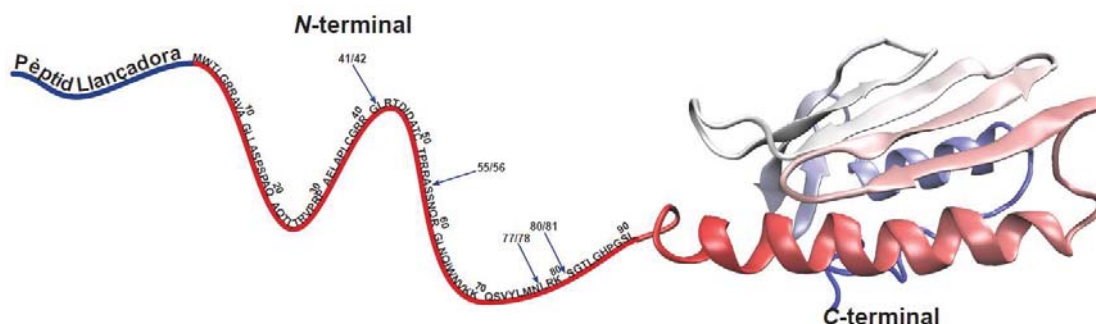


Figura R.14. Constructe dissenyat per la teràpia de reemplaçament proteic per FRDA al SNC: (pèptid llançadora)–FXN^{1–210}. S'observa els llocs de proteòlisi del *N*-terminal. Creada amb Visual Molecular Dynamics (VMD) i Adobe InDesign, fent servir la estructura PDB ID# 1LY7.

Tan mateix, aquesta estratègia no va tenir èxit degut a la ràpida hidròlisi de la proteïna, que no va permetre dur a terme la bioconjugació—la velocitat de proteòlisi era major que la velocitat de la reacció de bioconjugació. Tot i això, es va fer un seguiment de la estabilitat de la proteïna durant 6 mesos a 4, -20 i -80°C usant diverses tècniques de caracterització (MALDI-TOF, HPLC, HPLC-MS, SDS-PAGE, CD).

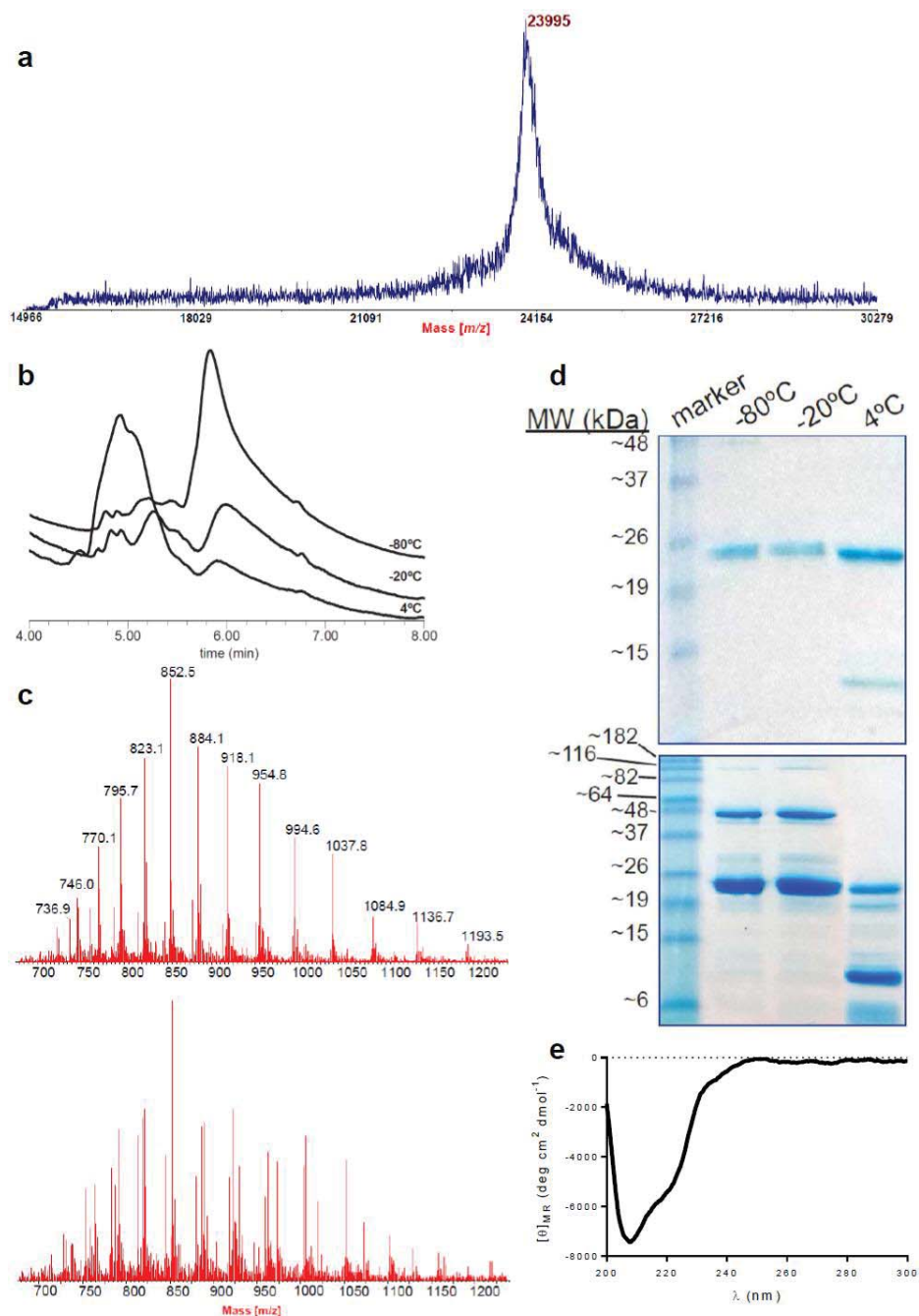


Figura R.15. Estabilitat de la FXN: (a) Espectre de MALDI-TOF de la proteïna a temps zero; (b) cromatogrames de RP-HPLC de les mostres guardades durant 6 mesos a 4, -20 i -80°C, on es pot veure un augment de degradació de -80 a 4°C (el pic a 6 min correspon a FXN, la resta és proteïna degradada); (c) espectre de HPLC-MS ionització per electrospai (ESI) de les mostres preservades a (**part superior**) -20 i (**part inferior**) 4°C durant una setmana (la mostra guardada a -80°C, similar a la de -20°C); (d) anàlisi per SDS-PAGE de les mostres després de (**part superior**) 4 setmanes i (**part inferior**) 3 mesos (marker: BenchMark Pre-Stained Protein Ladder, Invitrogen); i (e) espectre de CD de FXN en tampó fosfat 50 mM, pH 6.5. Creada usant GraphPad, Adobe Illustrator i InDesign.

La proteïna resulta ser poc estable a 4°C (vida mitjana de menys d'una setmana), mentre que a -20 i -80°C l'estabilitat es manté millor (mesos). Veure la **Taula R.1** per un resum de resultats, i la **Figura R.15** per la caracterització amb les diverses tècniques.

Taula R.1. Estabilitat de la frataxina a llarg termini a diverses temperatures, mostrant les diferències respecte la mostra temps zero.

Mètode d'anàlisi	Temperatura de preservació (°C)		
	4	-20	-80
MALDI-TOF ^{oo}	<i>n.d.</i>	<i>n.d.</i>	<i>n.d.</i>
HPLC-PDA	1 setmana	3 mesos	6 mesos
HPLC-MS	1 setmana	4 setmanes	6 mesos
SDS-PAGE	1 setmana	-	-
CD ^{pp}	<i>n.c.</i>	<i>n.c.</i>	<i>n.c.</i>

Addicionalment, es va analitzar l'estabilitat de la proteïna a 37°C (**Figura R.16**). S'observa que la proteïna s'ha hidrolitzat gairebé completament al cap de 7 h, i a les 21 h ni es detecta la banda.

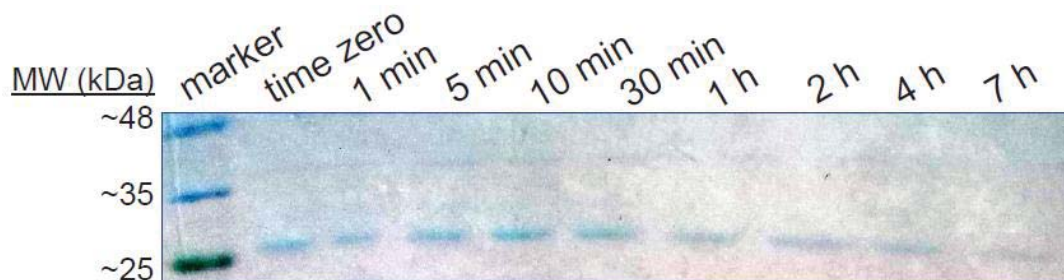


Figura R.16. Estabilitat de la frataxina a 37°C tampó fosfat pH 6.5, analitzat per SDS-PAGE (marcador: BlueStar Prestained Protein Marker, Nippon Genetics). Banda no observada després de 21 h (no ensenyat). Creada amb Adobe InDesign.

D'altra banda, el gen de la frataxina codifica per diverses isoformes (**Taula R.2**) que són expressades diferencialment en diversos teixits. Això dificulta una teràpia de reemplaçament proteic on es tinguin en compte totes aquestes isoformes. En canvi, el grup del Prof. Díaz-Nido ha desenvolupat unes partícules virals, basades en herpesvirus (HSV-1), que contenen tot el gen de la frataxina i que són capaces d'expressar les isoformes I, II i III. També s'ha demostrat la seva capacitat infectiva i terapèutica *in vivo*.

^{oo} *n.d.* ≡ no detectat, només pel temps zero.

^{pp} *n.c.* ≡ sense canvis observats.

Taula R.2. Isoformes metabòliques de la frataxina.

Nom de la isoforma	Seqüència	Proteòlisi	Longitud (nº residus)
precursor, <i>p</i>	FXN ¹⁻²¹⁰	-	210
intermedi ₄₂ , <i>i</i> ₄₂	FXN ⁴²⁻²¹⁰	MPP	169
madura ₅₆ , <i>m</i> ₅₆	FXN ⁵⁶⁻²¹⁰	MPP	155
degradada ₇₈ , <i>d</i> ₇₈	FXN ⁷⁸⁻²¹⁰	Ferro	133
madura ₈₁ , <i>m</i> ₈₁	FXN ⁸¹⁻²¹⁰	MPP	130

Tot i aquests resultats prometedors, aquestes partícules no són capaces de creuar la BHE, i per tant d'arribar al cervell. Per això, vam dissenyar una estratègia basada en la bioconjugació de pèptids llançadora en les lisines de les proteïnes de la envolta d'aquests virus (membrana lipídica amb proteïnes i glicoproteïnes).

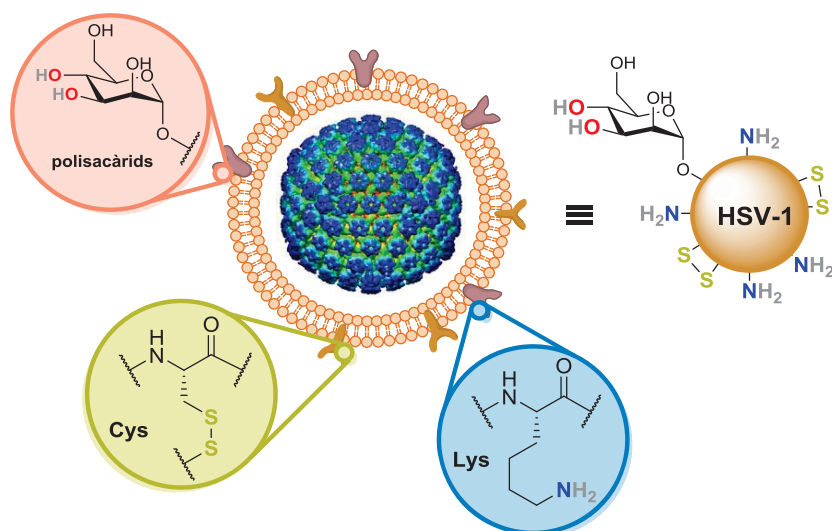


Figura R.17. Estructura simplificada de HSV-1, mostrant els grups reactius per a la bioconjugació: polisacàrids, cisteïnes (Cys) formant ponts disulfur, i lisines (Lys). Creada usant ChemBioDraw, amb l'estructura de la càpsida C de HSV-1,⁹⁹ EMDB ID# EMD-5659.

⁹⁹ Les càpsides C són les formes més properes als virions madurs.

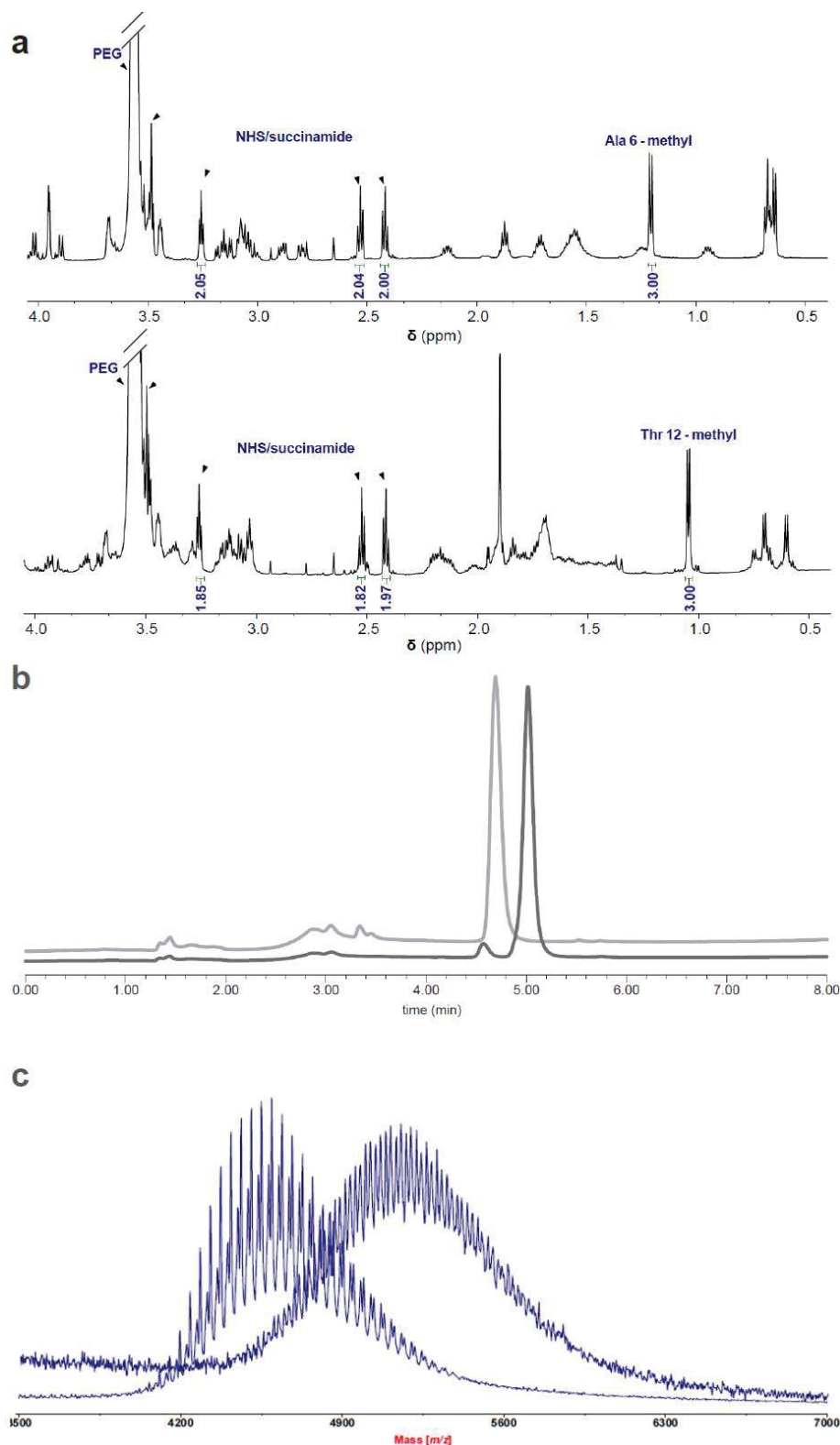


Figura R.18. Caracterització de NHS-PEG₃₅₀₀-rD-HAI i -rD-THR: **(a)** espectre de ¹H-RMN (part superior i inferior, respectivament), **(b)** cromatogrames de RP-HPLC usant una columna C₁₈ i un gradient lineal de 0 a 100% amb CH₃CN (gris fluix i fort, respectivament) i **(c)** espectre de MALDI-TOF MS (distribució de masses de la dreta i de l'esquerra, respectivament). Creada usant Adobe Illustrator i InDesign.

A part, per tal d'aconseguir una millor exposició dels pèptids llançadora i que poguessin interactuar amb el receptor del qual en són lligands (TfR), es va col·locar un espaiador entre el grup reactiu a lisines (ester de NHS) i el pèptid llançadora. Es va seleccionar un polietilenglicol de 3500 Da per dur a terme aquesta funció, ja que és un polímer soluble en aigua, de baixa immunogenicitat i aprovat per la FDA. Així, es van preparar els compostos NHS-PEG₃₅₀₀-(pèptid llançadora) usant metodologia de síntesi de pèptids en fase sòlida (SPPS) adaptada a les nostres condicions (pels pèptids llançadora *rD-HAI* i *rD-THR*). Posteriorment, es van caracteritzar per espectrometria de masses MALDI-TOF, RMN de protó i RP-HPLC (**R.18**; pureses >95%).

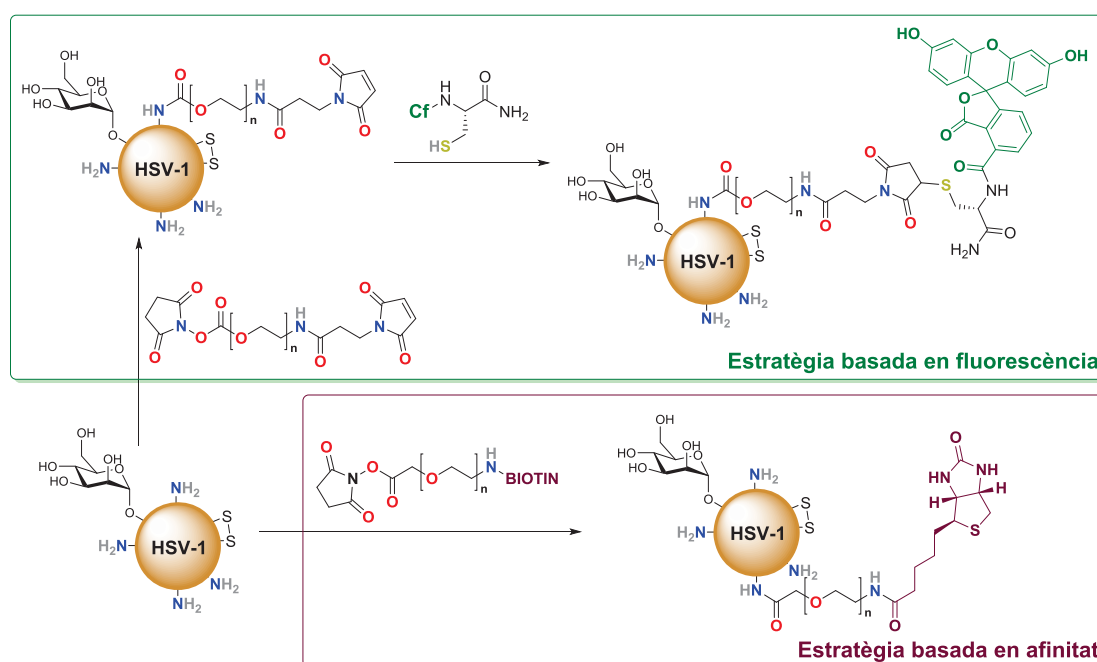


Figura R.19. Estratègies reporteres de bioconjugació. Totes les reaccions fetes en HBSS a pH 7.4. Creat usant ChemBioDraw.

Per tal de quantificar la funcionalització de les partícules virals es van dissenyar dues estratègies basades, respectivament, en fluorescència i afinitat (**Figura R.19**). Finalment, per caracteritzar aquests conjugats HSV-1 amb pèptids llançadora es van fer servir diverses tècniques (SDS-PAGE, western blot, espectrometria de masses, TEM, DLS i potencial ζ) (**Figura R.20**). Les tècniques que van ser més útils per a avaluar la bioconjugació van resultar DLS i potencial ζ , que van permetre seguir la mida d'aquestes partícules i la conjugació, respectivament.

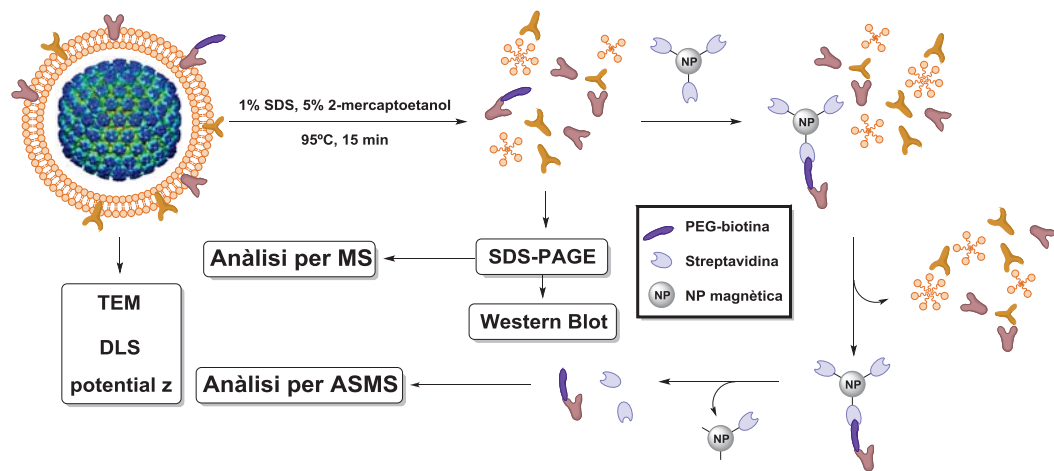


Figura R.20. Metodologies usades en la caracterització de les partícules virals de HSV-1. Creat usant ChemBioDraw, amb l'estructura de la càpsida C de HSV-1, EMDB ID# EMD-5659.

CONCLUSIONS

1. Un disseny híbrid que combina els pèptids llançadora de transport passiu (NMePhe)₄ i l'aminoàcid prolina ha assolit valors de solubilitat en aigua en el rang mil·limolar baix, incrementat en tres ordres de magnitud respecte el disseny previ.
2. El transport de (PhPro)₄ és set vegades superior comparat amb el pèptid (NMePhe)₄, ambdós portant NIP o L-DOPA. A més, el (PhPro)₄ manté la permeabilitat tant lliure com portant càrregues, a diferència del (NMePhe)₄ que disminueix el seu transport.
3. L'anàlisi del transport de la biblioteca dels 16 estereoisòmers ha revelat que la estereoquímica juga un paper important en la difusió passiva a través de membranes biològiques.
4. Tres anàlegs de la versió *retro-D* del pèptid llançadora HAI, tots compartint la substitució de la mateixa prolina, tenen un transport dues vegades el del pèptid original. Dos d'ells incrementen la diferència de transport respecte l'original (quatre i vuit vegades superior) un cop assajats en medi de cultiu.
5. Usant una petita modificació (acetilació de l'*N*-terminal), un nou mètode que combina models *in vitro* (cel·lulars) de la BHE i espectrometria de masses MALDI-TOF permet un increment en la sensibilitat de tres ordres de magnitud comparant amb el mètode estàndard (RP-HPLC-PDA), i el ús de medi de cultiu en l'assaig.
6. La injecció de pèptids llançadora formats per aminoàcids L (HAI i THR) produeix una baixa resposta immunològica (humoral), la qual encara és més baixa per les respectives versions *retro-D*, formades per aminoàcids D.
7. L'intent de bioconjuguar l'*N*-terminal de la frataxina (FXN) no han tingut èxit degut a la falta d'estabilitat de d'aquesta regió de la proteïna.

8. La unió de pèptids llançadora sobre herpesvirus usant la bioconjugació a lisines ha permès la modificació d'aquestes partícules virals en un sol pas, reduint la manipulació de la mostra i així preservant millor la seva integritat estructural. A més, l'ús de PEG₃₅₀₀ com a espaiador entre el virus i el pèptid llançadora dificulta el reconeixement per anticossos i al mateix temps manté la infectivitat.

9. La combinació de mètodes de biologia molecular (SDS-PAGE, western blot), de proteòmica (espectrometria de masses) i biofísics (TEM, DLS i potencial ζ) ha permès la caracterització dels virus modificats.

